



College of Engineering, Design and Physical Sciences

WNCC Research Centre

Metamaterials and their Applications on Antenna Gain Enhancement

Author:

ROOHOLLAH HAGHPANAHAN

Supervised by:

Dr. RAJAGOPAL NILAVALAN

Professor HAMED AL-RAWESHIDY

June 2015

A thesis submitted in fulfilment of the requirement for award of the degree of
Doctor of Philosophy in Systems Engineering

Submitted for examination

Abstract

This thesis is devoted to potential applications of metamaterials in antenna structures as well as metamaterials behaviour, characterisation, structure design, simulation and extraction of parameters. The focus of this work is on the practical application of metamaterial structures for antenna performance enhancement. This thesis comprises three key parts;

In the first part, theory of metamaterials is investigated including fields, polarisation, effective and average parameters, parameters extraction and transmission line (TL) model.

In part two, zero index metamaterials (ZIM) theory is studied. The use of ZIM to form a highly directive medium is illustrated. A comparative study between different ZIM structures is conducted with a special attention to their operational bandwidth. ANSYS HFSS is used to model ZIM structures where simulation results show a bandwidth between 7.4% and 14.0%. Then two novel ZIM structures with a bandwidth of up to 33% are proposed. The first proposed ZIM is used to form a highly directive shell. Four directive shells are designed and placed around the dipole antenna where a gain increase of up to 6.8 *dBi* is obtained along the desired direction. Further, proposed ZIM cells are integrated with a quasi-Yagi antenna in order to increase its gain. Simulation results demonstrate gain enhancement for frequencies over which the proposed structure expresses ZIM properties.

In part three, a new technique is established to design a metamaterial lens. The new technique is based on wave interference phenomena where engineered wave interference results in a desired spatial energy distribution. It is shown theoretically that having 180° phase difference between interfering waves results in a focused emission. Both hypothetical and metamaterial realisation models of a 180° phase shifter for a patch antenna are designed and simulated where a gain enhancement of 8 *dBi* and 5.77 *dBi* are achieved, respectively.

Further, the concept of intended phase shift between interfering waves is used to design a novel bi-reflectional ground plane which can focus the reflected emission and consequently, increase the antenna directivity. In the theoretical model, the Perfect-E and Perfect-H planes are combined to form a bi-reflectional plane, whereas the practical model is designed using the copper cladding for the Perfect-E plane and the mushroom structure for the perfect-H plane. Both square and hexagonal geometries are used to form the mushroom structure. Simulation results confirm a gain enhancement of 5.4 *dBi* for the design using the square mushroom structure and a gain enhancement of 3.3 *dBi* for the design using the hexagonal mushroom structure.

Table of Contents

List of Abbreviations.....	v
Glossary of Terms	vii
List of Figures	ix
List of Tables.....	xv
Acknowledgements	xvi
Chapter 1 Introduction	1
1 - 1 Motivation.....	1
1 - 2 Metamaterial Definition.....	1
1 - 3 Metamaterial Embedded Antennae.....	3
1 - 3 - 1 Composite Right/Left Handed (CRLH) Metamaterial Antennae.....	3
1 - 3 - 2 Metamaterial Shell-Based Antennae	6
1 - 3 - 3 Near-Field Coupling.....	9
1 - 3 - 4 DBE/MPC based Antennae	12
1 - 3 - 5 Mu-Zero Resonance (MZR) Antennae.....	14
1 - 3 - 6 SRR/CSRR Resonator Embedded Antennae	14
1 - 3 - 7 Meta-Surface Loaded Antennae	17
1 - 4 Scope of the Thesis	21
1 - 5 Contribution to Knowledge	22
1 - 6 Thesis Overview	23
Chapter 2 Planar Metamaterial Theory and Analysis	25
2 - 1 Introduction.....	25
2 - 2 Metamaterial Classification	26
2 - 2 - 1 Local and Non-Local Field Response of Metamaterials	27
2 - 2 - 2 Strong Spatial Dispersion (SSD).....	28
2 - 2 - 3 Weak Spatial Dispersion (WSD).....	29

2 - 2 - 4	Polarisation Current in Media with Weak Spatial Dispersion.....	29
2 - 2 - 5	Electric and Magnetic Polarisation Current	30
2 - 2 - 6	Material Parameters.....	31
2 - 2 - 7	Metamaterials and Weak Spatial Dispersion.....	32
2 - 3	Material Parameter Extraction	33
2 - 3 - 1	Average and Effective Constitutive Parameters.....	33
2 - 3 - 2	Effective Parameters.....	37
2 - 4	Transmission Line (TL) Theory	46
2 - 4 - 1	Equivalent Circuit for a Two-port Microwave Network.....	46
2 - 4 - 2	Metamaterial Unit Cell Equivalent Circuit.....	49
2 - 5	Summary.....	52
Chapter 3	Zero Index Metamaterials.....	54
3 - 1	Introduction.....	54
3 - 2	Theory of High Directive Media	55
3 - 3	Wave Propagation and Dispersion Relation in Anisotropic ZIM Medium.....	57
3 - 4	Zero Index Materials (ZIM) Unit Cells	60
3 - 5	ZIM Related Topologies	62
3 - 5 - 1	Effective and Physical Length.....	63
3 - 5 - 2	Fixed length ZIM with different Meander Structures	69
3 - 6	Novel ZIM Structure.....	71
3 - 6 - 1	Genetic Algorithm.....	72
3 - 6 - 2	Applying GA Optimisation to Proposed Cell.....	73
3 - 7	ZIM Embedded Antennae.....	81
3 - 7 - 1	Optical Transformation	81
3 - 7 - 2	High Directive Emission Using Transformation Optic	83
3 - 7 - 3	High Directive ZIM Shell.....	85

3 - 8 ZIM Loaded Planar Antenna	94
3 - 8 - 1 ZIM loaded Quasi-Yagi Antenna	95
3 - 8 - 2 Fabrication and Measurements	103
3 - 9 Summary	108
Chapter 4 Energy Spatial Redistribution based on Propagating Wave Interference using a Metamaterial Phase Shifter	111
4 - 1 Introduction.....	111
4 - 2 Energy Re-distribution.....	116
4 - 2 - 1 Plane Waves Interference	116
4 - 2 - 2 Gaussian Waves Interference	117
4 - 3 Antenna Gain Enhancement	121
4 - 3 - 1 180° Phase Shifter	122
4 - 4 Patch Gain Enhancement	124
4 - 5 Design Optimisation	129
4 - 6 Metamaterial Realisation of the Phase Shifter Layer	131
4 - 6 - 1 Unit Cell Design and Simulation Setup.....	133
4 - 6 - 2 Dispersion Diagram Extraction	134
4 - 6 - 3 Bloch Impedance Extraction	135
4 - 7 Cascading Topology	138
4 - 8 Unit Cell Optimisation.....	140
4 - 8 - 1 Applying GA Optimisation to CLRR.....	140
4 - 9 Interaction between the Metamaterial based 180° Phase Shifter and a Plane Wave.....	144
4 - 10 Patch Gain Enhancement using Metamaterial based 180° Phase Shifter	145
4 - 11 Fabrication and Measurements	149
4 - 12 Summary	151
Chapter 5 Bi-reflectional Ground Plane.....	153

5 - 1 Introduction.....	153
5 - 2 Theoretical Model.....	154
5 - 3 Practical Design	158
5 - 3 - 1 Electromagnetic Band Gap (EBG) Structures	158
5 - 3 - 2 Surface Waves	158
5 - 3 - 3 Impedance of a Flat Metal Sheet	161
5 - 3 - 4 High Impedance Surfaces	161
5 - 3 - 5 Square-Shape Mushroom Structure.....	162
5 - 3 - 6 Dipole Integrated with Proposed Bi-reflectional Ground Plane.....	173
5 - 3 - 7 Hexagonal-Shape Mushroom Structure	178
5 - 3 - 8 Dipole Integrated with Proposed Bi-reflectional Ground Plane.....	179
5 - 4 Summary	181
Chapter 6 Conclusions	183
6 - 1 Summary.....	183
6 - 2 Future Research	187
Appendix MATLAB Codes	188
References	195

List of Abbreviations

AMC	Artificial Magnetic Conductor
CLRR	Capacitively Loaded Ring Resonator
CPW	Coplanar Waveguide
CRLH	Composite Right/Left Handed
CSRR	Complementary Split Ring Resonator
DBE	Degenerated Band Edge
DNG	Double-Negative
EBG	Electromagnetic Band Gap
EM	ElectroMagnetic
ENG	Epsilon-Negative
ESA	Electrically Small Antenna
EZ	Epsilon Zero
FBW	Fractional Bandwidth
GA	Genetic Algorithm
LBC	Linked Boundary Condition
LH	Left Handed
LPDA	Log-Periodic Dipole Antenna
LWA	Leaky-Wave Antenna
MCP	Magnetolectric Coupling Parameter
MNG	Mu-Negative
MPC	Magnetic Photonic Crystal
MPIE	Multi Potential Integral Equation
MZ	Mu-Zero
MZR	Mu-Zero Resonator
NFRP	Near-Field Resonant Parasitic
NIM	Negative Index Materials
PML	Perfectly Matched Layer
PRS	Partially Reflective Surface
RF	Radio Frequency
RH	Right Handed

RIS	Reactance Impedance Surface
SRR	Split Ring Resonator
SSD	Strong Spatial Dispersion
TE	Transverse Electric
TEM	Transverse Electromagnetic
TL	Transmission Line
TM	Transverse Magnetic
UC-PBG	Uniplanar Compact Photonic Band Gap
UWB	Ultra-Wide Bandwidth
WSD	Weak Spatial Dispersion
ZIM	Zero Index Materials

Glossary of Terms

Accepted Power	The accepted power is the time-averaged power (in Watts) entering a radiating antenna structure through one or more ports.
Chu Limit	Chu limit is a fundamental limit on the quality factor. It sets a lower limit on the Q factor for a small radio antenna. In practice this means that there is a limit to the bandwidth of data that can be sent to and received from small antennae such as are used in mobile phones.
Directivity	Directivity is defined as the ratio of an antenna's radiation intensity in a given direction to the radiation intensity averaged over all directions.
Gain	Gain is four pi times the ratio of an antenna's radiation intensity in a given direction to the total power accepted by the antenna.
Permeability	The permeability is the degree of magnetisation of a substance in a given magnetic field.
Permittivity	The permittivity is a measure of the ability of a material to interact with an electric field and become polarised by the field.
Plasma frequency	The plasma frequency is a frequency at which rapid oscillation of the electron density in conducting media such as plasmas or metals occurs.
Quality Factor	The quality factor, Q , is a measure of how much energy is lost in the structure due to lossy materials. Higher Q indicates a lower rate of energy loss relative to the stored energy of the resonator
Radiated Power	Radiated power is the amount of time-averaged power (in Watts) exiting a radiating antenna structure through a radiation boundary.

Radiation Efficiency	The radiation efficiency is the ratio of the radiated power to the accepted power
Radiation Intensity	The radiation intensity, U , is the power radiated from an antenna per unit solid angle.
Realised Gain	Realised gain is four pi times the ratio of an antenna's radiation intensity in a given direction to the total power incident upon the antenna port(s).
Resonant Frequency	A resonant frequency is a natural frequency of a system determined by the physical parameters of the vibrating system. An Electrical resonance occurs in an electric circuit at a particular resonant frequency when the impedance of the circuit is at a minimum in a series circuit or at maximum in a parallel circuit.
<i>dBi</i>	Decibel-isotropic (<i>dBi</i>) is a logarithmic unit to express the forward gain of an antenna compared with the hypothetical isotropic antenna, which uniformly distributes energy in all directions.

List of Figures

FIG. 1-1. ALL POSSIBLE ISOTROPIC AND LOSSLESS MATERIAL IN E- μ PLANE [3].....	2
FIG. 1-2. TL THEORY, EQUIVALENT FOR SYMMETRICAL CRLH UNIT CELLS, (A) T-TYPE MODEL (B) π -TYPE MODEL [59]	3
FIG. 1-3. CRLH TL ANTENNA OPERATING AT ZEROth RESONANCE MODE (A) PERSPECTIVE VIEW (B) FABRICATED PROTOTYPE [24]	4
FIG. 1-4. CRLH SIW SLOT ANTENNA (A) PERSPECTIVE VIEW (B) FABRICATED PROTOTYPE [59].....	5
FIG. 1-5. MUSHROOM ZEROth ORDER RESONANCE ANTENNA [36]	5
FIG. 1-6. CPW FED ZEROth ORDER RESONANCE ANTENNA [60]	6
FIG. 1-7. CIRCULARLY POLARISED PATCH ANTENNA LOADED WITH MUSHROOM STRUCTURE (A) PERSPECTIVE VIEW (B) FABRICATED PROTOTYPE [61].....	6
FIG. 1-8. CENTRE-FED DIPOLE ANTENNA SURROUNDED BY AN ENG SHELL [33].....	7
FIG. 1-9. COUPLING BETWEEN DRIVEN AND THE NEAR-FIELD RESONANT PARASITIC (NFRP) ELEMENTS AND EQUIVALENT RLC MODEL CORRESPONDING TO ENTIRE ANTENNA SYSTEM [58].....	7
FIG. 1-10. AN ESA BASED ON INDUCTIVE MEANDER LINE STRUCTURE (A) PERSPECTIVE VIEW (B) FABRICATED PROTOTYPE [62]	9
FIG. 1-11. AN ESA BASED ON INDUCTIVE Z STRUCTURE (A) PERSPECTIVE VIEW (B) FABRICATED PROTOTYPE [19] ...	10
FIG. 1-12. ELECTRIC COUPLING, A ELECTRIC MONOPOLE ANTENNA (A) ELECTRICALLY COUPLED (B) MAGNETICALLY COUPLED [66].....	10
FIG. 1-13. MAGNETIC COUPLING, DRIVEN HALF-LOOP ANTENNA COUPLING WITH CLL NFRP ELEMENT [54]	11
FIG. 1-14. 3-D MAGNETIC COUPLED CLL NFRP ELEMENT (A) PERSPECTIVE VIEW (B) FABRICATED PROTOTYPE [54] 11	11
FIG. 1-15. DUAL-BAND CIRCULAR POLARISED ANTENNA WITH TWO PAIRS OF PROTRACTOR NFRP ELEMENT (A) PERSPECTIVE VIEW (B) FABRICATED PROTOTYPE [54]	12
FIG. 1-16. MAGNETOELECTRIC COUPLING, AN ELECTRIC MONOPOLE ANTENNA (A) COUPLED MAGNETICALLY (B) COUPLED TO A MAGNETIC NFRP STRUCTURE [54]	12
FIG. 1-17. (A) MICROSTRIP-DBE LAYOUT AND FABRICATED PROTOTYPE [44] (B) MICROSTRIP-MPC LAYOUT AND FABRICATED PROTOTYPE [69].....	13
FIG. 1-18. DUAL-BAND MZR ANTENNA, (A) PERSPECTIVE VIEW (B) FABRICATED PROTOTYPE [70].....	14
FIG. 1-19. SPHERICAL WIRE SPLIT RING ANTENNA (A) PERSPECTIVE VIEW (B) FABRICATED PROTOTYPE [74]	15
FIG. 1-20. INDUCTIVELY-FED VERTICAL SRR ANTENNA (A) PERSPECTIVE VIEW (B) FABRICATED PROTOTYPE (C) SIMULATED AND MEASURED RETURN LOSS [75]	15
FIG. 1-21. DUAL-BAND, DUAL POLARISED CSRR EMBEDDED ANTENNA (A) PERSPECTIVE VIEW (B) FABRICATED PROTOTYPE (C) SIMULATED AND MEASURED RETURN LOSS [76]	16
FIG. 1-22. TRIPLE-BAND ANTENNA WITH DIFFERENT POLARISATION (A) PERSPECTIVE VIEW (B) FABRICATED PROTOTYPE (C) SIMULATED AND MEASURED RETURN LOSS [76]	16
FIG. 1-23. RIS LOADED PATCH ANTENNA (A) PERSPECTIVE VIEW (B) RIS SURFACE (C) FABRICATED PROTOTYPE [83] 17	17

FIG. 1-24. PHOTOGRAPHS OF (A) PATCH ANTENNA WITH AMC GROUND PLANE (B) PRS SUPERSTRATE (C) RESONANT CAVITY FORMED BY PEC AND PRS [81]	18
FIG. 2-1. METAMATERIAL CLASSIFICATION.....	27
FIG. 2-2. SRR STRUCTURE AND ITS EQUIVALENT RESONANT CIRCUIT.....	34
FIG. 2-3. METAMATERIAL PERIODIC STRUCTURE.....	35
FIG. 2-4. MULTIPLE REFLECTIONS AT AIR-SAMPLE INTERFACES	38
FIG. 2-5. MULTIPLE REFLECTIONS SIGNAL FLOW	39
FIG. 2-6. MATERIAL PARAMETERS EXTRACTION FOR A DNG UNIT CELL (A) MODEL SETUP (B) RESULTS REPORTED IN [92] (C) RESULTS FROM HFSS SIMULATION AND MATLAB INTERPRETATION	45
FIG. 2-7. A RANDOM OBSTACLE LOCATED IN A WAVEGUIDE	46
FIG. 2-8. EQUIVALENT CIRCUIT FOR A TWO-PORT MICROWAVE NETWORK	48
FIG. 2-9. TRANSMISSION LINE MODEL AND RELATIVE DISPERSION DIAGRAM FOR (A) RH (B) LH MATERIALS	50
FIG. 2-10. TL THEORY, EQUIVALENT FOR SYMMETRICAL CRLH UNIT CELLS, (A) T-TYPE MODEL (B) Π -TYPE MODEL (C) IDENTICAL MODEL FOR PERIODIC CRLH UNIT CELL [59]	51
FIG. 2-11. DISPERSION DIAGRAM (A) UNBALANCED CRLH, $\omega_{se} \neq \omega_{sh}$ (B) BALANCED CRLH, $\omega_{se} = \omega_{sh}$.	51
FIG. 3-1. DIPOLE ANTENNA SURROUNDED BY ZIM MEDIA (A) SNELL'S LAW (B) DISTRIBUTION OF E-FIELD MAGNITUDE SIDE VIEW (C) DISTRIBUTION OF E-FIELD MAGNITUDE TOP VIEW.....	56
FIG. 3-2. E-FIELD DISTRIBUTION FOR A WAVE COMES FROM A DIPOLE ANTENNA IN (A) ANISOTROPIC VACUUM (B) ZERO-PERMITTIVITY MEDIUM	60
FIG. 3-3. ZERO INDEX REGION (BLUE) WITH SMALL LOSSES AND RESONANT REGION (RED) WITH LARGE IMAGINARY PART AND CONSEQUENTLY LARGE LOSSES INDICATED ON GRAPH OF (A) PERMITTIVITY OF ROD STRUCTURE (B) PERMEABILITY OF CSRR STRUCTURE	62
FIG. 3-4. ZIM TOPOLOGIES; (A) I-SHAPE (ROD), (B) C-SHAPE, (C) S-SHAPE, (D) W-SHAPE, (E) MEANDERLINE.....	63
FIG. 3-5. PHYSICAL AND EFFECTIVE LENGTH OF MEANDER-LINE ZIM STRUCTURE WITH COPPER TRACE WIDTH OF $50\mu\text{m}$ AND $300\mu\text{m}$	66
FIG. 3-6. RELATIVE PERMITTIVITY OF MEANDERLINE STRUCTURE WITH DIFFERENT COPPER TRACE WIDTH, REAL PART AND IMAGINARY PART.....	67
FIG. 3-7. RELATIVE PERMITTIVITY OF MEANDERLINE STRUCTURE WITH DIFFERENT COPPER TRACE WIDTHS, REAL PART AND IMAGINARY PART	67
FIG. 3-8. RESONANCE FREQUENCY OF MEANDERLINE ZIM STRUCTURES, FOR DIFFERENT NUMBER OF MEANDERS AND DIFFERENT LENGTH OF HORIZONTAL COPPER TRACE.....	68
FIG. 3-9. TL METAMATERIAL UNIT CELL EQUIVALENT.....	68
FIG. 3-10. FIXED-LENGTH ZIM AND THEIR CORRESPONDING RELATIVE PERMITTIVITIES	69
FIG. 3-11. PERMITTIVITY FOR CELLS WITH PAIRED SCATTERING PARTICLE	70
FIG. 3-12. S-PARAMETERS AND EXTRACTED EFFECTIVE MATERIAL PARAMETERS FOR PAIRED C-SHAPE.....	71
FIG. 3-13. PROPOSED UNIT CELL STRUCTURE	72
FIG. 3-14. COUNTINUOUS GA FLOWCHART	73

FIG. 3-15. S-PARAMETERS AND EXTRACTED EFFECTIVE MATERIAL PARAMETERS FOR PROPOSED STRUCTURE WITH EZ PROPERTY, (A) MAGNITUDE OF S-PARAMETERS, (B) PHASE OF S-PARAMETERS (C) EFFECTIVE RELATIVE PERMITTIVITY, (D) EFFECTIVE RELATIVE PERMEABILITY	75
FIG. 3-16. PROPOSED UNIT CELL STRUCTURE FORMED BY A SMALL PATCH ADDED TO THE CENTRE OF ROD STRUCTURE	76
FIG. 3-17. S-PARAMETERS AND EXTRACTED EFFECTIVE MATERIAL PARAMETERS FOR SECOND PROPOSED STRUCTURE WITH EZ PROPERTY, (A) MAGNITUDE OF S-PARAMETERS, (B) PHASE OF S-PARAMETERS (C) EFFECTIVE RELATIVE PERMITTIVITY, (D) EFFECTIVE RELATIVE PERMEABILITY	78
FIG. 3-18. PERMITTIVITY AND PERMEABILITY OF THE PATCH STRUCTURE	79
FIG. 3-19. BLOCH IMPEDANCE FOR (A) I-SHAPE (B) THE PROPOSED STRUCTURE, (C) REAL PART OF PERMITTIVITY OF BOTH STRUCTURES	80
FIG. 3-20. 2-D COORDINATE TRANSFORMATION FOR HIGHLY DIRECTIVE MEDIUM. (A) GEOMETRY OF FAN-SHAPED VIRTUAL SPACE (B) SIMPLIFIED VIRTUAL SPACE TO TRIANGLE SHAPE. (C) GEOMETRY OF THE TRIANGLE PHYSICAL SPACE [119].....	83
FIG. 3-21. EZ SHELL EMBEDDED DIPOLE ANTENNA, (A) UNIT CELL, (B) TRIMETRIC VIEW, (C) TOP VIEW	85
FIG. 3-22. (A) POLAR PLOT OF TOTAL GAIN IN dB_i , (B) CO-POLARISED GAIN IN dB_i , E-PLANE (LEFT) AND H-PLANE (RIGHT) (C) CROSS-POLARISED GAIN IN dB_i , E-PLANE (LEFT) AND H-PLANE (RIGHT)	86
FIG. 3-23. (A) SRR DESIGNED TO HAVE MZ PROPERTIES AROUND 15 GHz, (B) MZ SHELL EMBEDDED DIPOLE ANTENNA, TRIMETRIC VIEW (LEFT), TOP VIEW (RIGHT).....	87
FIG. 3-24. MZ SHELL EMBEDDED DIPOLE ANTENNA, (A) TOTAL GAIN 3-D POLAR IN dB_i , (B) CO-POLARISATION; GAIN IN dB_i , E-PLANE (LEFT) AND H-PLANE (RIGHT), (C) CROSS-POLARISATION; GAIN IN dB_i , E-PLANE (LEFT) AND H-PLANE (RIGHT).....	89
FIG. 3-25. FIRST ZIM SHELL DESIGN WITH BOTH EZ AND MZ PROPERTIES, (A) TRIMETRIC VIEW, (B) TOP VIEW.....	90
FIG. 3-26. SIMULATION RESULTS FOR FIRST ZIM SHELL, (A) TOTAL GAIN 3-D POLAR IN dB_i , (B) CO-POLARISATION; GAIN IN dB_i , E-PLANE (LEFT) AND H-PLANE (RIGHT) (C) CROSS-POLARISATION; GAIN IN dB_i , E-PLANE (LEFT) AND H-PLANE (RIGHT)	91
FIG. 3-27. SECOND ZIM SHELL DESIGN WITH BOTH EZ AND MZ PROPERTIES, (A) TRIMETRIC VIEW, (B) TOP VIEW... ..	92
FIG. 3-28. SIMULATION RESULTS FOR SECOND ZIM SHELL, (A) TOTAL GAIN 3-D POLAR IN dB_i , (B) CO-POLARISATION; GAIN IN dB_i , E-PLANE (LEFT) AND H-PLANE (RIGHT) (C) CROSS-POLARISATION; GAIN IN dB_i , E-PLANE (LEFT) AND H-PLANE (RIGHT)	93
FIG. 3-29. TYPICAL SCHEMATIC OF A QUASI-YAGI ANTENNA AND ITS DIMENSIONS	97
FIG. 3-30. EFFECTIVE PERMITTIVITY OF ZIM STRUCTURE	98
FIG. 3-31. ZIM EMBEDDED QUASI-YAGI ANTENNA (A) PROPOSED ANTENNA DESIGNS (B) TOTAL GAIN COMPARISON (C) RETURN LOSS COMPARISON.....	99
FIG. 3-32. CO- AND CROSS-POLARISED REALISED GAIN OF ORIGINAL AND ZIM LOADED QUASI-YAGI ANTENNA	102
FIG. 3-33. MANUFACTURED PROPOSED ANTENNAE, (A) FABRICATION PROCEDURE, (B) TRADITIONAL QUASI-YAGI, (C) QUASI-YAGI WITH PATTERN B ON TOP, (D) QUASI-YAGI WITH PATTERN C ON TOP.....	104

FIG. 3-34. MEASURED VALUES FOR PROPOSED ANTENNAE, (A) RETURN LOSS (DBI), (B) $ S_{21} $ AT $\varphi = 0$, (C) $ S_{21} $ AT $\varphi = 30$, (D) $ S_{21} $ AT $\varphi = 45$	106
FIG. 3-35. ANTENNA RADIATION PATTERN FOR TRADITIONAL QUASI-YAGI (BLUE LINE) , QUASI-YAGI WITH SINGLE SIDED PATTERN (B) (RED LINE) AND QUASI-YAGI WITH SINGLE SIDED PATTERN (C) (GREEN LINE).....	108
FIG. 4-1. GEDANKEN EXPERIMENT; TWO MONOCHROMIC WAVES WITH 180° PHASE DIFFERENCE AND EQUAL INTENSITY, FREQUENCY, POLARISATION AXIS, AND DIAMETERS PROPAGATING ALONG X- AND Y-DIRECTIONS	112
FIG. 4-2. MICROWAVE GAUSSIAN WAVES WITH SAME FREQUENCY, INTENSITY, POLARISATION AXIS WHICH ARE 180° OUT OF THE PHASE (A) GEDANKEN EXPERIMENT WITH AND WITHOUT PEC CONDITION ON THE FRINGE PLANE (B) THE ELECTRIC FIELD DISTRIBUTION (C) POYNTING VECTOR IS PARALLEL TO THE FRINGE PLANE AT $\Phi=45^\circ$	115
FIG. 4-3. GAUSSIAN BEAM VECTOR.....	117
FIG. 4-4. TWO GAUSSIAN WAVES WITH SAME FREQUENCY, ENERGY INTENSITY AND POLARISATION AXIS.....	118
FIG. 4-5. TWO GAUSSIAN WAVES WITH DIFFERENT PHASE SHIFT WHICH ARE PLACED IN $\lambda/3$ DISTANCE FROM EACH OTHER	120
FIG. 4-6. HUYGENS' PRINCIPLE	121
FIG. 4-7. 180° PHASE SHIFTER.....	122
FIG. 4-8. POYNTING VECTOR FOR (A) PROPAGATING PLANE WAVE IN THE AIR; SIDE VIEW (LEFT), FRONT VIEW (RIGHT) (B) INCIDENT PLANE WAVE UPON THE 180° PHASE SHIFTER; SIDE VIEW (LEFT), FRONT VIEW (RIGHT)	124
FIG. 4-9. SIMULATED STRUCTURE.....	124
FIG. 4-10. NORMALISED GAIN IN (A) H-PLANE PATTERNS, (B) E-PLANE PATTERNS, (C) RETURN LOSS (D) TABLE OF ANTENNA PARAMETERS.....	125
FIG. 4-11. VISUALISATION OF REAL PART OF POYNTING VECTOR FOR A SLAB OF 180° PHASE SHIFTER PLACED ON TOP OF PATCH ANTENNA	126
FIG. 4-12. VISUALISATION OF REAL PART OF POYNTING VECTOR FOR A SLAB OF ORDINARY DIELECTRIC PLACED ON TOP OF PATCH ANTENNA	126
FIG. 4-13. (A) NORMALISED GAIN IN H-PLANE, (B) NORMALISED GAIN IN E-PLANE, (C) RETURN LOSS (D) TABLE OF ANTENNA PARAMETERS.....	127
FIG. 4-14. SIMULATION RESULTS FOR OPTIMISED DESIGN (A) NORMALISED GAIN IN H-PLANE, (B) NORMALISED GAIN IN E-PLANE, (C) RETURN LOSS, (D) TABLE OF ANTENNA PARAMETERS.....	130
FIG. 4-15. DESIGN FLOWCHART	133
FIG. 4-16. CLRR (A)UNIT CELL GEOMETRY, (B) UNIT CELL TOP VIEW, NOMINAL DIMENSIONS ARE $A=B=3\text{MM}$, $L_1=L_2=2.4\text{MM}$, $W_1=W_2=0.3\text{MM}$, $G=0.5\text{MM}$, $D=0.4\text{MM}$ AND $L_4=1.2\text{MM}$	134
FIG. 4-17. CLRR SIMULATION RESULTS (A) DISPERSION DIAGRAM, (B) S-PARAMETERS, (C) BLOCH IMPEDANCE (D) PHASE SHIFT.....	137
FIG. 4-18. (A) CASCADING TOPOLOGY (B) METAMATERIAL REALISATION OF A 180° PHASE SHIFTER.....	139
FIG. 4-19. OPTIMISED CLLR CELL (A) DISPERSION DIAGRAM (B) S-PARAMETERS (C) BLOCH IMPEDANCE (D) PHASE SHIFT.....	141

FIG. 4-20. 180° PHASE SHIFTER, (A) DISPERSION DIAGRAM (B) S-PARAMETERS (C) BLOCH IMPEDANCE (D) PHASE SHIFT.....	143
FIG. 4-21. PLANE EXCITATION OF 180° PHASE SHIFTER STRUCTURE, (A) UNIFORM POYNTING VECTOR (B) NON-UNIFORM POYNTING VECTOR.....	144
FIG. 4-22. THE PRACTICAL DESIGN WITH BLOCK OF (A) 5 AND, (B) 8 PHASE SHIFTER SLABS (C) NORMALISED H-PLANE RADIATION PATTERN (D) NORMALISED E-PLANE RADIATION PATTERN (E) ANTENNA PARAMETERS.....	147
FIG. 4-23. RADIATION PATTERN OF ORIGINAL AND 180° PHASE SHIFTER BLOCK.....	148
FIG. 4-24. FABRICATED ANTENNAE, (A) PATCH, (B) PATCH WITH 180° METAMATERIAL PHASE SHIFTER.....	149
FIG. 4-25. MEASURED VALUES FOR PATCH ANTENNA WITH AND WITHOUT METAMATERIAL PHASE SHIFTER, (A) $ S_{21} $ AT $\varphi = 0^\circ$, (B) $ S_{21} $ AT $\varphi = 30^\circ$, (C) $ S_{21} $ AT $\varphi = 45^\circ$	150
FIG. 4-26. MEASURED RADIATION PATTERNS AT 11 GHz, (A) GAIN IN H-PLANE (dBi), (B) GAIN IN E-PLANE (dBi).....	152
FIG. 5-1. (A) ELECTRIC CONDUCTOR SURFACE; E-FIELD HAS AN ANTI-NODE AND H-FIELD HAS A NODE (B) MAGNETIC CONDUCTOR SURFACE; E-FIELD HAS A NODE AND H-FIELD HAS AN ANTI-NODE	154
FIG. 5-2. GAUSSIAN WAVE INCIDENT UPON DIFFERENT GROUND PLANE CONSISTING OF (A) PE PLANE SURROUNDED BY PH PLANE (B) PH PLANE SURROUNDED BY PE PLANE (C) PE PLANE.....	155
FIG. 5-3. DIPOLE ANTENNA MOUNTED ON TOP OF THEORETICAL BI-REFLECTIONAL GROUND (A) TOP VIEW (B) SIDE VIEW, SIMULATION RESULTS FOR PE AND BI-REFLECTIONAL GROUND (C) REALISED GAIN AT E-PLANE (D) REALISED GAIN AT H-PLANE	157
FIG. 5-4. SURFACE WAVE ON DIELECTRIC-VACUUM INTERFACE.....	159
FIG. 5-5. MUSHROOM STRUCTURE(A) SQUARE GEOMETRY UNIT CELL AND ARRAY (B) HEXAGONAL GEOMETRY UNIT CELL AND ARRAY (C) EQUIVALENT CIRCUIT OF STRUCTURE FOR SURFACE CURRENTS.....	163
FIG. 5-6. SQUARE MUSHROOM STRUCTURE TRANSMISSION LINE EQUIVALENT	164
FIG. 5-7. MUSHROOM STRUCTURE, MODIFIED MODEL TO BE APPLICABLE TO DRIVEN MODE APPROACH.....	166
FIG. 5-8. ONE-DIMENSIONAL DISPERSION DIAGRAM	167
FIG. 5-9. EIGENMODE SOLUTION (A) MODEL SET UP (B) PERIODIC BOUNDARY CONDITION	168
FIG. 5-10. TWO-DIMENSIONAL DISPERSION DIAGRAM FOR SQUARE MUSHROOM STRUCTURE.....	169
FIG. 5-11. WAVEGUIDE SIMULATION FOR SQUARE GEOMETRY MUSHROOM STRUCTURE	170
FIG. 5-12. REFLECTION PHASE FROM SQUARE MUSHROOM STRUCTURE	171
FIG. 5-13. LBC SIMULATION SET UP FOR SQUARE GEOMETRY MUSHROOM STRUCTURE.....	172
FIG. 5-14. REFLECTION PHASE FROM SQUARE MUSHROOM STRUCTURE	173
FIG. 5-15. DIPOLE ANTENNA MOUNTED OVER A BI-REFLECTIONAL GROUND PLANE MADE OF SQUARE MUSHROOM STRUCTURE (A) TOP VIEW (B) SIDE VIEW	173
FIG. 5-16. REALISED GAIN (dBi) ACHIEVED BY BI-REFLECTIONAL GROUND PLANE WITH DIFFERENT MUSHROOM STRUCTURE LATTICE CONSISTING OF M×N CELLS	174
FIG. 5-17. BI-REFLECTIONAL GROUND PLANES CONSISTING OF MUSHROOM LATTICE OF $[m \times m]$ CELLS (A) RETURN LOSS (B) REALISED GAIN (dBi)	175

FIG. 5-18. (A) RAY TRACING DIAGRAM FOR A BI-REFLECTIONAL GROUND PLANE (B) PHASE DIFFERENCE BETWEEN REFLECTED RAY FROM MUSHROOM LATTICE AND METAL	176
FIG. 5-19. PERFECT GROUND, HYPOTHETICAL MODEL AND GROUND MADE OF SQUARE MUSHROOM (A) RETURN LOSS (B) REALISED GAIN AT E-PLANE (C) REALISED GAIN AT H-PLANE	177
FIG. 5-20. HEXAGONAL MUSHROOM STRUCTURE (A) MODEL SET UP (B) REFLECTION PHASE	178
FIG. 5-21. DIPOLE ANTENNA MOUNTED OVER A BI-REFLECTIONAL GROUND PLANE MADE OF HEXAGONAL MUSHROOM STRUCTURE (A) TOP VIEW (B) SIDE VIEW	179
FIG. 5-22. PERFECT GROUND, HYPOTHETICAL MODEL AND GROUND MADE OF SQUARE AND HEXAGONAL MUSHROOM RESULTS (A) RETURN LOSS (B) NORMALISED REALISED GAIN AT E-PLANE (C) NORMALISED REALISED GAIN AT H-PLANE	180
FIG. 5-23. REALISED GAIN ACHIEVED FOR DIPOLE ANTENNA USING CONVENTIONAL GROUND PLANE, HYPOTHETICAL BI-REFLECTIONAL GROUND AND BI-REFLECTIONAL GROUND MADE OF A LATTICE OF SQUARE AND HEXAGONAL MUSHROOM STRUCTURE	181

List of Tables

TABLE 1-1. METAMATERIAL INSPIRED ANTENNAE	21
TABLE 3-1. ZIM STRUCTURE RESONANT FREQUENCY, ELECTRIC LENGTH AND PHYSICAL LENGTH	65
TABLE 3-2. UNIT CELL OPTIMISATION PARAMETERS, INITIAL AND FINAL VALUES	74
TABLE 3-3. PROPOSED ZIM UNIT CELL OPTIMISATION PARAMETERS, INITIAL AND FINAL VALUES.....	77
TABLE 3-4. PLANAR ANTENNAE	95
TABLE 4-1. OPTIMISATION PARAMETERS, INITIAL AND FINAL VALUES.....	129
TABLE 4-2. UNIT CELL OPTIMISATION PARAMETERS, INITIAL AND FINAL VALUES.....	140
TABLE 5-1. BI-REFLECTIONAL GROUND OPTIMISATION PARAMETERS, INITIAL AND FINAL VALUES	156

Acknowledgements

This research project would not have been possible without the support of many people. I wish to express my gratitude to my supervisor, Dr. Rajagopal Nilavalan who was abundantly helpful and offered invaluable assistance, support and guidance. Deepest gratitude are also due to the members of the supervisory committee, Prof. Hamed Al-Raweshidy and Dr. Ruth Mackay without whose knowledge and assistance this study would not have been successful. I would also like to convey thanks to the College of Engineering, Design and Physical Sciences for providing the financial means and laboratory facilities.

I would like to express my gratitude to my father, Dr. Abbas Haghpanahan who is and always will be a source of motivation and support, to my mother Ensiyeh, my sister, Dr. Houra Haghpanahan and my brother, Mehdi for their understanding and endless love, through the duration of my studies.

Chapter 1

Introduction

1 - 1 Motivation

Metamaterials are artificial materials that exhibit novel electromagnetic properties which cannot be found in nature. Utilisation of electromagnetic waves (EM) is a basis of many applications such as imaging technologies, wireless, optical communications and aerospace. Some of these applications require electromagnetic properties far beyond the material properties found in nature. However, sub-wavelength structured metamaterials have shown promises to provide engineerable electromagnetic properties which open new doors to microwave and photonic science and industry.

1 - 2 Metamaterial Definition

Study of metamaterials covers a vast range of artificial structures and electromagnetic properties. As a result of this, there is no universal definition of a metamaterial structure [1]. A metamaterial can be defined as a material which gains its properties from its structure rather than directly from its composition. However, this definition reflects certain natures of metamaterial, but not all. Actually, a metamaterial is a macroscopic composite of periodic or non-periodic structure, whose function is due to both the cellular architecture and the chemical composition. However, in this work metamaterials specifically mean a periodic array of engineered structure with a size smaller than the wavelength of excitation [2]. Electromagnetic properties of materials are characterised by their constituent parameters, permittivity and permeability. Other properties such as refractive

index, characteristic impedance, etc. can be defined by permittivity and permeability. Most natural materials exhibit a permeability equal to free space permeability μ_0 and permittivity greater than the permittivity of free space ϵ_0 [3]. However, metamaterials promise to provide engineerable permittivity and permeability which opens a door to realisation of many more possible material properties. Fig. 1-1 illustrates all possible isotropic and lossless materials in the ϵ - μ plane [1, 3].

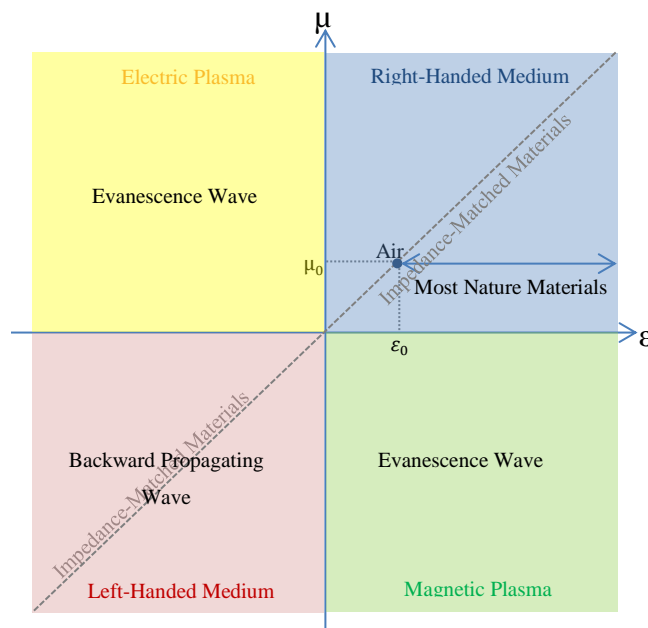


Fig. 1-1. All possible isotropic and lossless material in ϵ - μ plane [3]

Although the theory of materials with simultaneously negative permittivity and permeability were introduced by Veselago over 40 years ago [4], they have only been experimentally demonstrated [5-9] in the last 10 years and have drawn research attention in fascinating applications like invisibility cloaking [10-13] and super lenses [14-18]. Since then a lot of unit cell structures exhibiting different EM properties such as epsilon-negative (ENG), mu-negative (MNG), double negative (DNG) and zero index materials (ZIM) have been proposed.

Later metamaterials found their way into antenna designs where metamaterial cells were used in antenna structures to enhance their performance characteristics [19]. Plenty of novel applications such as patch antennae [20-23], infinite wavelength antennae [24-26], leaky wave antennae [27, 28], small antennae [29-

46] , low profile antennae [47, 48], high-directivity antennae [49, 50] and multifunctional antennae [51-57] were proposed.

1 - 3 Metamaterial Embedded Antennae

A metamaterial approach to antenna design is being applied to overcome the restrictions of traditional design schemes and usually aims to enhance antenna efficiency, bandwidth, weight, directivity, etc. [19].

It is known that the antenna radiation frequency is inversely related to the antenna size. Metamaterial structures are employed to manipulate the dispersion relation or the near field characteristic of an antenna in order to miniaturise the antenna size while maintaining good radiation efficiency. Some papers divided metamaterial-inspired antennae into two categories; leaky-wave antennae (LWAs) and the resonant type small antenna [58]. The work presented in this thesis studies such antennae by type and function of metamaterial used in antenna system.

1 - 3 - 1 Composite Right/Left Handed (CRLH) Metamaterial Antennae

Transmission line (TL) modelling of metamaterial structure has been widely used and developed as a powerful tool for understanding and design of metamaterial structures. A symmetric metamaterial structure can be modelled by including the right handed (RH) effect into a purely left handed (LH) circuit. Fig. 1-2 shows equivalent circuit models for a symmetrical composite right/left handed (CRLH) unit cell which supports both forward and backward wave propagation. In the T-type model, shown in Fig. 1-2a, the LH capacitors are located at the two ends while in the π -type model, shown in Fig. 1-2b, the LH capacitor is placed at the centre. The TL theory is investigated further in section 2 - 4

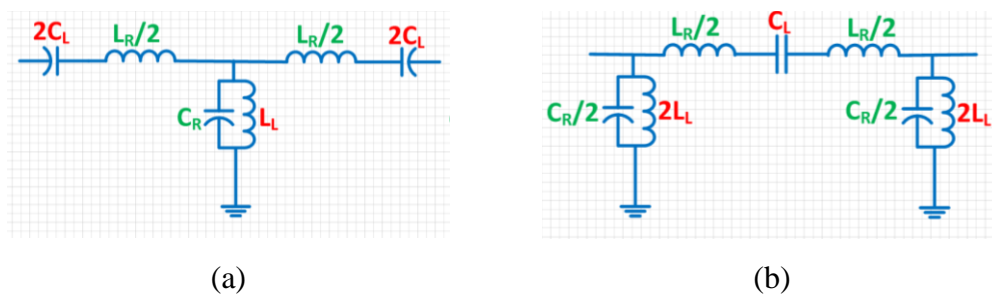


Fig. 1-2. TL theory, equivalent for symmetrical CRLH unit cells, (a) T-type model (b) π -type model [59]

This study reviewed the most interesting proposed CRLH antennae for which the TL theory was being used in their design procedure. The CRLH TL antennae are usually designed to operate on the negative and zeroth order resonance modes. The zeroth resonance, also known as the infinite wavelength, is a frequency point at which the frequency is independent of the physical length of the antenna.

An example of CRLH TL antenna is depicted in Fig. 1-3. The antenna is made from four unit cells and works at zeroth order resonance mode. Experimental measurement confirmed a return loss of 11 *dB*i at a resonance frequency of 4.88 *GHz* which shows a 75% size reduction compared to a conventional patch on the same substrate [24].

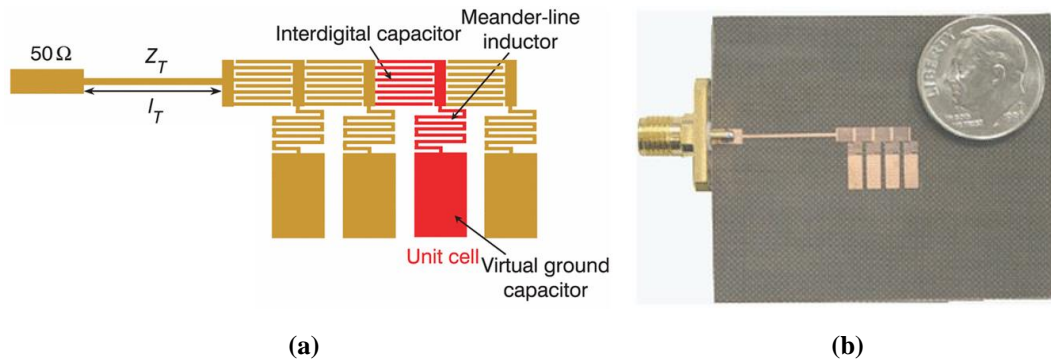


Fig. 1-3. CRLH TL antenna operating at zeroth resonance mode (a) perspective view (b) fabricated prototype [24]

The CRLH substrate integrated waveguide (SIW) is shown in Fig. 1-4. The antenna consists of a single element with two vias at both ends and an interdigital capacitor which makes the π -model suitable to apply. The structure is short-ended by vias which makes the series resonance occur. The antenna operates at the zeroth and $\pm 1^{st}$ resonance modes where the zeroth order resonance is the series resonance. The cut-off frequency of SIW TL was found to be around 11.3 *GHz* which shows considerable miniaturisation comparing to SIW slot antenna. For antenna size of $0.256\lambda_0 \times 0.318\lambda_0 \times 0.03\lambda_0$ and on -1^{st} resonance mode, resonance frequency of 7.25 *GHz* with fractional bandwidth (FBW)= 1.52% and a radiation efficiency of 76.5% were reported [59].

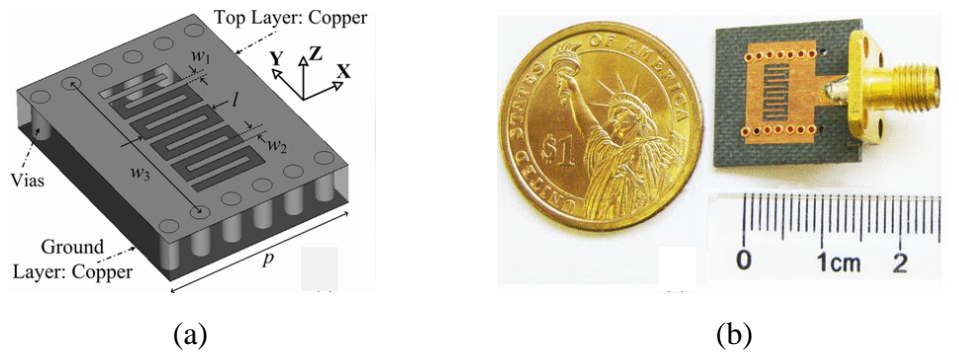


Fig. 1-4. CRLH SIW slot antenna (a) perspective view (b) fabricated prototype [59]

Another widely used CRLH structure is the mushroom structure where the capacitance comes from the distance between adjacent patches and the via connected to the ground provides inductance. A zeroth order resonance antenna using the mushroom structure is shown in Fig. 1-5. For antenna size of $0.167\lambda_0 \times 0.167\lambda_0 \times 0.018\lambda_0$ a resonance frequency of 3.38 GHz with fractional bandwidth less than 1% return loss of -12.34 dBi , a radiation efficiency of 70% and a peak gain of 0.87 dBi was stated [26]. Further miniaturisation was reported by applying an additional lumped inductor and a capacitor to the mushroom structure where a size of $0.104\lambda_0 \times 0.104\lambda_0 \times 0.056\lambda_0$ was achieved [36].

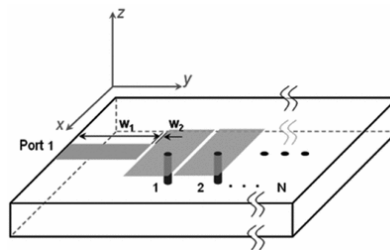


Fig. 1-5. Mushroom zeroth order resonance antenna [36]

The radiation efficiency of mushroom zeroth order resonance antenna is reduced due to the high current flow on the via.

A coplanar waveguide (CPW) feed was successfully applied to the zeroth order resonance antenna to increase the radiation efficiency. The proposed antenna is depicted in Fig. 1-6. A small size of $0.145\lambda_0 \times 0.172\lambda_0 \times 0.011\lambda_0$ at resonance frequency of 2.03 GHz was achieved. The measured FBW and the radiation frequency were found to be 6.8% and 62%, respectively [60].

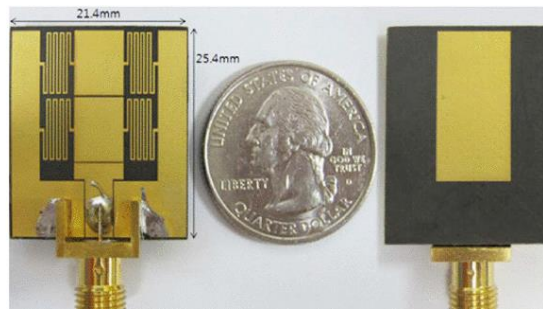
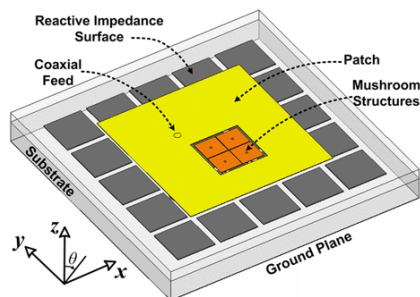
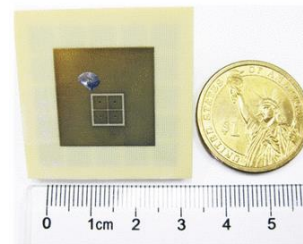


Fig. 1-6. CPW fed zeroth order resonance antenna [60]

An example of -1^{st} resonance mode, the mushroom-loaded patch antenna is depicted in Fig. 1-7. The -1^{st} resonance antennae are not as popular as zeroth order resonance antenna due to the low bandwidth and efficiency of -1^{st} resonance resonators. However, in the proposed antenna the mushroom top surfaces lay along a circularly polarised patch antenna edge. A reactance impedance surface (RIS) surface is used under the patch to boost the radiation efficiency. Experimental measurements showed a resonance frequency of 2.58 GHz for the antenna size of $0.177\lambda_0 \times 0.181\lambda_0 \times 0.025\lambda_0$. The fractional bandwidth was found to be 4.6%. Also a radiation efficiency of 72% with a peak realised gain of 3 dBi was achieved [61].



(a)



(b)

Fig. 1-7. Circularly polarised patch antenna loaded with mushroom structure (a) perspective view (b) fabricated prototype [61]

1 - 3 - 2 Metamaterial Shell-Based Antennae

The idea here is to enclose the electrically small antenna (ESA) by a resonant metamaterial shell to enhance its performance, especially antenna efficiency and bandwidth. In the theoretical model the ESA usually is loaded by epsilon-negative

(ENG), Mu-negative (MNG) or high-permeability shells to improve radiation efficiency. Different designs have been proposed in which a metamaterial shell leads a complete matching to antenna terminal impedance of 50Ω without any required external matching network [30, 33, 62]. One of earliest original designs is shown in Fig. 1-8 where a spherical ENG shell encloses a small dipole antenna [33].

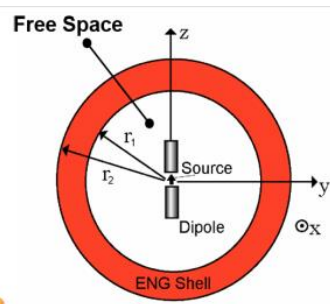


Fig. 1-8. Centre-fed dipole antenna surrounded by an ENG shell [33]

The empty space within the shell is excited by the electric field of driven dipole and, thus, exhibits capacitive character. Also the electric field excites the shell, however, because of negative permittivity, it acts as an inductor. This means the ENG shell acts as a lossy RLC resonator which interacts with the near field of the driven antenna and the whole antenna structure resonant frequency is given by:

$$f_r = \frac{1}{2\pi\sqrt{L_r C_r}} \quad (1-1)$$

Where L_r and C_r are the effective inductance and capacitance as shown in Fig. 1-9.

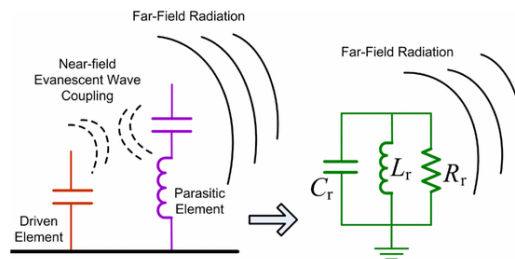


Fig. 1-9. Coupling between driven and the near-field resonant parasitic (NFRP) elements and equivalent RLC model corresponding to entire antenna system [58]

The ENG provides a bandwidth close to Chu limit with which a good impedance matching can be achieved. For the ESA when $ka \leq 0.5$, if a ground plane is involved or $ka \leq 1$, if no ground plane is involved, (k is the wavenumber and a is the radius of the antenna's circumscribing sphere) [58], the Chu lower limit Q_{Chu_LB} is given by [63]:

$$Q_{Chu_LB} = \text{Radiation Efficiency} \times \left(\frac{1}{(ka)^3} + \frac{1}{ka} \right) \quad (1-2)$$

where the Chu upper bound, $BW_{Chu_UB} = 2/Q_{Chu_LB}$. The dual version of the design depicted in Fig. 1-9, where an electrically small loop antenna was loaded by a MNG spherical shell, was also studied in [42]. The antenna was designed and fabricated using an inductive spiral structure. The results confirmed that the MNG shell did arrange matching of the antenna system to the feed. However, due to losses associated with each unit cell and also because many of these cells were used in the structure, the promised improvement in radiation efficiency was not achieved. It had been reported by Wheeler [64] that, for a small spherical magnetic dipole antenna with electric currents restricted to its surface, loading the antenna volume with an infinite permeability material would reduce the stored magnetic energy inside the sphere to zero, enabling the Chu lower bound to be achieved theoretically [65]. Later, the high permeability shell was applied to an electrically small dipole and monopole to approach the lower bound of Chu limits Q_{Chu_LB} [65]. It was observed that the magnetic polarisation currents induced on the high permeability shell have reduced the energy stored inside the shell leading to a lower Q_{Chu_LB} . Despite the promising improvements in theoretical metamaterial shell results, there are also practical difficulties. First, the unit cells have to be extremely small and secondly they need to have very low losses. However, it was stated that a single metamaterial unit cell is able to provide matching of an antenna system to the source while the radiation efficiency still remains high [62].

1 - 3 - 3 Near-Field Coupling

If a metamaterial unit cell is placed in the near-field region of a radiating antenna, coupling between the antenna element and the resonant metamaterial unit cell causes the entire antenna system to act as a NFRP element. This can provide complete matching to the source without any matching circuitry and almost 100% realised efficiency. Both the electric, magnetic and magnetoelectric coupling have been studied.

1 - 3 - 3 - 1 Electric Coupling

One of earliest proposed designs for an electric coupling metamaterial antenna is shown in Fig. 1-10, where a meander line element was printed on one side and a monopole antenna (which coaxially fed through a ground plane) on the other side of the Rogers RT/duroid 5880 substrate [62]. The experimental measurements showed an overall radiation efficiency of 94% at resonant frequency of 1.37 GHz, $ka \sim 0.49$, FBW of 4.1% and an impedance of nearly 50Ω .

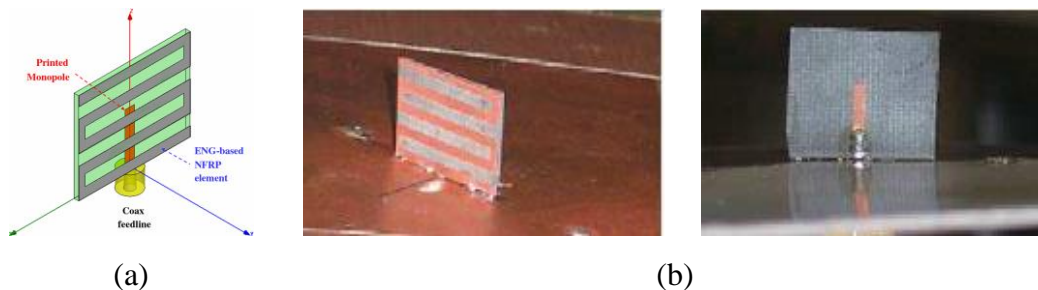


Fig. 1-10. An ESA based on inductive meander line structure (a) perspective view (b) fabricated prototype [62]

Another design, shown in Fig. 1-11, was made by substituting the meander line by an inductive Z-shape. The Z-shape was made of two J-shape traces connected through a lumped inductor enabling tuning of the antenna's frequency of resonance [58]. An antenna with CoilCraft $47nH$ inductor was manufactured and tested for both small ($120.6mm$ diameter copper disk) and larger ($457.2mm \times 457.2mm$) ground plane sizes and little difference was observed between two cases. This confirms that the antenna acts as a small monopole mounted on a finite ground plane [19]. An overall efficiency equal to 80% was measured at the

resonance frequency $f_r = 566.2 \text{ MHz}$, $ka = 0.398$ with a FBW = 3.0%, giving $Q = 4.03Q_{Chu_LB}$ [19].

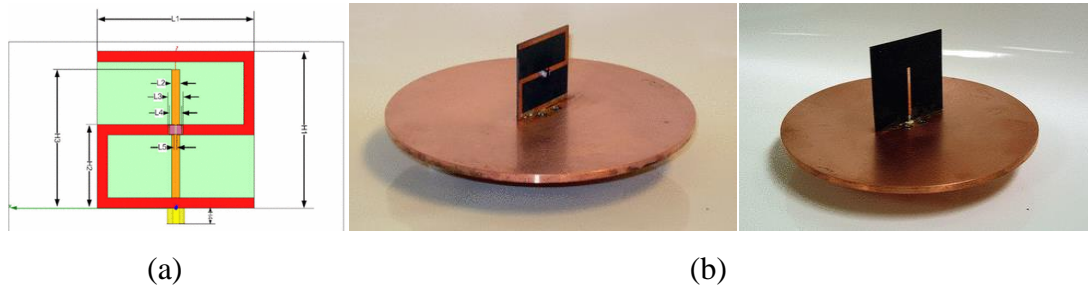


Fig. 1-11. An ESA based on inductive Z structure (a) perspective view (b) fabricated prototype [19]

Several novel designs of electric NFRP element have since been proposed [41, 54, 55]. NFRP element shown in Fig. 1-12a, was made from vertical and horizontal parts connected to each other through a lumped inductor. The upper horizontal part dimensions are defined to provide an impedance of 50Ω . In another design, shown in Fig. 1-12b, the vertical strip provides the inductance and the horizontal strip provides the capacitance. Driven monopole mostly induces the currents on the vertical strip of NFRP element which causes the entire antenna system works as a monopole and overall efficiency of 90% was demonstrated [66].

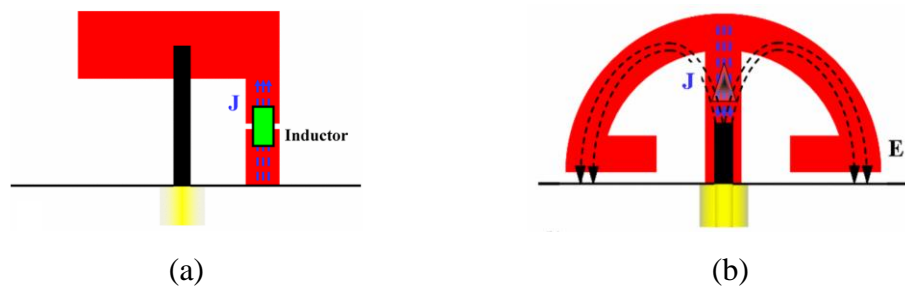


Fig. 1-12. Electric coupling, a electric monopole antenna (a) electrically coupled (b) magnetically coupled [66]

1 - 3 - 3 - 2 Magnetic Coupling

In similar fashion, Ziolkowski et al. reported [54, 67] that the ESA can be designed using a driven element and a metamaterial structure with magnetic response. For instance, as shown in Fig. 1-13, a capacitively loaded loop (CLL) was placed in near field of a half-loop antenna. The coupling between the

magnetic field of the half-loop antenna and CLL structure leads to a high radiation efficiency.

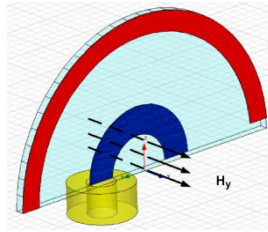


Fig. 1-13. Magnetic coupling, driven half-loop antenna coupling with CLL NFRP element [54]

More designs based on magnetic coupling were proposed and fabricated [54]. Another example is shown in Fig. 1-14.

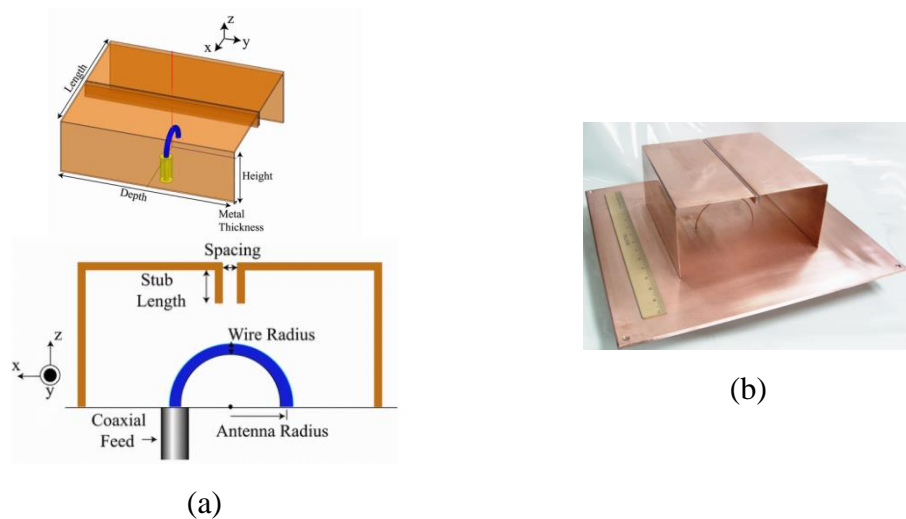


Fig. 1-14. 3-D magnetic coupled CLL NFRP element (a) perspective view (b) fabricated prototype [54]

As shown in Fig. 1-14.a , the 2-D CLL structure was replaced by its 3-D structure. The design was fabricated and successfully tested. Experimental measurements at resonance frequency of 300.96 MHz confirmed an overall radiation efficiency of 94% while near perfect matching to 50Ω was observed [45] . Ziolkowski's group proposed a circularly polarised double-band antenna using the magnetic CLL structure. The proposed design is shown in Fig. 1-15. Two pairs of protractor shape NFRP elements were mounted on top of a ground plane in a proper phasing between the resonances in order to achieve the circular polarisation. $ka\sim 0.322$ at the first resonance and $ka\sim 0.449$ at the second resonance with overall radiation efficiency of 90% were reported [54].

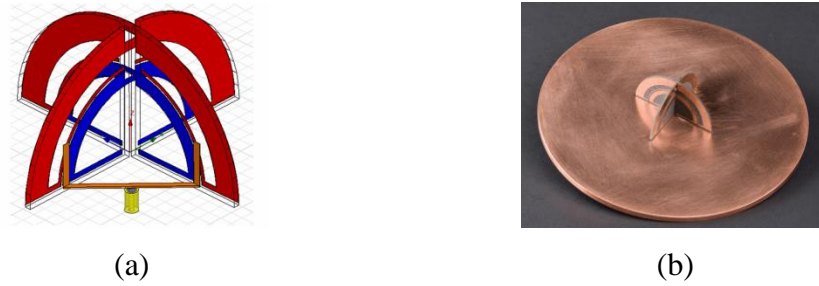


Fig. 1-15. Dual-band circular polarised antenna with two pairs of protractor NFRP element (a) perspective view (b) fabricated prototype [54]

1 - 3 - 3 - 3 Magnetolectric Coupling

The effect of an electric driven antenna on a magnetic NFRP element was studied where an electric monopole antenna was used to couple with CLL structure, shown in Fig. 1-16.a [19]. In a similar fashion, another ESA design was reported [68] where a monopole antenna was loaded by the split ring resonator (SRR) structures.

In contrast, as is shown in Fig. 1-16b, the magnetic field of the monopole could also be coupled with a distributed NFRP element. When offsetting the driven monopole from the centre, the magnetic flux through the CLL-based NFRP structure becomes asymmetrical and leads to driven electric currents. Consequently, these currents form a completed loop which radiates as a horizontal magnetic dipole [54].

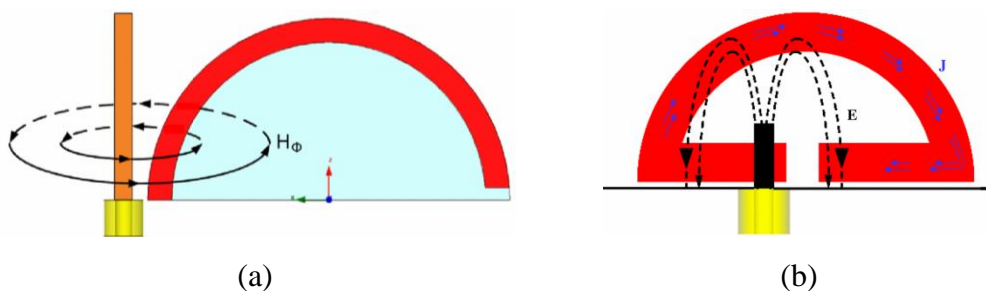


Fig. 1-16. Magnetolectric coupling, an electric monopole antenna (a) coupled magnetically (b) coupled to a magnetic NFRP structure [54]

1 - 3 - 4 DBE/MPC based Antennae

It is worth mentioning that not all metamaterial inspired antennae are designed based on near-field parasitic elements but there have been other designs such as

antenna based on degenerated band edge (DBE) [44] or magnetic photonic crystal (MPC) [69]. The dispersion engineering was used to analyse the performance of antenna where mode coupling leads to slow group velocity and consequently provides a small antenna with a good bandwidth [58]. The manufactured microstrip DBE antenna on an aluminium substrate, shown in Fig. 1-17a, had a gain of 4.5 dBi at 1.48 GHz with $\text{FBW} \approx 3.0\%$ [44]. Later, improved performance was reported by Volakis et al. [44], where a partially coupled microstrip line was implemented on a composite substrate with ferrite insert. The antenna size at 2.35 GHz is $0.173\lambda_0 \times 0.159\lambda_0 \times 0.1\lambda_0$ with realised gain of 6.2 dBi and $\text{FBW} = 8.8\%$. the antenna dimension and prototype are shown in Fig. 1-17b.

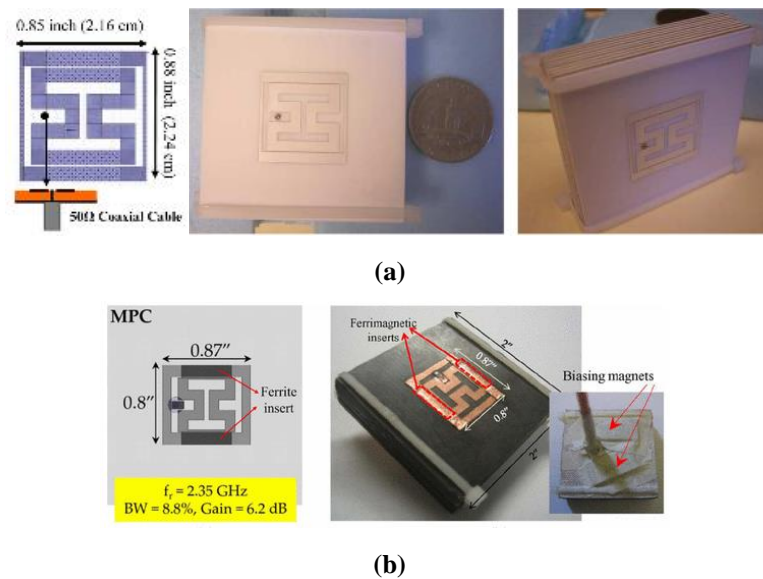


Fig. 1-17. (a) Microstrip-DBE layout and fabricated prototype [44] (b) Microstrip-MPC layout and fabricated prototype [69]

1 - 3 - 5 Mu-Zero Resonance (MZR) Antennae

This type of antenna consists of n unit cells, shown in Fig. 1-18a, where magnetic coupling was used to feed the antenna. An open-ended quarter-wavelength microstrip was used for input coupling. A fabricated prototype consisting of three unit cells is shown in Fig. 1-18b. The antenna has size of $0.103\lambda_0 \times 0.181\lambda_0 \times 0.1\lambda_0$ with resonance frequency of 7.3GHz , $\text{FBW} \approx 2.8\%$, maximum gain of 2.9 dBi and radiation efficiency of 86% [70].

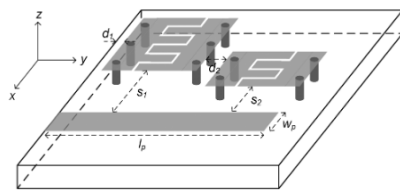


Fig. 14. Dual-band MZR antenna ($n_f = 4$ and $n_l = 6$).



Fig. 1-18. Dual-band MZR antenna, (a) perspective view (b) fabricated prototype [70]

1 - 3 - 6 SRR/CSRR Resonator Embedded Antennae

Miniaturisation of antenna using split ring resonator (SRR) and complementary split ring resonator (CSRR) designs have been reported [40, 68, 71-73]. SRR can be assumed to be a magnetic dipole while the CSRR is considered to be an electric dipole which has been experimentally confirmed to exhibit negative permeability. One interesting example of this type of antenna is shown in Fig. 1-19. In fact the antenna is an electrically small magnetic dipole antenna consisting of multiple wire split rings where each two adjacent split rings were flipped with respect to each other. The antenna resonates at frequency of 403 MHz giving the electric size as small as $ka = 0.184$ and the radiation efficiency more than 73% . This remarkable performance comes from not only the spherical nature of the antenna which provides more uniform distribution of current on the antenna surface but also from the lossless air filled internal space of the wire split rings [74].

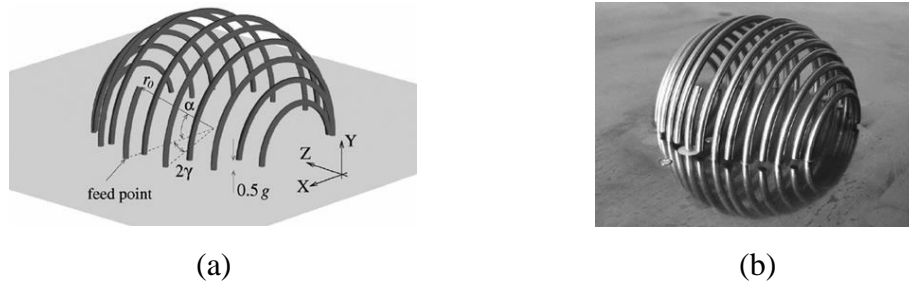


Fig. 1-19. Spherical wire split ring antenna (a) perspective view (b) fabricated prototype [74]

Another example of this type of antenna designed and manufactured at University of California Los Angeles (UCLA) is shown in Fig. 1-20. The entire structure forms a vertical SRR. The interdigital capacitor on the top surface stores the electric field, while metallic vias connect both ends of the top surface to the ground. A coaxial cable is used to feed the antenna which can be characterised as an inductor. Thus, the antenna can be modelled as an LC resonant circuit with a parallel radiation resistance associated with the capacitor. The simulated and measured return loss for the vertical SRR antenna is shown in Fig. 1-20c. the antenna has a size of $0.112\lambda_0 \times 0.051\lambda_0 \times 0.028\lambda_0$ at frequency of 2.85 GHz , giving $ka = 0.427$ with $\text{FBW} = 20.1\%$. The measured gain and radiation efficiency were found to be 2.05 dBi and 68.1% , respectively [75].

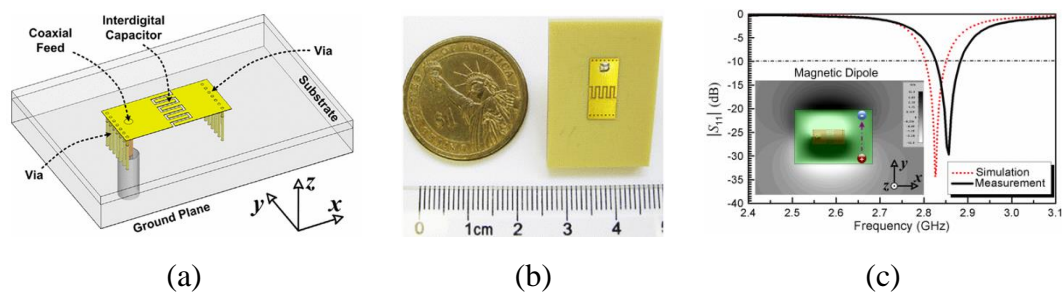


Fig. 1-20. Inductively-fed vertical SRR antenna (a) perspective view (b) fabricated prototype (c) simulated and measured return loss [75]

CSRR are resonant structures which behave as an electric dipole resonator. They have been used to couple the energy to the antenna patch. Fig. 1-21 shows an antenna in which two CSRR cells have been used. A periodic array of metal patches is placed between the CSRRs on the top surface and the ground plane to enhance the radiation efficiency. The substrate is a three-layer substrate where MEGTRON substrate was used in the top and bottom layers with an off-centre coaxial feed. The antenna is a dual-band antenna with the first band associated with CSRR resonance and the second band associated with the patch resonance.

For the patch size of $0.099\lambda_0 \times 0.153\lambda_0 \times 0.024\lambda_0$, the two bands were realised at 2.41 and 3.82 GHz, respectively. The corresponding radiation efficiencies were measured to be 22.8% and 74.5%, respectively [76].

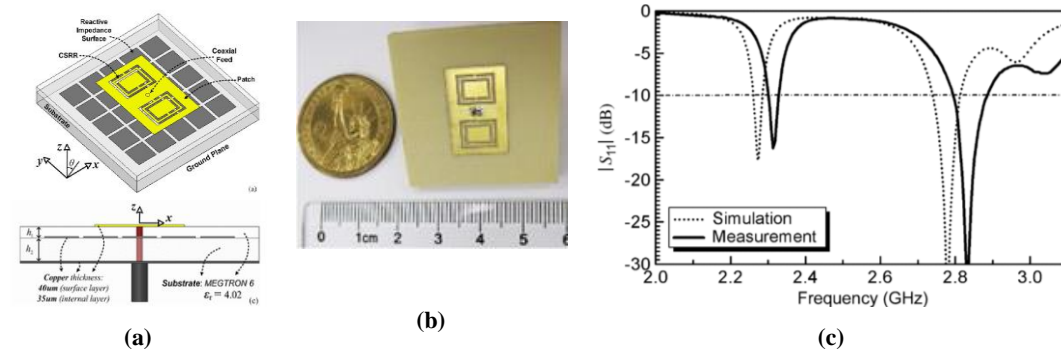


Fig. 1-21. Dual-band, dual polarised CSRR embedded antenna (a) perspective view (b) fabricated prototype (c) simulated and measured return loss [76]

In another design, shown in Fig. 1-22, two CSRRs were placed side by side reversely in respect to each other on the top surface while other design features were kept as in previous design. The antenna operates as a triple-band antenna where the first and third resonances are associated with CSRR and the middle resonance corresponds to the patch. For the patch size of $0.15\lambda_0 \times 0.17\lambda_0 \times 0.024\lambda_0$, the three bands were realised. As seen in Fig. 1-22, the three bands are well matched to be below -22dBi . The measured -10dBi bandwidth for the three bands is 1.61%, 3.27%, and 3.08%, respectively. A gain of 0.27, 3.31 and 4.45 dBi was measured at resonance frequencies. The corresponding radiation efficiencies to the resonant frequencies were measured to be 43.7%, 69.8% and 75.5%, respectively [76].

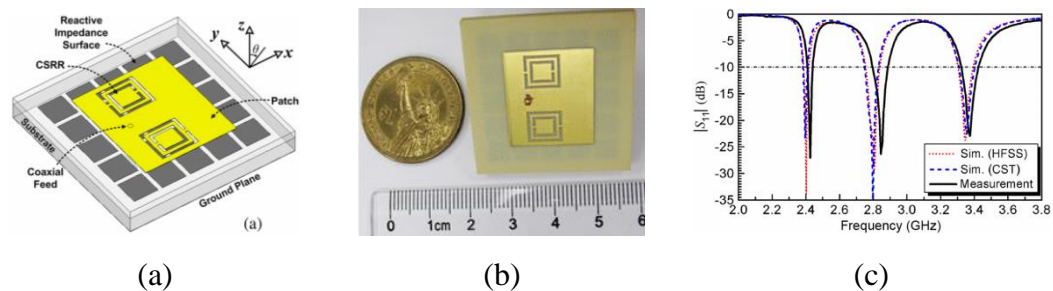


Fig. 1-22. Triple-band antenna with different polarisation (a) perspective view (b) fabricated prototype (c) simulated and measured return loss [76]

1 - 3 - 7 Meta-Surface Loaded Antennae

Meta-surfaces such as electromagnetic band gap (EBG) [77, 78], uniplanar compact photonic band gap (UC-PBG) [79, 80] and reactance impedance surface (RIS) [81-83] have been widely applied to microwave devices and antennae [77, 80-86]. The EBG, also known as artificial magnetic conductor (AMC), is a periodic array of resonant unit cells which exhibit a band-gap between two successive resonant modes over which the surface waves cannot propagate. Loading an antenna with an EBG surface can provide a smoother radiation pattern as well as a reduced front-to-back ratio. The proposed antenna by Mosallae and Saranbandi [83], shown in Fig. 1-23, was the first design employed RIS surface between the patch and the ground plane. It was reported that not only has the antenna been miniaturised but also its radiation characteristic and bandwidth have been considerably improved. The RIS substrate is made of trans-tech MCT-25 with a dielectric constant of 25, and a thickness of 4 mm.

Experimental measurements showed a resonance frequency of 1.92 GHz for the patch size of $0.102\lambda_0 \times 0.128\lambda_0 \times 0.038\lambda_0$ with a gain of 4.5 dBi while radiation efficiency was about 90%. The antenna also exhibited a FBW $\approx 6.7\%$ [83].

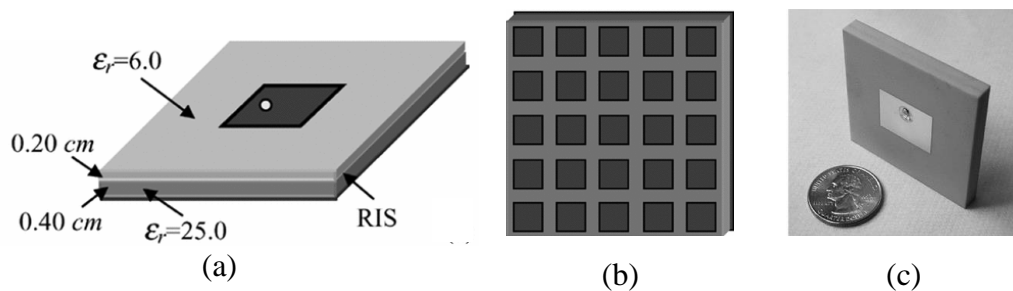


Fig. 1-23. RIS loaded patch antenna (a) perspective view (b) RIS surface (c) fabricated prototype [83]

Another example worth mentioning and that can also be categorised as a meta-surface antenna is a low profile high gain antenna shown in Fig. 1-24. The antenna consists of a patch surrounded by an artificial magnetic conductor (AMC) surface, and a partially reflective surface (PRS) which is placed a quarter wavelength distance away from the AMC surface. These surfaces form a cavity and thus an aperture which is half the size of conventional cavities. The experimental results for an antenna with the AMC area size of $7.1\lambda_0 \times 7.1\lambda_0$ and

the PRS area size of $5\lambda_0 \times 5\lambda_0$ showed a resonance frequency of 14.2 GHz . The antenna maximum gain was found to be 19 dBi and the fractional bandwidth of about 2% was confirmed [81].

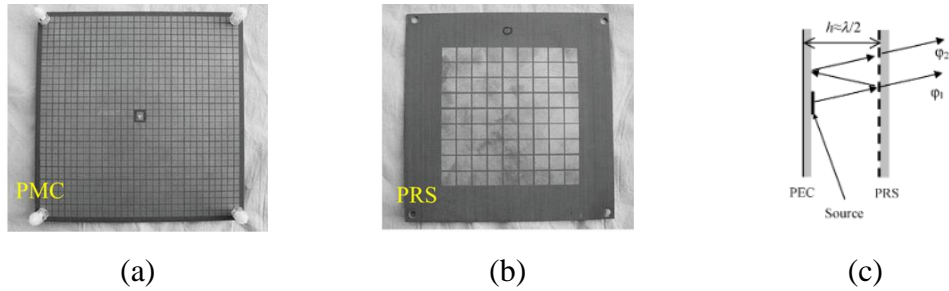
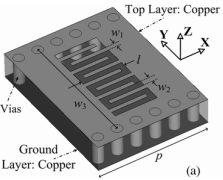
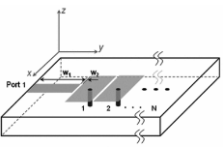


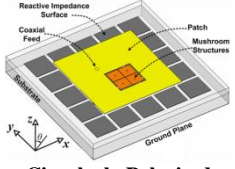
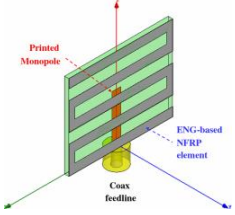
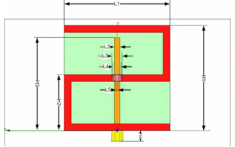
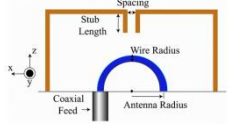
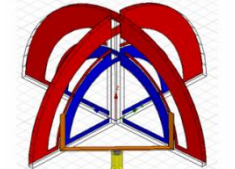
Fig. 1-24. Photographs of (a) patch antenna with AMC ground plane (b) PRS superstrate (c) resonant cavity formed by PEC and PRS [81]

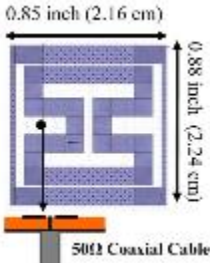
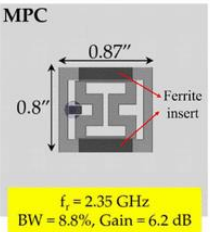
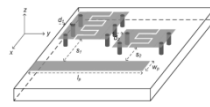
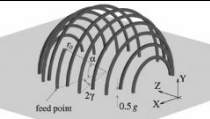
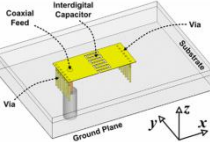
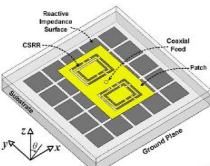
These selected antennae mentioned here are among many other metamaterial antennae that have been reported to date which unveil the potential applications of metamaterials on antenna structures design.

The ability of metamaterials to improve antennae radiation properties is now widely accepted and there is a rising hope that more interesting applications are going to be introduced in the near future.

A summary of the antennae reported in this chapter are presented in Table 1-1.

Antenna	Metamaterial Inspired Antenna Type	Gain	Antenna Efficiency	Resonance frequency	FBW
 <p>CRLH SIW Slot Antenna</p>	<p>CRLH-Based Antenna 0^{th} and $\pm 1^{st}$ resonance modes</p>	3.16 dBi	76.5%	11.3 GHz	1.52%
 <p>Mushroom Zeroth Order Antenna</p>	<p>CRLH-Based Antenna 0^{th} order resonance mode</p>	0.87 dBi	70%	3.38 GHz	$< 1\%$

Antenna	Metamaterial Inspired Antenna Type	Gain	Antenna Efficiency	Resonance frequency	FBW
 <p>Circularly Polarised Patch Antenna Loaded with Mushroom Structure</p>	<p>CRLH-Based Antenna -1st resonance mode</p>	<p>3 dBi</p>	<p>72%</p>	<p>2.58 GHz</p>	<p>4.6%</p>
 <p>ESA Based on Inductive Meander Line Structure</p>	<p>Metamaterial Shell-Based Antenna Electric Coupling</p>	<p>Not reported in literature</p>	<p>94%</p>	<p>1.37 GHz</p>	<p>4.1%</p>
 <p>ESA based on inductive Z structure</p>	<p>Metamaterial Shell-Based Antenna Electric Coupling</p>	<p>Not reported in literature</p>	<p>80%</p>	<p>566.2 MHz</p>	<p>3%</p>
 <p>Magnetic Coupled CLL NFRP Element</p>	<p>Metamaterial Shell-Based Antenna Magnetic Coupling</p>	<p>5.94 dBi</p>	<p>95%</p>	<p>297 MHz</p>	<p>1.36%</p>
 <p>Dual-Band Circular Polarised Antenna with Two Pairs of Protractor NFRP Element</p>	<p>Metamaterial Shell-Based Antenna Magnetic Coupling</p>	<p>5.36 dBi 6.2 dBi</p>	<p>71.1% 79.2%</p>	<p>1.22 GHz 1.57 GHz</p>	<p>0.86% 1.53%</p>

Antenna	Metamaterial Inspired Antenna Type	Gain	Antenna Efficiency	Resonance frequency	FBW
 <p>Microstrip-DBE Antenna</p>	DBE based Antenna	4.5 dBi	95%	1.48 GHz	3.0%
 <p>Microstrip-MPC Antenna</p>	MPC based Antenna	6.2 dBi	67%	2.35 GHz	8.8%
 <p>Dual-band MZR Antenna</p>	Mu-Zero Resonance Antenna	2.9 dBi	86%	7.3GHz	2.8%,
 <p>Spherical Wire Split Ring Antenna</p>	SRR Resonator Embedded Antenna	Not reported in literature	73%	403MHz	Not reported in literature
 <p>Inductively-Fed Vertical SRR Antenna</p>	SRR Resonator Embedded Antenna	2.05 dBi	68.1%	2.85 GHz	20.1%
 <p>Dual-Band, Dual Polarised CSRR Embedded Antenna</p>	CSRR Resonator Embedded Antenna	-2.13 dBi 5.04 dBi	22.8% 74.5%	2.41 GHz 3.82 GHz	0.91% 1.76%

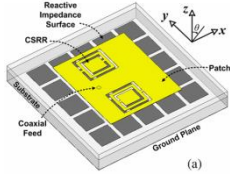
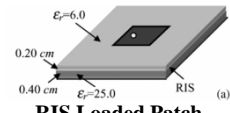
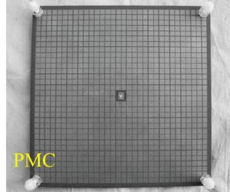
Antenna	Metamaterial Inspired Antenna Type	Gain	Antenna Efficiency	Resonance frequency	FBW
 <p>Triple-Band Antenna with Different Polarisation</p>	<p>CSRR Resonator Embedded Antenna</p>	<p>0.27 <i>dBi</i> 3.31 <i>dBi</i> 4.45 <i>dBi</i></p>	<p>43.7% 69.8% 75.5%</p>	<p>2.4 <i>GHz</i> 2.8 <i>GHz</i> 3.4 <i>GHz</i></p>	<p>1.61% 3.27% 3.08%</p>
 <p>RIS Loaded Patch Antenna</p>	<p>Meta-Surface Loaded Antenna</p>	<p>4.5 <i>dBi</i></p>	<p>90%</p>	<p>1.92 <i>GHz</i></p>	<p>6.7%</p>
 <p>Patch Antenna with AMC Ground Plane & PRS Superstrate</p>	<p>Meta-Surface Loaded Antenna</p>	<p>19 <i>dBi</i></p>	<p>Not reported in literature</p>	<p>14.2 <i>GHz</i></p>	<p>2%</p>

Table 1-1. Metamaterial inspired antennae

1 - 4 Scope of the Thesis

This study intended to develop applications of metamaterials in antennae structures as well as improving metamaterial performance itself. The aims of the research presented in this thesis are mainly two fold:

- I. Unit cell design for a specific group of metamaterials known as zero index metamaterials (ZIM). The aim here is to increase the metamaterial operational bandwidth.
- II. Applications of metamaterials in antenna structures. The aim here is to increase antenna directivity through beam forming conducted by metamaterials.

The research primarily focuses on achieving the following objectives:

- i. Metamaterials are resonant structures with inherently narrow bandwidth. This limits the potential applications of metamaterials for wideband

antennae. First, the operational bandwidth of ZIM structures proposed to date are to be determined. The effects of metal trace width, mutual coupling, electric and magnetic resonances within these cells on their operational bandwidth are to be investigated. Eventually, new ZIM structure designs with larger operational bandwidth are going to be proposed in this thesis.

- ii. Metamaterial based highly directive antennae can be achieved by integrating a bulky shell of metamaterials and an ordinary antenna. The required properties of a metamaterial shell are defined through the transformation optic (TO) technique. A unit cell is designed and simulated and the standard retrieval technique is applied to extract the effective material parameters. Then the unit cell geometrical dimensions are optimised through the genetic algorithm (GA) optimisation method to obtain the required effective material parameters. The optimised unit cell is tessellated to form a highly directive shell. Eventually, to obtain the highly directive antenna, the shell and antenna are integrated.

1 - 5 Contribution to Knowledge

The contributions of this research can be summarised as follows:

- 1- A comparative study of proposed ZIM cells up to date with special attention to their operational bandwidth and development of new ZIM unit cell structure with significant improvement in its operational bandwidth has been carried out. Effects of metal trace width, mutual coupling, electric and magnetic resonances within the cell on their operational bandwidth were investigated.
- 2- New directive shells consisting of ZIM structures for a dipole antenna have been developed; four different shells i.e., an epsilon-zero (EZ) shell, a Mu-zero (MZ) shell and two ZIM shells were designed and placed around the dipole antenna where directive radiation patterns were obtained.
- 3- Novel metamaterial embedded planar quasi-Yagi antenna designs with a higher gain [87] have been developed; ZIM structures were applied to the quasi-Yagi antenna to increase gain. The antenna gain increased for a

frequency range over which the proposed metamaterial structure exhibits ZIM properties.

- 4- A new technique to design a highly directive medium based on wave interference has been developed; It was shown that 180° phase difference between interfering waves results in a focused emission. This method was used to design a metamaterial lens to increase a patch antenna gain.
- 5- A novel ground plane to increase dipole antenna gain has been designed; the proposed ground plane consists of perfect electric and magnetic surfaces where metal and mushroom structures were used to form the perfect electric surface and the magnetic conductor surface, respectively.

1 - 6 Thesis Overview

Metamaterials offer a new opportunity in design and developing antennae and microwave devices. This thesis represents such a study for applications of metamaterial structures in antenna designs in order to increase antenna gain.

Chapter 2 introduces basic concepts and fundamental theories needed in study of metamaterials. This includes metamaterials classification, field response and polarisation currents. Techniques to extract material parameters from transmission and reflection coefficients are explained. Two major approaches to characterise metamaterial structures known as resonant approach and transmission line (TL) approach are investigated.

In **chapter 3** zero index materials (ZIM) are investigated. A comparative study is made between different ZIM structures such as rod, C-shape, S-shape and meanderline with special attention to their operational bandwidth. Two novel ZIM structures with significant increase in operational bandwidth are proposed. The proposed structure is then used to form a high directive shell in which required shell properties are determined by optical transformation technique. Four different shells are designed and simulation results are discussed. Further, the proposed structure is applied to the quasi-Yagi antenna to enhance its gain.

In **chapter 4**, a highly directive medium is designed by using a new method whereby the wave interference phenomenon is used to determine the required spatial properties of the lens. The theory of wave interference and the spatial energy distribution are discussed. Then, it is shown that 180° phase difference

between interfering waves can lead to highly directive emission. A hypothetically defined 180° phase shifter slab is used to increase the gain of the patch antenna. The practical realisation of the 180° phase shifter slab is formed by cascading capacitively loaded ring resonator (CLRR) unit cells and placing them on top of the patch antenna where significant gain enhancement is observed.

In **chapter 5**, the method developed in the previous chapter is used to design a novel directive ground plane, called a bi-reflectional ground plane, which can be used to increase the antenna gain. An electric and a magnetic conductor are used to form the bi-reflectional ground plane. Gain enhancement is achieved for the dipole antenna mounted on the top of the designed plane. Then, the square shape mushroom structure is designed for use as the magnetic conductor in the theoretical model. Further, the hexagonal shape mushroom structure is used to form the magnetic conductor. Gain enhancement is obtained in both cases; however, the hexagonal shape mushroom structure leads to higher gain.

Finally, **chapter 6** concludes the research findings of the thesis and presents the future work to be carried out in connection with the research presented in this thesis.

Chapter 2

Planar Metamaterial Theory and Analysis

In this chapter we attempt to introduce basic concepts needed later in this thesis and in a form on which we can build on in the following chapters. Macro- and micro-scale phenomena occurring within a metamaterial unit cell are investigated, including the study of electromagnetic field variation over a unit cell. Moreover, two major approaches to characterise a metamaterial structure, known as the resonant approach [88] and the transmission line (TL) [89] approach are also explained.

2 - 1 Introduction

Metamaterial structures are reciprocal composites formed by altering sub-wavelength unit cells. Finding the material parameters for such a medium is essential in a design procedure. To find out the material parameters we should answer two questions: can a periodic structure with sub-wavelength elements be considered as a homogenous effective medium? And how can we determine the effective parameters? Since the unit cell size is much smaller than the wavelength within the medium, the homogenous condition is satisfied. Thus, the macroscopic electromagnetic fields are determined by averaging the local fields. Then, the averaged permittivity and permeability are calculated from the averaged fields [90, 91]. These calculated constituent parameters are the ones being used in the Drude-Lorentz material model and are different from the effective constituent parameters. The optical properties of insulators first have been modelled by Lorentz by assuming that the electrons and ions in the matter form a system of harmonic oscillators that are excited to forced oscillations by a light wave propagating through the matter. The basic assumption is that the ions and

electrons forming a solid are located at fixed equilibrium positions in the solid determined by internal forces, if no external forces are applied. The electric field of a light wave propagating through the solid exerts forces on the charged particles which displaces them from their equilibrium positions, while the interaction with the surrounding atoms results in forces which tend to drive a displaced particle back into its equilibrium position. It is assumed that this force is proportional to the displacement x . The particles then can perform harmonic oscillations around their equilibrium positions with some frequency ω_0 . On the other hand, the interaction of an oscillator with other oscillators in its environment may transfer part of its vibrational energy to other oscillators. This results in a damping of the oscillations.

The derived material parameters are not accurate at microwave frequencies since the mutual coupling effects between adjacent cells have not been taken in account in the Drude-Lorentz material model. Instead, a numerical technique known as “Standard Retrieval Method” [92] is applied to derive the effective material parameters from the scattering parameters.

Later in this chapter we discuss the basics and fundamentals in the study of metamaterials. This includes study of the electric and magnetic fields and current polarisations, the magnetoelectric effect within the metamaterial medium, the averaged and effective material parameters and finally the use of TL theory in modelling metamaterial unit cells is presented.

2 - 2 Metamaterial Classification

Electromagnetic property of a material can be characterised by its permittivity, ϵ , its permeability, μ , and its magnetoelectric coupling parameters (MCP), ζ and ξ . Metamaterials can be classified in four categories; isotropic, anisotropic, bi-isotropic and bi-anisotropic. In Greek “isos” means equal and the word “tropos” means way. Accordingly, isotropic materials treat electromagnetic waves equally in all directions. An isotropic material can be expressed by two parameters, scalar ϵ and μ . In contrast, materials whose properties vary in different directions are called anisotropic where the material parameters can be expressed by tensors of ϵ and μ which contain 18-parameters. A common classification of metamaterials is shown in Fig. 1-1.

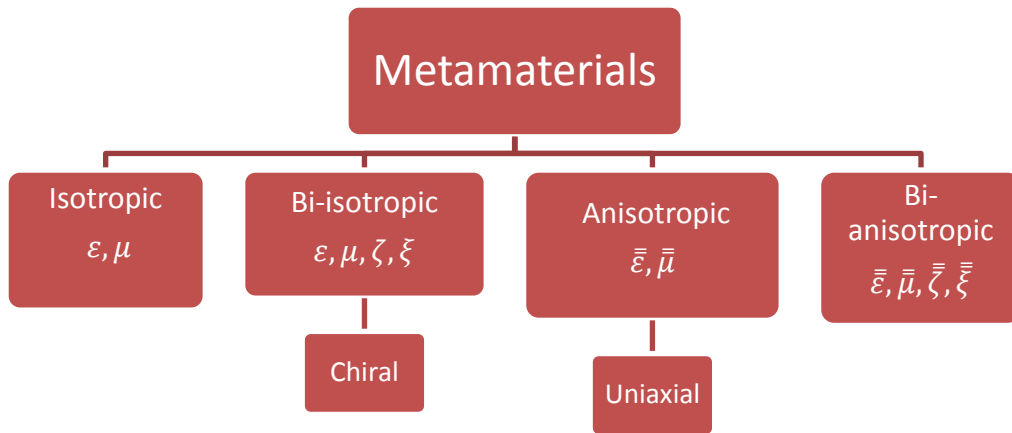


Fig. 2-1. Metamaterial Classification

There are many metamaterial structures which exhibit magnetoelectric coupling where the electric field causes the magnetic polarisation and vice versa. Isotropic and anisotropic metamaterials which exhibit magnetoelectric coupling are called bi-isotropic and bi-anisotropic respectively. Chiral materials are categorised as the sub-group of the bi-isotropic materials. In a chiral metamaterial medium, the special geometrical character of the constitutive unit cells (anti-symmetry with respect to mirror reflection) creates macroscopic effects that are observed as the rotation of the polarisation of the propagating field plane [1].

2 - 2 - 1 Local and Non-Local Field Response of Metamaterials

Metamaterial structures are usually resonant due to their internal capacitance and inductance which respond to the electric field or the magnetic field of an incident wave. This resonance enhancement combined with compression of electrical energy into a very small volume provides a dispersive medium with greatly enhanced energy density at critical locations in the structures by a factor of ≥ 1 million [93]. In general, spatial dispersive mediums represent either strong or weak spatial dispersion over a given frequency range.

To find out if a metamaterial structure over a range of frequency acts as a strong or weak spatial dispersive media, first, we need to understand local and nonlocal material parameters.

A medium exhibits local-field response when the E-fields and H-field have non-uniform distribution over a unit cell. Such a distribution occurs when the unit cell

size is small compared to the wavelength of the excitation wave i.e., $a/\lambda < 0.1$, where a is the distance between centres of two adjacent cells and λ is the wavelength within the host medium [94]. The non-locality occurs when the scatterer size or the distance between scatterers is not negligible compared to the wavelength within the medium. In this case, the incident wave would induce a polarisation current distribution on the scatterer. This polarisation depends on the size and shape of the scatterer. It also depends on the direction and polarisation of the incident wave i.e., θ and ϕ , since different angles of incident wave will result in different polarisation. A medium exhibits strong spatial dispersion (SSD) when the material parameters are non-local and accordingly, the usual material parameters lose their physical meaning. In contrast, weak spatial dispersion (WSD) happens in metamaterial structures with small optical size but complex geometry.

2 - 2 - 2 Strong Spatial Dispersion (SSD)

The strong spatial dispersion phenomenon is a result of the non-locality of the polarisation response within the medium [95]. By definition, the electric and magnetic susceptibilities relate the local electric and magnetic dipole moment of scatterer (the electric and magnetic polarisations) to the averaged electric and magnetic fields [96]. The average fields are nonlocal where the scatterers are optically large ($a \sim \lambda$). The average fields, susceptibilities and constituent parameters can be derived from integration of field distribution over a volume of size a^3 . The statistic equation of Lorentz-Lorenz-Clausius-Mossotti gives us a view of frequency range over which the lattice of scatterers are either local or nonlocal [94]:

$$E_{local} - E_{av} = \frac{(1 + C) p}{2\epsilon_0 V} \quad (2-1)$$

Where, p is the dipole moment, V is the unit cell volume, E_{av} is the averaged electric field, ϵ_0 is the free space permittivity and C is the correction factor by which the effect of wave interaction between the reference dipole and the adjacent dipoles within the lattice is being taken in account. The dipole moment could be

expressed as a function of the local field $p = \alpha E_{local}$. Where, α is the polarisability tensor. Substitution of p in (2-1) gives us:

$$P = \left(\frac{V}{\alpha} - \frac{1+C}{3\epsilon_0} \right)^{-1} E_{av} = k \cdot E_{av} \quad (2-2)$$

Where P the volume polarisation and k is the local electric susceptibility. Thus the local permittivity can be defined as $\epsilon = \epsilon_0 + k$ [94]. When the optical size of scatterer is not small enough i.e., $a/\lambda > 0.1$, the correction factor C is significant due to dramatic changes in the spatial dispersion. In other words, when the normalised optical size of scatterer ka is large, the local fields and polarisation in (2-1) are no longer local and the medium represents strong spatial dispersion.

2 - 2 - 3 Weak Spatial Dispersion (WSD)

Understanding WSD is of key importance in the investigation of metamaterials behaviour. WSD is caused by significant variation of the phase of polarisation current in scatterers as a result of a small variation of applied E-field over them. This small variation in such media would result in multipolar polarisation. Consequently, the polarisation at a certain point of scatterer is not only dependant on fields on that point but also it depends on the fields around it. The electric and magnetic polarisation currents are known as bi-anisotropy and artificial magnetism [97], respectively. In the case of a scatterer with complex shape when the medium is still local i.e., $a\lambda \sim 0.1$, a small phase shift over the unit cell can result in significant spatial dispersion due to sudden change of induced current polarisation [94].

2 - 2 - 4 Polarisation Current in Media with Weak Spatial Dispersion

The electric polarisation current at point r in a scatterer $J_i(r)$ can be calculated considering fields at that point as well as fields around it r' :

$$J_i(r) = \int_{v'} k_{ij}(r - r') E_j(r') dv' \quad (2-3)$$

Where, k_{ij} is the polarisation response dyadic and v' is the effective volume. The Taylor expansion of E-fields is given by [94]:

$$E(r') = E(r) + \nabla_1 E|_r (r'_1 - r_1) + \frac{1}{2} (\nabla_1 \nabla_2 E)|_r (r'_1 - r_1)(r'_2 - r_2) + \dots \quad (2-4)$$

Substitution of (2-4) in (2-3) while neglecting higher order terms gives us the average polarisation current as:

$$J(i) = j\omega(b_{ij}E_j + b_{ijk}\nabla_k E_j + b_{ijkl}\nabla_k \nabla_l E_j) \quad (2-5)$$

2 - 2 - 5 Electric and Magnetic Polarisation Current

The polarisation current of a multipolar medium can be expressed by spatial derivatives of multiple momenta [94],

$$J_\alpha = j\omega P_\alpha - \frac{j\omega}{2} \nabla_\beta \nabla Q_{\alpha\beta} + e_{\alpha\beta\gamma} \nabla_\beta M_\gamma + \frac{j\omega}{6} \nabla_\gamma \nabla_\beta O_{\alpha\beta\gamma} - \frac{1}{2} e_{\alpha\beta\delta} \nabla_\gamma \nabla_\beta S_{\delta\gamma} \quad (2-6)$$

Where, Latin indices denote coordinate axes (x, y, z) , P_α are Cartesian components of the electric dipole polarisation vector, $Q_{\alpha\beta}$ are the components of the electric quadruple polarisation tensor, M_γ are components of magnetic dipole polarisation vector, $S_{\delta\gamma}$ are the components of the magnetic quadruple polarisation tensor, $O_{\alpha\beta\gamma}$ are the components of the electric octopole polarisation tensor. \bar{e} represents the Levi-Civita tensor with the only non-zero components $e_{xyz, zxy, yzx} = 1$ and $e_{xzy, zyx, yxz} = -1$ and defines following operation:

$$(\nabla \times M)_\alpha = e_{\alpha\beta\gamma} \nabla_\beta M_\gamma \quad (2-7)$$

By keeping only the first two orders and discarding higher orders terms, (2-6) becomes:

$$J = j\omega P - \frac{j\omega}{2} \nabla \bar{Q} + \nabla \times M + \frac{j\omega}{6} \nabla \nabla \bar{Q} - \frac{1}{2} \nabla \times \nabla \bar{S} \quad (2-8)$$

Equation (2-8) shows that the polarisation current comprises of two components; one non-circulating polarisation current known as the electric polarisation, the other one is a circulating polarisation current known as the magnetic polarisation.

$$J = J_{elec} + \nabla \times T_{mag} \quad (2-9)$$

Where:

$$J_{elec} = j\omega P - \frac{j\omega}{2} \nabla \bar{Q} + \dots \quad (2-10)$$

And:

$$T_{mag} = M - \frac{1}{2} \nabla \bar{S} + \dots \quad (2-11)$$

2 - 2 - 6 Material Parameters

The electric field displacement D and magnetic fields H for a medium with WSD was defined in [94] through multiple polarisation for first and second orders where higher orders were omitted i.e., the electric and magnetic dipole, the electric and magnetic quadrupole and the electric octopole polarisation. The material equation for first order of WSD was reported to be [94]:

$$D = \bar{\epsilon} \cdot E + j\bar{\xi} \cdot B + \dots \quad (2-12)$$

$$B = \mu_0 H - j\bar{\xi}^T \cdot E + \dots \quad (2-13)$$

Where, $\bar{\xi}$ is the magnetoelectric coupling parameter (MCP). It contains the magnetic dipole susceptibility to the uniform part of the averaged electric field over the cell which is equal to electric dipole susceptibility to the vortex part of the averaged electric field. It also contains quadrupole susceptibility to the uniform part of the electric field. For a lossless medium, $\bar{\xi}$ is real. In an isotropic

medium, it is a scalar value and called “Chirality”. The material equation for second order approximation of WSD is also calculated in [94] as follows:

$$D = \bar{\epsilon}.E + j\bar{\xi}.B + \bar{b}\nabla\nabla E \quad (2-14)$$

$$H = (\bar{\mu})^{-1}B + j\bar{\xi}.E \quad (2-15)$$

The inverse of permeability tensor $(\bar{\mu})^{-1}$ is an effect of second order dispersion. It contains magnetic dipole susceptibility to the vortex part of the electric field and also contains the magnetic quadrupole susceptibility to the uniform part of the electric field.

2 - 2 - 7 Metamaterials and Weak Spatial Dispersion

In general, a metamaterial structure is a reciprocal composite formed by altering scatterer particles. The effect of a small phase shift of the averaged field over a domain occupied by the resonant scatterer particle is much significant compared to the empty or non-resonant interval between scatterer particles. The latter effect is usually small and averaged. The local fields over the non-resonant interval can be described through (2-1), however, a small phase shift of averaged field over the resonant scatterer causes multipolar polarisation which directs us to study metamaterials as a weak spatial dispersive medium. Based on the discussion made earlier, in the metamaterial composite the magnetoelectric coupling is the effect of the first order and the artificial magnetism is the effect of the second order of spatial dispersion, however, if higher multi-poles are induced in the structure both MCP and permeability carry contributions from higher orders. For media with spatial dispersion of the second order, equation (2-14) expresses a second derivative of the electric field which reveals that the medium cannot be defined only by permittivity, permeability and MCP. In other words, the metamaterial with magnetic response cannot be described by permittivity and permeability tensors alone unless a certain conditions satisfied. This is because the magnetic dipole susceptibility to the electric field and susceptibility to its spatial derivatives are not covariant i.e., are not measurable physical values. The exceptions are when there is no bi-anisotropy and if, simultaneously, the higher order multi-poles are negligible [94]. The last condition corresponds to the frequency at which the

induced polarisation current forms a closed loop while its density is uniform along this effective loop. Such a medium can be fabricated by structures performed as loops. For instance SRR introduced in [93] and [98] are formed by two strongly coupled broken loops with uniform polarisation current density which can be properly defined by permeability tensor.

2 - 3 Material Parameter Extraction

Electromagnetic fields within a bulk of metamaterials depend on inclusion properties as well as their positioning in the bulk matrix. The permittivity and permeability which are obtained through the standard retrieval technique are effective parameters while those used in the Drude-Lorentz model are known as the average material parameters. The effective and average constituents are in disagreement. This is due to the effect of spatial dispersion caused by cell size which is not infinitely small compared to the wavelength. Metamaterial sub-wavelength structures can be treated as a homogenous material if homogeneity conditions are satisfied i.e., $|\Delta\varphi| < \pi/2$. In fact, for a metamaterial with node-to-node phase shift $|\Delta\varphi| \ll \pi/2$, homogenisation technique would be ideally applicable in the same manner as conventional dielectrics [89]. The theory of effective media [99-101] was established to define the relationship between the local field responses and the macroscopic field responses on a sub-wavelength periodic structure. According to this theory, each unit cell is considered as a particle and the average local constitutive parameters are calculated from averaging the local field for different unit cells giving a general form of discrete Maxwell's equations [3].

2 - 3 - 1 Average and Effective Constitutive Parameters

The resonance characteristic of metamaterial structures causes electric and magnetic responses which could be defined by dispersive averaged permittivity and dispersive averaged permeability. The dispersion is described by the Drude-Lorentz model which can be obtained by averaging local fields [90]. The Drude-Lorentz model defines permittivity and permeability of a material as follows [3]:

$$\varepsilon(\omega) = \left(1 - \frac{F_e \omega^2}{(\omega^2 - \omega_{0e}^2 - i\gamma_e \omega)} \right) \quad (2-16)$$

$$\mu(\omega) = \left(1 - \frac{F_m \omega^2}{(\omega^2 - \omega_{0m}^2 - i\gamma_m \omega)} \right) \quad (2-17)$$

Where ω_{0m} and ω_{0e} are the magnetic and electric resonances, γ_e and γ_m are associated with the electric and magnetic losses (damping factor) and F_e and F_m represent the strength of the electric and magnetic resonances (oscillation factor). For the SRR shown in Fig. 2-2 (a), there is no fundamental electric response and thus, only the magnetic response is considered.



Fig. 2-2. SRR structure and its equivalent resonant circuit

To determine the parameters in the Drude-Lorentz model the equivalent resonant LC circuit of the SRR, shown in Fig. 2-2 (b), is used. Then, the parameters used in (2-16) are given by:

$$\omega_{0m} = \frac{1}{2\pi\sqrt{(L + \mu_0 S_0^2/V)C}} \quad (2-18)$$

$$F_m = \frac{\mu_0 S_0^2/V}{L + \mu_0 S_0^2/V} \quad (2-19)$$

$$\gamma_m = \frac{R}{2\pi(L + \mu_0 S_0^2/V)} \quad (2-20)$$

As mentioned earlier in this section, the averaged permeability calculated above does not perfectly match the effective permeability derived by full wave simulation. This is because in theory, the unit cell size is assumed to be infinitesimal while in reality, it is at a scale of below one-tenth of the wavelength which causes the SRR to be a spatial dispersive medium i.e., frequency and coordinate dependent.

The unusual response caused by spatial dispersion is studied by the spatial dispersion model on periodic artificial material shown in Fig. 2-3.

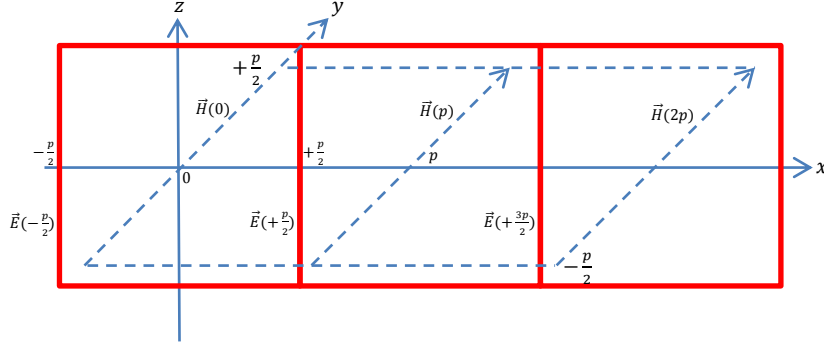


Fig. 2-3. Metamaterial periodic structure

The structure with periodic constant p , is excited by a plane wave propagating along the x -axis and polarised along the z -axis. The integral form of Maxwell's equations for the electric field can be written [94]:

$$\overline{E}_z \left(\left(n + \frac{1}{2} \right) p \right) - \overline{E}_z \left(\left(n - \frac{1}{2} \right) p \right) = i\omega \bar{\mu} p \overline{H}_y(np) \quad (2-21)$$

Where $n = 0, \pm 1, \dots$, the averaged electric field \overline{E}_z and the averaged magnetic field \overline{H}_y are calculated by integration along the line as follows:

$$\overline{E}_z(x) = \frac{1}{p} \int_{-\frac{p}{2}}^{+\frac{p}{2}} E(x, 0, z) dz \quad (2-22)$$

$$\overline{H}_y(x) = \frac{1}{p} \int_{-\frac{p}{2}}^{+\frac{p}{2}} H(0, y, z) dy \quad (2-23)$$

Accordingly, the average permeability is given by:

$$\bar{\mu} = \frac{1}{p^2 \overline{H}_y(0)} \int_{-\frac{p}{2}}^{+\frac{p}{2}} \int_{-\frac{p}{2}}^{+\frac{p}{2}} \mu H(x, 0, z) dx dz \quad (2-24)$$

In similar fashion the integral form of Maxwell's equation for the magnetic field and the average permittivity can be calculated by:

$$\overline{H}_y((n+1)p) - \overline{H}_y((n)p) = i\omega\overline{\varepsilon}p\overline{E}_x((n+\frac{1}{2})p) \quad (2-25)$$

$$\overline{\varepsilon} = \frac{1}{p^2\overline{E}_z(\frac{p}{2})} \int_{-\frac{p}{2}}^{+\frac{p}{2}} \int_{-\frac{p}{2}}^{+\frac{p}{2}} \varepsilon E(0, y, z) dx dz \quad (2-26)$$

Where ε and μ are the background medium permittivity and permeability, respectively. The Bloch boundary conditions for a unit cell are given by:

$$\overline{E}_z\left[\left(n+\frac{1}{2}\right)p\right] = \overline{E}_z\left(\frac{p}{2}\right)e^{i(n\varphi+\frac{\varphi}{2})} \quad (2-27)$$

$$\overline{H}_y(np) = \overline{H}_y(0)e^{in\varphi} \quad (2-28)$$

Where φ is the phase advance across a unit cell. The dispersion relation of the media is calculated by applying the Bloch condition to equation (2-21) and (2-25):

$$\sin\left(\frac{\varphi}{2}\right) = S \frac{\omega p \sqrt{\overline{\varepsilon}\overline{\mu}}}{2} \quad (2-29)$$

In which S is the sign function and is equal to 1 for media with positive $\overline{\varepsilon}$ and $\overline{\mu}$ and -1 when $\overline{\varepsilon}$ and $\overline{\mu}$ are both negative. Equation (2-29) confirms that the phase dispersion across a unit cell depends on both frequency and the periodic constant. The wave impedance of media can also be calculated by:

$$\eta(x) = \frac{\overline{E}_z(x)}{\overline{H}_y(x)} \quad (2-30)$$

To calculate the wave impedance, the electric field and magnetic field must be calculated at the same point. In fact, the averaged electric field in (2-21) is defined on the edges of one cubic lattice while the averaged magnetic field in (2-25) is calculated on the edge of second offset lattice. Therefore, the linear average of fields at a point located in the middle of two lattice edges is used to calculate

wave impedance. Averaging the electric field and the magnetic field in (2-30), provides two different solutions for wave impedance:

$$\eta = \sqrt{\frac{\mu}{\varepsilon}} \cos\left(\frac{\varphi}{2}\right)^S \quad (2-31)$$

In which $S = 1$ for the structure with major electric response while for those with predominantly magnetic response, $S = -1$.

2 - 3 - 2 Effective Parameters

In addition to the field averaging solution, another approach known as standard retrieval method was developed to obtain the effective parameters. In this approach, a propagating wave is assumed to be incident upon a thin slab and thereafter the scattering parameters derived by full wave simulation are used to calculate the effective permittivity and permeability. The extraction of material parameters are briefly reviewed in next sections.

2 - 3 - 2 - 1 Nicolson-Ross-Weir Method

The equations published by Nicolson, Ross and Weir [102] enable the calculation of the complex permittivity and permeability of a material sample from the measured S-parameters. The correlation between S-parameters and material properties is derived here by considering multiple reflections of a unit amplitude wave incident upon the sample interfaces within a waveguide [103]. Fig. 2-4 shows a slab with width d and constitutive parameters ε_2 and μ_2 which has been placed in a medium with constitutive parameters ε_1 and μ_1 . For simplicity, the surrounding medium is assumed to be air.

A plane wave is incident upon the air-slab interface and is partially reflected as well as partially transmitted. Since the slab width, d is limited, the transmitted wave will exit from the other side of the slab with a phase shift. The transmitted wave is partially reflected again at the slab-air interface. This procedure will continue forever. The scattered parameter and the transmitted parameter can be calculated by summing all reflected and transmitted waves, respectively:

$$\begin{aligned}
S_{11} &= \frac{V_{ref}}{V_{inc}} = \Gamma + \Gamma' \tau \tau' e^{-j2k_2 d} + \Gamma'^3 \tau \tau' e^{-j4k_2 d} + \dots \\
&= \Gamma + \frac{\Gamma' \tau \tau' e^{-j2k_2 d}}{1 - \Gamma'^2 e^{-j2k_2 d}}
\end{aligned} \tag{2-32}$$

$$S_{21} = \frac{V_{tran}}{V_{inc}} = \tau \tau' e^{-jk_2 d} + \Gamma'^2 \tau \tau' e^{-j3k_2 d} + \dots = \frac{\tau \tau' e^{-j2k_2 d}}{1 - \Gamma'^2 e^{-j2k_2 d}} \tag{2-33}$$

Where Γ and Γ' are the reflection coefficients:

$$\Gamma = \frac{\eta_2 - \eta_1}{\eta_1 + \eta_2} = -\frac{\eta_1 - \eta_2}{\eta_1 + \eta_2} = -\Gamma' \tag{2-34}$$

Where τ and τ' are the transmission coefficients for the air-slab interface and the slab-air interface:

$$\tau = \frac{2\eta_2}{\eta_1 + \eta_2} \tag{2-35}$$

$$\tau' = \frac{2\eta_1}{\eta_1 + \eta_2} \tag{2-36}$$

And k_2 is the wave number in the slab:

$$k_2 = \omega \sqrt{\epsilon_2 \mu_2} \tag{2-37}$$

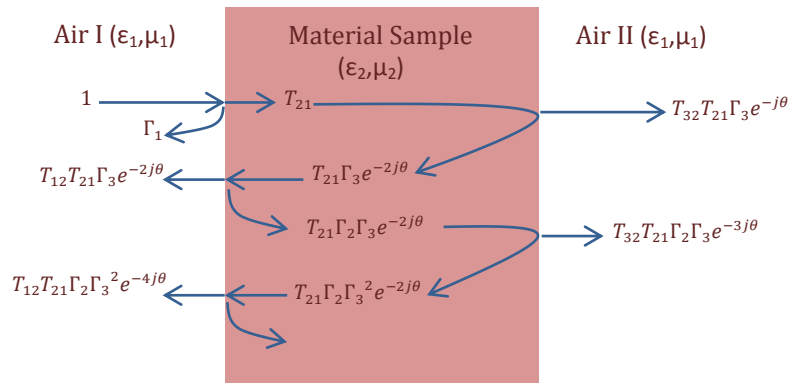


Fig. 2-4. Multiple reflections at air-sample interfaces

S_{11} and S_{21} can be simplified as:

$$S_{11} = \frac{\eta_2 - \eta_1}{\eta_1 + \eta_2} \frac{1 - e^{-j2k_2d}}{1 - \left(\frac{\eta_2 - \eta_1}{\eta_1 + \eta_2}\right)^2 e^{-j2k_2d}} = \frac{(\eta^2 - 1)(1 - Z^2)}{(\eta + 1)^2 - (\eta - 1)^2 Z^2} \quad (2-38)$$

$$S_{21} = \frac{4\eta_2\eta_1}{(\eta_1 + \eta_2)^2} \frac{e^{-j2k_2d}}{1 - \left(\frac{\eta_2 - \eta_1}{\eta_1 + \eta_2}\right)^2 e^{-j2k_2d}} = \frac{4\eta Z}{(\eta + 1)^2 - (\eta - 1)^2 Z^2} \quad (2-39)$$

Where $\eta = \frac{\eta_2}{\eta_1}$ and $Z = e^{-j2k_2d}$. If only the first two reflections are considered, the signal flow graph for such a model can be drawn as shown in Fig. 2-5 [102].

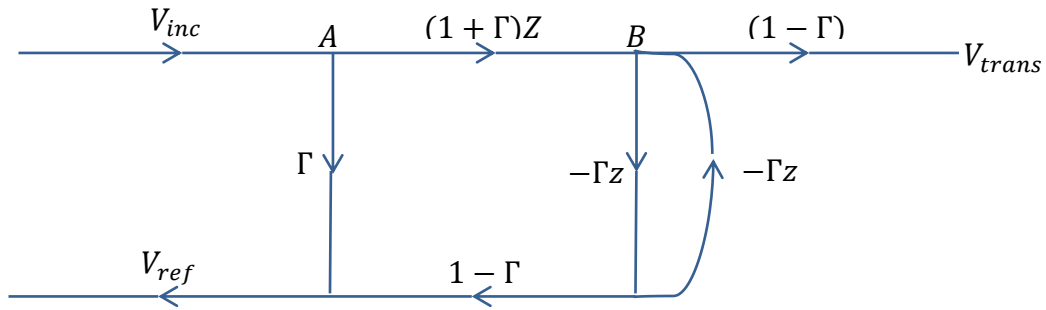


Fig. 2-5. Multiple reflections signal flow

Where, V_{inc} is the amplitude of the incident signal, V_{ref} is the amplitude of reflected signal and V_{trans} is the amplitude of transmitted signal. In the graph shown in Fig. 2-5 it has been assumed that $1 + \Gamma = \tau$. According to the Masson's signal flow rules [102] one can write S_{11} and S_{21} as follows:

$$S_{11} = \frac{V_{ref}}{V_{inc}} = \frac{\Gamma(1 - \Gamma^2 Z^2) - \Gamma(1 - \Gamma^2)Z^2}{1 - \Gamma^2 Z^2} = \frac{(1 - Z^2)\Gamma}{1 - \Gamma^2 Z^2} \quad (2-40)$$

$$S_{21} = \frac{V_{tran}}{V_{inc}} = \frac{(1 - \Gamma^2)Z}{1 - \Gamma^2 Z^2} \quad (2-41)$$

One can obtain Γ and Z by substituting S-parameters in the above equations. The NRW [102] method is used to extract the constitutive parameters. To make the computation simpler V_1 , V_2 and X are defined as:

$$V_1 = S_{21} + S_{11} \quad (2-42)$$

$$V_2 = S_{21} - S_{11} \quad (2-43)$$

$$X = \frac{1 - V_1 V_2}{V_1 - V_2} = \frac{\Gamma^2 - 1}{2\Gamma} \quad (2-44)$$

Therefore:

$$\Gamma = X \pm \sqrt{X^2 - 1} \quad (2-45)$$

The sign in the above equation must be chosen to satisfy $|\Gamma| \leq 1$. Also Z can be obtained using similar calculus:

$$Y = \frac{1 + V_1 V_2}{V_1 + V_2} = \frac{Z^2 + 1}{2Z} \quad (2-46)$$

Then:

$$Z = Y \pm \sqrt{Y^2 - 1} \quad (2-47)$$

It should be noted that the sign in above equation is chosen to keep $|Z| \leq 1$ satisfied. Also the relation between Γ and Z can be written as:

$$Z = \frac{V_1 - \Gamma}{1 - V_1 \Gamma} \quad (2-48)$$

$$\Gamma = \frac{Z - V_2}{1 - V_2 Z} \quad (2-49)$$

One can calculate the constitutive parameters of the model having Γ and Z values in hand:

$$\frac{\mu_{r2}}{\varepsilon_{r2}} = \eta^2 = \left(\frac{1 + \Gamma}{1 - \Gamma} \right) = c_1 \quad (2-50)$$

$$\mu_{r2} \varepsilon_{r2} = \left(\frac{jC}{\omega d} (\ln(Z) + j2m\pi) \right)^2 = c_2 \quad (2-51)$$

And finally:

$$\varepsilon_{r2} = \sqrt{\frac{c_2}{c_1}} \quad (2-52)$$

The logarithm function in (2-51) is a multi-branch function which only the right branch gives the right value and validates the obtained constitutive parameters. If the slab width d is small compared to the wavelength, the logarithm function can be replaced by its approximation [104]:

$$1 - Z = 1 - \frac{V_1 - \Gamma}{1 - V_1 \Gamma} = \frac{(1 - V_1)(1 + \Gamma)}{1 - V_1 \Gamma} \quad (2-53)$$

$$\eta = \frac{1 + \Gamma}{1 - \Gamma} = \frac{1 + Z}{1 - Z} \frac{1 - V_2}{1 + V_2} \quad (2-54)$$

And because $k_2 d$ is less than one, Z could be approximated as:

$$Z = e^{-jk_2 d} = \cos k_2 d - j \sin k_2 d \xrightarrow{k_2 d \ll 1} Z = 1 - jk_2 d \quad (2-55)$$

Substitution of this approximation into (2-56) provides an approximation for the constitutive parameters:

$$\eta = \sqrt{\frac{\mu_{r2}}{\varepsilon_{r2}}} = \frac{1 + Z}{1 - Z} \frac{1 - V_2}{1 + V_2} \approx \frac{2 - jk_2 d}{jk_2 d} \frac{1 - V_2}{1 + V_2} = \frac{2}{jk_0 \sqrt{\varepsilon_{r2} \mu_{r2} d}} \frac{1 - V_2}{1 + V_2} \quad (2-56)$$

$$\mu_{r2} \approx \frac{2}{jk_0 d} \frac{1 - V_2}{1 + V_2} \quad (2-57)$$

An approximation of permittivity can be achieved as follows:

$$S_{11} = \frac{(\eta^2 - 1)(1 - Z^2)}{(\eta + 1)^2 - (\eta - 1)^2 Z^2} \approx \frac{(\eta^2 - 1)(1 - (1 - jk_2 d)^2)}{(\eta + 1)^2 - (\eta - 1)^2 (1 - jk_2 d)^2} \quad (2-58)$$

$$2S_{11} \approx j \frac{\left(\frac{\mu_{r2}}{\varepsilon_{r2}} - 1\right)}{\sqrt{\frac{\mu_{r2}}{\varepsilon_{r2}}}} k_0 \sqrt{\varepsilon_{r2} \mu_{r2} d} \implies \varepsilon_{r2} \approx \mu_{r2} + j \frac{2S_{11}}{k_0 d} \quad (2-59)$$

Also another approximation of permittivity which relates it to V_1 and V_2 can be calculated:

$$\eta^2 = \frac{\mu_{r2}}{\varepsilon_{r2}} = \left(\frac{1+\Gamma}{1-\Gamma}\right)^2 = \frac{X+1}{X-1} = \frac{1+V_1}{1-V_1} \frac{1-V_2}{1+V_2} \quad (2-60)$$

Substituting this relation into (2-57), one can approximate permittivity:

$$\varepsilon_{r2} = \frac{\mu_{r2}}{\frac{1+V_1}{1-V_1} \frac{1-V_2}{1+V_2}} \approx \frac{jk_0 d \frac{1-V_2}{1+V_2}}{\frac{1+V_1}{1-V_1} \frac{1-V_2}{1+V_2}} \approx \frac{2}{jk_0 d} \frac{1-V_1}{1+V_1} \quad (2-61)$$

It has been confirmed experimentally that the effective permittivity ε_{r2} and permeability μ_{r2} calculated using these expressions have good accuracy.

2 - 3 - 2 - 2 Scattering parameters extraction and validation

It was mentioned in the NRW method discussion that when the slab thickness is small, Z can be approximated and the constitutive parameters are obtained without ambiguity. Next, the method used by Smith et al. [92] to extract the constitutive parameters of a split ring resonator (SRR) is demonstrated. ANSYS HFSS is used to derive S-parameters, then the extraction method is applied to S-parameters to retrieve the constitute parameters. This has been done in MATLAB.

In this method both transfer and 'ABCD' matrices of a metamaterial are calculated using its transmission line model. Then the relationship between the S-parameters and those matrices are defined. If the incident wave upon the slab is shown by matrix \bar{F} and the transmitted wave shown by matrix \bar{F}' then the relationship between these two waves can be defined by:

$$\bar{F}' = \begin{pmatrix} \bar{E}' \\ \bar{H}' \end{pmatrix} = T\bar{F} = T \begin{pmatrix} \bar{E} \\ \bar{H} \end{pmatrix} \quad (2-62)$$

Where \bar{E} and \bar{H} are the electric and magnetic fields of the incident wave upon the slab, \bar{E}' and \bar{H}' are the electric and magnetic fields of transmitted wave and T is the transfer matrix which can be defined with the help of transmission line theory:

$$T = \begin{pmatrix} \cos(n_2 k_0 d) & jz \sin(n_2 k_0 d) \\ \frac{j}{z} \sin(n_2 k_0 d) & \cos(n_2 k_0 d) \end{pmatrix} \quad (2-63)$$

Where n_2 is the refractive index and z is normalized impedance to the free wave characteristic impedance. The scattering matrix can be obtained by using the transfer matrix. For a symmetric homogenous environment the relationships below are satisfied:

$$S_{11} = S_{22} = \frac{1}{T_{11} + \frac{1}{2}(T_{12} + T_{21})} = \frac{1}{\cos(n_2 k_0 d) + \frac{j}{2}(z + \frac{1}{z})\sin(n_2 k_0 d)} \quad (2-64)$$

$$S_{21} = S_{12} = \frac{\frac{1}{2}(T_{12} - T_{21})}{T_{11} + \frac{1}{2}(T_{12} + T_{21})} = \frac{\frac{j}{2}(z - \frac{1}{z})\sin(n_2 k_0 d)}{\cos(n_2 k_0 d) + \frac{j}{2}(z + \frac{1}{z})\sin(n_2 k_0 d)} \quad (2-65)$$

Then, z and n_2 can be calculated from above equations:

$$n_2 = \sqrt{\mu_{r2} \varepsilon_{r2}} = \frac{1}{k_0 d} \cos^{-1} \left(\frac{1}{2S_{21}} (1 + S_{21}^2 - S_{11}^2) \right) \quad (2-66)$$

$$z = \sqrt{\frac{\mu_2}{\varepsilon_2}} = \sqrt{\frac{\mu_{r2}}{\varepsilon_{r2}}} = \sqrt{\frac{(1 + S_{11})^2 - S_{21}^2}{(1 - S_{11})^2 - S_{21}^2}} \quad (2-67)$$

And finally:

$$\mu_{r2} = n_2 z \quad (2-68)$$

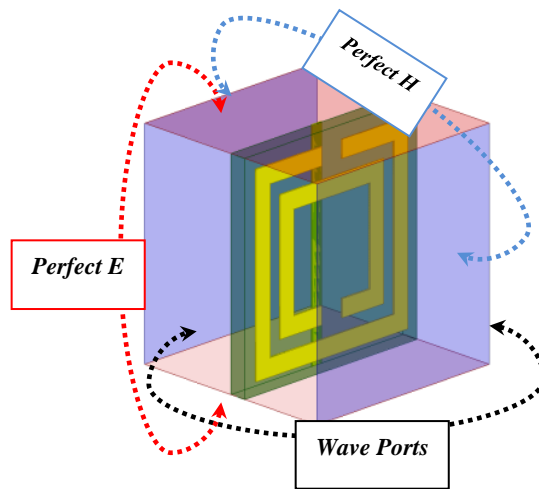
$$\varepsilon_{r2} = \frac{n_2}{z} \quad (2-69)$$

It can be seen that an inverse cosine function with a complex input has been used to calculate n_2 . Again this function is a multi-branch function and only the right branch leads us to correct answers. An equivalent logarithm function can be substituted for the inverse cosine function:

$$\cos^{-1}(x) = \pm j \ln(x + j\sqrt{1-x^2}) \quad (2-70)$$

Again, the solutions of (2-70) exhibit the multi branch ambiguity problem. The effective permittivity and permeability for a DNG metamaterial are derived using standard retrieval method. To do so, first the model shown in Fig. 2-6.a was set up. The unit cell is cubic with a cell dimension of 2.5 mm using the FR4 substrate ($\epsilon_r = 4.4, \delta = 0.02$) with thickness of 0.25 mm. A copper SRR and a thin wire are located on opposite sides of the substrate. The copper thickness is 18 μm . The thin wire has a width of 0.14 mm and the same length as the unit cell length. Both rings in the SRR have width of 0.2 mm and the gap of 0.3 mm. The outer ring length of the SRR is 2.2 mm and the gap between the inner and the outer rings is 0.15 mm.

The Perfect-E and Perfect-H boundary conditions are applied to the lateral walls forcing the electric field parallel to the thin wire and the magnetic field normal to the SRR plane. These boundary conditions are mounted at a distance around 10 times larger than the substrate thickness away from the structure to avoid the effect of field distribution on the derived S-parameters. Thereafter, the scattering parameters are derived by the waveguide simulation in which a propagating plane wave is incident upon the unit cell structure. Simulation results showed a very good agreement with the results presented in [92].



(a)

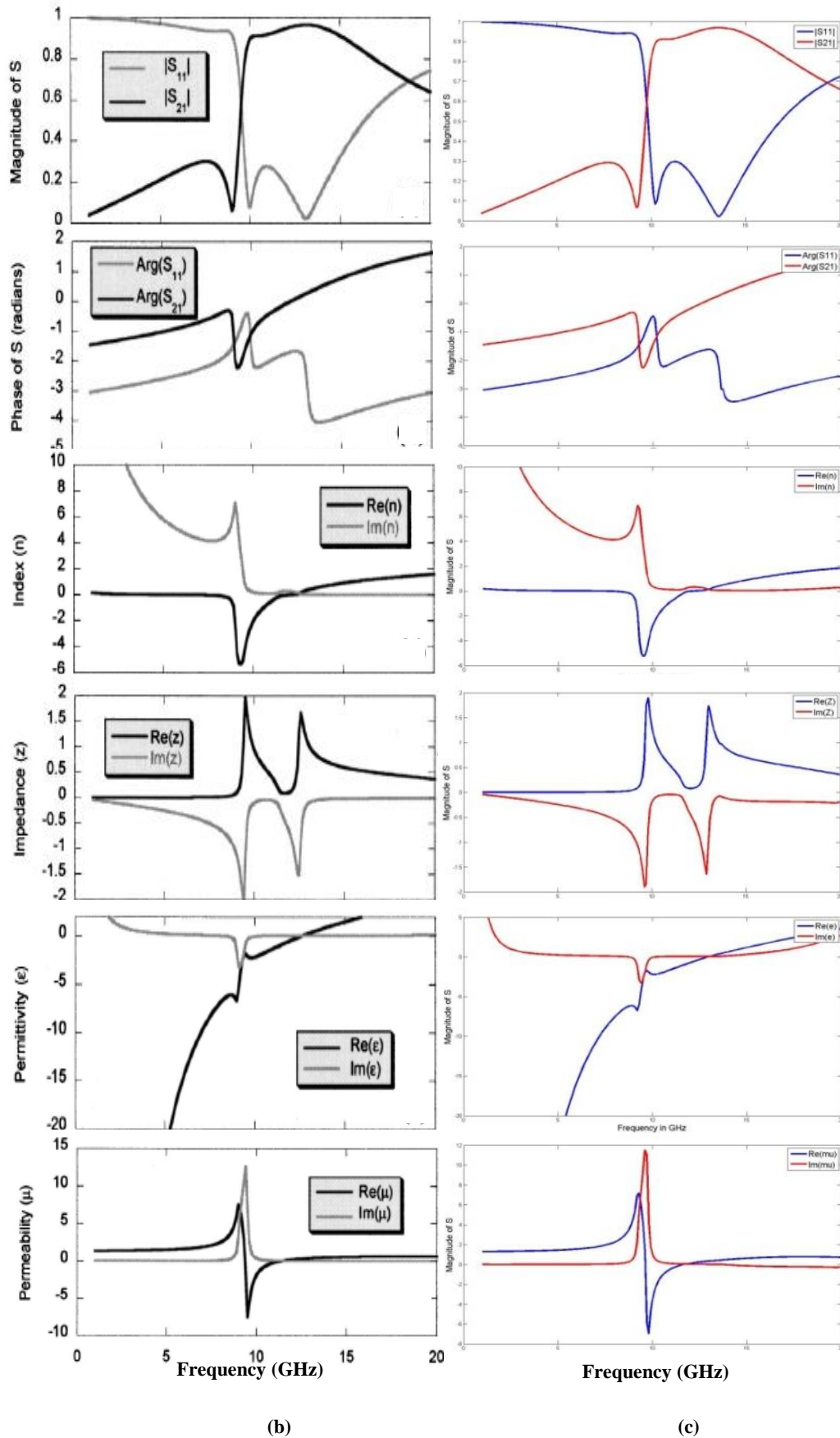


Fig. 2-6. Material parameters extraction for a DNG unit cell (a) model setup (b) results reported in [92] (c) results from HFSS simulation and MATLAB interpretation

2 - 4 Transmission Line (TL) Theory

TL modelling of metamaterial structures has been widely used and developed as a powerful tool for understanding and designing metamaterial structures. A symmetric metamaterial structure can be modelled by including the RH effect into a purely LH circuit which supports both forward and backward waves. In this section, the circuit equivalent of a two-port microwave network is studied. Then, the TL model of a particular metamaterial cell is presented.

2 - 4 - 1 Equivalent Circuit for a Two-port Microwave Network

Assume an obstacle is placed within a long waveguide as shown in Fig. 2-7. If there are no other obstacles, then only the TE_{10} mode exists as $z \rightarrow -\infty$, and the electric and the magnetic fields at Port I can be represented as:

$$E_{1y} = \sqrt{\frac{2}{a}} \sin \frac{\pi x}{a} V_1(z) \quad (2-71)$$

$$H_{1x} = -\sqrt{\frac{2}{a}} \sin \frac{\pi x}{a} I_1(z) \quad (2-72)$$

Where $V_1(z)$ and $I_1(z)$ are the equivalent voltage and current at Port I.

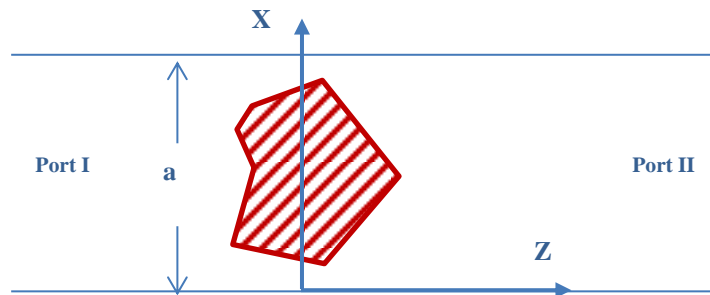


Fig. 2-7. A random obstacle located in a waveguide

Substitution of (2-71) and (2-72) into Maxwell's equations, will give the transmission line equations [105]. The current and voltage on the surface of the obstacle are related as:

$$\frac{d^2 V_1(z)}{d^2 z} + k_{10}^2 V_1(z) = 0 \quad (2-73)$$

$$\frac{d^2 I_1(z)}{d^2 z} + k_{10}^2 I_1(z) = 0 \quad (2-74)$$

Where k_{10} is the wave number for the TE_{10} mode. Solutions of the transmission line equations can be presented as follows,

$$V_1(z) = V_1^+ e^{k_{10}z} + V_1^- e^{-k_{10}z} \quad (2-75)$$

$$I_1(z) = I_1^+ e^{k_{10}z} + I_1^- e^{-k_{10}z} \quad (2-76)$$

In which $V_1(z)$ and $I_1(z)$ are the equivalent voltage and current. The plus and minus signs are representing the amplitude of the propagating wave through, and the reflected wave from the obstacle, respectively. Relations between V^+ , V^- , I^+ and I^- can be represented by:

$$\frac{V_1^+}{I_1^+} = \frac{V_1^-}{I_1^-} = \frac{\omega\mu}{K_{10}} = Z_0 \quad (2-77)$$

Where, Z_0 is the characteristic impedance of the transmission line. In a similar fashion, the relationships for the incident wave upon the other side of the obstacle can be written,

$$V_2(z) = V_2^+ e^{k_{10}z} + V_2^- e^{-k_{10}z} \quad (2-78)$$

$$I_2(z) = I_2^+ e^{k_{10}z} + I_2^- e^{-k_{10}z} \quad (2-79)$$

Next the voltage and current at the $z = 0$ plane, where the obstacle is located, are considered. V_1 and I_1 in (2-75) and (2-76), represent the voltage and current extrapolated back to the $z = 0^-$ plane from $-\infty$, V_2 and I_2 in (2-78) and (2-79) represent the voltage and current extrapolated back to the $z = 0^+$ plane from $+\infty$. In general, $V_1 \neq V_2$ and $I_1 \neq I_2$ at the presence of an obstacle. The voltages are related to the currents through the impedance matrix:

$$\begin{bmatrix} V_1 \\ V_2 \end{bmatrix} = \begin{bmatrix} Z_{11} & Z_{12} \\ Z_{21} & Z_{22} \end{bmatrix} \begin{bmatrix} I_1 \\ I_2 \end{bmatrix} \quad (2-80)$$

Or simply:

$$[V] = [Z][I] \quad (2-81)$$

Where Z is the impedance matrix and is defined by properties of the obstacle. In the case of a reciprocal obstacle, the impedance matrix is symmetric. Fig. 2-8 shows an equivalent circuit diagram for a two port network.

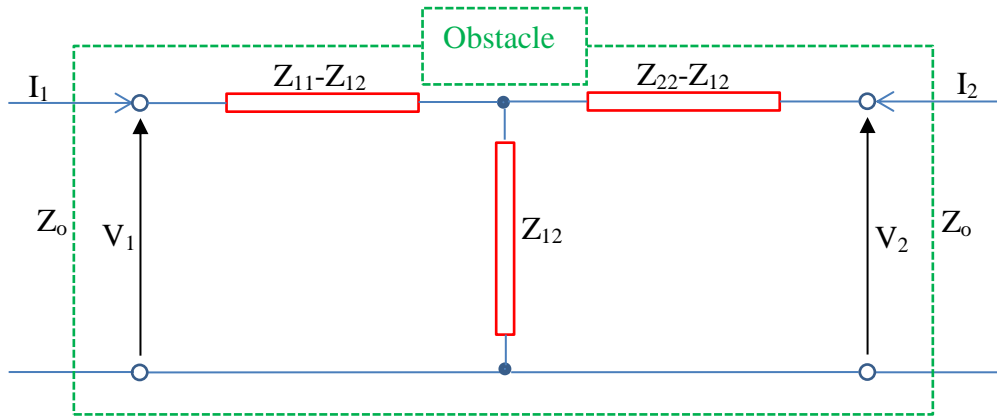


Fig. 2-8. Equivalent circuit for a two-port microwave network

The impedance matrix $[Z]$ is convenient for analysing the network problems. However, when the obstacle is analysed by a mode matching method, the scattering matrix is used rather than the impedance matrix. A scattering matrix $[S]$ relates the amplitudes of the incident wave to the amplitudes of reflected waves as follows [106]:

$$\begin{bmatrix} V_1^- \\ V_2^- \end{bmatrix} = \begin{bmatrix} S_{11} & S_{12} \\ S_{21} & S_{22} \end{bmatrix} \begin{bmatrix} V_1^+ \\ V_2^+ \end{bmatrix} \quad (2-82)$$

Both the impedance $[Z]$ and scattering $[S]$ matrices depend on properties of the obstacle and are related to each other [105]. If it is assumed that the obstacle is reciprocal, then $[Z]$ and $[S]$ are symmetric matrices:

$$\frac{Z_{11}}{Z_0} = \frac{(1 + S_{11}) + (1 - S_{22}) + S_{12}^2}{\Delta S} \quad (2-83)$$

$$\frac{Z_{12}}{Z_0} = \frac{2S_{12}}{\Delta S} \quad (2-84)$$

$$\frac{Z_{22}}{Z_0} = \frac{(1 - S_{11})(1 + S_{22}) + S_{12}^2}{\Delta S} \quad (2-85)$$

Where:

$$\Delta S = (1 - S_{11})(1 - S_{22}) - S_{12}^2 \quad (2-86)$$

In the above equations, $[Z]$ has been assumed to be a symmetric matrix.

2 - 4 - 2 Metamaterial Unit Cell Equivalent Circuit

A symmetric metamaterial structure can be modelled by including the RH effect into a purely LH circuit. To do so, first the LH material equivalent circuit is defined. Series capacitance and shunt inductance combination supports a backward wave, and thus can be used to model a non-resonant LH material [107]. This equivalent circuit describes a low-loss perfect LH material which is non-resonant and broad band. The phase constant β for such materials is given by the following dispersion relation:

$$\beta = -\frac{1}{\omega\sqrt{C_L L_L}} \quad (2-87)$$

On the other hand, the series inductance and the shunt capacitance can model a low-loss RH material. The dispersion relation for a RH material can be written as:

$$\beta = \omega\sqrt{C_R L_R} \quad (2-88)$$

The RH and LH transmission line models and relative dispersion diagrams are shown in Fig. 2-9.

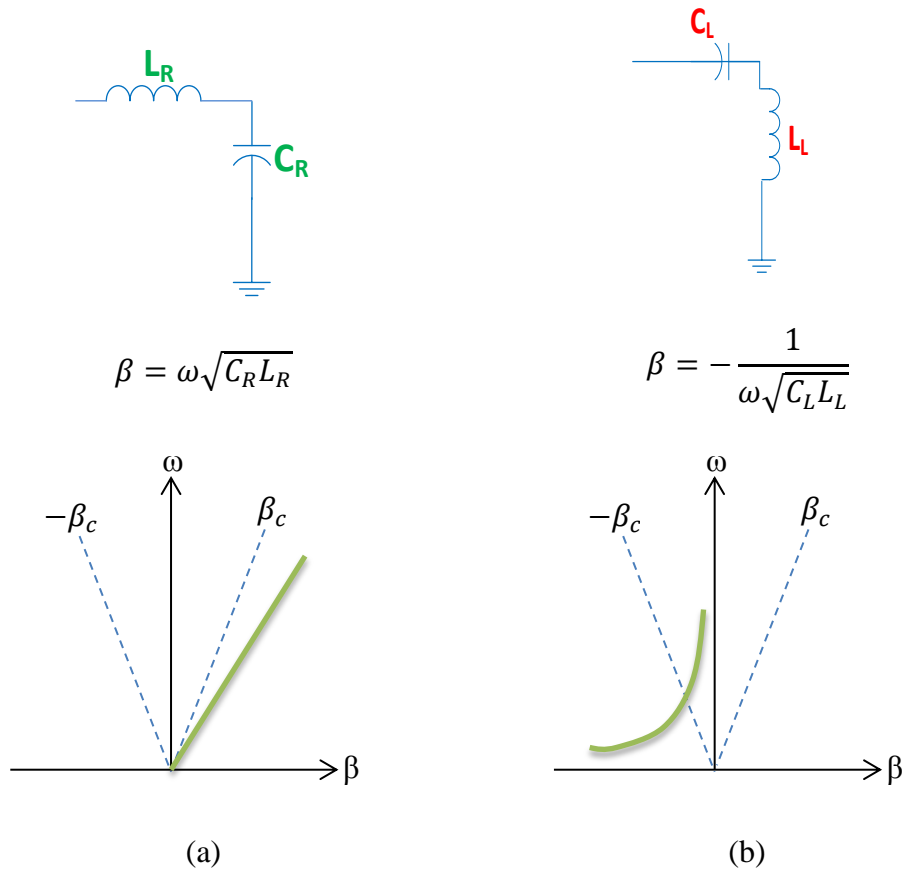


Fig. 2-9. Transmission line model and relative dispersion diagram for (a) RH (b) LH materials

However, in practice LHM structures exhibit unavoidable associated parasitic RH effects which make them resonant, lossy and narrow-band. Such structures are called composite right/left handed (CRLH) structures and both the LH and RH transmission line models must be combined to model them [107]. Fig. 2-10 shows equivalent circuit model for a symmetrical CRLH unit cell. In the T-type model, shown in Fig. 2-10 (a), the LH capacitors are located at the two ends while in the π -type model, shown in Fig. 2-10 (b), the LH capacitor is placed at the centre. Metamaterial structures such as the mushroom structure [78] belong to the T-type model while structures like the CRLH substrate integrated wave guide (SIW) [59] are modelled using the π -type circuit. However, for a lattice of unit cells, the periodic boundary conditions are applied and both the T-type and the π -type models become identical. The universal model for a typical symmetric unit cell in a periodic structure is shown in Fig. 2-10c.

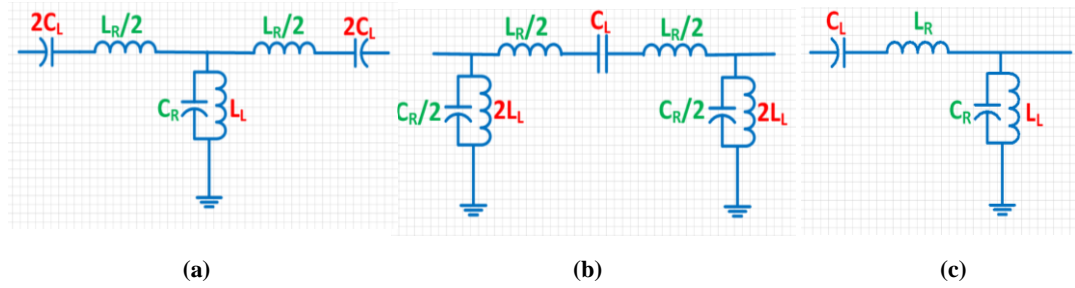


Fig. 2-10. TL theory, equivalent for symmetrical CRLH unit cells, (a) T-type model (b) π -type model (c) identical model for periodic CRLH unit cell [59]

The dispersion relation for periodic CLRH structures is given by [108]:

$$\beta(\omega) = \frac{1}{p} \cos^{-1} \left(1 - \frac{1}{2} \left(\frac{\omega_L^2}{\omega^2} + \frac{\omega^2}{\omega_R^2} - \frac{\omega_L^2}{\omega_{se}^2} - \frac{\omega_L^2}{\omega_{sh}^2} \right) \right) \quad (2-89)$$

Where, p is the unit cell length and:

$$\omega_L = \frac{1}{\sqrt{C_L L_L}}, \omega_R = \frac{1}{\sqrt{C_R L_R}}, \omega_{se} = \frac{1}{\sqrt{C_L L_R}}, \omega_{sh} = \frac{1}{\sqrt{C_R L_L}} \quad (2-90)$$

The corresponding dispersion diagram is shown in Fig. 2-11 . CLRH structures support backward wave propagation at lower frequencies and forward wave propagation at higher frequencies. At $\beta = 0$, the two frequency points are referred to as the infinite wavelength points with a band gap in between. The CRLH structure is balanced when the shunt resonant frequency and the series resonant frequency are equal. However, it is called unbalanced CLRH when the shunt and series resonances occur at different frequencies. Unbalanced CLRH structures exhibit an electromagnetic band gap over which the electromagnetic waves cannot propagate.

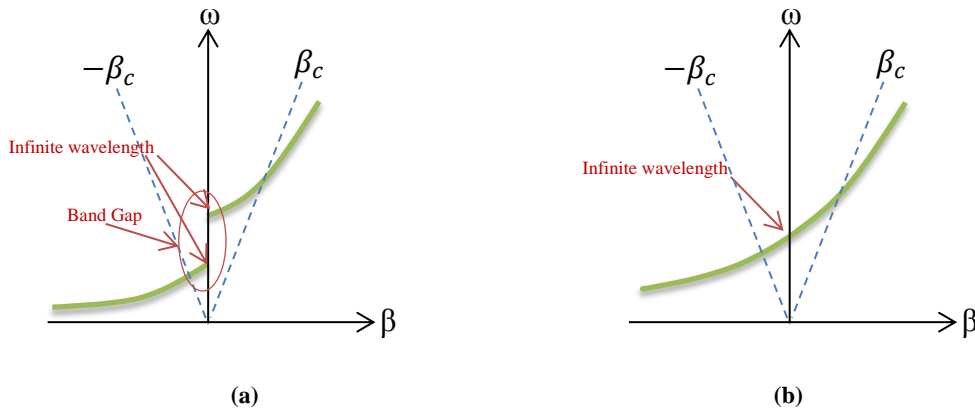


Fig. 2-11. Dispersion diagram (a) Unbalanced CRLH, $\omega_{se} \neq \omega_{sh}$ (b) Balanced CRLH, $\omega_{se} = \omega_{sh}$

Depending on the unit cell geometry and boundary conditions, usually only one zero-order resonance is excited. For an open-ended structure the shunt resonance, and for a close-ended structure the series resonance, is excited. When a unit cell is repeated to form a metamaterial structure, multiple resonances including the negative, zeroth, and positive resonance could occur. The resonance modes for an M-stage metamaterial structure can be derived from the dispersion diagram when the following resonance condition is satisfied [108]:

$$\beta_P = \frac{n\pi}{l} \begin{cases} n = 0, \pm 1, \dots, \pm(M-1) \\ \text{for T-type unit cell} \\ \\ n = 0, \pm 1, \dots, \pm M \\ \text{for } \pi\text{-type unit cell} \end{cases} \quad (2-91)$$

The patch antenna resonates when the half-wavelength field distribution is formed over the patch. A CRLH material can have the same half-wavelength field distribution, but at much lower frequency which results in a much smaller patch antenna when made of CRLH unit cells.

2 - 5 Summary

In this chapter basic concepts and fundamental theories needed in the study of metamaterials have been introduced. Metamaterial classification, field response and polarisation current over a unit cell have been described. Techniques to extract material parameters from transmission and reflection coefficients have been explained.

The average constitutive material parameters for a sub-wavelength range unit cell have been calculated using the Drude-Lorentz model and by averaging local fields within the cell. Moreover, another approach known as standard retrieval method has been introduced to obtain the effective material parameters. In this latter approach, a propagating wave is assumed to be incident upon a thin slab and thereafter the scattering parameters derived by full wave simulation are used to calculate the effective permittivity and permeability. As an example, the effective constitutive parameters of a split ring resonator (SRR) were derived where S-parameters were obtained through a full wave simulation conducted by ANSYS

HFSS. Afterward the derived S-parameters have been imported to MATLAB by which the standard retrieval technique was coded. Finally, the use of transmission line (TL) approach in modelling metamaterials unit cells and the TL model for the right-handed and left-handed mediums and their dispersion diagram were presented.

Chapter 3

Zero Index Metamaterials

In this chapter, the electromagnetic properties of planar zero index materials (ZIM) for an electromagnetic plane wave are investigated. Different structures are studied with respect to their electrical characteristics giving special attention to their operational bandwidth. Metamaterial structures such as rods, C-shape, S-shape, W-shape and meander-line structures are designed and simulated, then the standard retrieval techniques are applied to extract the material parameters from the scattering parameters. The obtained results for different ZIM structures are used to analyse their performance. Two novel broadband ZIM structures are proposed. The proposed structures are simulated and results are discussed. Further, a highly directive quasi-Yagi antenna is designed by integrating the proposed ZIM unit cell onto the antenna substrate.

3 - 1 Introduction

Metamaterials are inherently narrowband and lossy structures. This limits the potential applications of metamaterials. So far, plenty of metamaterial applications in microwave devices have been reported whilst among those, zero index materials (ZIM) whose permittivity and permeability are simultaneously or individually equal to zero [109], as a type of metamaterial, have attracted a lot of interest because of their wider bandwidth, low loss and easy fabrication characteristics.

Further developments in the study of metamaterials unveil that when waves are incident from the inside of a ZIM heading toward free space, the refracted wave will be refracted towards the normal to the interface. This characteristic can be

deployed to boost the directivity of an antenna [110]. Enoch et al. experimentally demonstrated that the energy radiated by a source embedded in a slab of ZIM will be concentrated in a narrow cone in the surrounding media [49]. This potentially gave a lead to microwave researchers to investigate further antenna designs. Later, metamaterial embedded substrates known as directive antenna substrates, composed of a periodic collection of rods, or of both rods and rings, were introduced [111]. A directivity improvement of 2 *dBi* for the horn antenna loaded by three layers of ZIM was reported in [112]. A narrow directive beam was achieved for a structure composed of a finite number of periodic rows of metallic cylinders excited by an electric line source [113]. The wave emitted from a monopole microwave antenna propagating into a metallic grid slab was studied in [114]. Highly directive emission based on anisotropic metamaterials with a narrow hyperbola spatial dispersion pattern was investigated in [115].

The directivity and efficiency of an electromagnetic emission can significantly improve by embedding the source in an anisotropic matrix with one component of the physical parameters, i.e. permittivity and permeability, near zero in a given direction [116]. In the next section, the propagation of an EM wave through ZIM media is studied.

3 - 2 Theory of High Directive Media

Pendry et al. demonstrated in [117] that a network of thin wires behaves like a low density plasma of very heavy charged particles with a plasma frequency in the GHz range. The EM properties of such a structure can be characterised by a plasma frequency:

$$\epsilon_{eff} = 1 - \frac{\omega_p^2}{\omega^2} \quad (3-1)$$

Where ω_p is the plasma frequency and so that the refractive index is given by:

$$n = \sqrt{\epsilon_{eff} \times \mu_{eff}} \quad (3-2)$$

Where ϵ_{eff} and μ_{eff} are the effective permittivity and permeability, respectively. The refractive index approaches zero when the operating frequency is very close to the plasma frequency.

According to Snell's law, when a wave propagates from a ZIM media into free space the angle of refraction is close to zero i.e., the refracted wave will be normal to the interface. The relationship between the angle of incidence and refraction for an incident wave upon an interface between two media with different indices of refraction is:

$$n_1 \sin \phi_1 = n_2 \sin \phi_2 \quad (3-3)$$

For ZIM we have:

$$n_1 \approx 0 \rightarrow n_2 \sin \phi_2 \approx 0 \xrightarrow{n_2 \neq 0} \sin \phi_2 \approx 0 \rightarrow \phi_2 \approx 0 \quad (3-4)$$

A theoretical model, shown in Fig. 3-1, is set up and simulated using ANSYS HFSS. In this model a dipole antenna was placed in ZIM media. The refracted wave is normal to the ZIM- air interface.

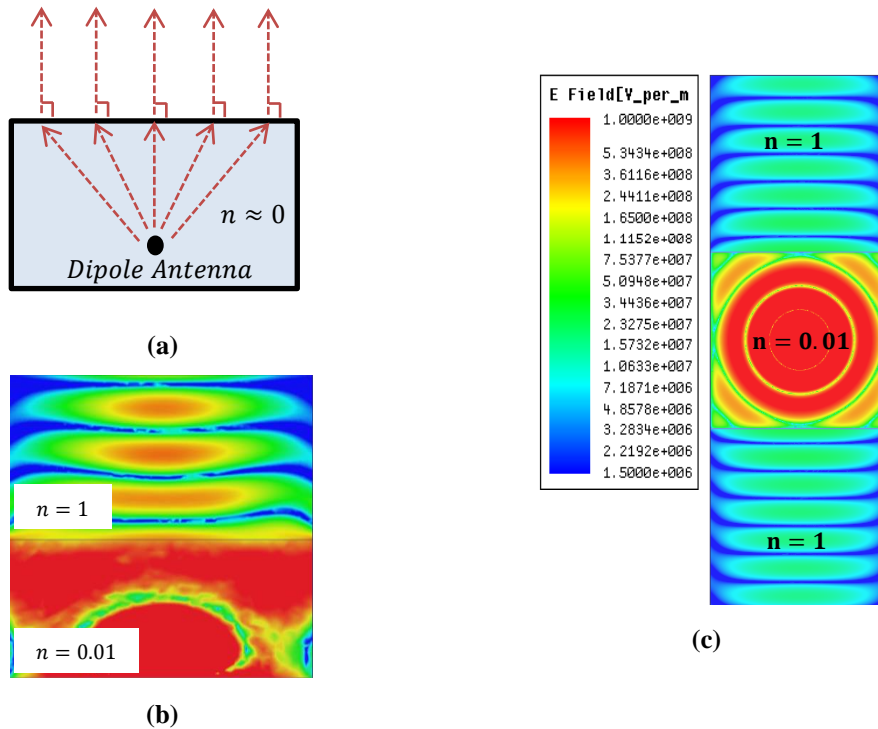


Fig. 3-1. Dipole antenna surrounded by ZIM media (a) Snell's law (b) Distribution of E-field magnitude side view (c) Distribution of E-field magnitude top view

The dipole emission forms a doughnut-shape radiation pattern. However, as the emitted wave impinges on the ZIM-air interface, it is forced to propagate as a plane wave. This property provides an excellent opportunity to design high-directive antennae.

3 - 3 Wave Propagation and Dispersion Relation in Anisotropic ZIM Medium

It was stated earlier in this chapter that the directivity and efficiency of an electromagnetic emission can significantly improve by embedding the source in an anisotropic matrix with one component of the physical parameters, i.e. permittivity and permeability, near zero in a given direction [116] . For clarity to demonstrate the ability of a ZIM to control the EM wave emission and why a medium with one low-value permittivity and permeability tensor parameters would lead to directive emission, the wave propagation and dispersion relation for an anisotropic ZIM needs to be investigated. The dispersion relation for an anisotropic medium with two generic tensors ϵ^{ij} and μ^{ij} is given by [118]:

$$\omega^4 - 2(\psi^{ij}k_i k_j)\omega^2 + \frac{\epsilon^{ij}k_i k_j}{\det(\epsilon)} \frac{\mu^{mn}k_m k_n}{\det(\mu)} = 0 \quad (3-5)$$

Where:

$$\psi^{ij} = \frac{1}{2} \epsilon^{imn} \epsilon^{jpg} \epsilon_{nq}^{-1} \mu_{mp}^{-1} \quad (3-6)$$

For the sake of simplicity it is assumed that the anisotropic material is characterised by diagonal constitutive parameter tensors:

$$\bar{\epsilon} = \epsilon_0 \text{diag}[\epsilon_{rx}, \epsilon_{ry}, \epsilon_{rz}] \quad (3-7)$$

$$\bar{\mu} = \mu_0 \text{diag}[\mu_{rx}, \mu_{ry}, \mu_{rz}] \quad (3-8)$$

Then the last term of (3-5) reads:

$$\frac{\varepsilon_{rx}k_{rx}^2 + \varepsilon_{ry}k_{ry}^2 + \varepsilon_{rz}k_{rz}^2}{\varepsilon_{rx}\varepsilon_{ry}\varepsilon_{rz}} \times \frac{\mu_{rx}k_{rx}^2 + \mu_{ry}k_{ry}^2 + \mu_{rz}k_{rz}^2}{\mu_{rx}\mu_{ry}\mu_{rz}} \quad (3-9)$$

The coefficient in the second term of (3-5) takes the form:

$$\begin{aligned} k_{rx}^2 \left(\frac{1}{\varepsilon_{ry}\mu_{rz}} + \frac{1}{\varepsilon_{rz}\mu_{ry}} \right) + k_{ry}^2 \left(\frac{1}{\varepsilon_{rx}\mu_{rz}} + \frac{1}{\varepsilon_{rz}\mu_{rx}} \right) \\ + k_{rz}^2 \left(\frac{1}{\varepsilon_{ry}\mu_{ry}} + \frac{1}{\varepsilon_{ry}\mu_{rx}} \right) \end{aligned} \quad (3-10)$$

Finally, the dispersion relation can be written as follows:

$$\begin{aligned} (\varepsilon_{rx}\varepsilon_{ry}\varepsilon_{rz}\mu_{rx}\mu_{ry}\mu_{rz})\omega^4 \\ + [\varepsilon_{rx}\mu_{rx}k_{rx}^2(\varepsilon_{ry}\mu_{rz} + \varepsilon_{rz}\mu_{ry}) \\ + \varepsilon_{ry}\mu_{ry}k_{ry}^2(\varepsilon_{rx}\mu_{rz} + \varepsilon_{rz}\mu_{rx}) \\ + \varepsilon_{rz}\mu_{rz}k_{rz}^2(\varepsilon_{rx}\mu_{ry} + \varepsilon_{ry}\mu_{rx})]\omega^2 \\ + (\varepsilon_{rx}k_{rx}^2 + \varepsilon_{ry}k_{ry}^2 + \varepsilon_{rz}k_{rz}^2)(\mu_{rx}k_{rx}^2 + \mu_{ry}k_{ry}^2 \\ + \mu_{rz}k_{rz}^2) = 0 \end{aligned} \quad (3-11)$$

A 2-D EM problem can be decomposed into TE polarisation with the electric field along the z-axis and TM polarisation with the magnetic field along the z-axis. Thus, the dispersion relation given by (3-11) can be rewritten as:

$$\frac{k_{TE_y}^2}{\mu_{rx}\varepsilon_{rz}} + \frac{k_{TE_x}^2}{\mu_{ry}\varepsilon_{rz}} = k_0^2 \quad (3-12)$$

$$\frac{k_{TM_y}^2}{\varepsilon_{rx}\mu_{rz}} + \frac{k_{TM_x}^2}{\varepsilon_{ry}\mu_{rz}} = k_0^2 \quad (3-13)$$

In which, k_0 is the free space wave number and $k_{TE_x}^2$ and $k_{TM_y}^2$ are the x- and y-components of wave number within the medium for TE and TM polarisation, respectively. A typical anisotropic ZIM structure is designed to have either zero permittivity or permeability in one direction and positive constant values in other directions. These positive values ideally provide impedance matching to the surrounding environment. Assuming a slab of anisotropic ZIM unit cell is placed

in the xy-plane, the permittivity and permeability tensor for such mediums can be written as:

$$\bar{\bar{\epsilon}} = \begin{bmatrix} \delta & 0 & 0 \\ 0 & \epsilon & 0 \\ 0 & 0 & \epsilon \end{bmatrix} \quad (3-14)$$

$$\bar{\bar{\mu}} = \begin{bmatrix} \delta & 0 & 0 \\ 0 & 1 & 0 \\ 0 & 0 & 1 \end{bmatrix} \quad (3-15)$$

For simplicity, setting $\mu_{ry} = \mu_{rz} = 1$ and $\epsilon_{ry} = \epsilon_{rz} = \epsilon > 0$; then (3-12) and (3-13) take the form:

$$\frac{k_{TE_y}^2}{\mu_{rx}} + k_{TE_x}^2 = \epsilon k_0^2 \quad (3-16)$$

$$\frac{k_{TM_y}^2}{\epsilon_{rx}} + \frac{k_{TM_x}^2}{\epsilon} = k_0^2 \quad (3-17)$$

It can be declared that for near-zero values of ϵ_{rx} and μ_{rx} , k_{TM_y} and k_{TE_y} have to be small values in order to satisfy the dispersion relation given by (3-16) and (3-17). In other words, the wave is forced to propagate along the x-direction with a very small component of the wave vector in the y-direction [119].

The physical explanation of this phenomenon can be addressed by the lossy nature of metamaterial structure [115]. Here, the permittivity and permeability along the x-direction (ϵ_{rx} and μ_{rx}) are complex-values which lead to quick attenuation for large values of $|k|$ in the x-direction. Specifically, in the case of permittivity and permeability with the real part equal or less than the imaginary part (anisotropic ZIM), the attenuation is even more significant. This forces the wave vector along the y-direction, k_y , to remain small. On the other hand, assuming a wave comes from a source inside the slab of ZIM incident upon the interface, then the tangential wave vector, k_y , must be conserved across the interface which forces the refracted wave to also have a small k_y and propagate along the x-direction. Fig. 3-2 shows the E-field distribution of a wave emitted by the dipole antenna and propagating along the x-direction for an anisotropic vacuum and an anisotropic zero permittivity medium. It can be seen in the zero-permittivity

medium the x-component of the wave vector remains small, forcing the emitted wave to propagate as a plane wave.

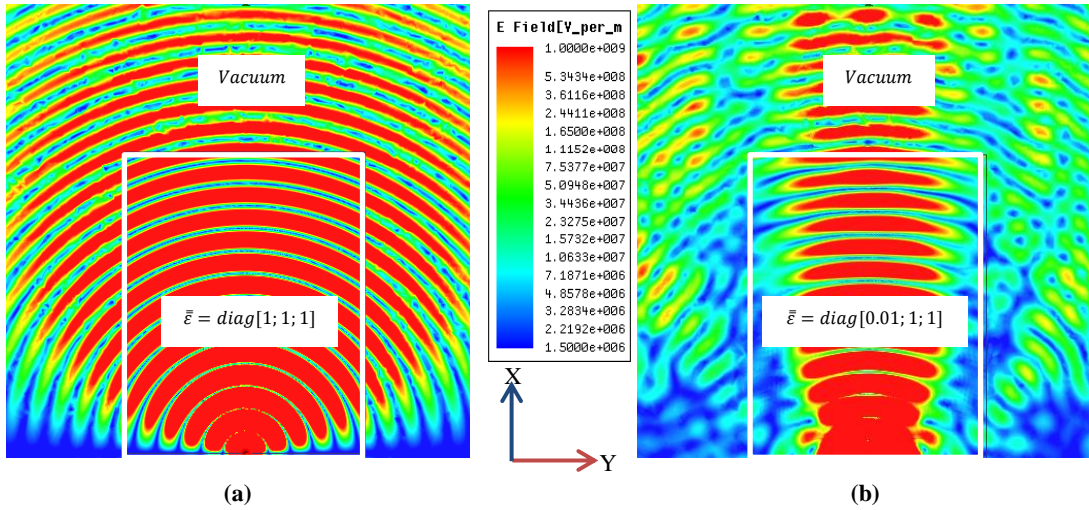


Fig. 3-2. E-field distribution for a wave comes from a dipole antenna in (a) anisotropic vacuum (b) zero-permittivity medium

3 - 4 Zero Index Materials (ZIM) Unit Cells

One of the main concerns in applications of metamaterial is the losses associated with the resonances of the structure. However, for ZIM structures the zero index properties are realised in frequencies much higher than the resonant frequency over which resonant losses are accordingly small. ZIM structures can have permittivity and permeability simultaneously or individually equal to zero. A macroscopically circulating current within a structure forms a magnetic dipole momentum which leads to a magnetic response and consequently a zero-permeability region. However, presence of an electric dipole momentum within a structure causes an electric response for the structure and a zero-permittivity region near the plasma frequency. A structure with fundamental electric (magnetic) response exhibits negative permittivity (permeability) around the resonant frequency which changes toward positive values from negative values as frequency increases and crosses the zero line at a frequency point higher than the resonant frequency. For instance, the effective permittivity for the rod structure with the electric response and the effective permeability of the CSRR structure with the magnetic response is shown in Fig. 3-3. It can be seen the resonant and the zero index regions are separated. The imaginary part of the permittivity (permeability) which is associated with medium losses remains fairly small over

the ZIM frequency range. This work has focused on structures with the electric response and zero-permittivity as they have more varieties of design and simpler shapes.

According to the Drude-Lorentz model of a material, the permittivity and permeability are given by [13]:

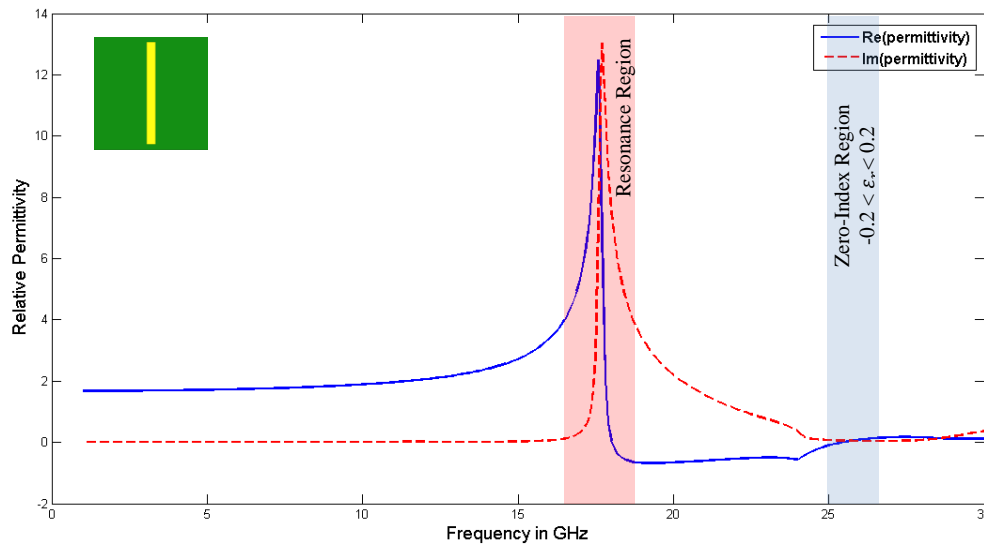
$$\varepsilon(\omega) = \varepsilon_0 \left(1 - \frac{\omega_{ep}^2 - \omega_{e0}^2}{\omega^2 - \omega_{e0}^2 + i\gamma_e \omega} \right) \quad (3-18)$$

$$\mu(\omega) = \mu_0 \left(1 - \frac{\omega_{mp}^2 - \omega_{m0}^2}{\omega^2 - \omega_{m0}^2 + i\gamma_m \omega} \right) \quad (3-19)$$

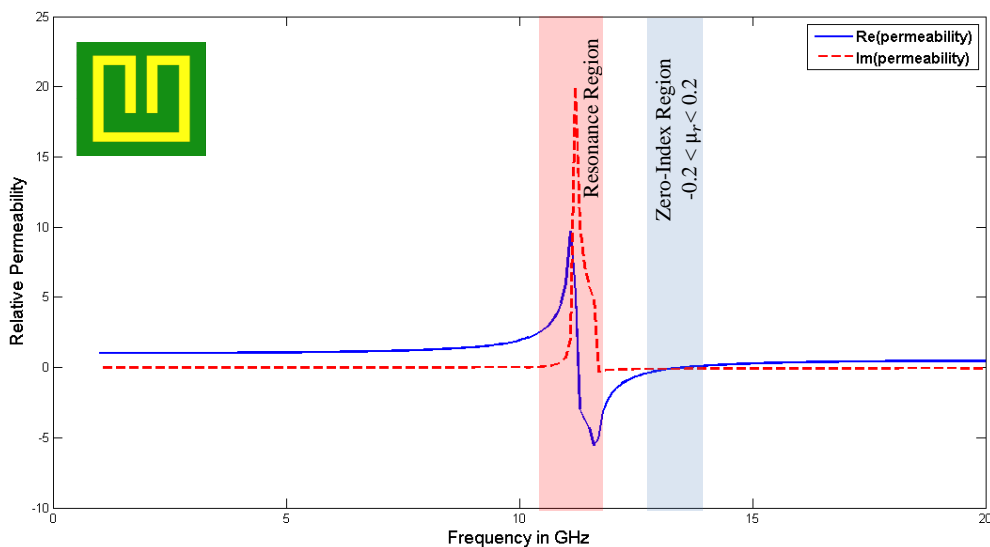
Where γ is the dissipation of plasmon energy, and ω_0 and ω_p are the electric resonant and plasma frequencies, respectively. There are frequencies around the plasma frequency over which the permittivity is infinitesimal and consequently, the refractive index is near zero. These frequencies define the bandwidth of a ZIM structure:

$$n = \sqrt{\varepsilon\mu} \xrightarrow{|\varepsilon| \rightarrow 0} 0 \quad (3-20)$$

Following the assumption stated in [120], the ZIM bandwidth is defined by the frequency range over which $|\varepsilon| < 0.2$.



(a)



(b)

Fig. 3-3. Zero index region (blue) with small losses and resonant region (red) with large imaginary part and consequently large losses indicated on graph of (a) permittivity of rod structure (b) permeability of CSRR structure

3 - 5 ZIM Related Topologies

In this section a comparative study of different structures with electric response has been made with special attention to their operational bandwidth. Metamaterial structures such as rods, C-shape, S-shape, W-shape and meander-line structures were designed and simulated, then the standard retrieval technique applied to extract the material parameters from the scattering parameters. The meander-line inductor is used to reduce the area occupied by the element. Having more

meanders within a unit cell means a longer conductive strip can be fitted within a unit cell. It means the half wavelength resonance frequency decreases followed by a lower plasma frequency for the structure. An increase in the number of meanders not only reduces the resonant and plasma frequencies of the cell but it also affects the characteristic capacitance and inductance of the cell by introducing more mutual coupling between the now closer adjacent conductors. Different realised ZIM structure topologies are shown in Fig. 3-4. All these structures exhibit an electrical response which results in a negative permittivity below their plasma frequency.

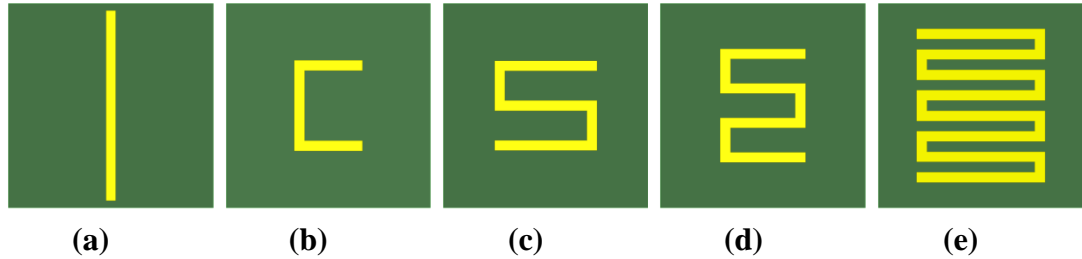


Fig. 3-4. ZIM topologies; (a) I-Shape(Rod), (b) C-Shape, (c) S-Shape, (d) W-Shape, (e) Meanderline

3 - 5 - 1 Effective and Physical Length

For a microstrip structure whose height is far smaller than both its width and length and also its length is larger than its width, the dominant mode is the TM_{010} mode. The resonant frequency of the microstrip as a function of its length is calculated by [121]:

$$(f_r)_{010} = \frac{1}{2L\sqrt{\epsilon_r}\sqrt{\mu_0\epsilon_0}} = \frac{c_0}{2L\sqrt{\epsilon_r}} \quad (3-21)$$

Where, c_0 is the speed of light in free space and L is the physical length of the scatterer. The effective dielectric value is constant at low and intermediate frequencies, its value then starting to increase until it reaches the value of the dielectric constant of the substrate. In fact, the effective dielectric constant has a value in the range of $1 < \epsilon_{eff} < \epsilon_r$. For a dielectric constant much larger than unity, the effective dielectric constant stays closer to the nominal dielectric

constant. At low frequencies, the initial value of the effective dielectric constant is called the static value of dielectric constant and can be calculated as [122]:

$$\varepsilon_{r_{eff}} = \frac{\varepsilon_r + 1}{2} + \frac{\varepsilon_r - 1}{2} \frac{1}{\sqrt{1 + 12 \frac{h}{w}}} \quad (3-22)$$

Where w is the width of copper trace and h is the height of copper trace from the ground. Moreover, the fringe fields must be considered in the calculation of the electrical length (also known as the effective length). Therefore (3-21) must be modified to include edge effects and can be rewritten as [121]:

$$(f_r)_{010} = \frac{c_0}{2L_{eff}\sqrt{\varepsilon_{r_{eff}}}} \quad (3-23)$$

MATLAB was interfaced to ANSYS HFSS to carry out the presented simulations. Different ZIM structures were coded in MATLAB (see Appendix A) and simulated using ANSYS HFSS. The resonant frequency, plasma frequency, operational bandwidth and the physical length for each structure are listed in Table 3-1. The F4B substrate with dielectric constant of $\varepsilon_r = 2.65$ and a loss tangent of $\delta = 0.001$ were used to design the ZIM structures.











Shape (n= number of Meanders)	Resonant Frequency (GHz)		Plasma Frequency (GHz)		ZIM Bandwidth (%)		Effective Length (mm)		Physical Length (mm)
	Copper Trace Width		Copper Trace Width		Copper Trace Width		Copper Trace Width		
	50 μ m	200 μ m	50 μ m	200 μ m	50 μ m	200 μ m	50 μ m	200 μ m	
 n=0	23.87	23.87	23.55	26.3	9.59	10.02	3.8	3.8	3.77
 n=1	8.39	9.41	12.1	13.52	12.81	13.98	10.87	9.69	9.77
 n=2	6.19	7.12	9.7	11.15	9.49	8.67	14.75	12.81	12.77
 n=3	5.25	6.36	8.6	10.4	10.58	9.81	17.38	14.36	15.77
 n=4	4.66	5.93	7.92	9.88	10.86	9.52	19.60	15.38	18.77
 n=5	4.32	5.59	7.4	9.45	7.43	11.64	21.15	16.3	21.77
 n=6	4.06	5.59	6.96	9.3	10.49	9.14	22.48	16.3	24.77
 n=7	3.72	5.50	6.75	9.19	10.96	9.38	24.53	16.5	27.77
 n=8	3.72	5.59	6.5	9.248	11.54	9.18	24.53	16.3	30.77
 n=9	3.47	5.85	6.22	9.45	11.25	8.93	26.33	15.61	33.77

Table 3-1. ZIM structure resonant frequency, electric length and physical length

Simulation results suggest that for a fixed cell size, as the number of meanders increases the physical length increases and so the resonant frequency decreases.

Such a decrease in resonant frequency is expected as the physical length and consequently the electrical length of the conductor strip increases. It can be seen in Table 3-1 that for the rod, C-shape and S-shape the effective electrical and physical lengths are identical. However, as it is shown in Fig. 3-5, for structures with four or more meanders the rate of effective length increase falls until the effective length remains almost unchanged for structures with more than six meanders.

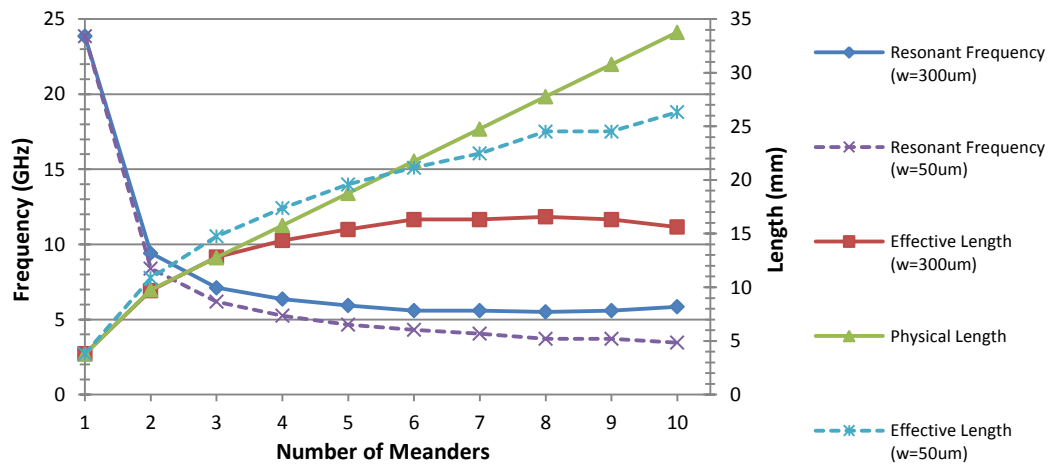


Fig. 3-5. Physical and effective length of meander-line ZIM structure with copper trace width of 50 μm and 300 μm

One can argue that as the number of meanders increases the distance between strip lines decreases, resulting in a stronger mutual coupling between strip lines and consequently a larger variation in the capacitance and inductance of the structure. In the meander inductor, adjacent conductors have equal and opposite current flows, which reduce the total inductance. Mutual coupling effects are usually small if the spacing is greater than three strip widths [123]. This suggests that by using narrower copper trace, the resonant frequency can be shifted down even further. The permittivity of the meanderline ZIM structure with eight meanders for different copper trace widths is shown in Fig. 3-6.

For a copper trace width of 50 μm the effect of mutual coupling is reduced dramatically where for the first five meanders the effective length is greater than the physical length due to the existence of fringing fields. A resonant frequency of 3.3 GHz was obtained for a copper trace width of 50 μm . Varying the trace width could provide a ZIM region at lower frequencies which is absolutely desired for many RF applications, but it does not affect the bandwidth, the bandwidth

remaining almost unchanged. Meanderline inductors also have the advantage of lower eddy current resistance [123]. From Fig. 3-6, it can be concluded that as the copper trace width decreases, the resonant frequency also decreases.

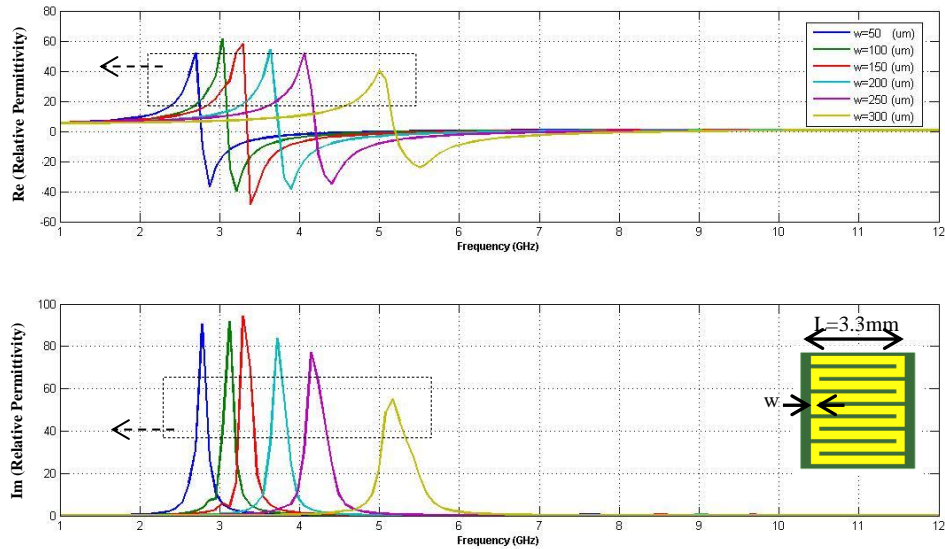


Fig. 3-6. Relative Permittivity of meanderline structure with different copper trace width, real part and imaginary part

For a metamaterial structure with fixed cell size, as the length of horizontal copper traces increases i.e., L increases (See Fig. 3-7), the resonant frequency and consequently the plasma frequency occur at lower frequencies.

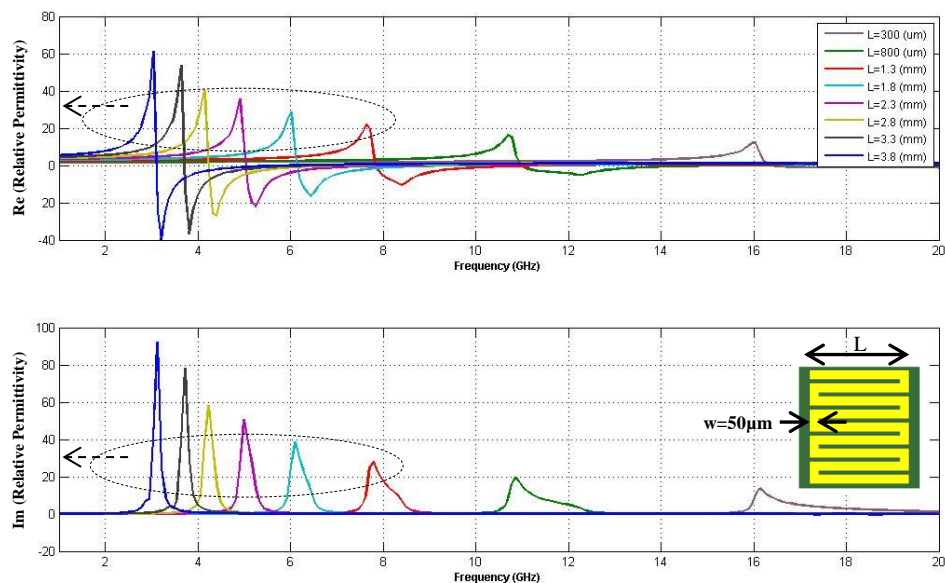


Fig. 3-7. Relative Permittivity of meanderline structure with different copper trace widths, real part and Imaginary part

However, as shown in Fig. 3-8, for structures with larger L i.e., $L > 1.3 \text{ mm}$, increasing the number of meanders results in a decrease in fundamental frequencies. The resonant frequency continues to be shifted down until a particular number of meanders is reached i.e., $n=6$ where adding more meanders to the structure then increases the resonant frequency. This is because the strip lines are then too close to each other and the mutual inductance between them is rising. However, using a thinner copper trace reduces the mutual inductance which allows more meanders to be fitted into the structure. This will increase the physical length of the scatterer which results in a lower resonant frequency.

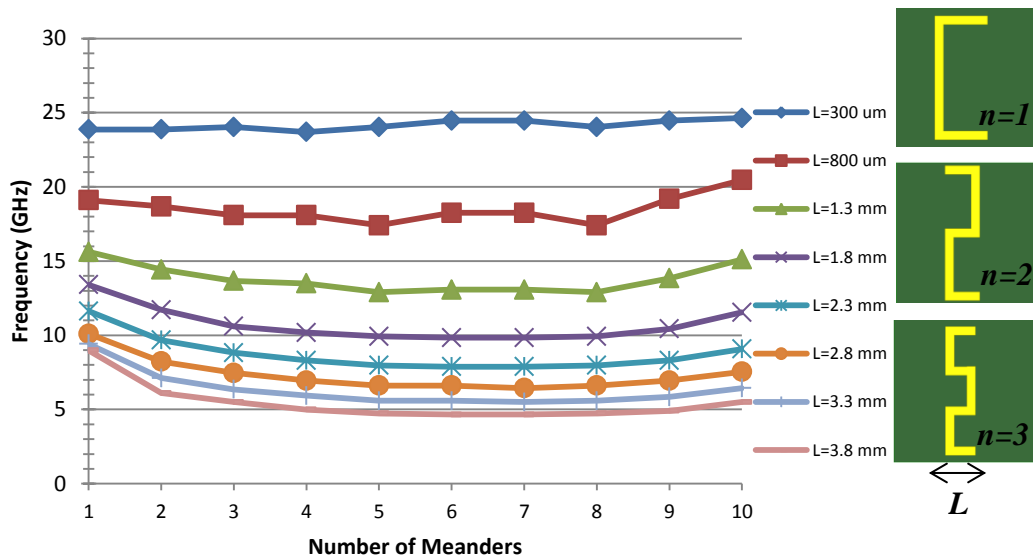


Fig. 3-8. Resonance frequency of meanderline ZIM structures, for different number of meanders and different length of horizontal copper trace

As explained earlier in section 2 - 4 - 2 , a metamaterial TL equivalent comprises of shunt and series inductors and capacitors (Fig. 3-9).

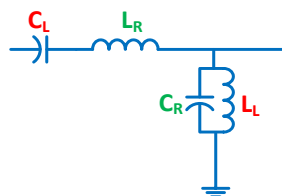


Fig. 3-9. TL metamaterial unit cell equivalent

Topologies presented in Fig. 3-4 show different values of inductance and capacitance. This causes different resonant and plasma frequencies and bandwidth for each unit cell.

3 - 5 - 2 Fixed length ZIM with different Meander Structures

In this section, the effects of meanders on both resonant and plasma frequencies and also operational bandwidth are studied. To do so, ZIM structures with different numbers of meanders i.e., Rod, C-Shape, S-Shape and W-Shape shown in Fig. 3-10, were designed with a fixed total physical length in each case.

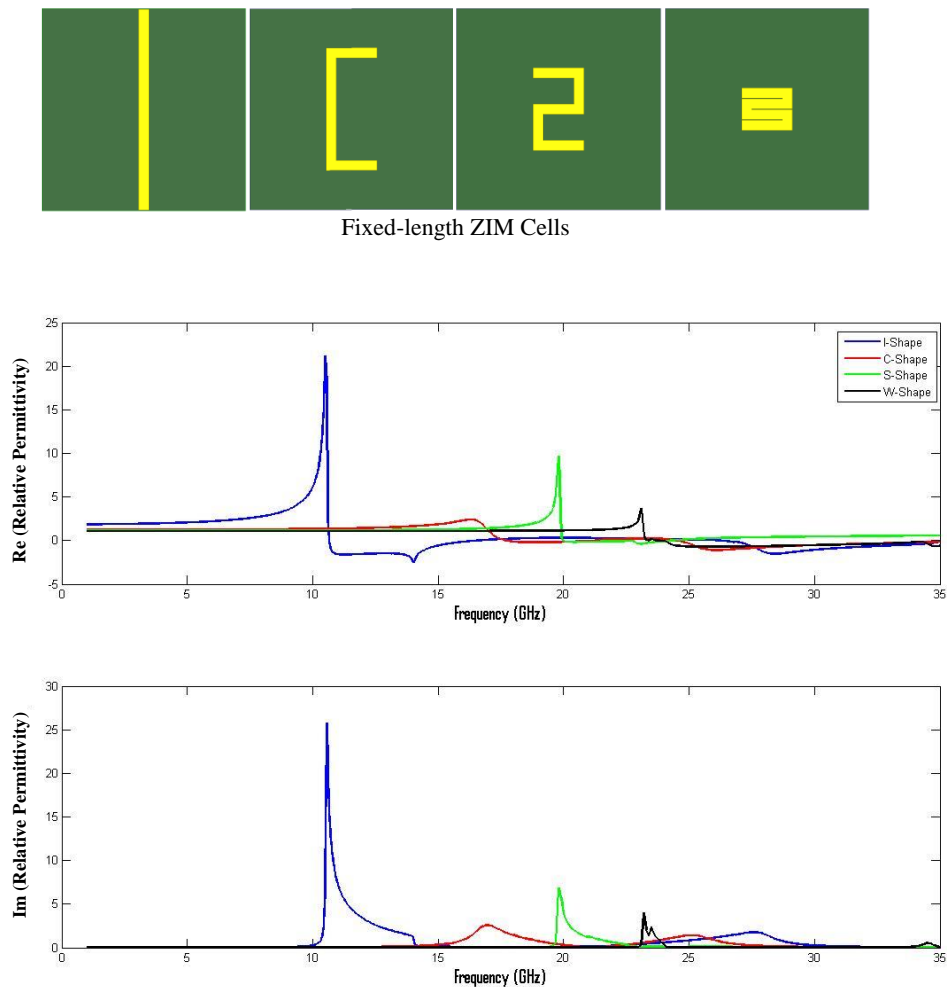


Fig. 3-10. Fixed-length ZIM and their corresponding relative permittivities

The standard retrieval method is used to extract the corresponding permittivity values for each ZIM structure. However, it should be noted that the standard

retrieval method is valid only when the homogenisation condition is valid. In other words, the permittivity diagram shown in Fig. 3-10 is valid only if the magnetoelectric coupling parameter (MCP) is zero. Except for the I-shape, the other structures shown in Fig. 3-10 exhibit the conductivity current that is strongly non-uniform and does not form a closed loop. The displacement currents are widely spread around the effective loop forming multipolar particles. The scattering particles are paired in both sides of the substrate to avoid the medium bi-anisotropy and eliminate the MCP effect. The permittivity for cells with paired scattering particles is shown in Fig. 3-11.

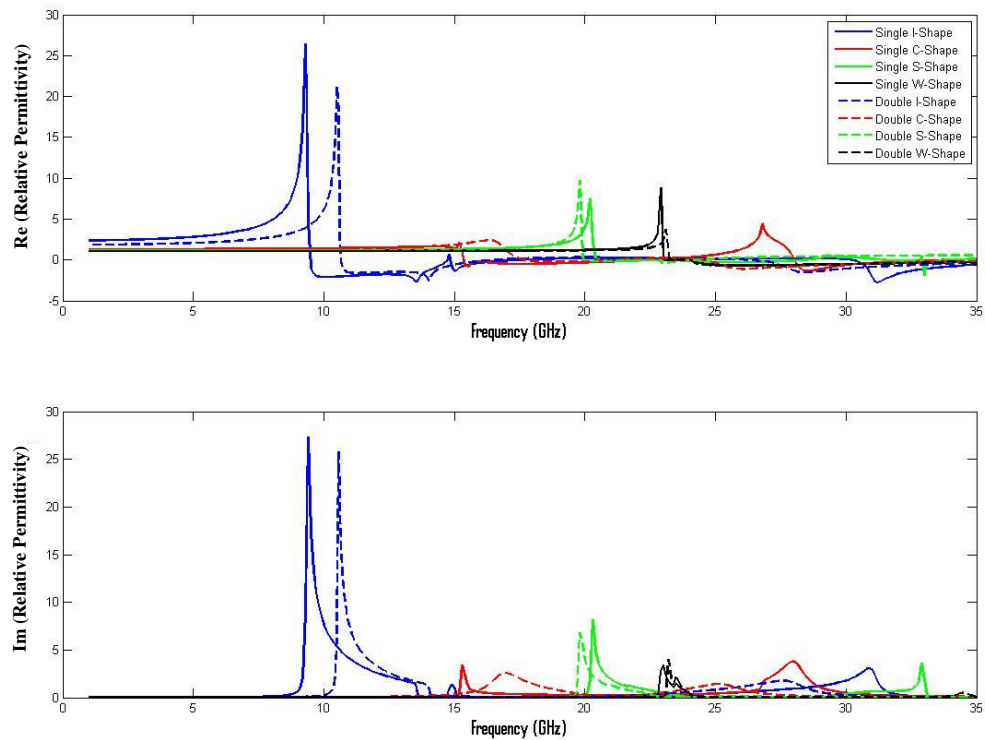


Fig. 3-11. Permittivity for cells with paired scattering particle

The dashed lines in Fig. 3-11 represent the permittivity for the structure with paired scattering parameters. One can say that for structures with a higher number of meanders, higher resonant frequencies are obtained. However, in the case of bandwidth, a generalised statement cannot be given due to complexities associated with mutual coupling and higher order resonances. It is clear that the I-shape provides a smoother electric response and smoother relative permittivity.

Scattering parameters and retrieved parameters for a paired C-Shape is shown in Fig. 3-12.

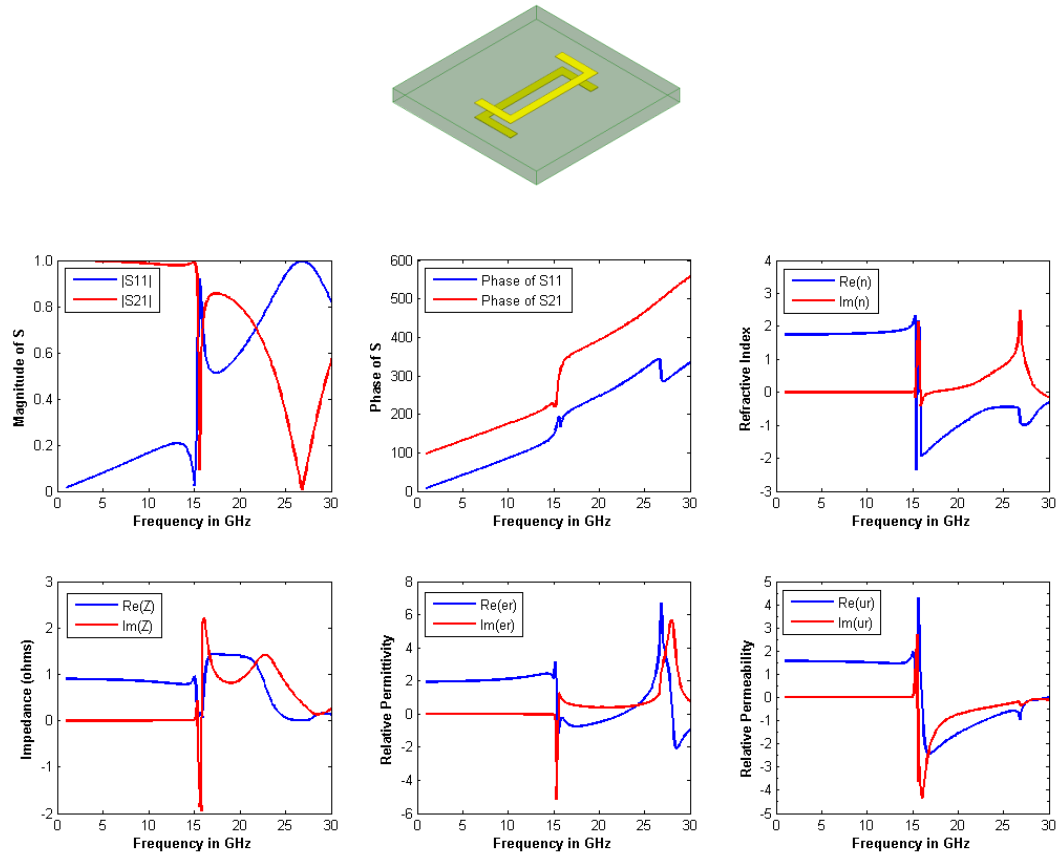


Fig. 3-12. S-parameters and extracted effective material parameters for paired C-Shape

3 - 6 Novel ZIM Structure

After studying the most popular ZIM structures proposed to date, two novel structures are proposed which exhibit ZIM properties through the electric response. The first structure is a combination of I-shape and meander line structures which by taking advantage of both structures provides a broader operational bandwidth. The first structure is shown in Fig. 3-13. The top and bottom horizontal parts and the middle meanderline trace are added to the I-shape structure. This increases the overall inductance resulting in a lower plasma frequency. The structure was designed using the Roger RT/duroid 6010 substrate with $\epsilon_r = 10.2$ and the dielectric loss tangent $\delta = 0.0023$.

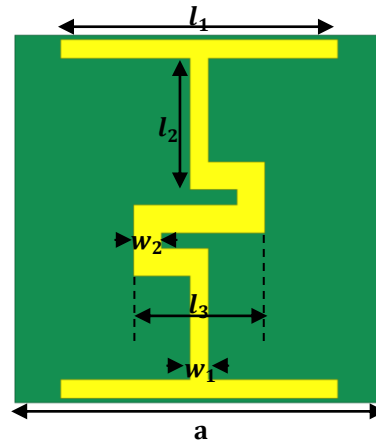


Fig. 3-13. Proposed unit cell structure

The unit cell dimensions were optimised to maximise the *FBW* of the structure using a GA optimisation method.

3 - 6 - 1 Genetic Algorithm

The *GA* flowchart is shown in Fig. 3-14 [144]. The *GA* input parameters are called *chromosomes* and a group of chromosomes is known as a *population*. Each chromosome is the input to an objective function f . The cost associated with each chromosome is calculated by the *cost function* one at a time or in parallel. It is the cost that determines the fitness of an individual in the population. A low cost implies a high fitness [145]. Most fit members of the population are assigned to the highest probability of being selected for mating. The two most common ways of choosing mates are the roulette wheel and tournament selection. In the roulette wheel the cost function assigns a fitness to possible solutions or chromosomes. This fitness level is used to associate a probability of selection with each individual chromosome. Like the roulette wheel in a casino, usually a proportion of the wheel is assigned to each of the possible selections based on their fitness value. The tournament selection involves running several "tournaments" among a few individuals chosen at random from the population. The winner of each tournament (the one with the best fitness) is selected for crossover. Mutation induces random variations in the population. The mutation rate is the portion of bits or values within a population that will be changed [145]. If a problem has a solution over the defined optimisation space, the solution will converge. The generational process is stopped when a termination condition is met. The

termination condition could be either a certain number of iterations or when the cost value is below an acceptable minimum.

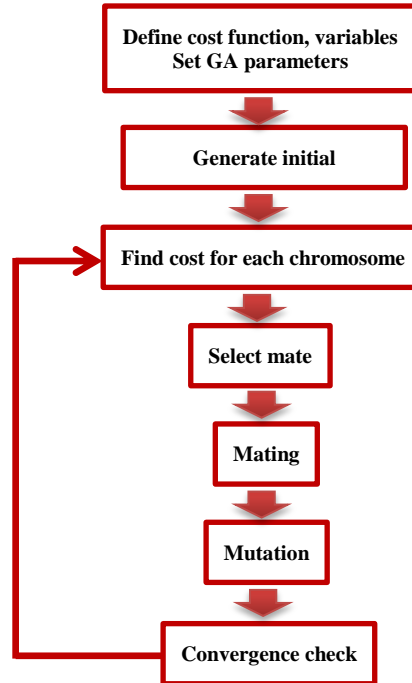


Fig. 3-14. Continuous GA flowchart

3 - 6 - 2 Applying GA Optimisation to Proposed Cell

For our purposes, a matrix with each row corresponding to a chromosome representing the population and a cost function was defined. The geometry parameters are the input of GA. All independent physical dimensions except the substrate thickness and the unit cell size were subject to optimisation. The substrate thickness was 0.8 mm , which is one of the standard thicknesses for the Roger RT/duroid 6010 substrate. The cost function was defined to measure the zero-permittivity region bandwidth by evaluating the difference between the frequency points at which the permittivity is equal to ± 0.2 . The cost function is given by:

$$\text{cost}(X) = f|_{\varepsilon=0.2} - f|_{\varepsilon=-0.2} \quad (3-24)$$

Where X is the array of simulated cell dimensions:

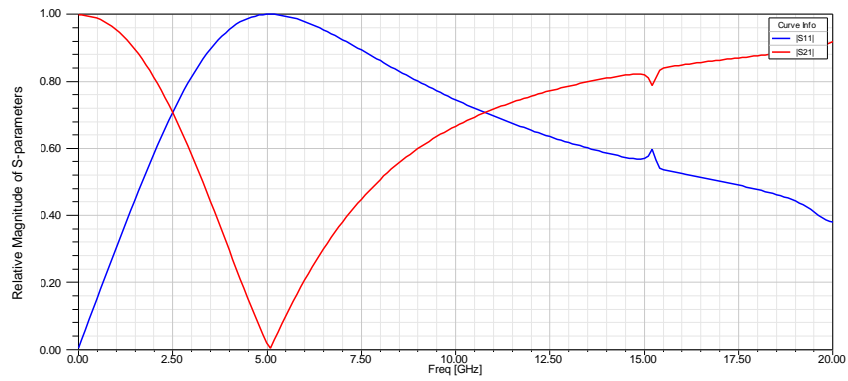
$$X = [a, L_1, L_2, L_3, w_1, w_2, g] \quad (3-25)$$

The S-parameters for each member of the population were obtained by ANSYS HFSS full wave simulation. These S-parameters were used to calculate the permittivity and relatively the zero-permittivity region for each member of population. This procedure continued for 1000 iterations to find a X which maximises the cost function. The initial and final optimised dimensions are stated in Table 3-2.

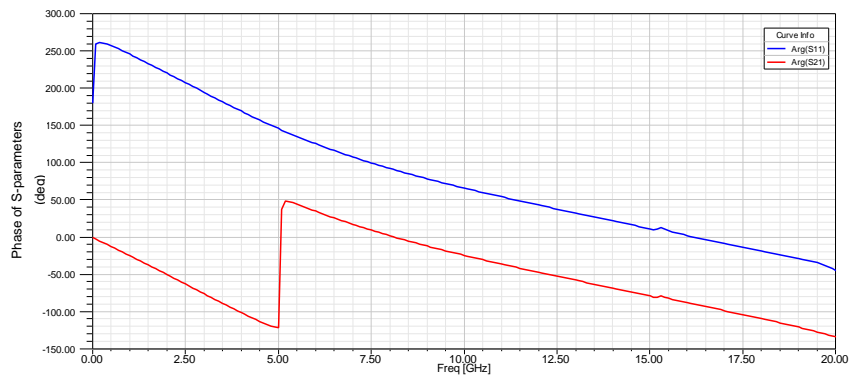
Variable	Initial Design	Final Design
a	4 mm	4 mm
L₁	3.5 mm	3 mm
L₂	0.9 mm	1.13 mm
L₃	1.5 mm	0.81 mm
w₁	0.2 mm	0.2 mm
w₂	0.2 mm	0.3 mm
g	0.1 mm	0.05 mm
$f_{\epsilon_{eff}=-0.2}$	8.4 GHz	10.885 GHz
$f_{\epsilon_{eff}=+0.2}$	9.1 GHz	12.5 GHz
f_p	8.8 GHz	11.5 GHz
$FBW = \frac{f_{\epsilon_{eff}=+0.2} - f_{\epsilon_{eff}=-0.2}}{f_p}$	8%	14%

Table 3-2. Unit cell optimisation parameters, initial and final values

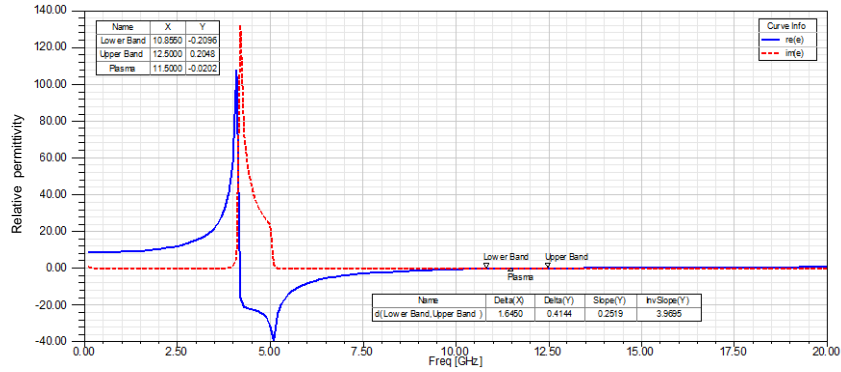
The structure is simulated for excitation by an incident plane wave polarised along the y-direction and propagating along the x-direction. The simulation results confirmed the electric response of the structure providing the ZIM properties. The simulation results for the optimised structure are shown in Fig. 3-15.



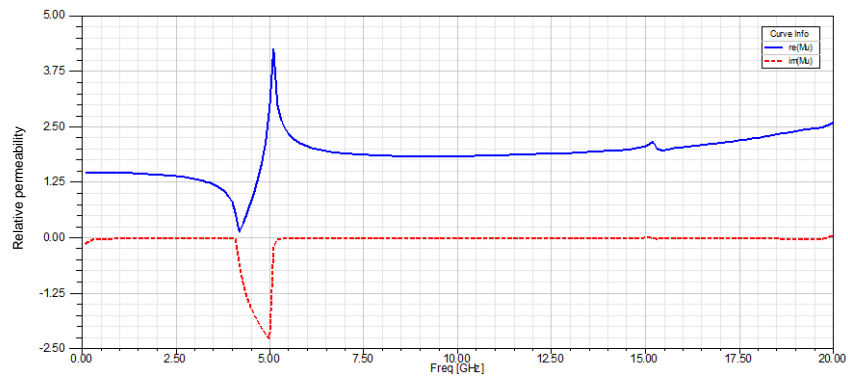
(a)



(b)



(c)



(d)

Fig. 3-15. S-parameters and extracted effective material parameters for proposed structure with EZ property, (a) magnitude of S-parameters, (b) phase of S-parameters (c) effective relative permittivity, (d) effective relative permeability

It was discussed earlier in this chapter that the simplicity of an I-shape structure leads to a very smooth response to an excitation wave where higher order resonant modes occur at higher frequencies compared to a more complex structure like the meanderline. However, the shorter length of copper trace used for the I-shape structure causes the frequency of resonance to occur at higher frequency which makes the structure unsuitable for many RF applications. However, in some high frequency applications like UWB antennae the I-shape structure might be the best choice. Here, a novel wideband ZIM unit cell structure is proposed. The structure is made up of an I-shape structure with an added patch to the centre of the structure. The proposed structure is shown in Fig. 3-16. The structure was designed using the FR4-epoxy substrate with $\epsilon_r = 4.4$ and the dielectric loss tangent $\delta = 0.02$.

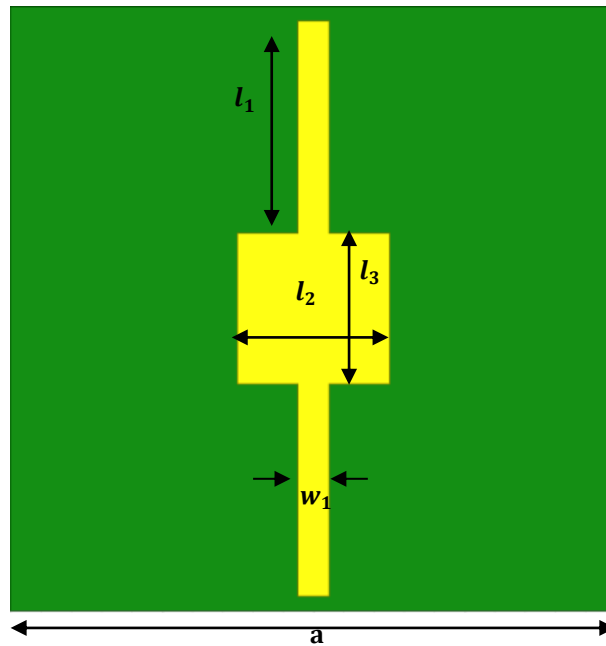


Fig. 3-16. Proposed unit cell structure formed by a small patch added to the centre of rod structure

Further optimisation is applied using GA optimisation method in order to achieve maximum possible bandwidth. The initial and final optimised values are given in Table 3-3.

Variable	Rod	Initial Design	Final Design
a	4 mm	4 mm	4 mm
L₁	3.8	1.45 mm	1.45 mm
L₂	N/A	1.3 mm	1 mm
L₃	N/A	0.9 mm	1 mm
w₁	0.2 mm	0.2 mm	0.2 mm
$f_{\epsilon_{eff}=-0.2}$	23.3 GHz	25.6 GHz	24.4 GHz
$f_{\epsilon_{eff}=+0.2}$	25.5 GHz	32.7 GHz	32.8 GHz
f_p	24 GHz	26.3 GHz	25.2 GHz
FBW $= \frac{f_{\epsilon_{eff}=+0.2} - f_{\epsilon_{eff}=-0.2}}{f_p}$	9.1%	26.9%	33%

Table 3-3. Proposed ZIM unit cell optimisation parameters, initial and final values

Simulation results for the optimised structure are shown in Fig. 3-17.

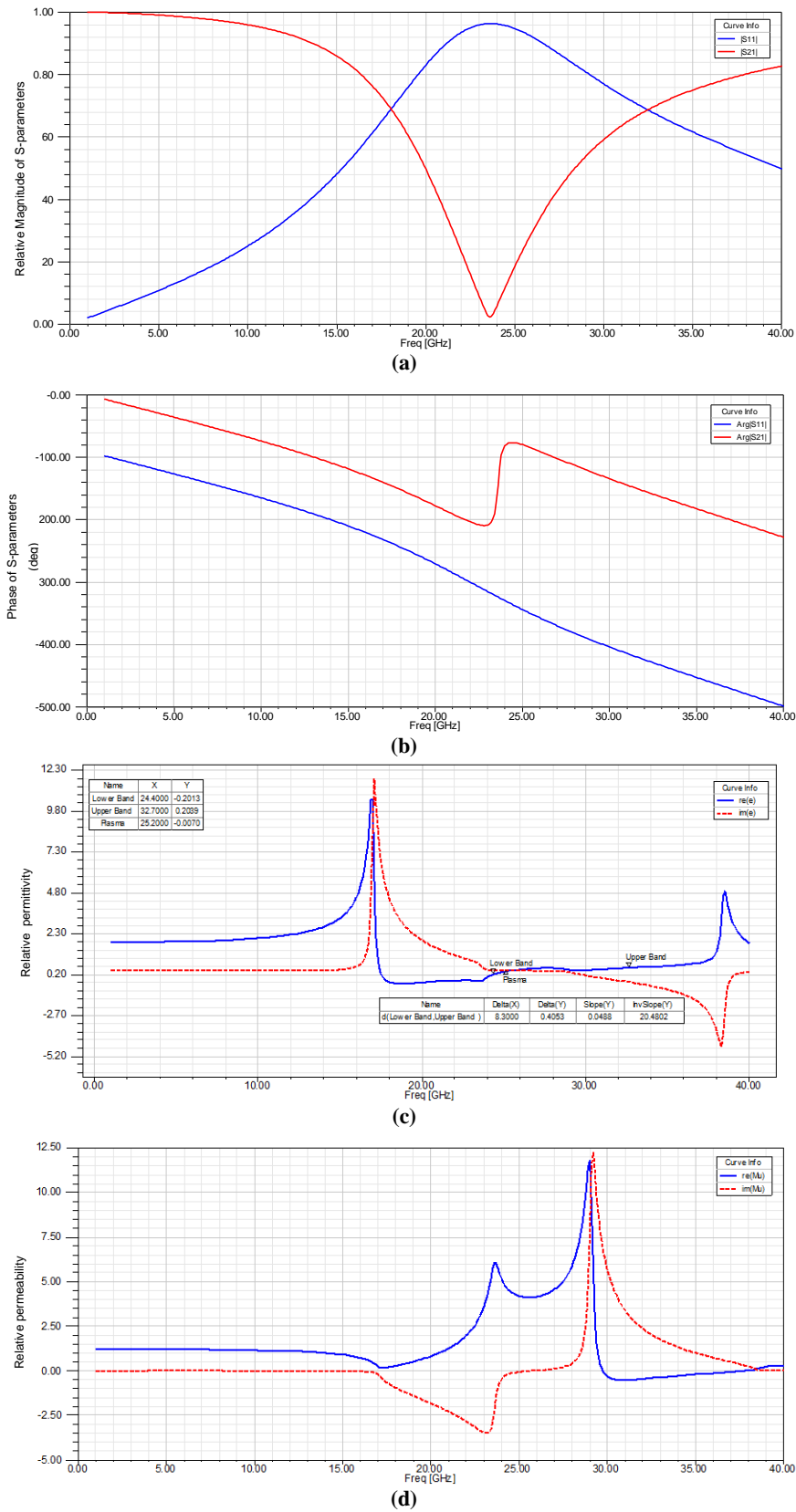
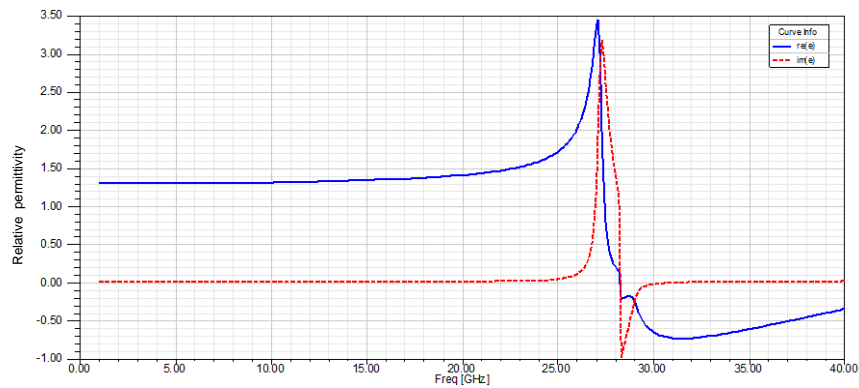
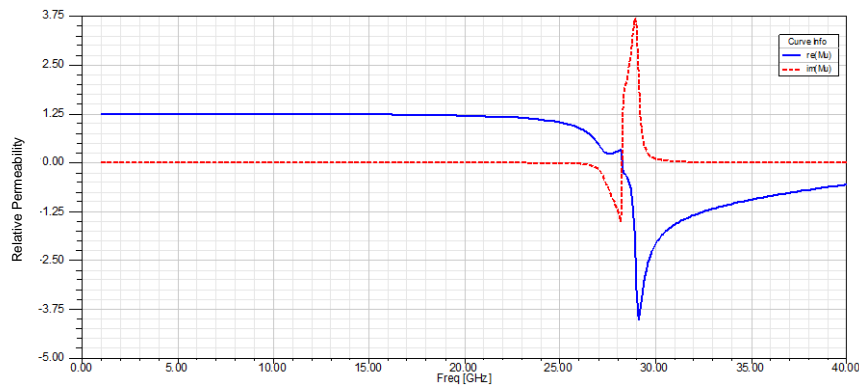


Fig. 3-17. S-parameters and extracted effective material parameters for second proposed structure with EZ property, (a) magnitude of S-parameters, (b) phase of S-parameters (c) effective relative permittivity, (d) effective relative permeability

For the optimised structure a fractional bandwidth of 33% was achieved which shows a significant increase in operational bandwidth compared to an I-shape structure with a bandwidth of 9.1%. To understand how the added patch leads to significant bandwidth enhancement, the response of the patch structure itself to an identical excitation was studied. The patch exhibits an electric response at frequencies just above I-shape resonance. The permittivity and permeability of the patch are shown in Fig. 3-18.



(a)



(b)

Fig. 3-18. Permittivity and permeability of the patch structure

A close observation between the Bloch impedance diagrams of the proposed structure and the I-shape, shown in Fig. 3-19, can give a physical explanation. When the imaginary part of the wave impedance is much higher than its real part, the wave cannot propagate through the medium due to cancellation of its E- or H-field component. As can be seen in Fig. 3-19, for both structures, there are two regions over which the imaginary part of Z is noticeably higher than its real part, where waves within the medium are evanescent. However, for the proposed unit

cell, the evanescent regions become closer, leaving less propagating region in between.

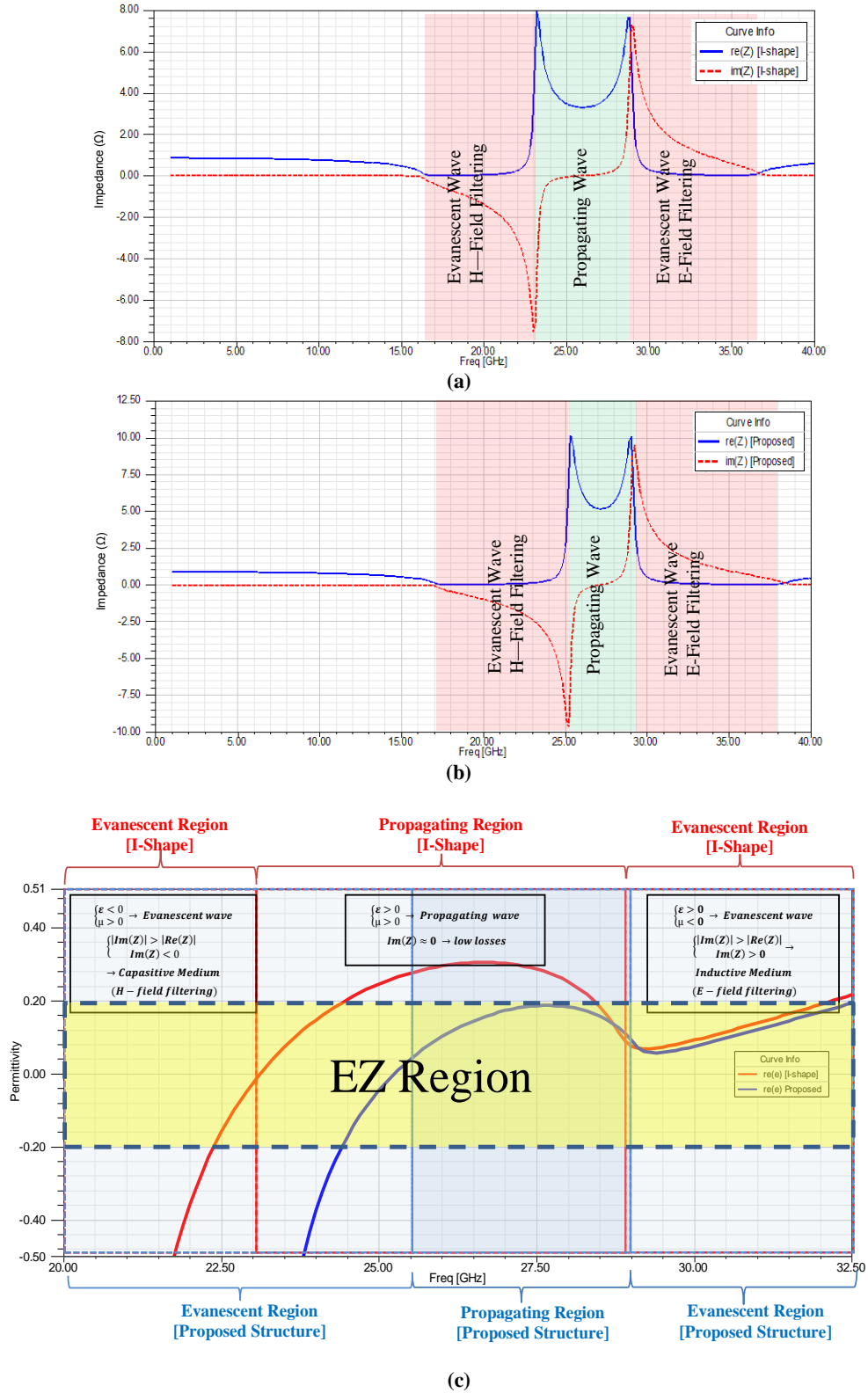


Fig. 3-19. Bloch impedance for (a) I-shape (b) the proposed structure, (c) real part of permittivity of both structures

One can divide the frequency region into three domains; evanescent wave with $\epsilon < 0$ and $\mu > 0$, propagating wave with $\epsilon > 0$ and $\mu > 0$ and the evanescent wave with $\epsilon > 0$ and $\mu < 0$. When the excitation wavelength is comparable to the unit cell size, the structure resonates resulting in a negative permittivity region. Over the range of frequency with negative permittivity response, waves cannot propagate through the structure as constitutive parameters (i.e., ϵ and μ) hold opposite signs. As frequency increases from the plasma frequency, the permittivity becomes positive enabling propagation of the wave. However, for higher frequencies, there is a second evanescent region for both the I-shape and the proposed structure. This is due to the magnetic response of the structure where the permeability is negative. Positive permittivity and negative permeability in this frequency range lead to an inductive medium which filters the E-field within the structure. For the proposed design such degradation in E-field happens for a permittivity just below 0.2, providing the ZIM bandwidth of near 33%.

3 - 7 ZIM Embedded Antennae

The study categorises ZIM embedded antenna structures into two different types; one type where ZIM forms a highly directive shell surrounding the antenna, and another type where ZIM cells are placed on a planar antenna to enhance the antenna directivity. In both types the ZIM structures act as a lens. There is a powerful mathematical tool called “optical transformation” proposed in 2006 [124] as a design strategy to manipulate EM waves within inhomogeneous and anisotropic media which helps in understanding why a slab of ZIM structure can act as a lens.

3 - 7 - 1 Optical Transformation

A media is called a transformation media when it can perform coordinate transformation. The transformation media represents two important properties; 1) The optical path in the transformation media is same as the one in virtual media [125]. 2) The transformation media is reflectionless if the outer boundary remains unchanged before and after a coordinate transformation. It can be said that the

metric of the transformation space is continuous on the boundary in a direction normal and parallel to the interface between the transformation and the surrounding medium [126]. The form invariance of Maxwell's equation under coordinate transformation has been proved in [127-130]. Maxwell's equations in the original medium can be written as:

$$\nabla \times E + i\omega\mu \cdot H = 0 \quad (3-26)$$

$$\nabla \times H - i\omega\varepsilon \cdot E = 0 \quad (3-27)$$

Where ε and μ are the constitutive parameters of the real media and the transformation of coordinates between the real and the virtual media is given by:

$$X' = M'(X) \quad (3-28)$$

It has been proved that Maxwell's equations in the virtual media are form invariant and can be written as:

$$\nabla' \times E' + i\omega\mu' \cdot H' = 0 \quad (3-29)$$

$$\nabla' \times H' - i\omega\varepsilon' \cdot E' = 0 \quad (3-30)$$

Where E' and H' are the electric and the magnetic fields in the virtual media, respectively. ε' and μ' are the constitutive parameters of the virtual media. The relationship between the electric field, the magnetic fields and the material constant of the real and the virtual media can be written as [3]:

$$E'(X') = (\Lambda^T)^{-1}E(X) \quad (3-31)$$

$$H'(X') = (\Lambda^T)^{-1}H(X) \quad (3-32)$$

$$\mu'(X') = \Lambda \cdot \mu(X) \cdot \Lambda^T / \det(\Lambda) \quad (3-33)$$

$$\varepsilon'(X') = \Lambda \cdot \varepsilon(X) \cdot \Lambda^T / \det(\Lambda) \quad (3-34)$$

Where Λ is the Jacobian transformation matrix and is defined as:

$$\Lambda_{ki} = \frac{\partial x'_k}{\partial x_i} \quad (3-35)$$

$$[\Lambda_{ij}]^{-1} = \frac{\partial x_i}{\partial x'_j} \quad (3-36)$$

Next, the optical transformation is used to define parameters for a high directive media.

3 - 7 - 2 High Directive Emission Using Transformation Optic

This section presents analytical calculations of a transformation optic required to focus a propagating wave in a certain direction as it passes through the transformed medium. The wave is assumed to propagate in 2-D space as shown in Fig. 3-20.

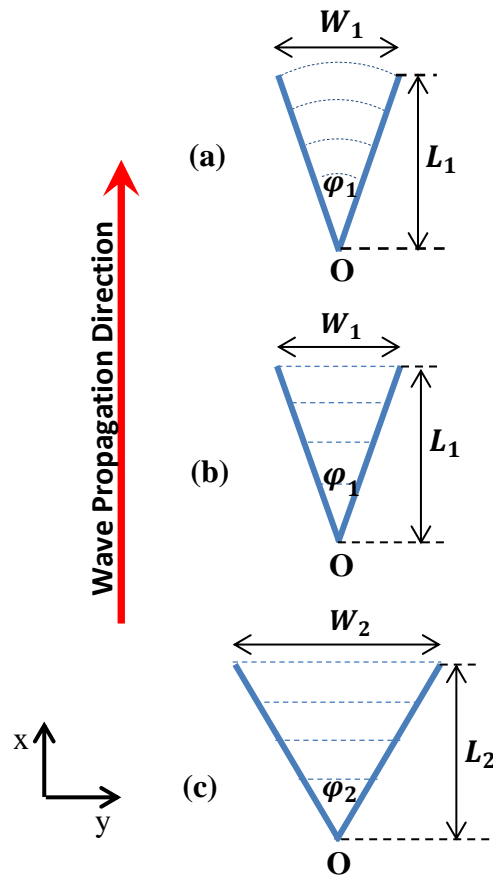


Fig. 3-20. 2-D coordinate transformation for highly directive medium. (a) geometry of fan-shaped virtual space (b) Simplified virtual space to triangle shape. (c) geometry of the triangle physical space [119]

A highly directive medium requires the coordinate transformation shown in Fig. 3-20. An air field fan-shape virtual space with a central angle of φ_1 which is represented by (x', y', z') is mapped to a triangle with vertex angle of φ_2 in the physical space which is represented by (x, y, z) [119] with constitutive parameters $\varepsilon_r(x, y)$ and $\mu_r(x, y)$. The coordinate transformation from the virtual space (x', y', z') to the physical space (x, y, z) can be written as:

$$x' = \frac{L_2}{L_1} x \quad (3-37)$$

$$y' = \frac{W_2}{W_1} y \quad (3-38)$$

$$z' = z \quad (3-39)$$

The permittivity and permeability tensors in the physical medium, $\bar{\bar{\varepsilon}}_r(x, y)$ and $\bar{\bar{\mu}}_r(x, y)$ can be calculated using the invariant Maxwell's equations expressed in (3-33) and (3-34) as:

$$\bar{\bar{\varepsilon}}_r' = \bar{\bar{\mu}}_r' = \begin{bmatrix} L_2 W_1 / L_1 W_2 & 0 & 0 \\ 0 & L_1 W_2 / L_2 W_1 & 0 \\ 0 & 0 & L_1 W_1 / L_2 W_2 \end{bmatrix} \quad (3-40)$$

For the sake of simplicity, a further assumption that $L_1 = L_2$ can be made, thus the constitutive tensors are simplified to:

$$\bar{\bar{\varepsilon}}_r' = \bar{\bar{\mu}}_r' = \begin{bmatrix} \left(\frac{W_1}{W_2}\right)^2 & 0 & 0 \\ 0 & 1 & 0 \\ 0 & 0 & 1 \end{bmatrix} \quad (3-41)$$

Equation (3-41) expresses that for a high directive medium along the x-direction i.e., $W_2 \gg W_1$, both permittivity and permeability must remain small along the x-direction.

3 - 7 - 3 High Directive ZIM Shell

From (3-41) it can be concluded that to have highly directive emission along a given direction, low values of the permittivity and permeability are required along that direction. In this section, EZ and MZ shells as well as a combined EZ and MZ shell are investigated. An EZ shell was formed by tessellating the unit cell proposed in section 3 - 6 . Then, the effect of the EZ shell on the radiation pattern of a dipole antenna was investigated. The proposed cell was rescaled to exhibit EZ properties over a range of frequency from 14.5 to 16 GHz. As shown in Fig. 3-21 (a), the unit cell is an anisotropic structure which expresses the EZ properties along the x-direction while giving positive values for the permittivity in other directions. A dipole antenna was designed to operate at 15.3 GHz. The EZ shell was placed around the dipole antenna to increase its directivity. The designed shell is shown in Fig. 3-21(b) and (c).

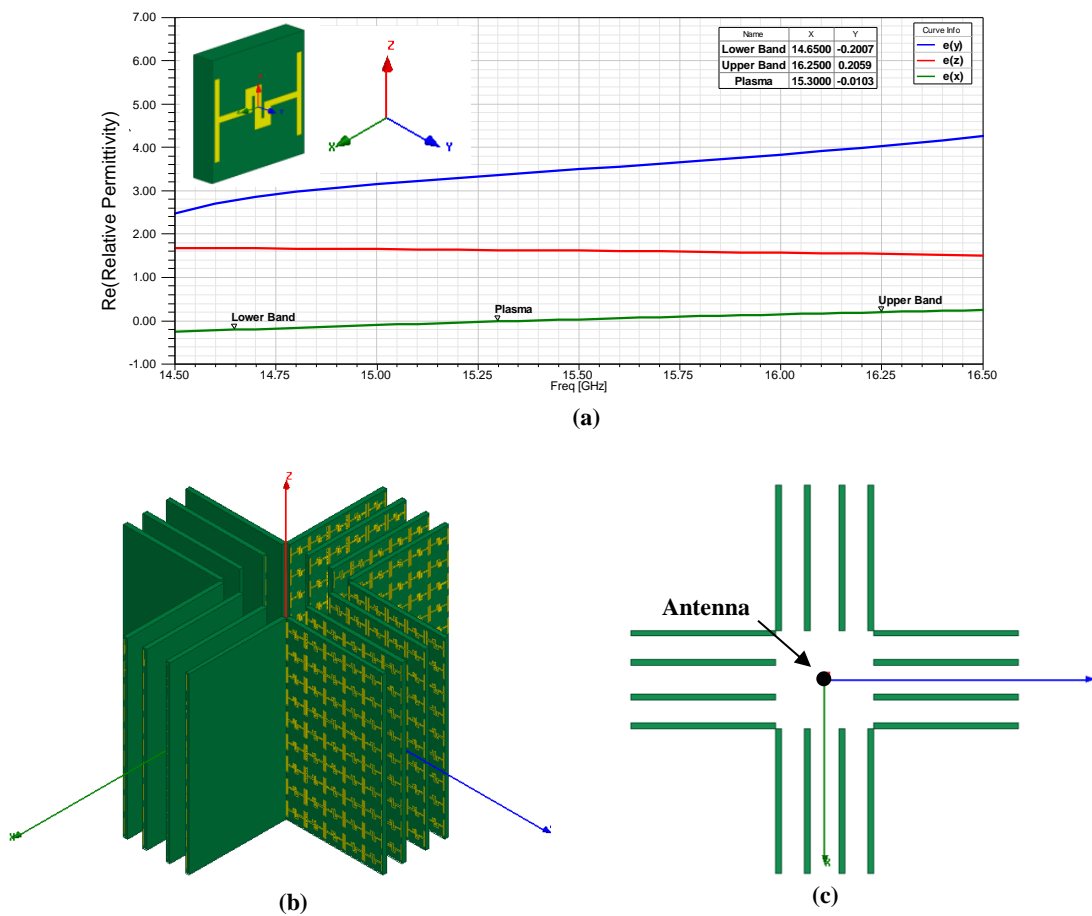


Fig. 3-21. EZ shell embedded dipole antenna, (a) unit cell, (b) trimetric view, (c) top view

The simulation results for the EZ shell are shown in Fig. 3-22.

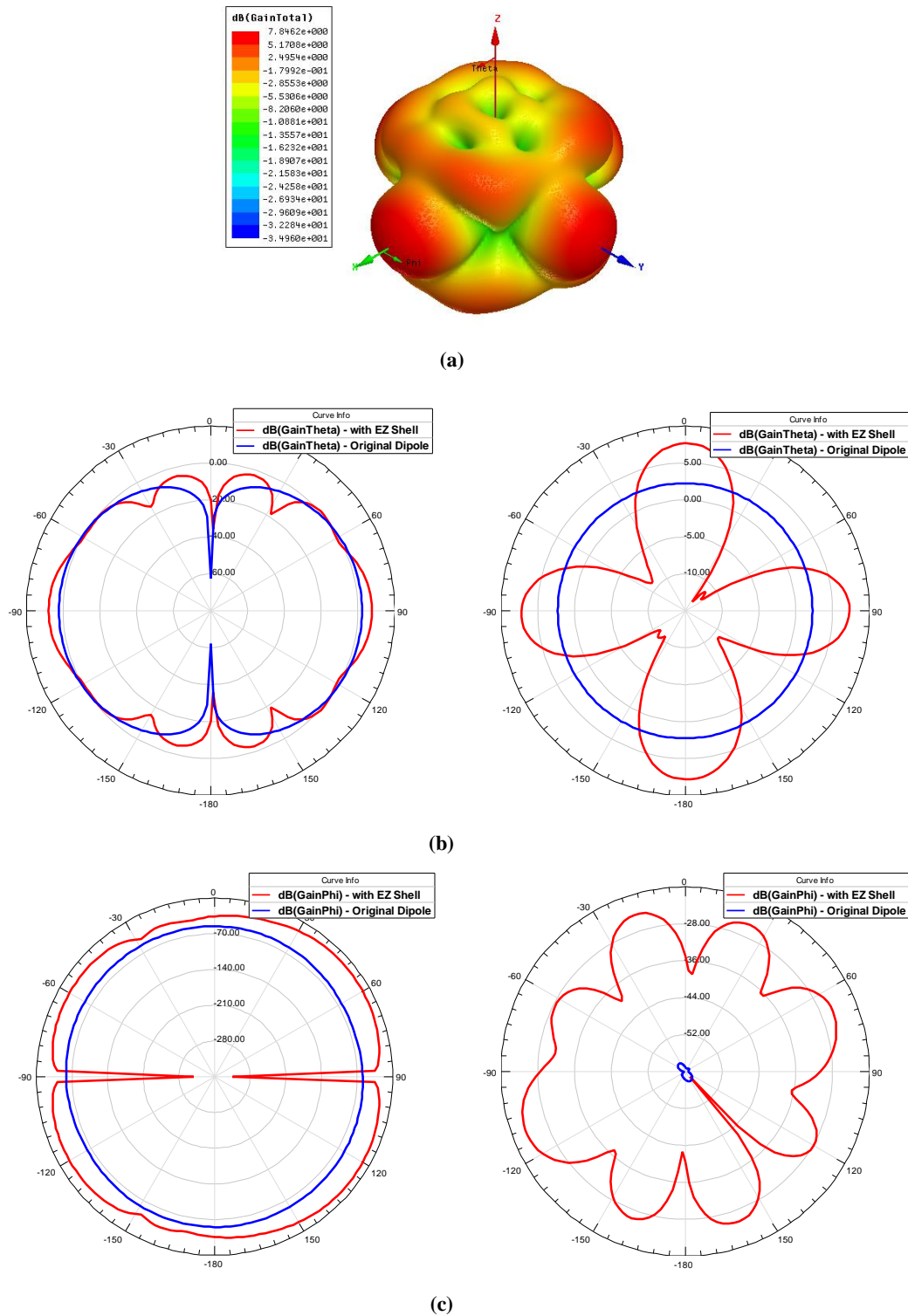


Fig. 3-22. (a) Polar plot of total gain in *dBi*, (b) co-polarised gain in *dBi*, E-plane (left) and H-plane (right) (c) cross-polarised gain in *dBi*, E-plane (left) and H-plane (right)

Simulation results confirm a total gain of 7.84 *dBi* along the EZ direction. This means that the EZ shell acts as a lens which provides 5.5 *dBi* gain enhancement compared to the gain of the dipole antenna without the shell (i.e., 2.3 *dBi*). The

notches in the cross polarisation pattern shown in Fig. 3-22.(c) are due to the symmetric boundary conditions applied within the model. Since the dipole radiation pattern is symmetrical, the symmetric boundary condition can be used to model only part of the structure, which reduces the size and complexity of the design. In some cases, using a symmetric boundary condition can reduce the simulation time from several weeks to a few days.

Further, the effect of media with zero permeability on the antenna radiation was investigated. Zero permeability can occur within structures with a magnetic response. For this purpose, the well-known SRR structure can be used. As shown in Fig. 3-23.(a), the SRR was designed to exhibit the MZ region at around 15.3 GHz. Then, the SRR unit cells were repeated to form the surrounding MZ shell (see Fig. 3-23.(b)).

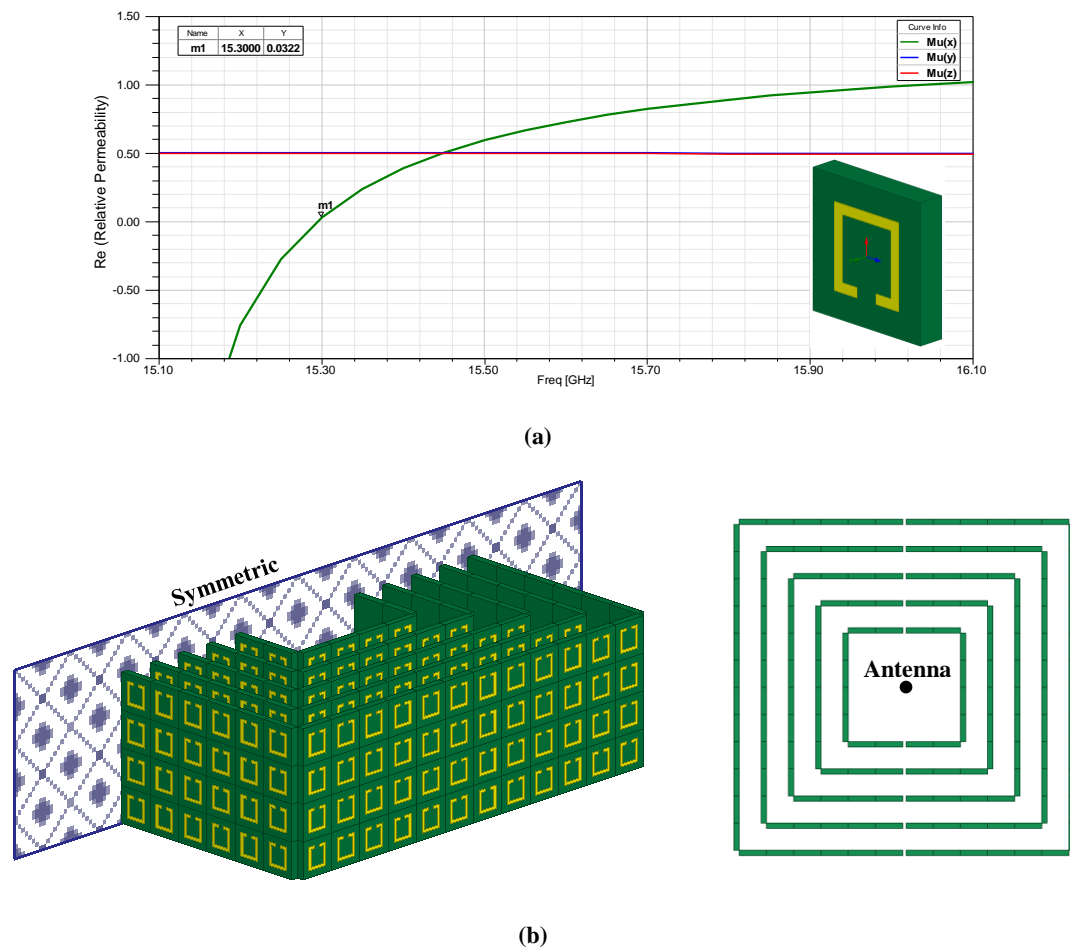


Fig. 3-23. (a) SRR designed to have MZ properties around 15 GHz, (b) MZ shell embedded dipole antenna, trimetric view (left), top view (right)

The SRR unit cell size is kept equal to the proposed structure unit cell i.e., $4\text{ mm} \times 4\text{ mm}$. The magnetic response happens at higher frequency for a substrate with lower dielectric constant and therefore, Rogers RT/duroid 5880 with a dielectric constant of 2.2 was chosen as the substrate.

The simulation results for the MZ shell, shown in Fig. 3-24, illustrate that the MZ shell redirects the maximum of the radiated beam toward a direction closer to the horizon. The dipole radiated beam is effectively pushed to a collimated wave in the H-plane providing a maximum total gain of 4.9 dBi along the MZ direction. More gain enhancement can be achieved by using more layers of the MZ substrate around the dipole antenna. The notches in the cross-polarisation pattern shown in Fig. 3-24.(c) are because of the symmetric boundary conditions applied within the model to speed up the simulation time.

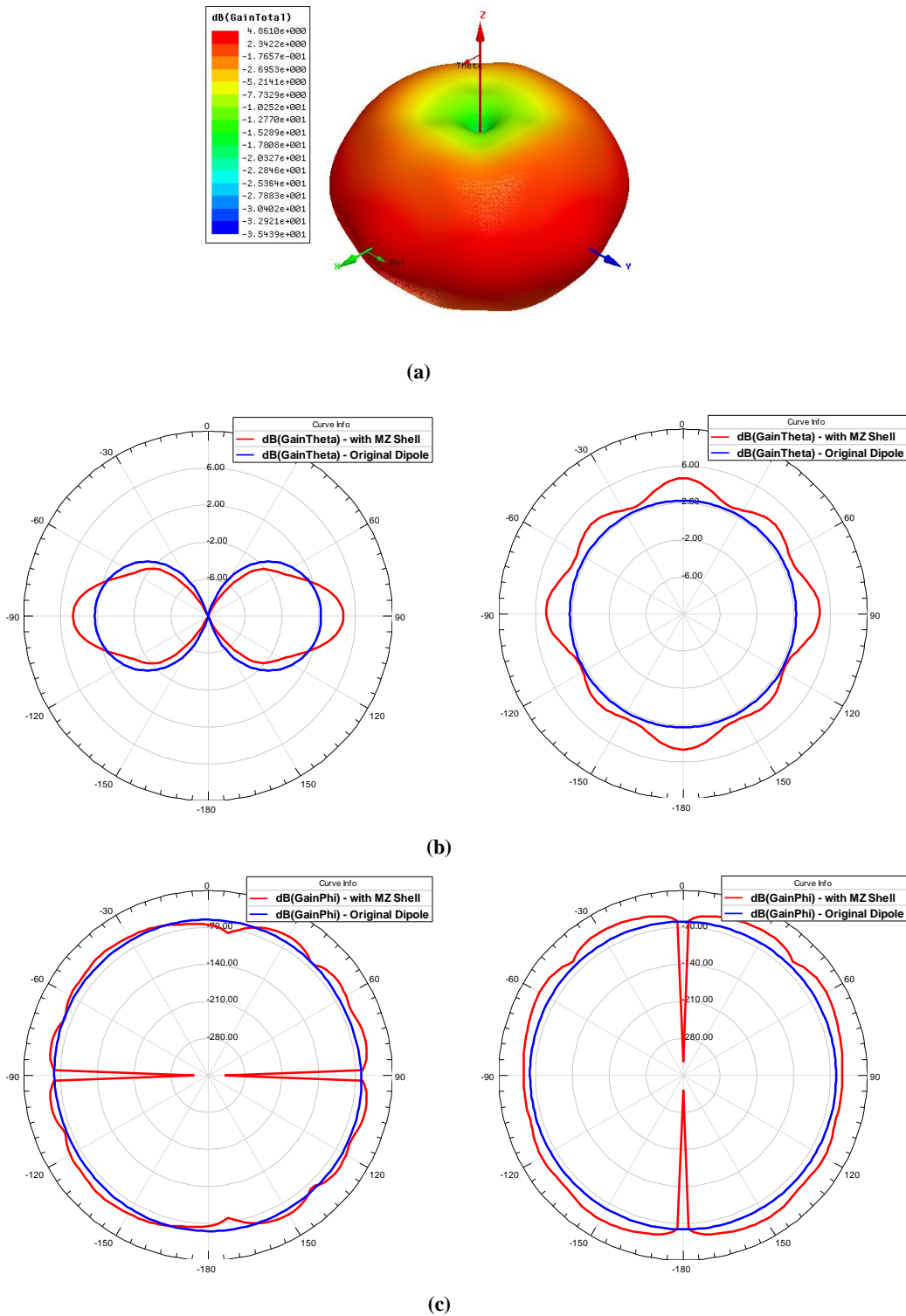


Fig. 3-24. MZ shell embedded dipole antenna, (a) total gain 3-D polar in *dBi*, (b) co-polarisation; gain in *dBi*, E-plane (left) and H-plane (right), (c) cross-polarisation; gain in *dBi*, E-plane (left) and H-plane (right)

Equation (3-41) describes that for a highly directive media both the permittivity and permeability must remain small. Formerly, the EZ and MZ shells were studied. The ZIM shell can be obtained when the permittivity and permeability are

simultaneously zero. However, designing the ZIM using the EZ and MZ structures proposed earlier is not geometrically possible due to the EZ and MZ cells intersecting. Two structures are suggested as the ZIM shell; first, the EZ cells are placed within the layers of the MZ shell and then second, the EZ shell is filled by the MZ cells. The first ZIM shell design is demonstrated in Fig. 3-25.

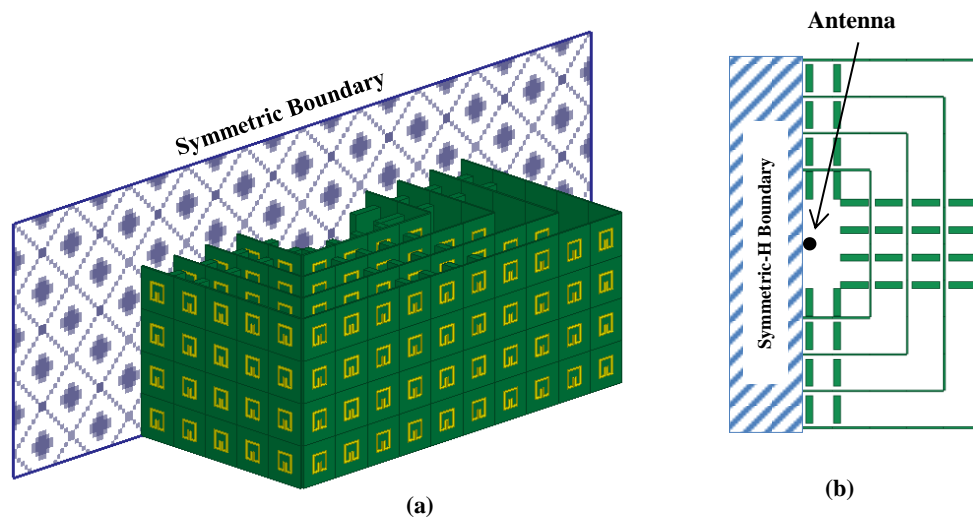


Fig. 3-25. First ZIM shell design with both EZ and MZ properties, (a) trimetric view, (b) top view

Simulation results for the first ZIM shell are shown in Fig. 3-26.

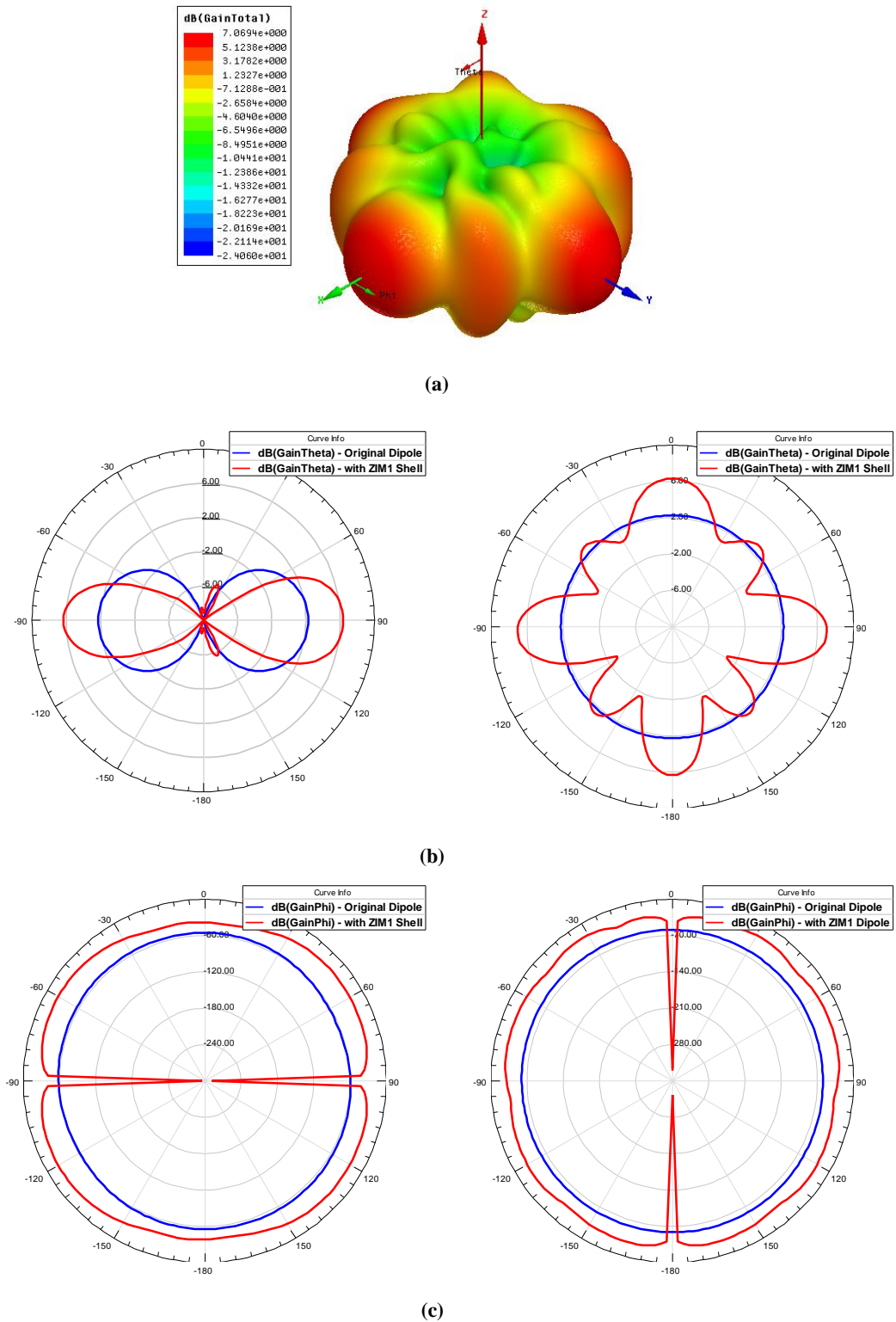


Fig. 3-26. Simulation results for first ZIM shell, (a) total gain 3-D polar in dBi , (b) co-polarisation; gain in dBi , E-plane (left) and H-plane (right) (c) cross-polarisation; gain in dBi , E-plane (left) and H-plane (right)

The obtained radiation pattern shows high directivity emission with a total gain of up to 7 dBi . Here, the obtained total gain is more than the total gain acquired by

the MZ shell and less than the total gain achieved by the EZ shell. The second ZIM shell design is shown in Fig. 3-27.

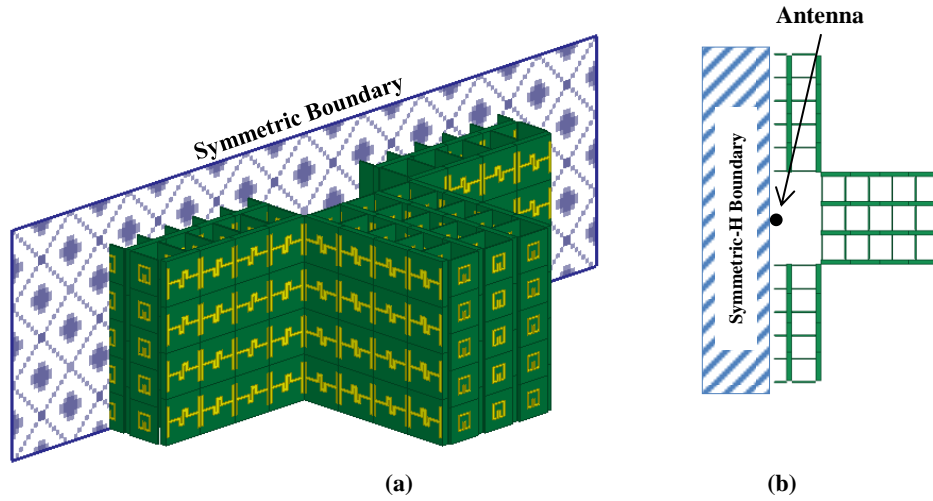


Fig. 3-27. Second ZIM shell design with both EZ and MZ properties, (a) trimetric view, (b) top view

Simulation results for the second ZIM shell are shown in Fig. 3-28. The total gain of 9.15 dBi is achieved in the second design where the MZ cells are placed between the EZ shell layers. Again here the notches in the cross-polarisation pattern, shown in Fig. 3-28.(c), are because of defined symmetric boundary conditions and are not real. The second ZIM shell shows the most gain enhancement compared to the other shells proposed so far. However, since the MZ cells do not form a continuous periodic structure in the last structure, it does not form a perfect ZIM with simultaneously zero permittivity and zero permeability at the dipole resonant frequency (i.e., 15.3 GHz).

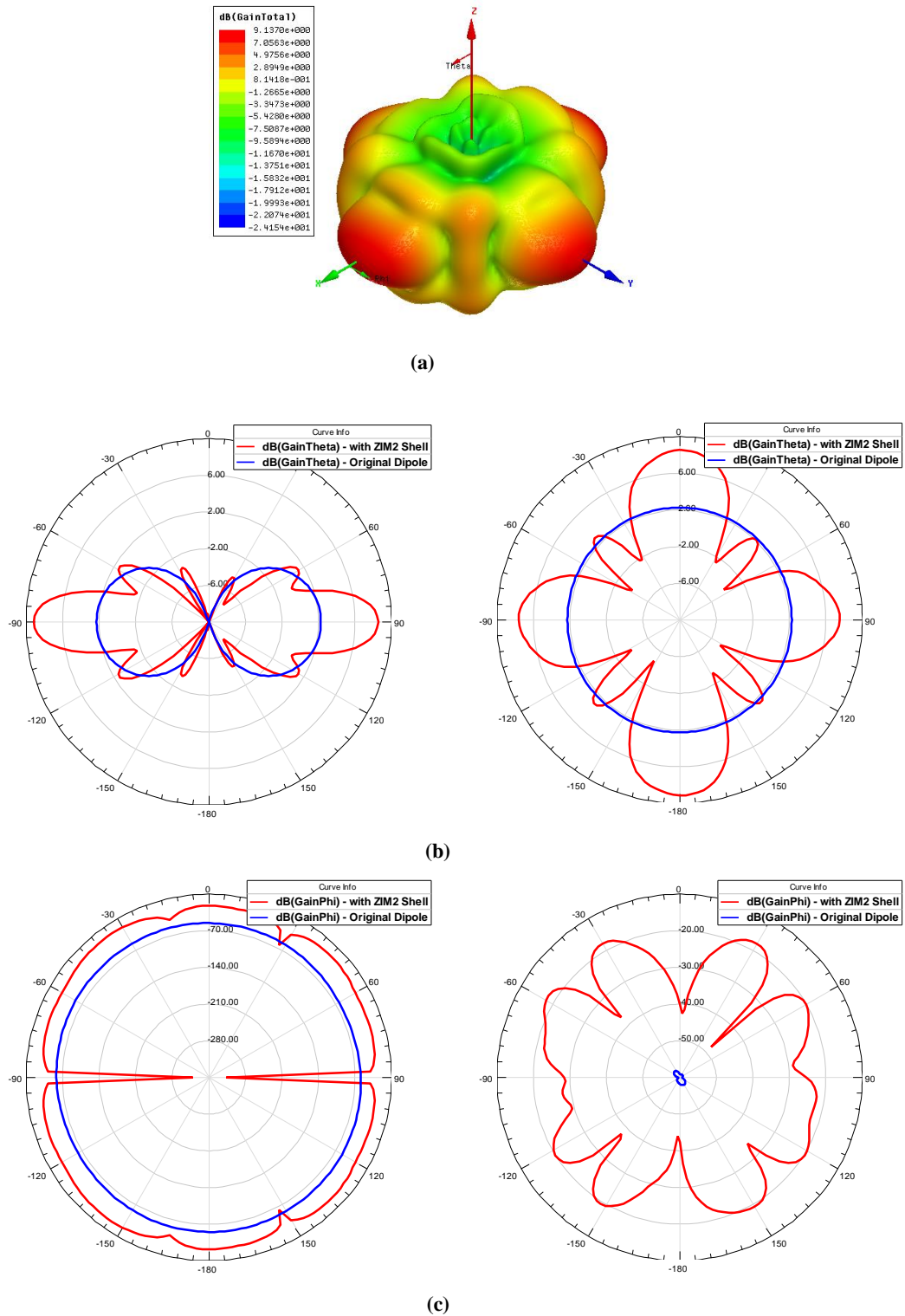


Fig. 3-28. Simulation results for second ZIM shell, (a) total gain 3-D polar in dBi , (b) co-polarisation; gain in dBi , E-plane (left) and H-plane (right) (c) cross-polarisation; gain in dBi , E-plane (left) and H-plane (right)

In the case of a TM polarised wave, using an EZ shell is enough to satisfy the high directive media condition. In a similar fashion, a MZ shell acts as a lens for a TE polarised wave propagating through it. However, for emissions such as the dipole

antenna radiation where polarisation is neither pure TE nor pure TM, the simultaneously EZ and MZ properties are required.

3 - 8 ZIM Loaded Planar Antenna

ZIM embedded planar antennae are considered more practical because despite the ZIM shell, integration of ZIM structures on a planar antenna is fairly easy using standard lithography methods. Also, usually ZIM embedded planar antennae do not require more space compared to their original structure which make them a suitable choice when a compact antenna is needed.

Planar antennae such as patch and slot antennae with wideband and easy fabrication characteristics are effective for a portable terminal and have been the pursuit of antenna designers for many years. There are various types of planar antennae with different principles and applications. Some popular planar antennae are listed in Table 3-4. A planar antenna can be categorised either as a broadside or an end-fire antenna. In the broadside antennae, the main radiation beam is aligned along the normal axis to the plane of antenna. In contrast, in end-fire antenna the main radiation lobe lays along the axis parallel to the antenna plane. Microstrip patch antennae are inherently narrowband; although wider bandwidth could be achieved using techniques such as aperture coupling, introducing a parasitic slot inside the patch, or slot antenna with microstrip feeding, but this will require more design and fabrication considerations. Temporarily, end-fire antennae such as Vivaldi present better bandwidth compared to patches or slots; however, they are usually larger than resonant patches or slots.

Planar quasi-Yagi antenna has both broadband characteristics of travelling wave radiators and the compactness of resonant type antenna and is useful in miniaturised communication systems because of its advantages such as low profile, low cost, lightweight.



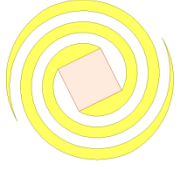


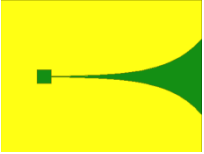

Antenna	Structure	Directivity	Polarisation	Bandwidth	Pattern
Patch		Medium	Linear/Circular	Narrow	Broadside
Slot		Low/Medium	Linear	Medium	Broadside
Spiral		Medium	Linear/Circular	Wide	Broadside
Bow-Tie		Medium	Linear	Wide	Broadside
Quasi-Yagi		Medium/High	Linear	Wide	End-fire
Vivaldi		Medium/High	Linear	Wide	End-fire
LPDA		Medium	Linear	Wide	End-fire

Table 3-4. Planar antennae

3 - 8 - 1 ZIM loaded Quasi-Yagi Antenna

In this section, we have presented an example of ZIM structure on microwave devices where the recently proposed structure is loaded on a quasi-Yagi antenna substrate. The achieved antenna system demonstrates a higher directivity for a range of frequency over which the ZIM structure poses a near zero permittivity.

3 - 8 - 1 - 1 Antenna Design

The quasi-Yagi antenna is designed to work at K_u band with the central operating frequency of 10 GHz. The typical schematic diagram for a quasi-Yagi antenna is

shown in Fig. 3-29 [131]. Rogers RT/duroid 5880 with dielectric constant of 2.2 was chosen as the substrate. Before starting calculations of the antenna dimensions, the free space wavelength λ_0 and the guide wavelength λ_G are required:

$$\lambda_0 = \frac{c_0}{f_0} = 30 \text{ mm} \quad (3-42)$$

To calculate the guide wavelength, first we need to calculate the microstrip width to substrate height ratio, w/h and ϵ_{eff} :

$$\frac{w}{h} = \frac{8e^\zeta}{e^{2\zeta} - 2} = \frac{8e^{1.1594}}{e^{2 \times 1.1594} - 2} = 3.1244 \quad (3-43)$$

Where:

$$\zeta = \frac{Z_0 \sqrt{2(\epsilon_r + 1)}}{120} + \frac{1}{2} \left(\frac{\epsilon_r - 1}{\epsilon_r + 1} \right) \left(\ln \frac{\pi}{2} + \frac{1}{\epsilon_r} \ln \frac{4}{\pi} \right) = 1.1594 \quad (3-44)$$

Then, the effective dielectric constant ϵ_{eff} , can be derived by substituting (3-45) to obtain:

$$\epsilon_{eff} = \frac{\epsilon_r + 1}{2} + \frac{\epsilon_r - 1}{2} \left[\frac{1}{\sqrt{1 + \frac{12}{w/h}}} + 0.04 \left(1 - \frac{w}{h} \right)^2 \right] = 1.981 \quad (3-45)$$

And the guide wavelength λ_G is calculated by:

$$\lambda_G = \frac{\lambda_0}{\sqrt{1.981}} = 21.3147 \text{ mm} \quad (3-46)$$

Next, the antenna dimensions shown in Fig. 3-29 are calculated. The microstrip feed width w_1 is defined to provide an impedance of 50Ω .

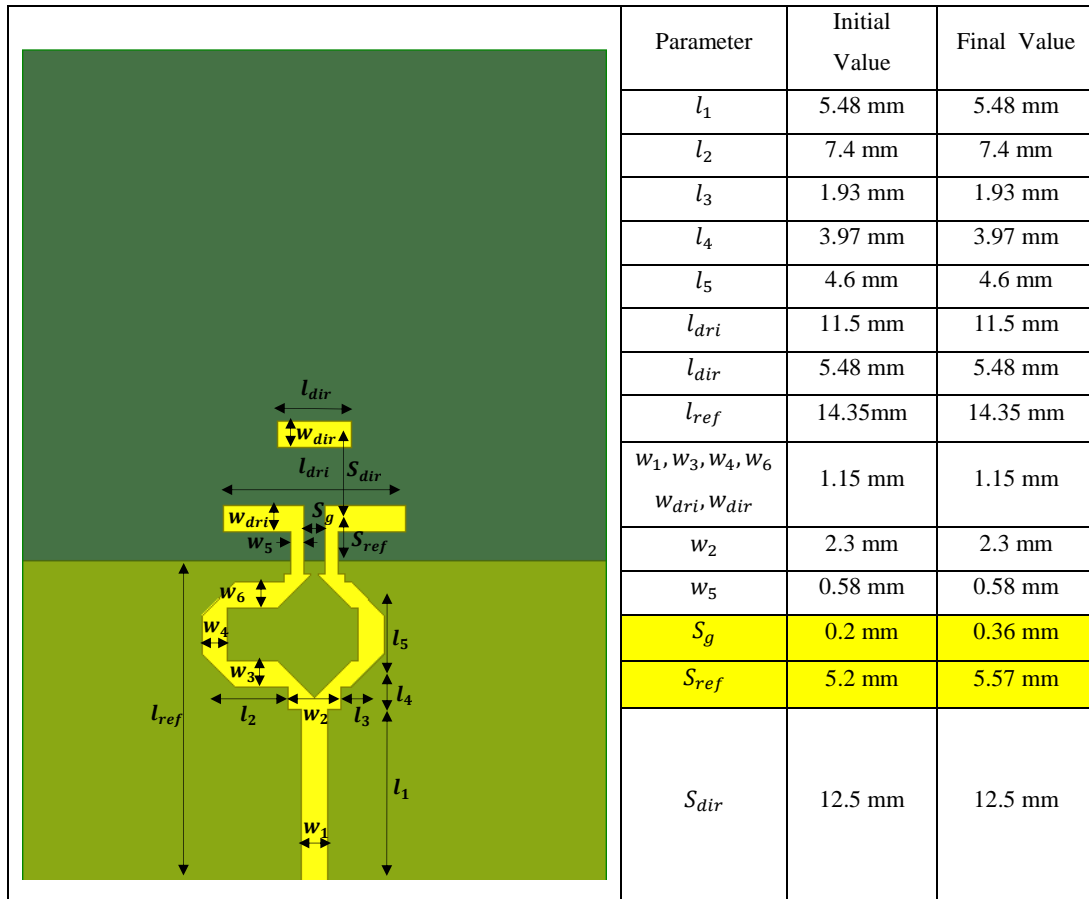


Fig. 3-29. Typical schematic of a quasi-Yagi antenna and its dimensions

In order to align the work with previously published designs [131, 132], copper trace widths w_3, w_4, w_6, w_{dir} are kept the same as the microstrip feed width of w_1 . Also, the T-junction power divider width w_2 and the coplanar stripline width w_5 , are set as $2w_1$ and $0.5w_1$, respectively. A parametric study of the quasi-Yagi antenna conducted in [132] showed that the distance of the driver from the reflector ground S_{dir} , and the length of the driver l_{dri} , have the most effect on the antenna operation. It was also reported that the best operation can be achieved when S_{dir} is set to be a quarter of the guide wavelength and l_{dir} is approximately the same as the guide wavelength. The length difference between the T-junction power divider sides is $\frac{\lambda_G}{4}$ which causes a half wave length delay i.e., 180° phase shift, and consequently enables odd modes to propagate across the coupled microstrips [133].

3 - 8 - 1 - 2 ZIM loaded quasi-Yagi Antenna

Next, the proposed ZIM structure was loaded onto the original quasi-Yagi antenna. The effective permittivity of the ZIM structure, shown in Fig. 3-30, expresses an EZ region at frequencies between 10.4 GHz and 11.8 GHz.

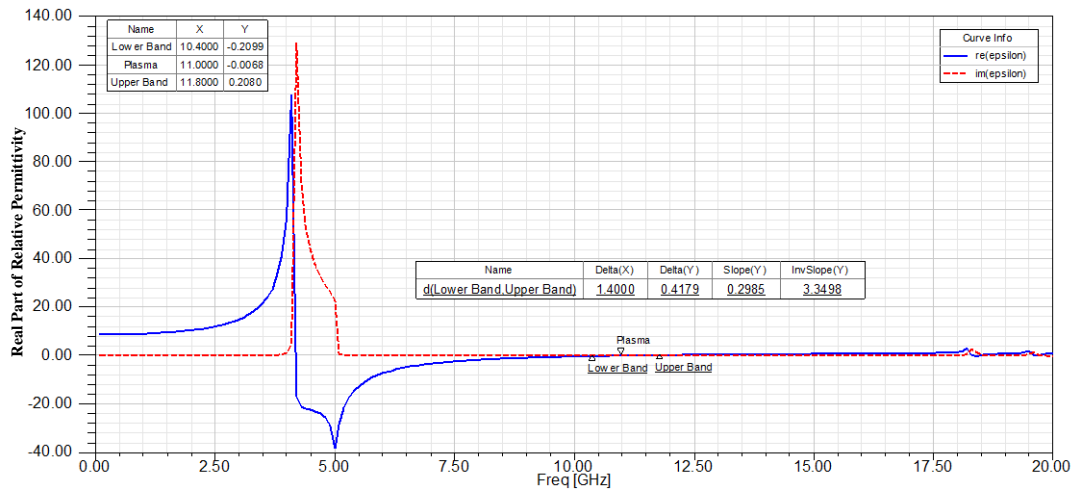
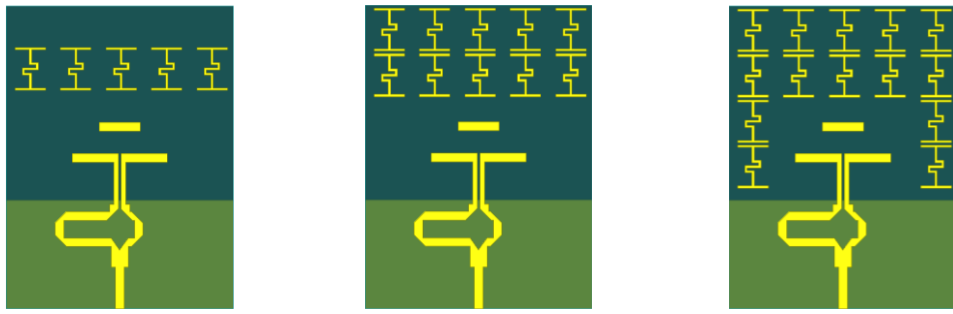


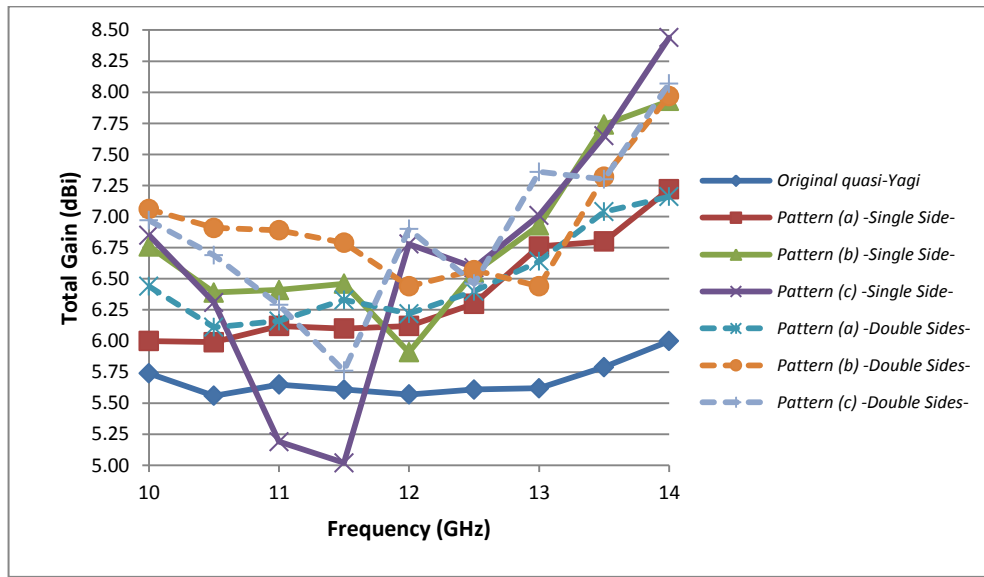
Fig. 3-30. Effective Permittivity of ZIM structure

First, a row of ZIM structures was added to the quasi-Yagi antenna and the proposed design was simulated at five frequency points over the proposed ZIM bandwidth i.e., 10, 10.5, 11, 11.5, 12, 12.5, 13, 13.5 and 14 GHz. Simulation results confirm the gain enhancement for the ZIM embedded quasi-Yagi antenna over the ZIM unit cell bandwidth.

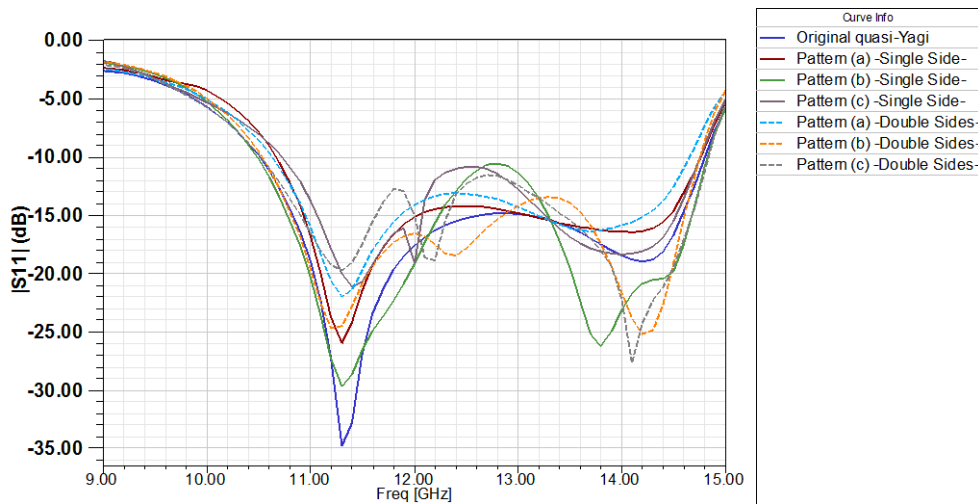
In a second design, two rows of ZIM structures were applied to the antenna. Finally, the proposed design was simulated at the same frequency points as the first design. The designs and simulation results for both scenarios are illustrated in Fig. 3-31.



(a)



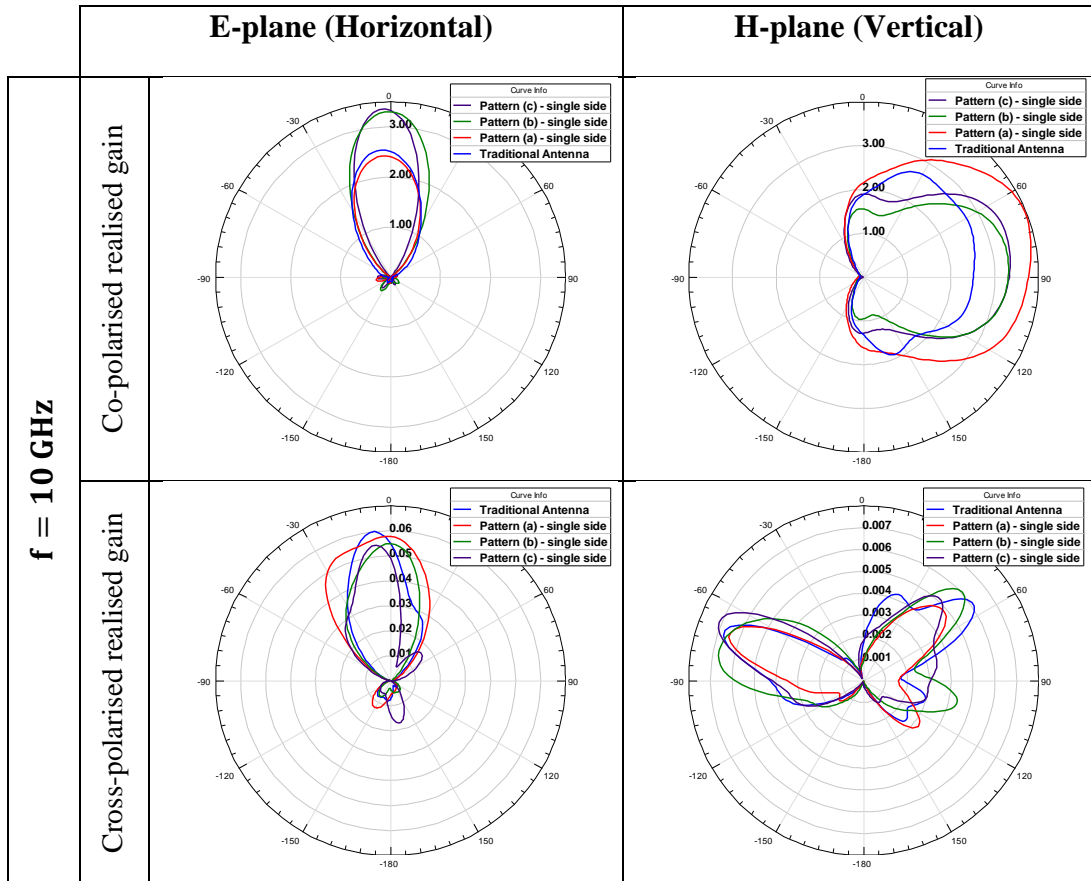
(b)

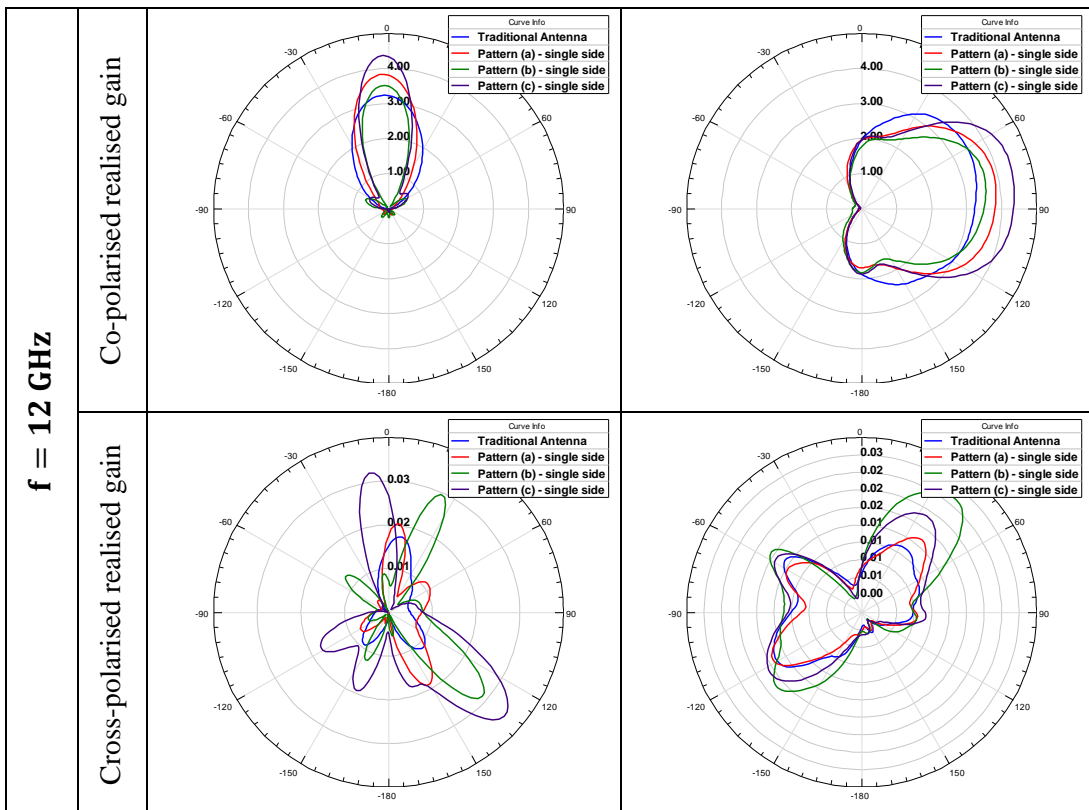
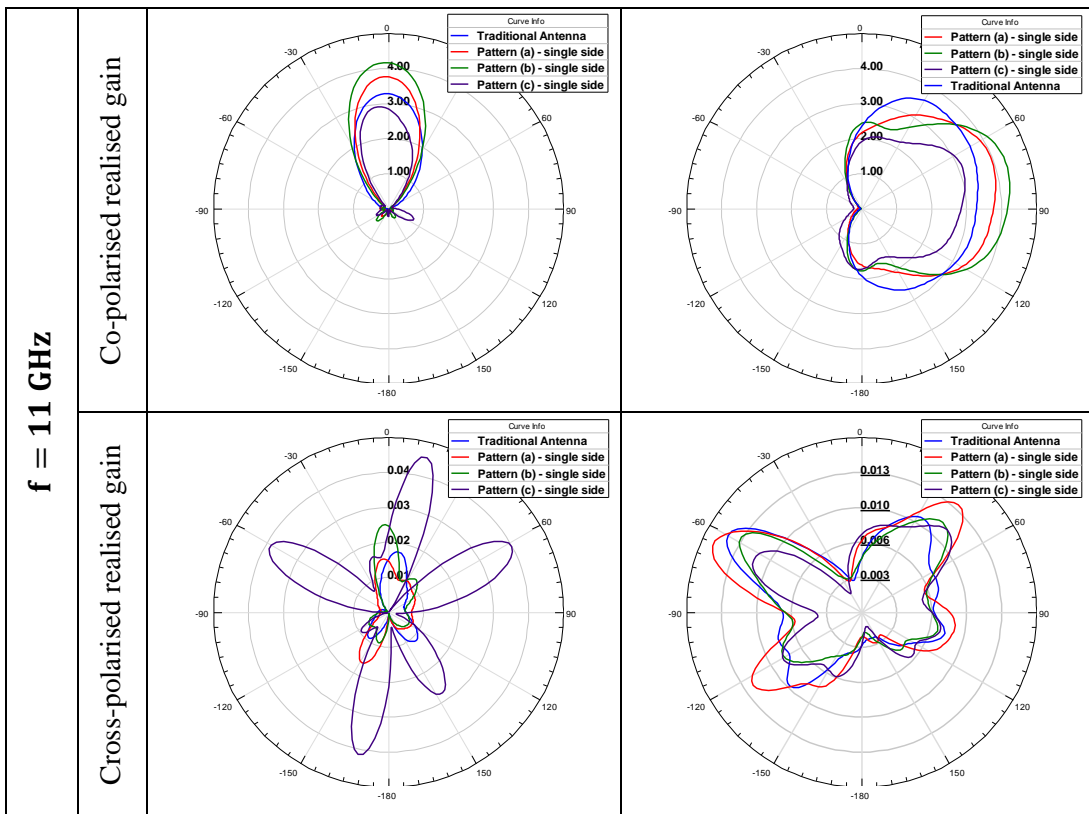


(c)

Fig. 3-31. ZIM embedded quasi-Yagi antenna (a) proposed antenna designs (b) total gain comparison (c) return loss comparison

The radiation pattern shows some reflections at the back of the antenna due to a slight mismatch between the air impedance and the ZIM medium impedance. Higher gain can be achieved by minimising the backward reflection. This can be done using optimisation techniques.





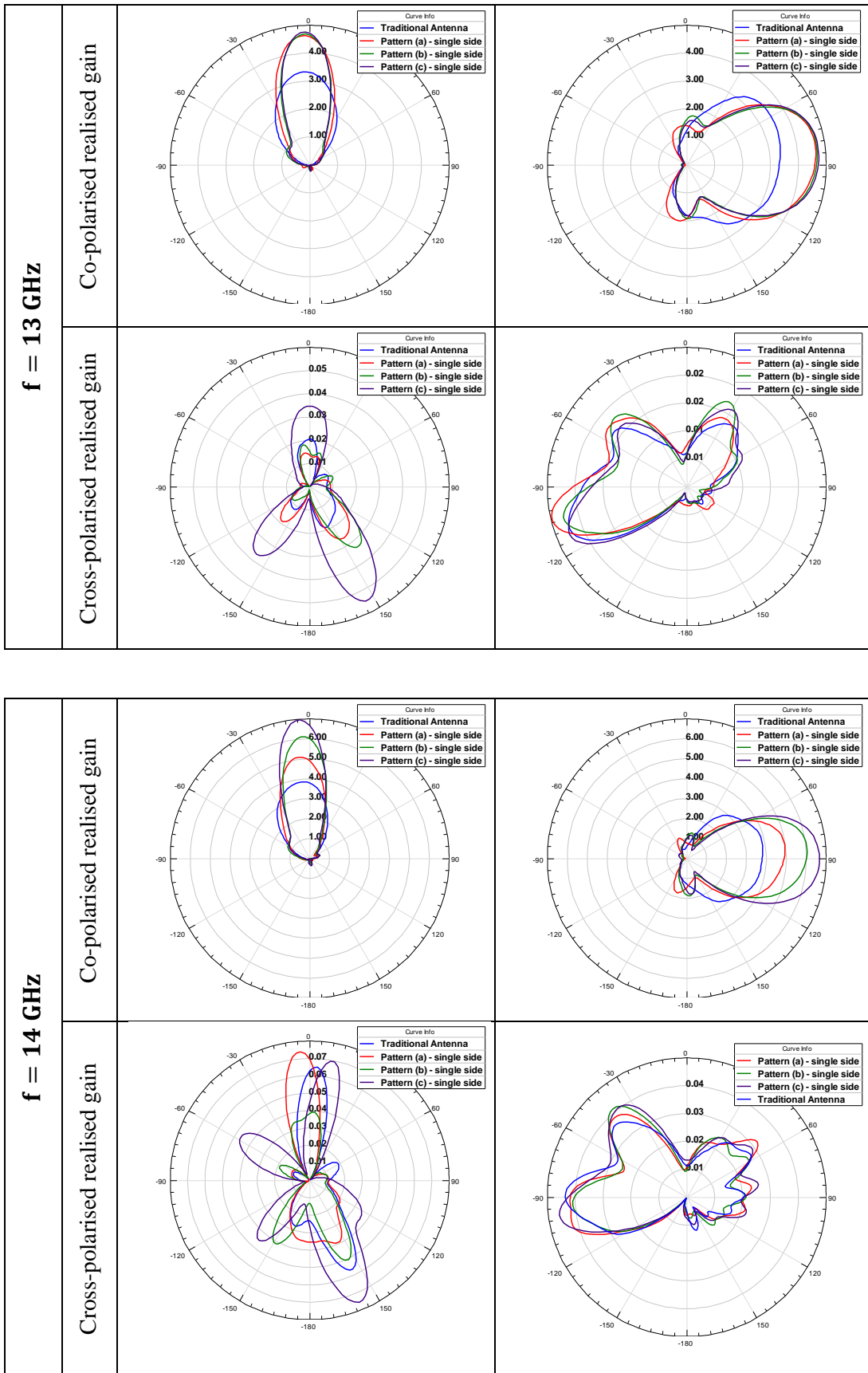
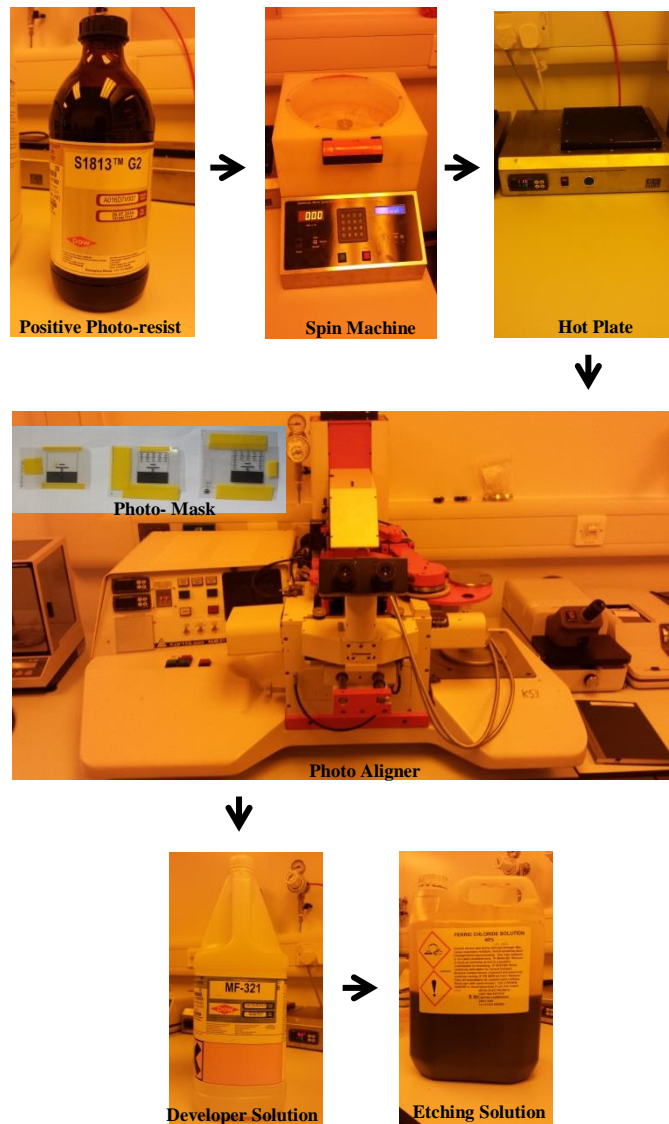


Fig. 3-32. Co- and cross-polarised realised gain of original and ZIM loaded quasi-Yagi antenna

3 - 8 - 2 Fabrication and Measurements

The fabrication procedure for the proposed antennae is shown in Fig. 3-33. All proposed antennae were manufactured on the Rogers RT/duroid 5880 laminate. The S1813 photo-resist solution was applied on both sides of the laminate. To have a uniform thin layer of photo-resist, the laminate was placed inside a spin machine. The spin machine was set to three steps; 3 seconds at a speed of 570 *rpm*, 30 seconds at a speed of 970 *rpm* and 2 seconds at a speed of 2140 *rpm*.

Next, the laminate was baked at 115°C for 60 seconds. The proposed designs were then printed on synthetic over projection paper to create photo-masks. Then, the photo-mask and processed laminate were placed under a photo aligner machine. An optimised exposure time of 45 seconds was found after several exposure times were tested. Immediately, after the exposure, the laminate was developed in the MF321 solution. At this stage several developing times were conducted and the best developing time was found to be 40 seconds at the room temperature were a minimum of round edges and tiny holes in the structure were observed. Eventually, the laminate was etched with ferric chloride acid for 20 – 25 minutes. The etching time was reduced by heating up the solution to 65°C.



(a)

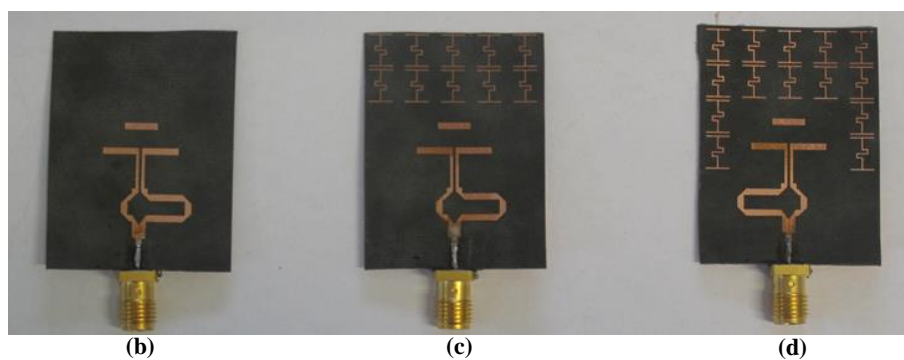


Fig. 3-33. Manufactured proposed antennae, (a) fabrication procedure, (b) traditional quasi-Yagi, (c) quasi-Yagi with pattern b on top, (d) quasi-Yagi with pattern c on top

All proposed antennae were characterised using a linearly polarised horn antenna (ETS.LINDGREN 3115) and a vector network analyser (Agilent Technologies

N5230A) allowing measurements of the reflection coefficients of microwaves in 1 – 18 GHz range.

After calibration with the network analyser, the return loss was measured for each antenna configuration. The far field distance for proposed antennae at a frequency of 10 GHz is calculated as follows:

$$\text{Far field distance} = \frac{2D^2}{\lambda} = 6 \text{ cm} \quad (3-47)$$

Where D is the maximum dimension of the antenna and λ is the wavelength of the radio wave. The distance between the antenna and the receiver horn was set to 0.5 m to ensure measuring of the antenna far field. Then, the proposed antenna was connected to port 1 of the network analyser as a transmitter antenna and the horn antenna was connected to the port 2 of the network analyser as a receiver antenna. The measured values for S_{11} and S_{21} are shown in Fig. 3-34.

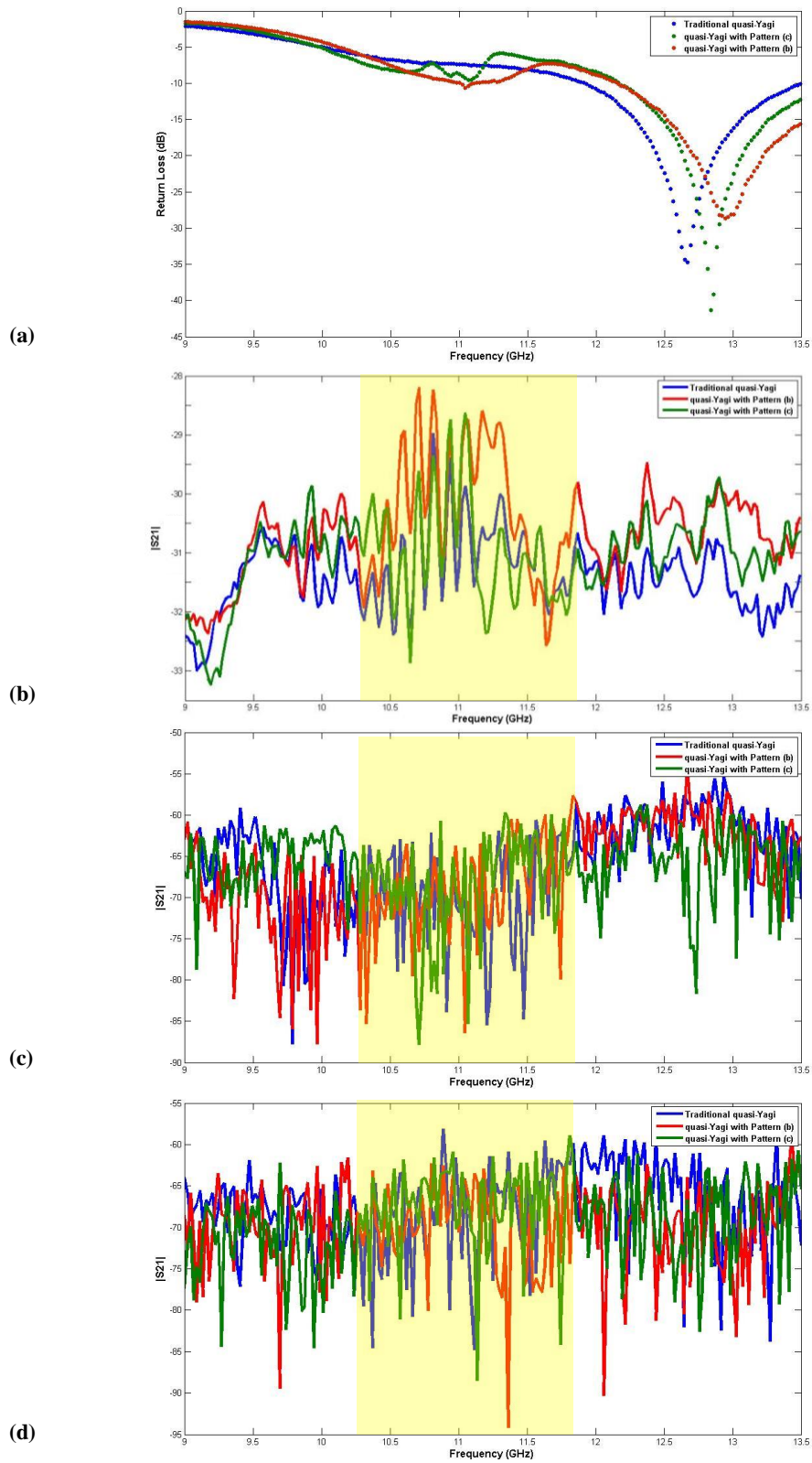
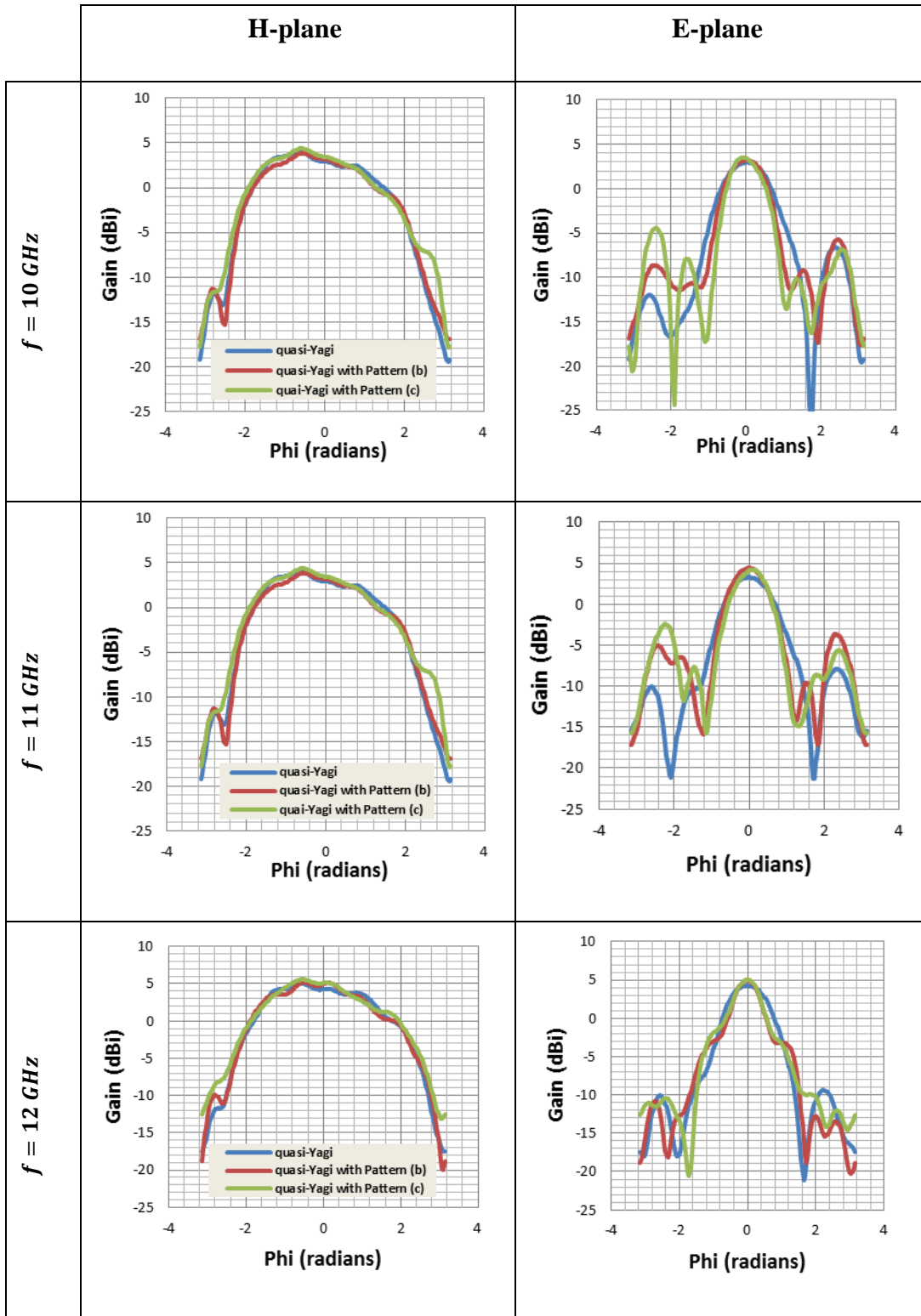


Fig. 3-34. Measured values for proposed antennae, (a) return loss (dBi), (b) $|S_{21}|$ at $\varphi = 0$, (c) $|S_{21}|$ at $\varphi = 30$, (d) $|S_{21}|$ at $\varphi = 45$

Measurement results show slight improvement in gain for the proposed antennae compared to a traditional quasi-Yagi antenna, however, the gain improvement is less than 2 dBi. The measured antenna radiation patterns are shown in Fig. 3-35.



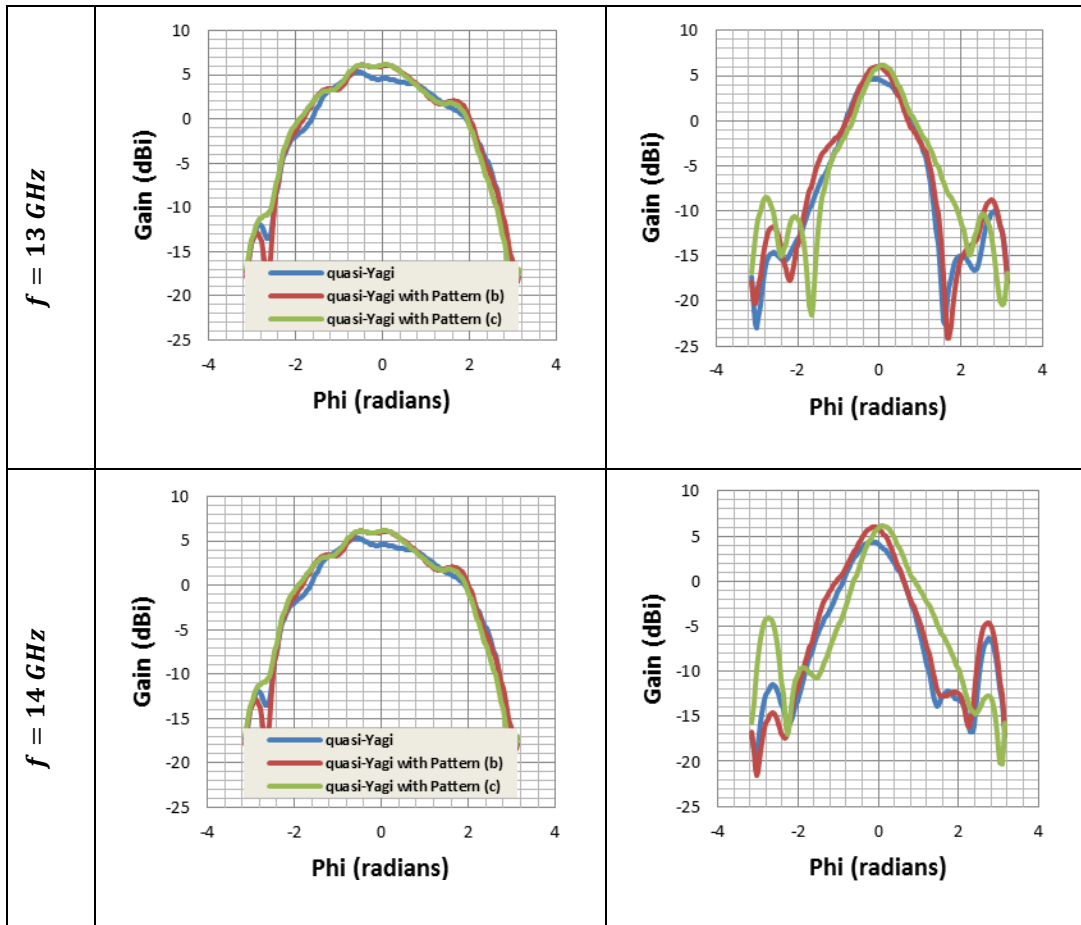


Fig. 3-35. Antenna radiation pattern for traditional quasi-Yagi (blue line), quasi-Yagi with single sided pattern (b) (red line) and quasi-Yagi with single sided pattern (c) (green line)

3 - 9 Summary

In this chapter zero index material (ZIM) fundamentals and their possible application to directive EM emission antennae has been demonstrated. Wave propagation and dispersion relationships in a slab of ZIM structure have been presented. Different topologies for a ZIM unit cell from a simple I-shape to meanderline structures formed by different numbers of meanders were designed and the resonant frequency, plasma frequency and operational bandwidth were compared.

The results suggested that there is a non-linear relationship between the physical and effective length of the scatterer. It was also demonstrated that thinner copper trace provides lower resonant frequency and consequently, lower plasma frequency as well as lower losses associated with resonance. It was found that the lowest resonant and plasma frequencies can be achieved for a meanderline

structure formed by six meanders. The FBW for the different structures proposed was found to be in the range of 8~11%.

A novel ZIM structure with a plasma frequency of 11.5 GHz and a FBW of 14% was introduced. Moreover, a second ZIM unit cell design was proposed where its structure was made of an I-shape structure with an added patch in the centre of the structure. The proposed unit cell exhibited ZIM property within K band (i.e., 18 – 27 GHz) with a plasma frequency of 25.2 GHz. A fractional bandwidth of 33% was achieved which showed a significant increase in operational bandwidth compared to an I-shape structure with a bandwidth of 9.1%.

Further, ZIM embedded antenna structures were categorised into two different types;

- **ZIM shell based antenna** where ZIM cells form a shell around the antenna.
- **ZIM cells integrated on a planar antenna** where ZIM cells are placed on the antenna substrate.

In both cases, the ZIM structures acted as a lens, boosting the antenna directivity. The optical transformation was used to define the required material parameters for the shell to achieve a highly directive emission. Accordingly, epsilon-zero (EZ) cells, mu-zero (MZ) cells and ZIM cells were used to tailor four different shell designs. Then, these shells were placed around the dipole antenna. All designs were simulated and co-and cross-polarised gain patterns in both E- and H-planes were plotted.

In the case of the EZ shell, simulation results showed a total gain of 7.84 dBi along a direction with the epsilon-zero property. This means that the EZ shell provides 5.5 dBi gain enhancement compared to the gain of the dipole antenna without a shell (i.e., 2.3 dBi). In the second case, the dipole antenna was surrounded by the MZ shell where a total gain of 4.9 dBi was achieved illustrating that the EZ shell is more directive than the MZ shell. Further, the EZ shell and MZ shell were combined to form a ZIM shell with simultaneously zero permittivity and zero permeability. Two different structure designs were suggested for the ZIM shell; in the first ZIM shell design, the EZ cells were placed within the layers of the MZ shell where a total gain of 7 dBi was achieved.

In contrast, the second ZIM shell was designed by placing the MZ cells between the EZ shell layers where a total gain of up to 9.15 *dBi* was obtained.

Further, the proposed ZIM structure was integrated to the quasi-Yagi antenna. Simulation results showed that the antenna gain increases for a frequency range over which the proposed metamaterial structure exhibits ZIM properties (10.4 – 11.8 *GHz*). The antenna gain was improved even further by using two rows of the ZIM structure while the antenna operational bandwidth remained almost the same. Additional gain enhancement could be achieved by using multiple layers of the ZIM structure, however, this will increase the overall antenna profile.

Chapter 4

Energy Spatial Redistribution based on Propagating Wave Interference using a Metamaterial Phase Shifter

In this chapter, the wave interference phenomenon and energy distribution in space are investigated. It is shown that a highly directive emission can be achieved for two interfering waves with equal intensity, frequency, and polarisation axis that are 180° out of phase. Thereafter, a new technique is developed based on wave interference to define the required properties for a metamaterial lens. Further, a theoretically defined lens slab is used to increase the gain of the patch antenna. Finally, metamaterial realisation of the lens slab is formed using a capacitively loaded ring resonator (CLRR) unit cell.

4 - 1 Introduction

In classic electromagnetism, the superposition principle is used to determine the wave interference pattern. When two waves propagate through a medium, the interference of the waves causes the medium to take on a shape which results from the net effect of the two individual waves upon the particles of the medium [134]. The question is, can one extend the wave interference phenomenon as a kind of waves interaction?

The possibility of light-light interaction has been reported in [2]. The scattering of light by light is possible in quantum electrodynamics as a low probability second-order process represented by a Feynman diagram of the box type [135]. P. Dowling argued that under certain circumstances it is possible to consistently interpret interference as the specular reflection of two electromagnetic waves off

each other in vacuum [136]. He showed the specular reflection of two waves for monochromatic beams of light with 180° phase difference and equal intensity, frequency, polarisation axis, and diameters, orthogonally intersect in free space. To observe the interaction of two microwave waves, we have considered a Gedanken experiment illustrated in Fig. 4-1. In this experiment, the wave excited by port 1 propagates along the x-direction with the E-field and H-field along the z-axis and y-axis, respectively. The wave excited by port 2 propagates along the y-direction with the E-field and H-field along the z-axis and x-axis, respectively. Both waves have equal intensity, frequency, polarisation-axis and diameters but are 180° out of phase.

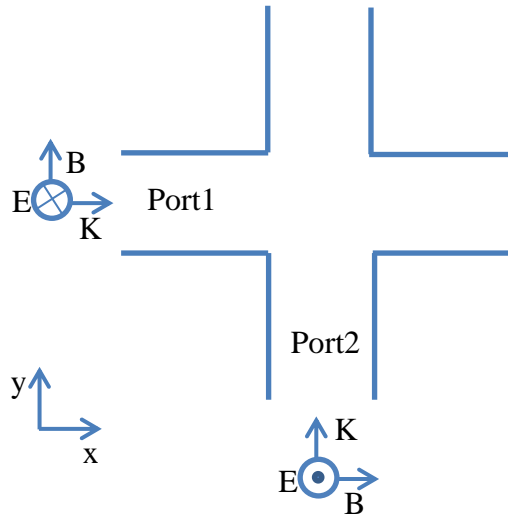


Fig. 4-1. Gedanken experiment; two monochromatic waves with 180° phase difference and equal intensity, frequency, polarisation axis, and diameters propagating along x- and y-directions

In general, for a harmonically varying electromagnetic wave, the time averaged energy density $u(r, t)$ and Poynting vector $S(r, t)$ can be calculated from [136]:

$$u(r, t) = (1/16\pi)(E \cdot E^* + B \cdot B^*) \quad (4-1)$$

$$S(r, t) = \frac{c}{8\pi} \text{Re}[E \times B^*] \quad (4-2)$$

The interference fringe can be defined as a set of points (x, y, z) where the energy density is minimum due to destructive interference. The electric and magnetic fields can be written as the summation of horizontal and vertical fields with

respect to a defined coordinate system shown in Fig. 4-1. Thus, plane wave solutions to Maxwell's equations can be written as:

$$E = E_h + E_v \quad (4-3)$$

$$B = B_h + B_v \quad (4-4)$$

$$E = E_0(e^{i\eta} - e^{i\xi})\hat{z} \quad (4-5)$$

$$B = E_0(e^{i\eta}\hat{x} + e^{i\xi}\hat{y}) \quad (4-6)$$

Where:

$$\xi = kx - \omega t \quad (4-7)$$

$$\eta = ky - \omega t \quad (4-8)$$

Therefore the timed averaged energy density can be written by using the above equations:

$$u_p = \frac{1}{8\pi}(E_0^2) \quad (4-9)$$

$$u_n = \frac{1}{8\pi}(E_0^2) \quad (4-10)$$

$$u = \frac{1}{8\pi}E_0^2[2 - \cos(k(x - y))] \quad (4-11)$$

The cosine term represents the interference of two waves and it is equal to zero for out-of-phase waves. To minimize the averaged energy intensity on the interference plane one can write:

$$\cos(k(x - y)) = 0 \quad (4-12)$$

$$y = x - n\lambda, \quad n = 0, \pm 1, \pm 2, \dots \quad (4-13)$$

There are an infinite number of fringes which satisfy (4-13). To simplify simulation, the beam width is chosen to be equal to the wavelength, $d = \lambda$. This will consider only one fringe over the middle of the cube diagonally. The evaluation of the field on the fringe plane gives:

$$E_{x=y} = 0 \quad (4-14)$$

$$B_{x=y} = E_0 e^{i\xi}(\hat{x} + \hat{y}) \quad (4-15)$$

As it can be seen, on the fringe plane the electric field vanishes and the magnetic field is transverse to the fringe plane. The evaluated time averaged energy intensity in (4-1), is only caused by the magnetic field. It is not related to the interference effects since the horizontal and vertical magnetic fields are orthogonal and cannot interfere. This energy intensity is constant over the whole area and is equal to:

$$u_{x=y} = \frac{1}{4\pi} E_0^2 \quad (4-16)$$

Based on the energy conservation law, the energy cannot vanish, but we understand that the electric field, and consequently its energy, vanish on the fringe plane. To find out where the energy goes in this phenomenon the energy flow can be checked by investigating the Poynting vector. One can calculate the Poynting vector in the same way as for the averaged field intensity:

$$S_p = \frac{c}{8\pi} E_0^2 \hat{x} \quad (4-17)$$

$$S_n = \frac{c}{8\pi} E_0^2 \hat{y} \quad (4-18)$$

$$S = \frac{c}{8\pi} E_0^2 \{1 - \cos[k(x - y)]\} (\hat{x} + \hat{y}) \quad (4-19)$$

Again here the cosine term represents the interference of two waves. For two incoherent waves on the fringe plane the interference vanishes and the total power flow through the fringe plane is equal to zero. The boundary conditions on the fringe plane can be written as follows:

$$E_{\parallel} |_{x=y} = 0 \quad (4-20)$$

$$B |_{x=y} \equiv B_{\parallel} \rightarrow B_{\perp} |_{x=y} \equiv 0 \quad (4-21)$$

The symbols \parallel and \perp represent parallel and normal directions to the fringe plane, respectively. These conditions are equal to the boundary conditions for a perfectly conducting surface (PEC). The experiment model was set up in ANSYS HFSS once with a PEC plane in the fringe plane and once without it. Fig. 4-2 shows the simulation results for two Gaussian waves with same frequency, intensity and polarisation axis which are 180° out of the phase, once with a PEC material placed

on the fringe plane and once without using any material. As expected, the specular reflection of waves can be observed and the results for both cases are identical.

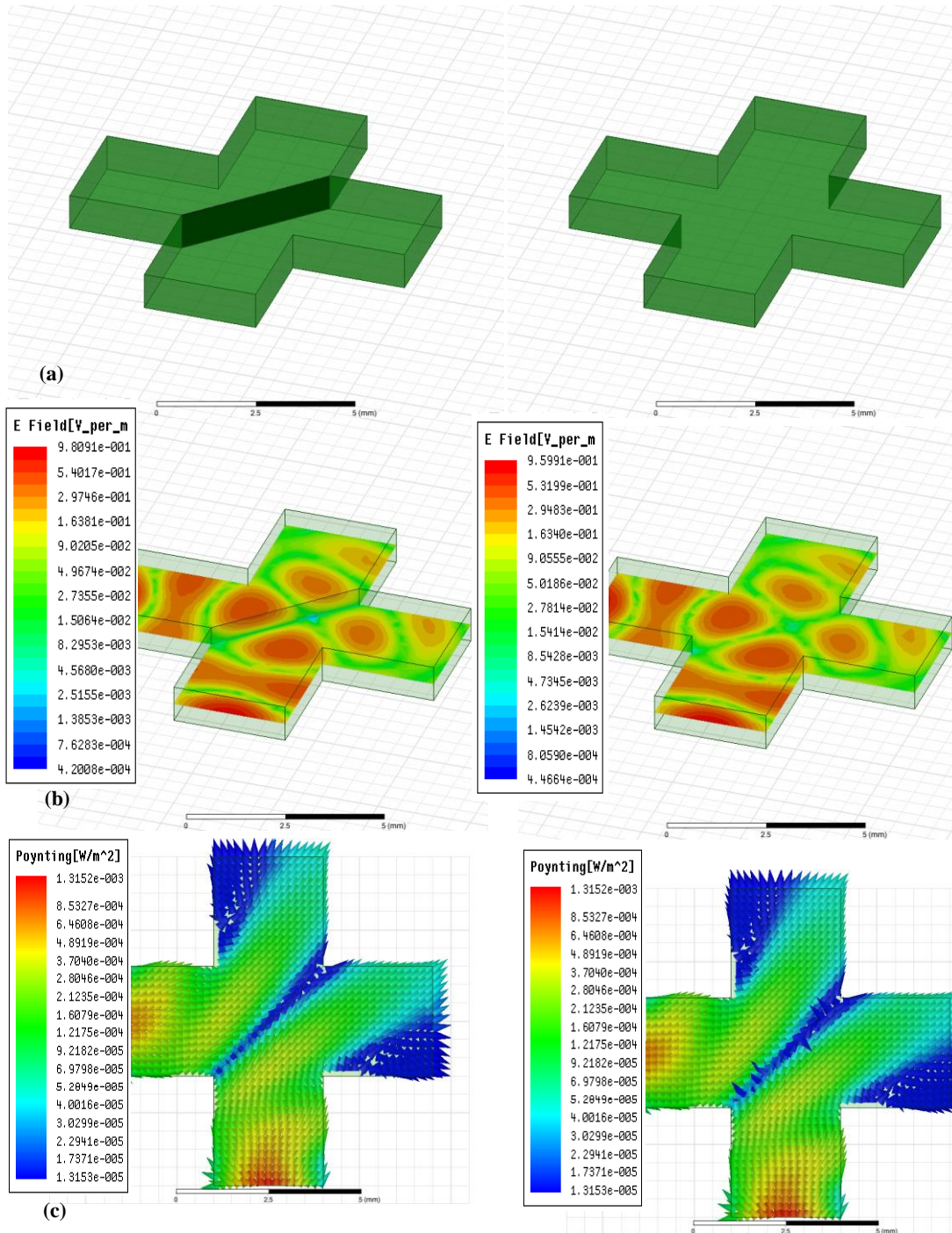


Fig. 4-2. Microwave Gaussian waves with same frequency, intensity, polarisation axis which are 180° out of the phase (a) Gedanken experiment with and without PEC condition on the fringe plane (b) The electric field distribution (c) Poynting vector is parallel to the fringe plane at $\phi=45^\circ$

4 - 2 Energy Re-distribution

4 - 2 - 1 Plane Waves Interference

Assume that two waves with the same frequency, intensity and polarisation axis but different phase are interfering one to another. The total electric field can be written as:

$$\begin{aligned} E_t &= E_1 + E_2 = E_0 e^{i(kx - \omega t - \varphi_1)} \hat{z} + E_0 e^{i(kx - \omega t - \varphi_2)} \hat{z} \\ &= 2E_0 \left[\cos\left(kx - \omega t - \frac{\varphi_1 + \varphi_2}{2}\right) \cos\left(\frac{\varphi_1 - \varphi_2}{2}\right) \right. \\ &\quad \left. + i \sin\left(kx - \omega t - \frac{\varphi_1 + \varphi_2}{2}\right) \cos\left(\frac{\varphi_1 - \varphi_2}{2}\right) \right] \end{aligned} \quad (4-22)$$

$$E_t = 2E_0 \cos\left(\frac{\varphi_1 - \varphi_2}{2}\right) e^{i(kx - \omega t - \frac{\varphi_1 + \varphi_2}{2})} \hat{z} \quad (4-23)$$

In the interest of simplicity, it can be assumed that the waves have a square cross-section and therefore the magnetic and Poynting vector can be calculated as follows:

$$B_t = 2E_0 \cos\left(\frac{\varphi_1 - \varphi_2}{2}\right) e^{i(kx - \omega t - \frac{\varphi_1 + \varphi_2}{2})} \hat{y} \quad (4-24)$$

$$S(r, t) = \frac{c}{8\pi} \text{Re}[E \times B^*] = \frac{c}{2\pi} \cos^2\left(\frac{\varphi_1 - \varphi_2}{2}\right) \hat{x} \quad (4-25)$$

$$S(r, t) = \frac{c}{4\pi} [1 + \cos(\varphi_1 - \varphi_2)] \hat{x} \quad (4-26)$$

The Poynting vector shows that the energy flow in the direction that the two waves propagate is related to the phase difference between the waves. When there is no phase difference between the two waves the energy flow is maximum. In contrast, when the phase difference is equal to an integer multiple of 2π , the energy cannot propagate in the wave's direction.

Equations (4-24)-(4-26) describe that as the phase difference between two waves increases, less energy flows in the direction of propagation and eventually, for a phase difference equal to 2π , the energy cannot flow in the propagation direction. On the other hand, the energy conservation law states that the total energy of an

isolated system cannot change. This brings up a question that if energy cannot flow in the direction which the waves travel, where does it go?

One can say that the energy is re-distributed in space such that there is less energy at the points with destructive interference and more energy at the points where constructive interference is happening.

In practice, the wavefront is not a plane wave, especially, in places closer to its source like in an antenna. Next, the interference phenomenon is studied for Gaussian waves as they are closer to a real wavefront.

4 - 2 - 2 Gaussian Waves Interference

In general, the analytical formula of a Gaussian beam illustrated in Fig. 4-3, can be written as:

$$E^{inc} = E_0 \frac{W_0}{W(L)} e^{-\left(\frac{D^2}{W(L)^2}\right)} e^{-j(k \cdot (r-r_0) - k \frac{D^2}{2R(L)} + \Psi(L))} \quad (4-27)$$

Where:

$$R(L) = L \left[1 + \left(\frac{\pi W_0^2 n}{L \lambda} \right)^2 \right] \quad (4-28)$$

$$\Psi(L) = \text{atan} \left[\frac{L \lambda}{\pi W_0^2 n} \right]^2 \quad (4-29)$$

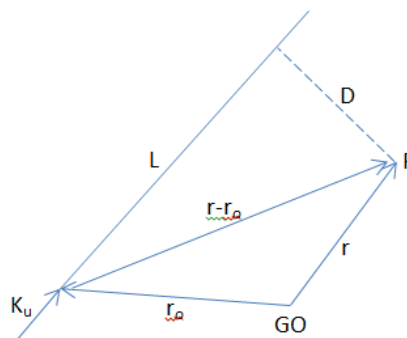


Fig. 4-3. Gaussian beam vector

To investigate the effect of phase difference on the energy distribution in space a simple 2-D scenario can be considered. As shown in Fig. 4-4, assume that there are two Gaussian waves with the same frequency, energy intensity and polarisation axis but different phase offset are propagating through a medium.

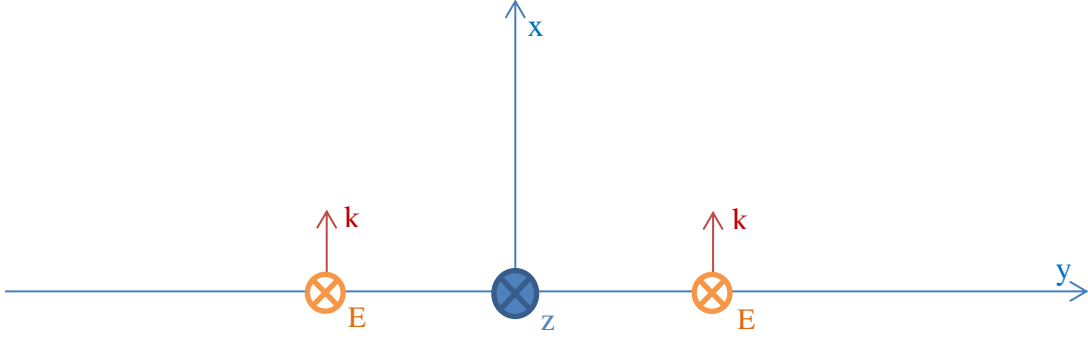


Fig. 4-4. Two Gaussian waves with same frequency, energy intensity and polarisation axis

Here the electric field can be written as:

$$E_1 = \frac{W_0}{W(x)} e^{-\frac{y^2+z^2}{W(x)^2}} e^{-j(kx+k\frac{(y-d)^2+z^2}{2R(x)}-\Psi(x)-\frac{\varphi}{2})} \quad (4-30)$$

$$E_2 = \frac{W_0}{W(x)} e^{-\frac{(y-d)^2+z^2}{W(x)^2}} e^{-j(kx+k\frac{(y+\frac{d}{2})^2+z^2}{2R(x)}-\Psi(x)+\frac{\varphi}{2})} \quad (4-31)$$

Where, d and φ are the distance and phase difference between sources, respectively. To simplify calculations, the effect of the distance between sources in amplitude variation in the far field zone is ignored. It follows that:

$$E_{tz} \approx E_0 e^{-\frac{y^2+z^2}{W(x)^2}} \left[e^{-j\left(\xi+k\frac{yd}{2R(x)}+\frac{\varphi}{2}\right)} + e^{-j\left(\xi-k\frac{yd}{2R(x)}-\frac{\varphi}{2}\right)} \right] \quad (4-32)$$

$$E_{tz} = E_0 e^{-\frac{(y^2+d^2+z^2)}{W(x)^2}} \cos\left(k\frac{yd}{2R(x)} - \frac{\varphi}{2}\right) e^{-j\xi} \quad (4-33)$$

Where, $\xi = k\left(x + \frac{y^2+z^2+d^2}{2R(x)}\right) - \Psi(x)$. When the observation point is far enough away from the origin, further simplification can be applied by discarding the first term within the cosine function. Also the electric field component along the x- and y-direction can be written as:

$$E_{tx} = -j \frac{2z}{kw(x)^2} E_0 e^{-\left(\frac{y^2+d^2+z^2}{W(x)^2}\right)} \cos\left(k \frac{yd}{2R(x)} - \frac{\varphi}{2}\right) e^{-j\xi} \quad (4-34)$$

$$E_{ty} = 0 \quad (4-35)$$

And the magnetic field can be written:

$$\begin{aligned} B_{tx} &= -j \frac{2y}{kw(x)^2} E_{tz} \\ &= -j \frac{2y}{kw(x)^2} E_0 e^{-\left(\frac{y^2+d^2+z^2}{W(x)^2}\right)} \cos\left(k \frac{yd}{2R(x)} - \frac{\varphi}{2}\right) e^{-j\xi} \end{aligned} \quad (4-36)$$

$$B_{ty} = \frac{E_0}{c} E_{tz} = \frac{E_0}{c} e^{-\left(\frac{y^2+d^2+z^2}{W(x)^2}\right)} \cos\left(k \frac{yd}{2R(x)} - \frac{\varphi}{2}\right) e^{-j\xi} \quad (4-37)$$

$$B_{tz} = 0 \quad (4-38)$$

And finally the energy flow defined by the real Poynting vector can be expressed as follows:

$$\begin{aligned} S_x &= \frac{c\varepsilon_0 E_0^2}{2} \cos^2\left(k \frac{yd}{2R(x)} - \frac{\varphi}{2}\right) e^{-2\left(\frac{y^2+d^2+z^2}{W(x)^2}\right)} \left(1 \right. \\ &\quad \left. + \cos\left(2\left[k\left(x + \frac{y^2+z^2+d^2}{2R(x)}\right) - \Psi(x)\right]\right)\right) \hat{x} \end{aligned} \quad (4-39)$$

$$\begin{aligned} S_y &= c\varepsilon_0 E_0^2 \cos^2\left(k \frac{yd}{2R(x)} - \frac{\varphi}{2}\right) \left(\frac{2y}{kw(x)^2}\right) e^{-2\left(\frac{y^2+d^2+z^2}{W(x)^2}\right)} \sin\left(2\left[k\left(x + \frac{y^2+z^2+d^2}{2R(x)}\right) \right. \right. \\ &\quad \left. \left. - \Psi(x)\right]\right) \hat{y} \end{aligned} \quad (4-40)$$

$$\begin{aligned} S_z &= c\varepsilon_0 E_0^2 \cos^2\left(k \frac{yd}{2R(x)} - \frac{\varphi}{2}\right) \left(\frac{2z}{kw(x)^2}\right) e^{-2\left(\frac{y^2+d^2+z^2}{W(x)^2}\right)} \sin\left(2\left[k\left(x + \frac{y^2+z^2+d^2}{2R(x)}\right) \right. \right. \\ &\quad \left. \left. - \Psi(x)\right]\right) \hat{z} \end{aligned} \quad (4-41)$$

The term within the cosine squared function is representing the effect of phase difference on the total energy flow in the space. The first term of the argument of the cosine squared function approaches to zero in two cases;

- 1- when $y \rightarrow 0$; which means all the space points near the perpendicular bisector construction of the line that connects two sources.
- 2- When the radius of curvature of the beam's wavefronts is large enough $R(x) \rightarrow \infty$; which means that all the space points where either $x \rightarrow 0$ or $x \rightarrow \infty$.

One can say that in these two space zones the energy flow only depends on the phase difference between the two sources. As the phase difference increases, the total energy flow near the perpendicular bisector construction of the line connecting the two sources decreases and it will approach zero when the sources are 180° out of phase. Fig. 4-5 shows simulation results for two Gaussian waves with different phase shifts which are placed in $\lambda/3$ distance from each other.

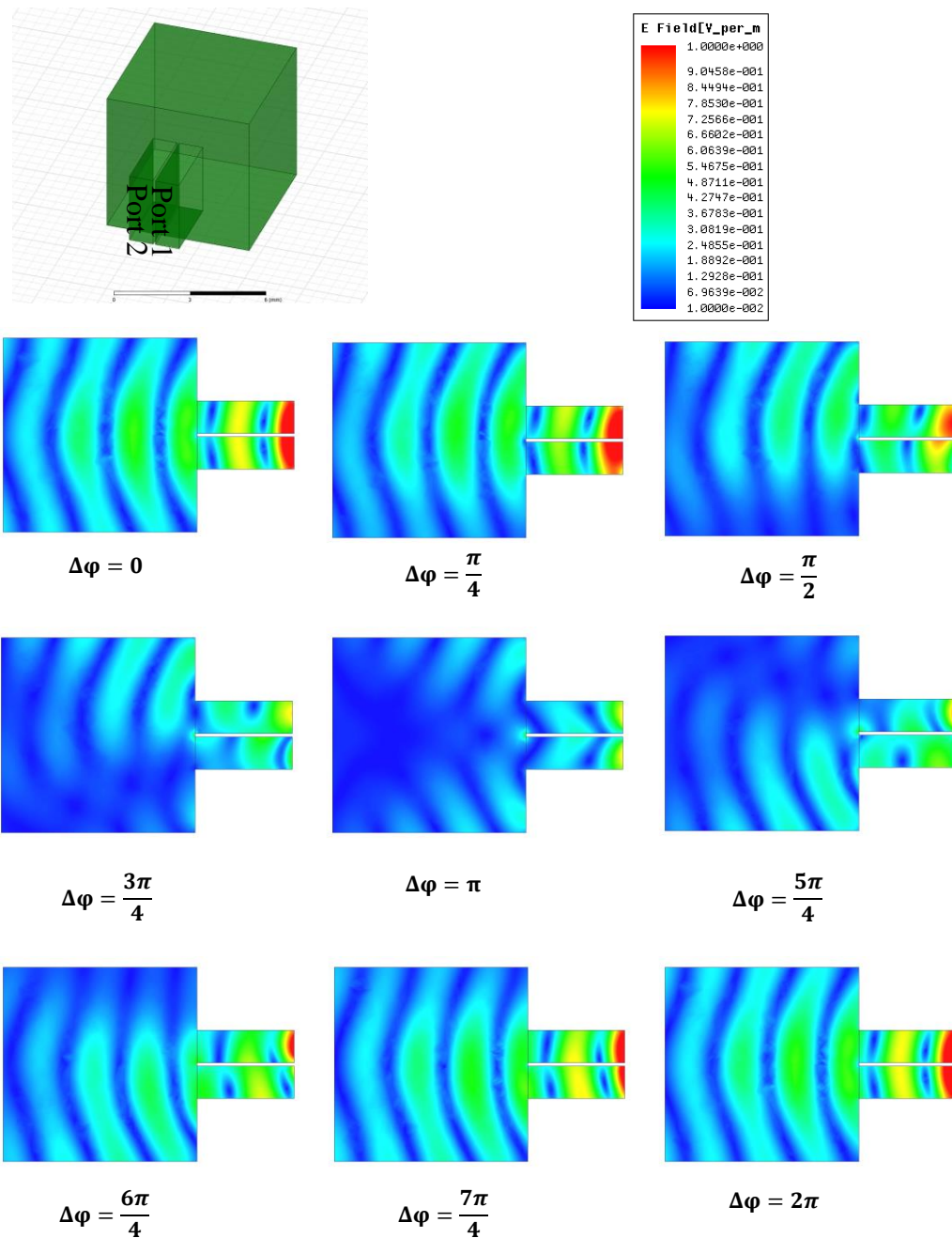


Fig. 4-5. Two Gaussian waves with different phase shift which are placed in $\lambda/3$ distance from each other

4 - 3 Antenna Gain Enhancement

The interference pattern of two waves depends on three factors;

- 1- amplitudes of the interfering waves
- 2- frequencies of the interfering waves
- 3- phase difference between the two interfering waves

This section discusses attempts to increase antenna gain by applying a controlled phase shift technique. As it was argued earlier in this chapter, interference of waves will re-distribute energy in space. Under certain circumstances waves can bounce off each other and change the direction of energy flow. This brings an idea to mind that if the interference pattern could be made into a desired pattern where the energy flow is pushed in a certain direction, a high directive emission in that direction could be achieved.

Huygens' Principle states that every point on a wavefront may be considered a source of secondary spherical wavelets which spread out in a forward direction at the speed of light [121]. As it is shown in Fig. 4-6, the new wavefront is tangential surface to all of the secondary wavelets.

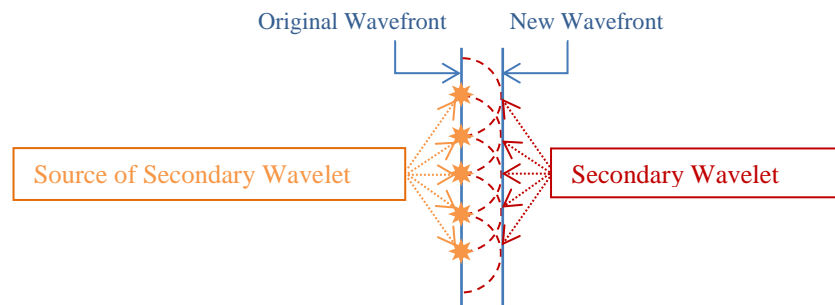


Fig. 4-6. Huygens' principle

Interpretation of waves as a set of point sources on one hand and the interference pattern of two adjacent sources and its relation to the phase difference of the sources on the other hand provide a possible way to direct the energy flow in a desired direction such that higher gain antenna can be made.

The controlled phase shift concept is shown in Fig. 4-7. The wavefront has been represented by three point sources which have the same frequency, amplitude and phase. A phase shifter of 180° has been placed in same potential surface i.e., parallel to the wavefront. The wave cannot propagate through the straight line as

the interference of the out coming wave from the phase shifter and the wave around the phase shifter are out of phase. The real Poynting vector will bend showing that energy flow is re-distributed.

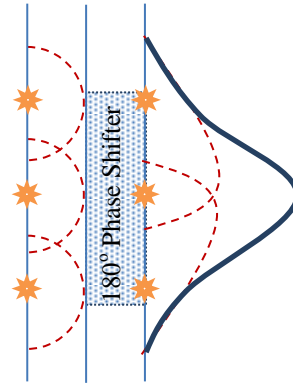


Fig. 4-7. 180° Phase Shifter

4 - 3 - 1 180° Phase Shifter

The effect of a medium on the properties of a wave propagating through a medium is described by the dispersion relation. The dispersion relation of a wave can be written as [137]:

$$k^2 = n^2 \frac{\omega^2}{c^2} \quad (4-42)$$

Where, n is the refractive index of the medium, k is the wavenumber and c is speed of light in the free space. The phase advance for a given wave propagating within the medium depends on the medium thickness and the refractive index and is calculated by:

$$\varphi = kd \quad (4-43)$$

Assume a plane wave is incident upon two slabs of equal thickness but different EM properties. The phase difference between the waves propagating out of the slabs at the other sides can be calculated by:

$$\Delta\varphi = |k_1d - k_2d| \quad (4-44)$$

Where k_1 and k_2 are the wavenumbers of the propagating waves within the two slabs and d is the slab thickness.

By substituting the dispersion equation into (4-44), the relationship between the refractive index n and the phase advance $\Delta\varphi$ can be obtained:

$$\Delta\varphi = \frac{d\omega}{c} |(n_1 - n_2)| \quad (4-45)$$

$$\Delta\varphi = \frac{2\pi d}{\lambda} |(n_1 - n_2)| \quad (4-46)$$

To obtain 180° phase difference between the exiting waves from the other sides of the slabs, it can be written:

$$\frac{2\pi d}{\lambda} |(n_1 - n_2)| = n\pi \quad n = 1,3,5, \dots \quad (4-47)$$

$$|(n_1 - n_2)| = \frac{n\lambda}{2d} \quad n = 1,3,5, \dots \quad (4-48)$$

When (4-48) is satisfied, the exiting waves from the composite medium are 180° out of phase. If we assume the difference between refractive indices of layers in such a composite medium is equal to 2, then:

$$d = \frac{\lambda}{4} \quad (4-49)$$

Based on theory discussed previously, a plane incident wave has been projected on a slab with refractive index of $n_{slab} = 3$ surrounded by vacuum. Here the difference between refractive indices is $\Delta n = 2$. To avoid undesired scattering, the wave impedance η , is kept equal to the air impedance by defining the constitutive parameters of the slab to be equal to 3 (i.e., $\epsilon_r = \mu_r = 3$). ANSYS HFSS was used to simulate the destructive interference pattern for a wave propagating through the interface of air and the slab and simulation results are shown in Fig. 4-8.

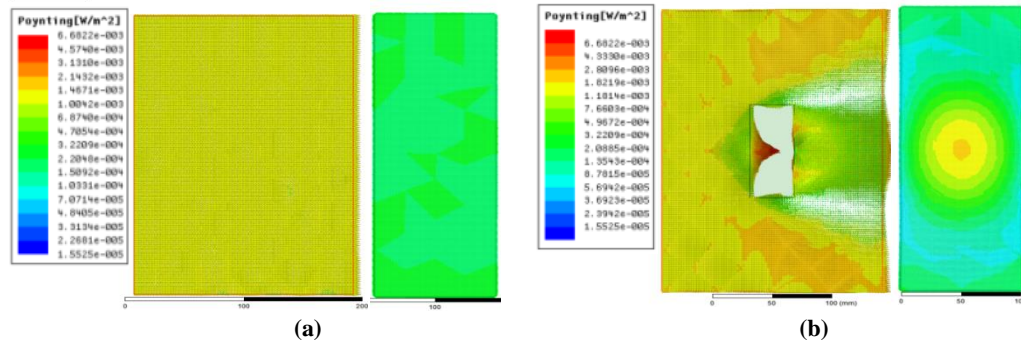


Fig. 4-8. Poynting vector for (a) propagating plane wave in the air; side view (left), front view (right) (b) incident plane wave upon the 180° phase shifter; side view (left), front view (right)

4 - 4 Patch Gain Enhancement

In this section, the phase shifting concept discussed earlier in this chapter is applied to a patch antenna in order to improve its gain. In fact, the energy emitted by the antenna is spatially re-distributed resulting in a higher gain antenna. To do so, a simple inset fed rectangular patch antenna with resonance frequency of 10.7 GHz is designed. Next, a layer of material with refractive index of 3 and the impedance matched to the air is theoretically defined and placed on the top of the patch antenna. The thickness of the layer is set equal to the quarter wavelength of the patch resonance frequency. This thickness causes 180° phase difference between the wave propagating through the slab and the wave propagating in the air. The simulated structure is shown in Fig. 4-9.

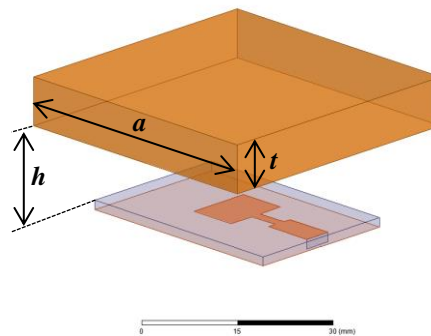
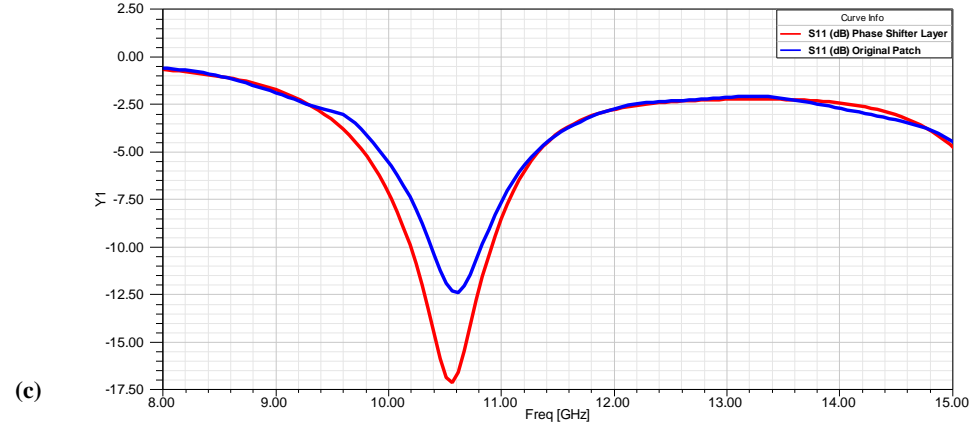
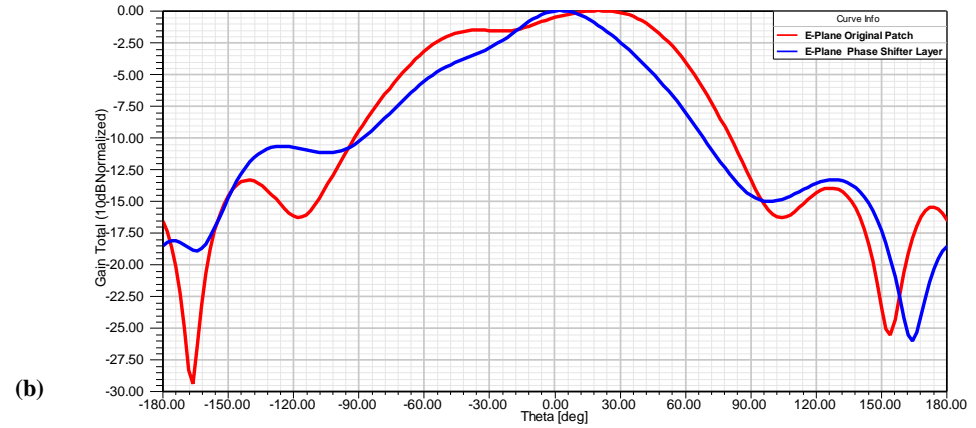
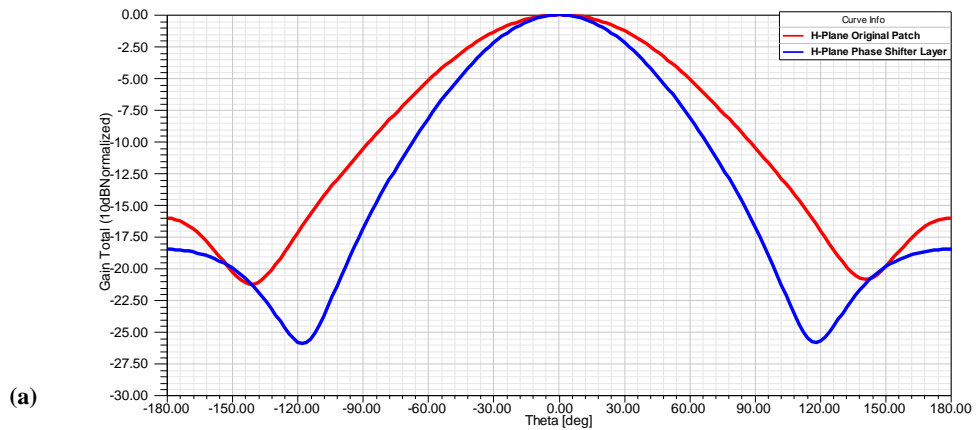


Fig. 4-9. Simulated structure

The full wave simulations of the patch with and without the 180° phase shifter layer are shown in Fig. 4-10. The simulation results confirm that the 180° phase shifter slab placed on the top of patch can improve the antenna gain by 1.7 dBi .



(c)

Quantity	Original Patch	Enhanced Patch
Peak Gain (dBi)	6.91	8.64
Radiation Efficiency	0.995	0.989
Front to Back Ratio		
Ground plane size	117.37	66.31
26.1 mm×37.8 mm		

(d)

Fig. 4-10. Normalised gain in (a) H-plane patterns, (b) E-plane patterns, (c) return loss (d) table of antenna parameters

The propagating wave through the slab is concentrated along the normal direction forming a highly directive emission. The effect of the phase shifter slab on the energy flow can be traced by visualisation of Poynting vector, shown in Fig. 4-11. It can be seen that the energy flow at the edges of the slab, where the out of phase waves meet, is bending toward the centre.

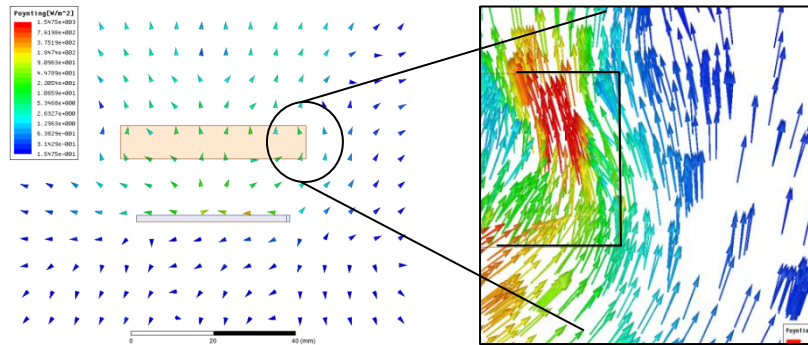


Fig. 4-11. Visualisation of real part of Poynting vector for a slab of 180° phase shifter placed on top of patch antenna

One can also argue that the slab acts as a lens which concentrates the propagating wave toward a focal point. To address this argument, a second structure has been simulated but this time the layer is defined to have constitutive parameters of $\epsilon_r = 3$ and $\mu_r = 1$. The new layer will not give 180° phase shift and also its impedance is not perfectly matched to the impedance of free space. The simulation result for this situation is shown in Fig. 4-12.

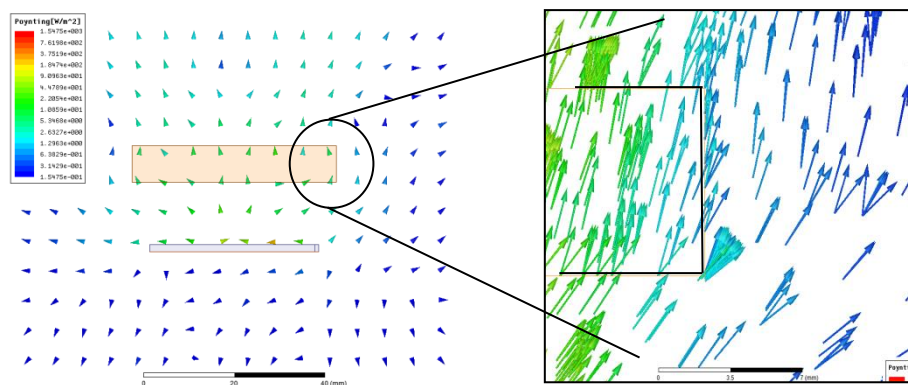
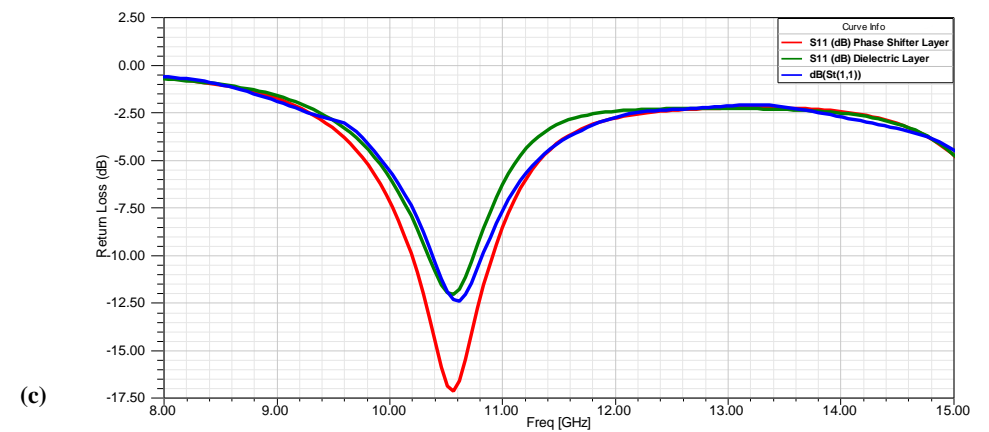
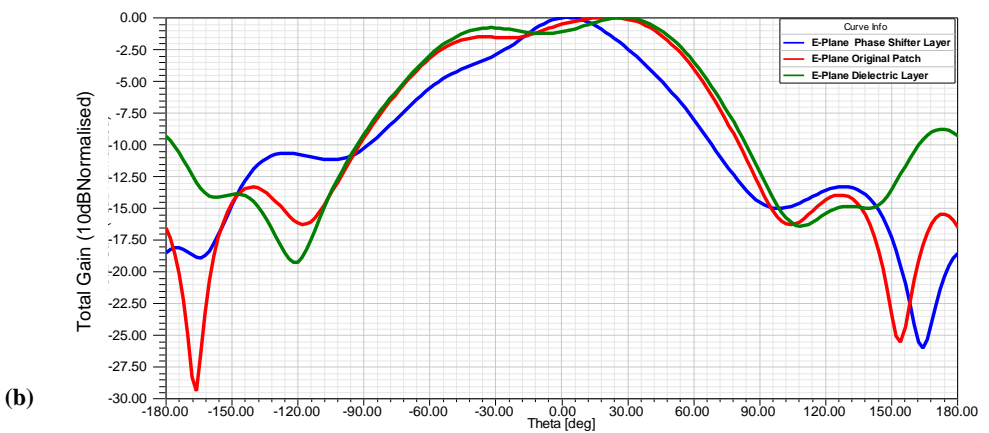
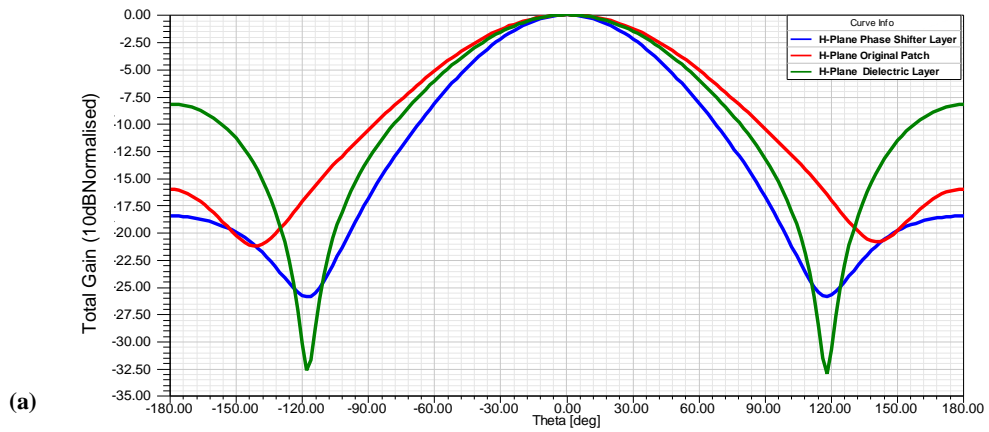


Fig. 4-12. Visualisation of real part of Poynting vector for a slab of ordinary dielectric placed on top of patch antenna

A comparison between the radiation patterns, return loss and antenna parameters of the phase shifter slab, dielectric slab and original patch has been made in Fig. 4-13.



Quantity	Original Patch	Dielectric Enhancement	Phase Shifter Enhancement
Peak Gain (dBi)	6.91	7.37	8.64
Radiation Efficiency	0.995	0.988	0.989
Front to Back Ratio			
Ground plane size	117.37	23.19	66.31
26.1 mm×37.8 mm			

(d)

Fig. 4-13. (a) Normalised gain in H-plane, (b) Normalised gain in E-plane, (c) return loss (d) table of antenna parameters

The dielectric layer is shown to act as a lens and increases the antenna gain. However, gain improvement using the 180° phase shifter slab is far more than what can be achieved by an ordinary dielectric. In the case of the dielectric slab, the front to back ratio significantly decreases as the result of the impedance mismatch between the air and dielectric.

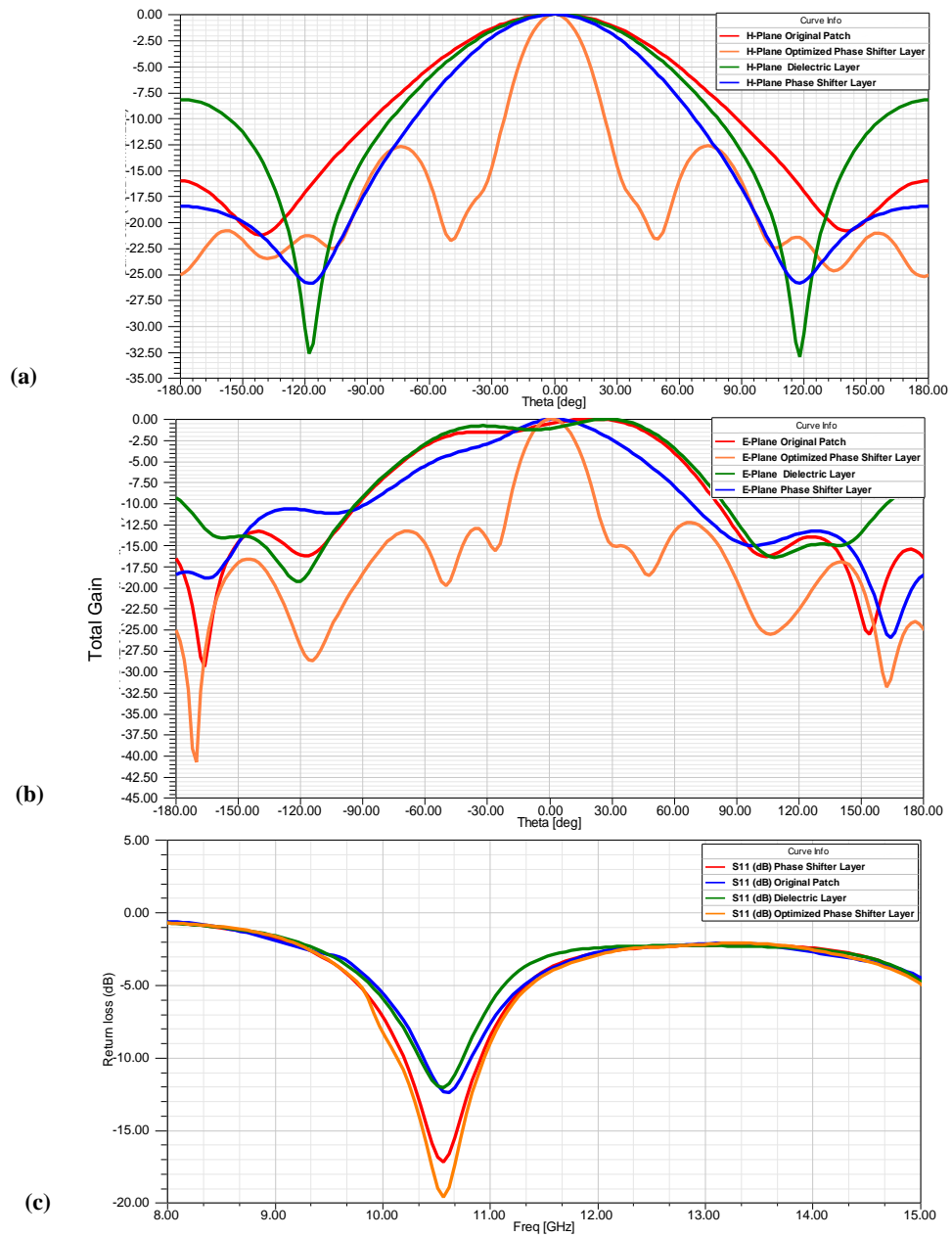
4 - 5 Design Optimisation

The structure design was further optimised by use of a Genetic Algorithm (GA) to achieve the maximum possible gain enhancement. A cost function is defined to maximise the total gain along the normal direction to the patch. Initial design values and final optimised design values are reported in Table 4-1.

Parameters		Initial Design Values (mm)	Final Design Value (mm)
Slab Width	a	60	45.69
Slab Length	a	60	45.69
Slab Thickness	t	7	8.17
Distance from Antenna	h	10	15.54

Table 4-1. Optimisation parameters, initial and final values

Using optimised dimensions for the slab a significant gain enhancement as high as 15 *dBi* can be achieved. It also gives a reduced return loss at resonant frequency. Fig. 4-14 shows simulation results for the optimised design.



Quantity	Original Patch	Dielectric Enhancement	Phase Shifter Enhancement	Optimised Phase Shifter
Peak Gain	6.91	7.37	8.64	15
Radiation Efficiency	0.995	0.988	0.989	~0.999
Front to Back Ratio				
Ground plane size	117.38	23.19	66.31	319.05
26.1 mm×37.8 mm				

(d)

Fig. 4-14. Simulation results for optimised design (a) normalised gain in H-plane, (b) normalised gain in E-plane, (c) return loss, (d) table of antenna parameters

Normalised radiation patterns illustrate very highly directive emission in both E- and H- planes. It is noted that the wave emitted from the patch is not a plane wave at the distance where the slab is placed. This is so that the slab thickness of 8.17 mm (which is more than the theoretically calculated thickness of 7 mm i.e., $\lambda/4$) provides the maximum possible directivity.

4 - 6 Metamaterial Realisation of the Phase Shifter Layer

Up to now, the ability of the wave interference concept to simplify the design of highly directive emission has been studied. A 180° phase shifter slab was designed and shown to theoretically enhance the directivity of the patch antenna. Next, a practical design of 180° phase shifter was investigated.

While the unit cell of a metamaterial can be made considerably smaller than the free space wavelength, there remains a significant variation of the phase across the unit cell at operational frequencies in nearly all metamaterial structures reported to date [138]. W. Eccleston in [139] showed that when left-handed and right-handed unit cells are alternatively cascaded, a relatively frequency insensitive zero phase shift can be achieved by a finite length guiding structure [139]. This phenomenon is termed “infinite wavelength” [140]. Using a similar technique, the phase advance over the metamaterial unit cell can be used to generate 180° phase shift.

Ideally, a unit cell which causes $\Delta\varphi$ phase shift at a particular frequency can be cascaded to form a structure with the total phase shift equal to the phase shift obtained by each individual cell multiplied by the number of cells. However, tessellating metamaterial cells introduces new design concerns like mutual coupling between adjacent cells which must be taken into account. It must be noted that the mutual coupling between adjacent cells might become dominant over the individual cell properties which leads to invalidation of the cascading technique. The ratio between the unit cell size and the scattering element within the cell needs to be kept low to lessen the mutual coupling effect between two adjacent cells. Most of the recently proposed metamaterial structures have made of scattering elements whose size are an appreciable fraction of the operational wavelength which allows one to model the metamaterial media as an effective medium with constructive parameters ϵ and μ [138].

In the design of the 180° phase shifter slab, the size of the unit cell is kept as small as around one-tenth of the free space wavelength ($< \lambda_0/10$) to satisfy the effective medium condition and also minimise the mutual coupling effects. The design flowchart for metamaterial realisation of the 180° phase shifter and its integration to a patch antenna is shown in Fig. 4-15. The procedure involved three steps:

- 1-Design of unit cell
- 2-Design of 180° phase shifter slab
- 3-Design of antenna system

At the first step the unit cell is designed and its one-dimensional dispersion diagram and impedance are extracted. Then the unit cell is optimised to exhibit the desired phase advance and impedance (i.e., matched to the impedance of free space). Next the 180° phase shifter slab, formed by cascading optimised unit cells is simulated and the phase shift over the slab is extracted. The slab is excited by a plane wave and the similarity of its behaviour with the theoretical model of slab, shown in Fig. 4-8, is investigated. Finally, the highly directive antenna system comprises the designed 180° phase shifter placed on top of the patch antenna which was simulated and the results are discussed below.

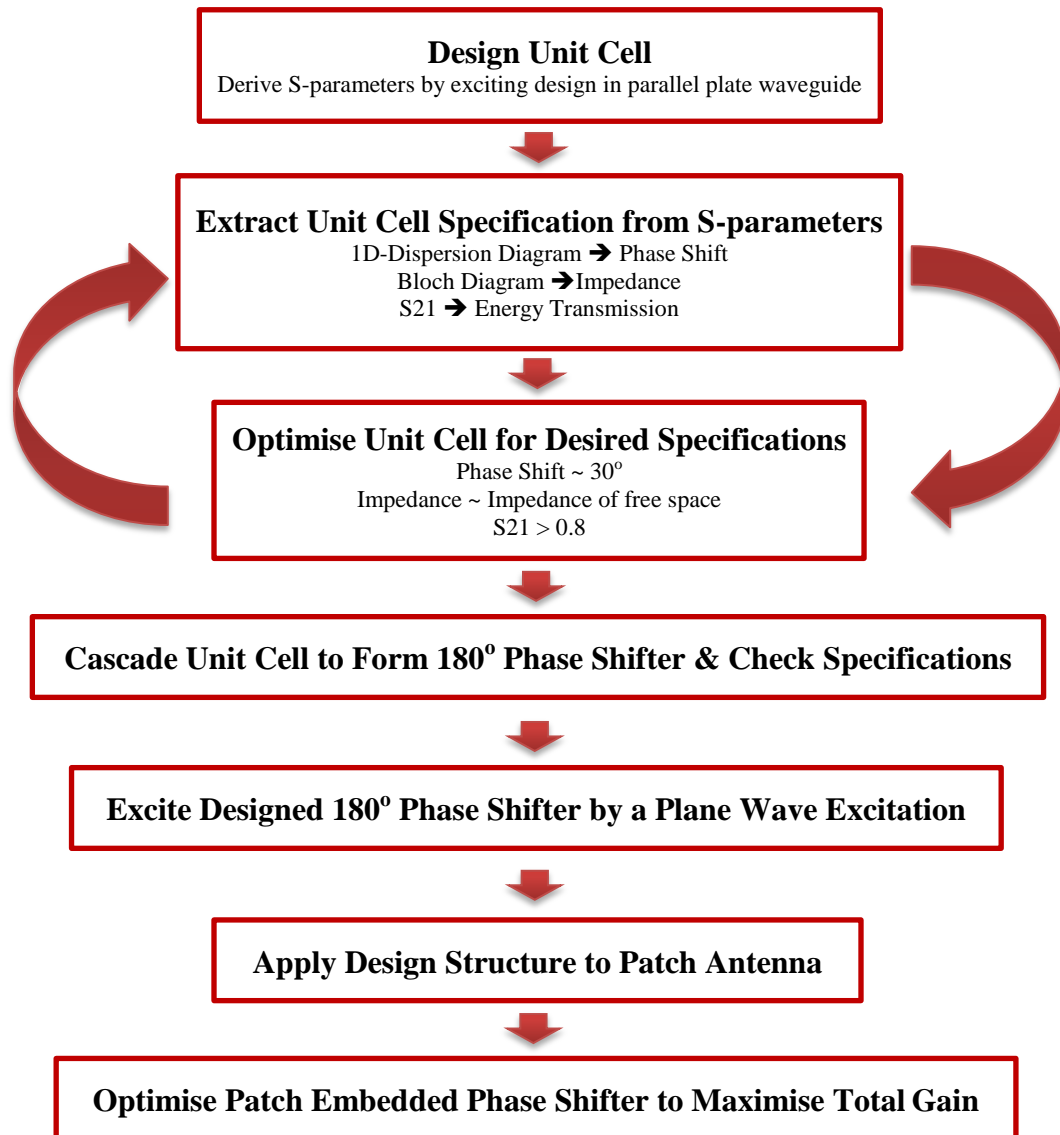


Fig. 4-15. Design flowchart

4 - 6 - 1 Unit Cell Design and Simulation Setup

To obtain 180° phase shift, six metamaterial unit cells were cascaded where each individual cell exhibited 30° phase advance. A broadside coupled capacitively loaded ring resonator (CLRR) made of copper [47] was utilised as the building block. The geometry of the CLRR unit cell is illustrated in Fig. 4-16.

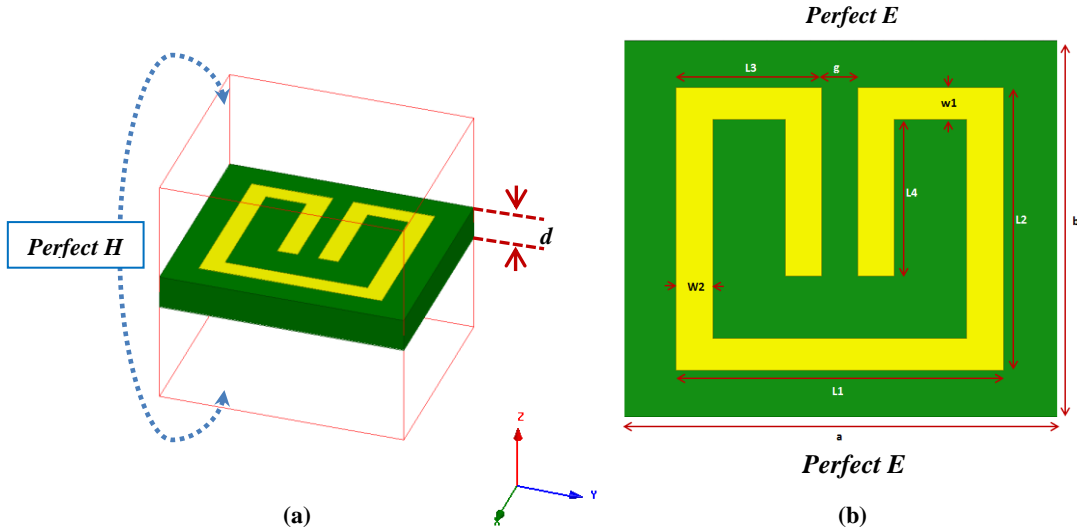


Fig. 4-16. CLRR (a) unit cell geometry, (b) unit cell top view, nominal dimensions are $a=b=3\text{mm}$, $L_1=L_2=2.4\text{mm}$, $W_1=W_2=0.3\text{mm}$, $g=0.5\text{mm}$, $d=0.4\text{mm}$ and $L_4=1.2\text{mm}$

The CLRR element is resonant with the resonant frequency determined mainly by the loop inductance and the capacitance of the strips. Referring to Fig. 4-16, the cell size along the x- and y-axis are both set to $a = b = 3\text{mm}$, the scattering element length and width are $L_1 = L_2 = 2.4\text{mm}$, respectively. The x-depth of the capacitive strip is $L_4 = 1.2\text{mm}$ and finally the copper trace width for parallel and normal to the incident E-field are $W_1 = W_2 = 0.3\text{mm}$. The scattering element is designed to be embedded on the Rogers RT/duroid 5880, a low loss dielectric characterised with $\epsilon_r = 2.2$, $\mu_r = 1.0$ and $\tan\delta_{loss} = 0.0009$ [47].

The unit cell is simulated inside an ideal parallel-plate waveguide from which the complex reflection and transmission coefficients are calculated. The perfect electric and perfect magnetic boundary conditions are applied to the lateral walls in the x- and z-direction, respectively. Two wave ports were placed in the y-direction with the E-field defined along the x-direction. Next, the results obtained from simulation were used to calculate the phase advance over the CLRR unit cell.

4 - 6 - 2 Dispersion Diagram Extraction

The one-dimensional dispersion can be derived by substituting complex reflection and transmission coefficients (S-parameters) matrices into the dispersion relation. The S-parameters are obtained by ANSYS HFSS using the driven mode solution

approach. This method is fast but it can only show quasi-TEM modes excited by the defined ports. The dispersion relation is given by:

$$\beta_{cell} = \cos^{-1} \left(\frac{1 - S_{11}S_{22} + S_{21}S_{12}}{2S_{21}} \right) \quad (4-50)$$

Meanwhile the phase advance of a wave traveling the same distance but through the air can be calculated:

$$\beta_{air} = \frac{2\pi \times a \times f_0}{c_0} \quad (4-51)$$

Where, a is the cell thickness, f_0 is the frequency of the wave and c_0 is the speed of light in the free space. Now, the phase difference between propagating waves through the cell and the surrounding air can be written as:

$$\Delta\varphi = |\beta_{cell} - \beta_{air}| \quad (4-52)$$

The one-dimensional dispersion diagram (Fig. 4-17.a) shows the structure resonates within the simulated frequency range. It also shows that the unit cell has a band-gap at frequencies higher than the frequency of interest.

4 - 6 - 3 Bloch Impedance Extraction

Impedance matching between the unit cell and the free space (air) is another concern that must be considered in the design of the unit cell. The complex wave impedance of a medium is strongly related to the flux of energy of the wave propagating in the medium [141]. Mismatch between the free space and the unit cell impedance results in undesired reflections from the metamaterial structure which reduces the power of the wave propagating through the cell.

Bloch impedance is the ratio between the voltage and current at the terminal of the periodic structure and can be calculated from the S-parameters as below [142]:

$$Z_{cell} = \frac{2jZ_o S_{21} \sin(\beta_{cell})}{(1 - S_{11})(1 - S_{22}) - S_{21}S_{12}} \quad (4-53)$$

Where, Z_o is the impedance of free space and is equal to $\sqrt{\mu_0/\epsilon_0} = 376.7 \Omega$. The Bloch impedance diagram is plotted to confirm that the designed unit cell is matched to the system impedance (i.e., the free space impedance).

The simulation results for the nominal dimensions of the unit cell are shown in Fig. 4-17. The dispersion diagram shows that the unit cell has a band-gap at frequencies higher than the frequency of interest. The matching capability of the unit cell can be evaluated from S-parameters and impedance diagrams shown in Fig. 4-17.b) and c). At the frequency of interest (i.e., 10.7 GHz), the unit cell shows a return loss less than 0.1 and a real impedance of 409 Ω and an imaginary part of $-0.5j$ which is fairly small. The phase shift obtained from the proposed unit cell based on the formulation given in (4-52) is shown in Fig. 4-17d).

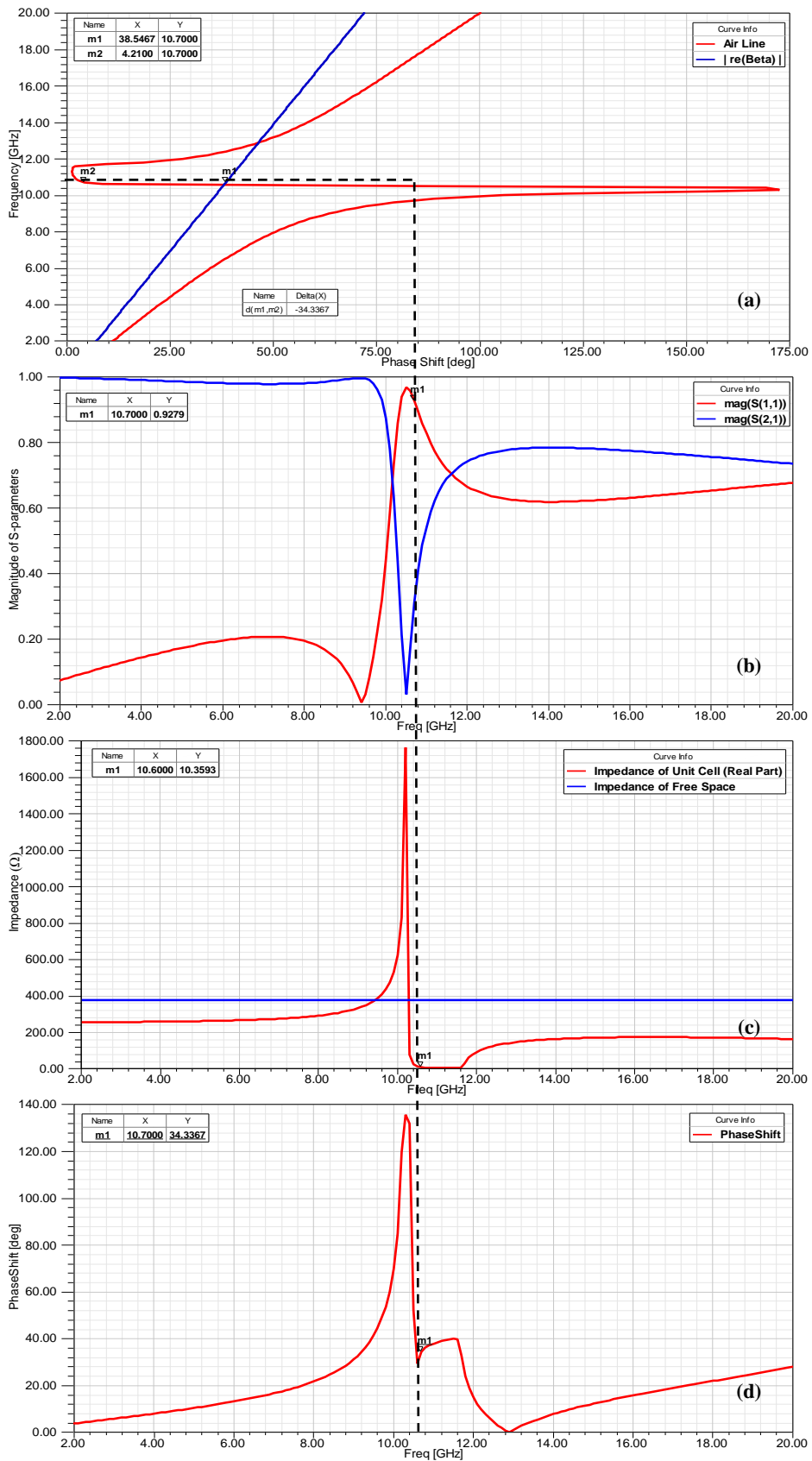


Fig. 4-17. CLRR simulation results (a) dispersion diagram, (b) S-parameters, (c) Bloch impedance (d) phase shift

4 - 7 Cascading Topology

The propagation constant is a well-known applied concept in the design of two-port networks such as filters which usually use a cascaded section topology. In a cascaded topology (Fig. 4-18) the propagation constant, the attenuation constant and the phase constant of individual sections can be simply added up to find the total propagation constant, attenuation constant and phase constant of the entire structure [143]. A cascaded topology block diagram is shown in Fig. 4-18.a). The output to input voltage ratio for each network is equal to:

$$\frac{V_1}{V_2} = \sqrt{\frac{Z_{i1}}{Z_{i2}}} e^{\gamma_1} \quad (4-54)$$

$$\frac{V_2}{V_3} = \sqrt{\frac{Z_{i2}}{Z_{i3}}} e^{\gamma_2} \quad (4-55)$$

$$\frac{V_{n-1}}{V_n} = \sqrt{\frac{Z_{i(n-1)}}{Z_{in}}} e^{\gamma_n} \quad (4-56)$$

Where, $\sqrt{\frac{Z_{in}}{Z_{im}}}$ are the impedance scaling terms. The overall voltage ratio can be written as:

$$\frac{V_1}{V_n} = \frac{V_1}{V_2} \times \frac{V_2}{V_3} \times \dots \times \frac{V_{n-1}}{V_n} = \sqrt{\frac{Z_{i1}}{Z_{in}}} e^{\gamma_1 + \gamma_2 + \gamma_3 + \dots + \gamma_n} \quad (4-57)$$

Therefore for n-cascaded unit cells all having matched impedance and facing each other, the total propagation constant is equal to:

$$\gamma_{Tot} = \gamma_1 + \gamma_2 + \gamma_3 + \dots + \gamma_n \quad (4-58)$$

Fig. 4-18.b) represents a block of six cascaded unit cells which form the 180° phase shifter slab. Here, a phase shift of 30° occurs over each individual cell. A 30° phase shift has been chosen for each individual cell because of the gradient of the Bloch impedance and also the gradient of the phase shift diagram is less compared

to a cell with a higher phase shift. As can be seen in Fig. 4-17.b) and Fig. 4-17.d) , slower changes in the phase shift and the impedance of the unit cell over frequencies around the frequency of interest provide wider bandwidth performance. Referring to Fig. 4-17.d), the peak of the phase shift diagram occurs at the resonant frequency. Losses due to resonance of the cell can be avoided by designing a cell to work at frequencies far from the frequency of resonance. For the proposed cell, 30° phase shift happens just before the resonant frequency of the cell providing a low imaginary part of the impedance and consequently, low losses associated with the structure's resonance. Cells with lower phase shift also can be designed at the cost of cascading more unit cells which introduces more complexity into the simulation and fabrication.

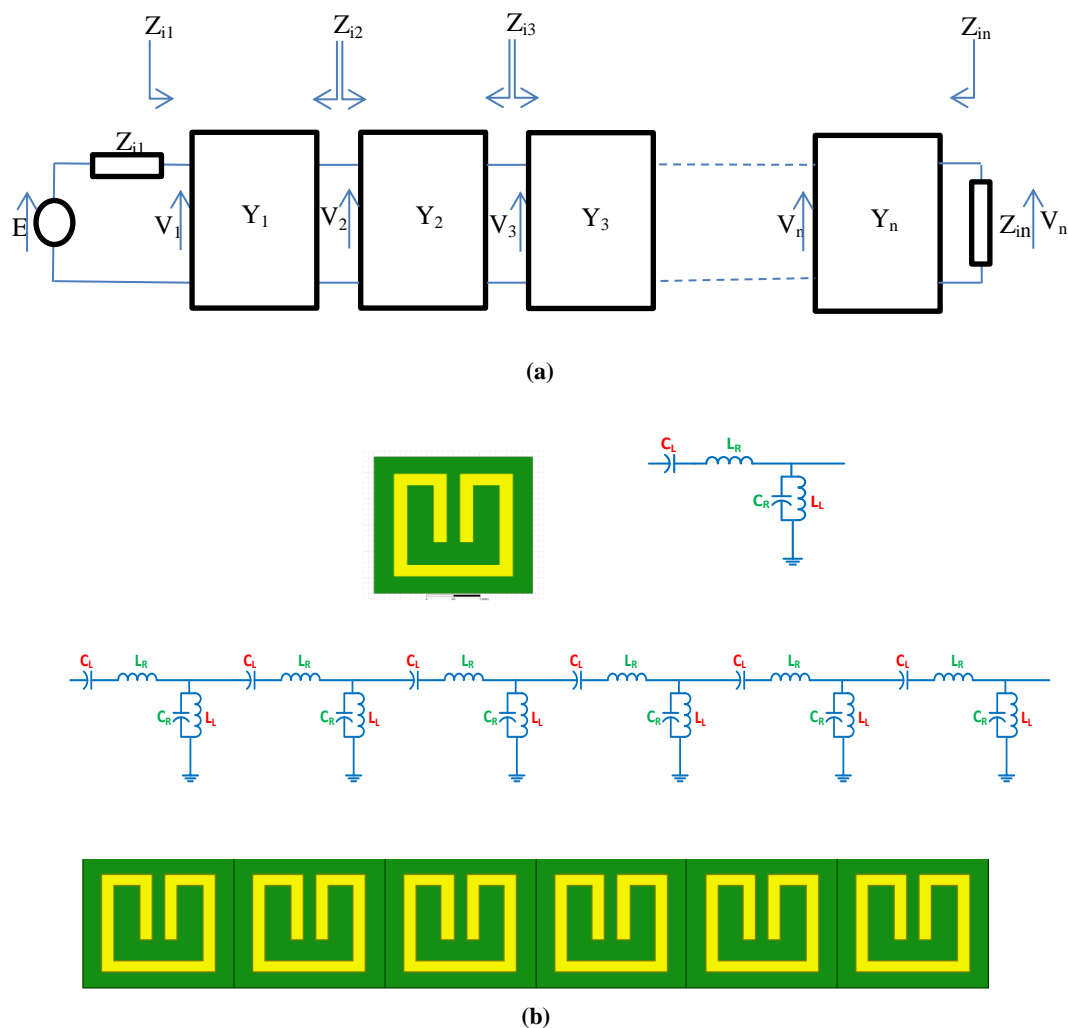


Fig. 4-18. (a) Cascading Topology (b) Metamaterial realization of a 180° phase shifter

4 - 8 Unit Cell Optimisation

The 180° phase shift involves six unit cells where each cell contributes 30° phase shift. The GA was used to optimise the CLRR unit cell to exhibit 30° phase shift while its impedance perfectly matched to that of air.

4 - 8 - 1 Applying GA Optimisation to CLRR

For our purposes, a matrix with each row corresponding to a chromosome representing the population and a cost function was defined. The geometry parameters are the input to GA. All independent physical dimensions except the substrate thickness were subject to optimisation. The substrate thickness was 0.381mm , which is one of the standard thicknesses for Rogers RT/duroid 5880. The cost function evaluates the difference between the phase shift of the simulated cell and the desired phase shift (i.e., 30°) as well as the difference between the cell impedance and the air impedance and finally the transmitted wave amplitude (i.e. S_{21}). The cost function is given by:

$$\text{cost}(X) = \frac{||\text{re}(\beta) - 30^\circ|}{30^\circ} + \frac{|\text{re}(Z_b) - Z_o|}{Z_o} + 0.8 \times ||S_{21}| - 1| \quad (4-59)$$

Where X is the array of simulated cell dimensions:

$$X = [a, b, L_1, L_2, L_4, w_1, w_2, g] \quad (4-60)$$

Table 4-2 shows the initial geometry parameters and their final optimised values.

Variable		Initial Design (mm)	Final Design (mm)
Unit-cell width	a	3	3
Unit-cell length	b	3	2.7
Scattering object width	L₁	2.4	2.3
Scattering object length	L₂	2.4	2
Capacitive strip length	L₄	1.2	0.9
Vertical copper trace	w₁	0.3	0.2
Horizontal copper trace	w₂	0.3	0.2
gap	g	0.5	0.3

Table 4-2. Unit Cell optimisation parameters, initial and final values

The S-parameters for each member of the population were obtained by ANSYS HFSS full wave simulation. These S-parameters were exported to MATLAB to

calculate the phase shift, the Bloch impedance and eventually the cost that was used in the GA optimisation. This procedure continued until the calculated cost was lower than the acceptable cost. The simulation results for optimised CLRR is shown in Fig. 4-19.

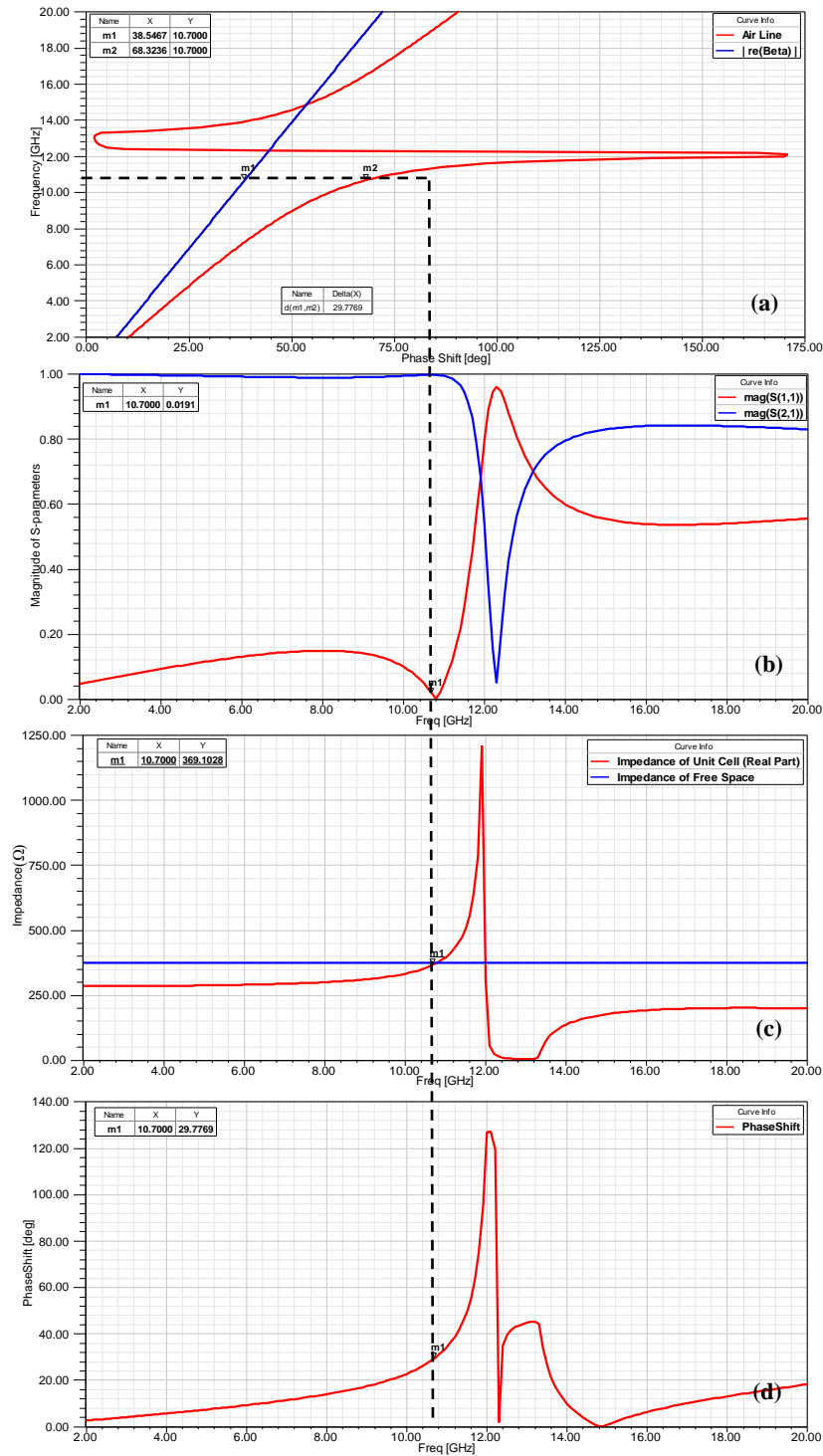


Fig. 4-19. Optimised CLRR cell (a) dispersion diagram (b) S-parameters (c) bloch impedance (d) phase shift

Fig. 4-19.a) and d) show that the optimised unit cell expresses the phase shift of almost 30° at frequency of 10.7 GHz . A perfect impedance matching to the air can also be observed from results shown in Fig. 4-19.b) and c). six unit cells were cascaded (Fig. 4-18) to form the 180° phase shifter metamaterial realisation. Simulation results are shown in Fig. 4-20.

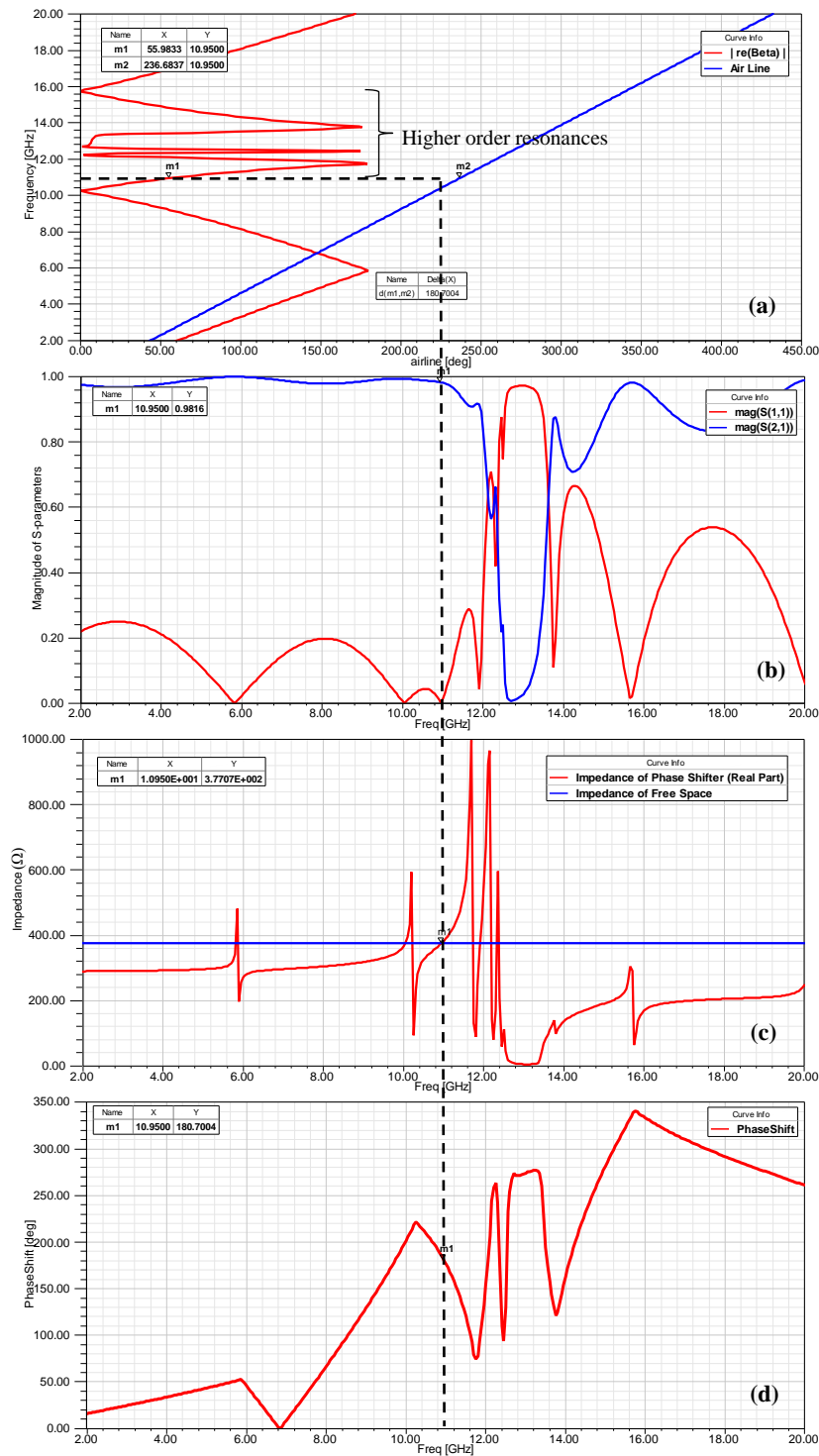


Fig. 4-20. 180° phase shifter, (a) dispersion diagram (b) S-parameters (c) Bloch impedance (d) phase shift

Based on argument made earlier in the cascading topology section, a phase shift of 180° is expected at frequency of 10.72 GHz where each individual cell shows 30° phase shift. Despite this fact, it is indicated by the dashed line in Fig. 4-20.d)

that 10.95 GHz is the frequency point at which the phase shift of 180° can be obtained. This shows a 230 MHz or 2% shift in frequency.

This shift in frequency could be related to minor resonances that occur below the frequency of interest. These resonances can be seen clearly in Fig. 4-20.a and Fig. 4-20.b) and are associated with mutual coupling between adjacent cells. The mutual coupling effect can be reduced further by using a substrate with a higher dielectric constant as well as decreasing the size ratio between the scattering element within the unit cell and the unit cell itself. Apart from the frequency shift, the Bloch impedance and transmitted wave amplitude are quite satisfying and agreed with what was expected from a cascading topology.

4 - 9 Interaction between the Metamaterial based 180° Phase Shifter and a Plane Wave

Eight 180° phase shifters were tessellated to form a larger slab shown in Fig. 4-21. The incident wave was a plane wave with E-field polarised along the x-axis and propagation along the y-axis. Referring to Fig. 4-21.a), the wave propagating from point A to point B (named Ψ_1) through the metamaterial structure has a phase advance of 53.39° , while the wave traveling from point C to point D (named Ψ_2) through the air has a phase advance of 236° resulting in a phase difference of 180° between Ψ_1 and Ψ_2 . Energy will push into the area in front of the structure due to destructive interference between Ψ_1 and Ψ_2 at the top and bottom edges of the structure front face.

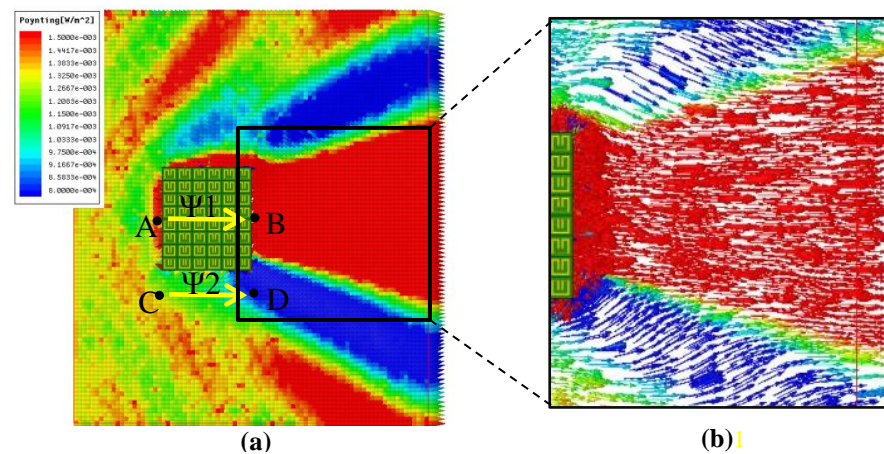


Fig. 4-21. Plane excitation of 180° phase shifter structure, (a) uniform Poynting vector (b) non-uniform Poynting Vector

4 - 10 Patch Gain Enhancement using Metamaterial based 180° Phase Shifter

Following the design in section 4 - 3 of a theoretically defined 180° phase shifter, the metamaterial realisation of a 180° phase shifter is placed on top of the patch antenna to assess any improvement in the antenna directivity. To do so, five slabs of 180° phase shifter which were illustrated in section 4 - 9 , were used to form a large block. Then, this block was placed on top of the patch antenna as shown in Fig. 4-22.a). The slabs were laid along the patch E-plane where the E-field is parallel to scattering elements and the H-field is perpendicular to the scattering elements plane. This particular positioning satisfies the conditions that were used to design the CLRR unit cell i.e., the waveguide simulation. Due to the complexity of the geometry, simulation of an embedded patch requires a huge amount of time and computing resources.

Fig. 4-22.b) shows a second design where eight slabs were used to form a larger block with slab lengths expanded to be the same length as the theoretical slab specified in section 4 - 3 . Both the first and second designs showed significant improvement in the antenna gain by factors of 3 *dBi* and 6.5 *dBi*, respectively. The maximum gain of 13.56 *dBi* was achieved with the larger 180° phase shifter block comprised of eight phase shifter slabs. This maximum gain is less than the maximum gain of 15 *dBi* reported in section 4 - 3 for the theoretically defined 180° phase shifter slab. The difference between maximum gains in the theoretical and practical design could be due to:

- 1- Unlike the theoretical 180° phase shifter slab, the metamaterial cells are inherently anisotropic structures. This means that the desired phase shift happens whenever required boundary conditions are satisfied and the structure is excited in an appropriate direction. For instance, in the presented design the E-fields must be along the scattering elements i.e., y-axis, the H-fields perpendicular to the scattering element plane i.e., x-axis and the excitation along the z-axis. Assuming the wave vector \vec{k} , which demonstrates the direction of propagation is represented by its component along the coordinate system unit vectors, i.e., \vec{k}_x , \vec{k}_y and \vec{k}_z , then only \vec{k}_z

which satisfies the simulation condition will interact with the proposed metamaterial phase shifter.

- 2- The resonant nature of metamaterial cells causes inherent losses which degrade the power of a propagating wave, however, to avoid resonant losses for the proposed phase shifter structure, the operating frequency (i.e., 10.95 GHz) is defined to be far from the resonant frequency (i.e., 12.3 GHz). The corresponding imaginary part of the wave impedance and its associated losses at operating frequency remains fairly small.

However, in the case of the proposed phase shifter block, the lower maximum directivity in the practical design is mostly related to the first of these reasons while the second reason is not a matter of concern. Simulation results of the metamaterial phase shifter embedded patch are shown in Fig. 4-22.

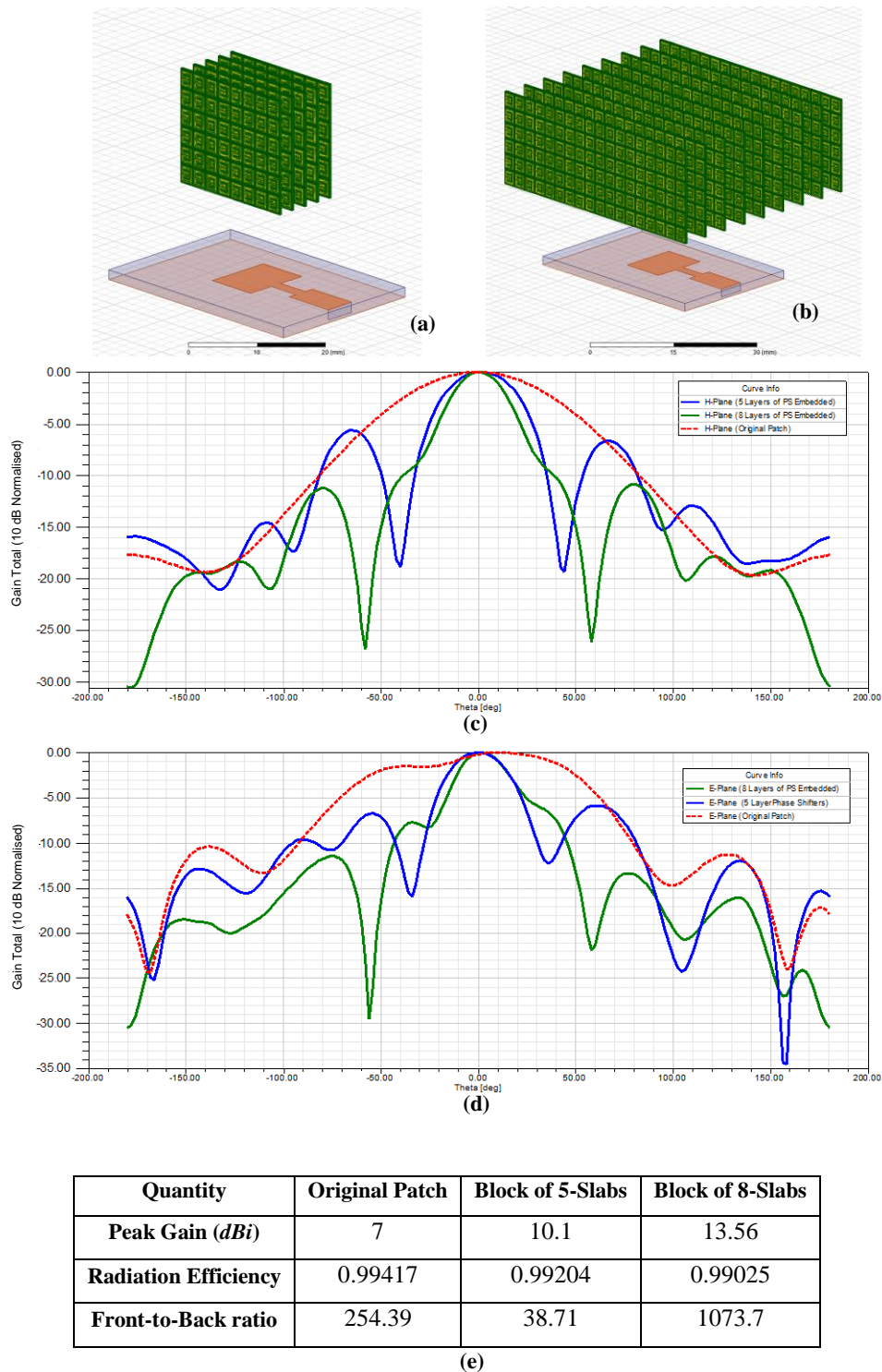


Fig. 4-22. The practical design with block of (a) 5 and, (b) 8 phase shifter slabs (c) normalised H-plane radiation pattern (d) normalised E-plane radiation pattern (e) antenna parameters

The 180° phase shifter larger block embedded patch antenna is simulated for some specific frequencies between 9 and 12 GHz. Simulation results are shown in Fig. 4-23.

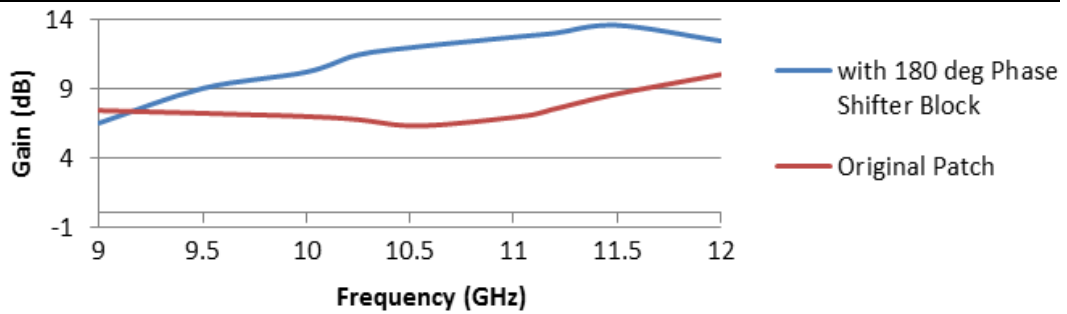
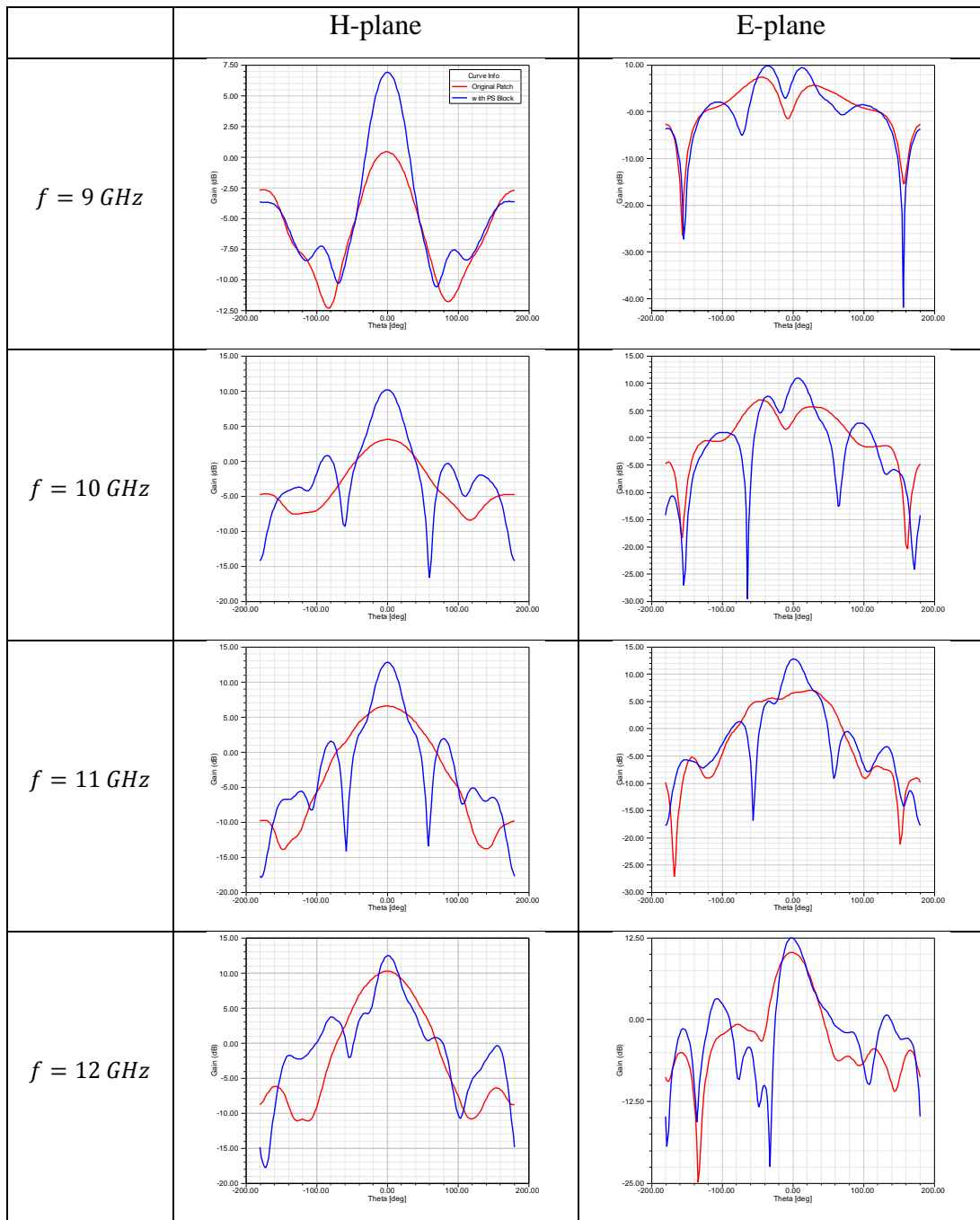


Fig. 4-23. Radiation pattern of original and 180° phase shifter block

Since running the simulation for each frequency point would take several days, a simpler convergence condition was defined -when the stopping criteria for the adaptive path solutions was set to 5% difference in the magnitude of the energy of two successive solutions- to shorten the simulation time. Usually, accurate results are obtained when the stopping criteria is set to 2% difference between the magnitude of the energy between two successive solution. Therefore, the antenna gain values may not be securely accurate values.

4 - 11 Fabrication and Measurements

The same procedure explained in section 3 - 8 - 2 was followed to fabricate the patch antenna and the 180° metamaterial phase shifter. The fabricated antenna and metamaterial phase shifter are presented in Fig. 4-24.

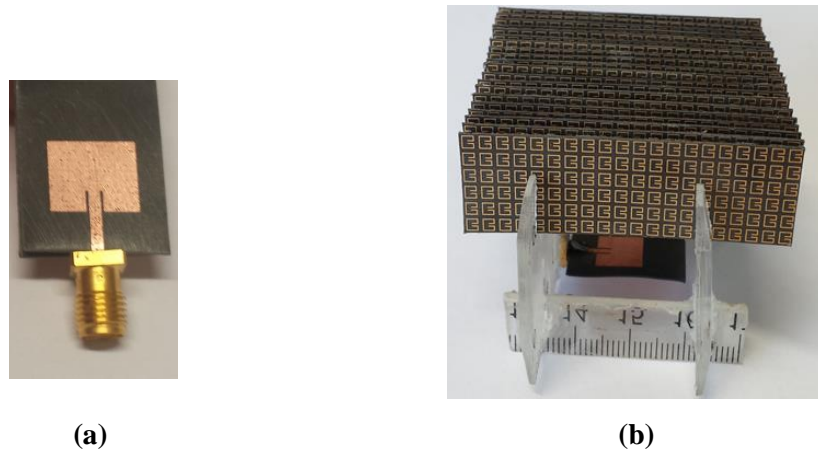


Fig. 4-24. Fabricated antennae, (a) patch, (b) patch with 180° metamaterial phase shifter

A vector network analyser (Agilent Technologies N5230A) was used to measure the return loss for the patch antenna with and without metamaterial phase shifter. Then, the patch antenna was connected to port 1 as a transmitter antenna and a horn antenna (ETS.LINDGREN 3115) was connected to port 2 as a receiver antenna. The distance between the antenna and the receiver horn was set to half a meter to ensure measurement of the antenna far field. The measured values for S_{11} and S_{21} are shown in Fig. 4-25.

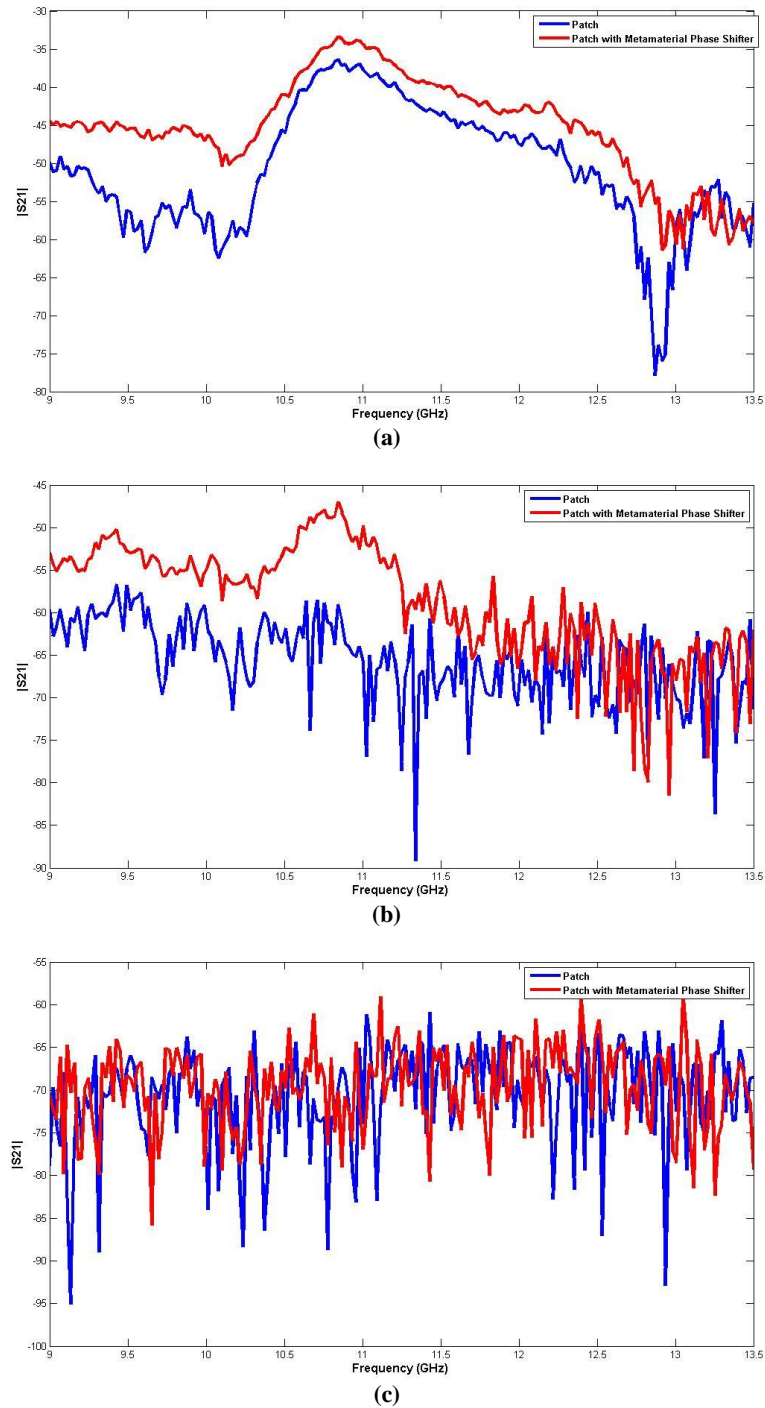


Fig. 4-25. Measured values for patch antenna with and without metamaterial phase shifter, (a) $|S_{21}|$ at $\varphi = 0^\circ$, (b) $|S_{21}|$ at $\varphi = 30^\circ$, (c) $|S_{21}|$ at $\varphi = 45^\circ$

As expected, S_{21} was increased by using the metamaterial phase shifter. Fig. 4-25.a) and b) show gain enhancement of up to 10 *dB* at angles of $\varphi = 0^\circ$ and $\varphi = 30^\circ$ in the azimuth plane.

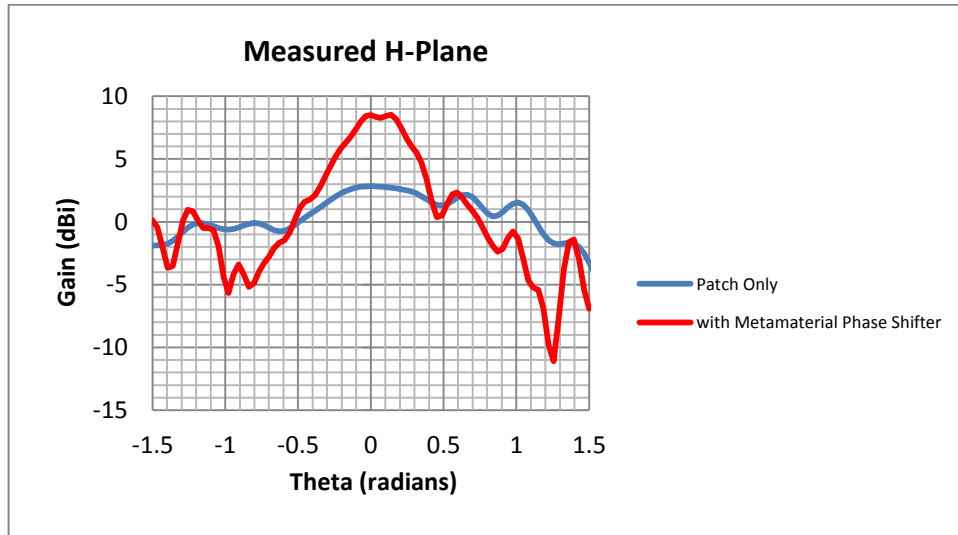
4 - 12 Summary

In this chapter, the wave interference and the energy spatial distribution for interfering waves were studied. Interference between two plane waves with equal intensity, frequency, and polarisation axis but 180° phase difference were investigated. Since Gaussian waves are representing more physical wavefront especially for a region closer to the radiator, the interference between two Gaussian waves with equal intensity, frequency, and polarisation axis but 180° phase difference were also studied. The effect of phase difference between interfering waves on the energy distribution in space were mathematically studied and numerically illustrated. It was shown that highly directive emission can be achieved when two interfering waves with equal intensity, frequency, polarisation axis but 180° phase difference are propagating along the same direction.

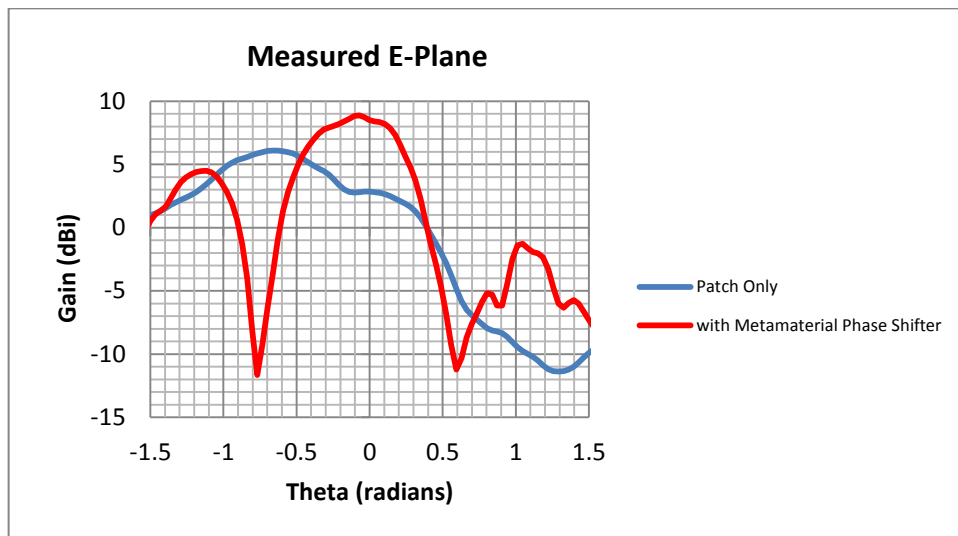
A new technique was developed based on the wave interference phenomenon to define required spatial properties for a metamaterial lens slab.

A hypothetical lens slab was defined to provide 180° phase shift (i.e., $\epsilon_r = \mu_r = 3$) between waves propagating through the slab and waves propagating through the surrounding air. Then, the lens slab was placed on top of a patch antenna to increase the antenna gain. A model was set up and simulated using ANSYS HFSS and a genetic algorithm (GA) optimisation method was used to find the best dimensions for the slab. A total gain of 15 dBi was achieved which showed more than 8 dBi gain enhancement. Further, the new method is deployed to design metamaterial realisation of the hypothetical lens slab. The capacitively loaded ring resonator (CLRR) unit cell was used to design a practical model. Each unit cell was designed to shift the phase by 30° by which cascading six unit cells provided 180° phase shift. The proposed phase shifter was tested by a plane wave excitation and the real part of the Poynting vector was used to visualise the energy flow. The metamaterial lens slab was placed on top of the patch antenna to increase its directivity. The simulation results demonstrated a gain of up to 13.56 dBi for the proposed antenna structure which shows almost 6.6 dBi gain enhancement. The maximum gain achieved by the physical metamaterial lens slab is less than the one achieved by the hypothetical lens slab. The difference between maximum gains in the hypothetical and practical design is explained to be primarily due to metamaterial cells being inherently anisotropic structures. Further, the radiation

patterns for the patch antenna with and without phase shifter were measured inside a chamber. The measurement results at frequency of 11 GHz are shown in Fig. 4-26.



(a)



(b)

Fig. 4-26. Measured radiation patterns at 11 GHz, (a) gain in H-plane (dBi), (b) gain in E-plane (dBi)

Measurement results show that the antenna gain could be improved up to 6 dBi using 180° phase shifter. As it can be seen the patch antenna radiation pattern is not symmetric. This is due to a slight bend in the antenna ground plane at the time of measurement. Even more gain enhancement is expected for a patch antenna with a symmetric pattern.

Chapter 5

Bi-reflective Ground Plane

In this chapter, the phase shift concept discussed in the previous chapter is deployed to make a novel directive ground plane which can be used to enhance antenna gain. First, a hypothetical model consisting of a magnetic conductor surrounded by an electric conductor is used to find the optimised ground plane dimensions. Next, electromagnetic band gap (EBG) structures are deployed to design a practical realisation of the proposed ground plane. Both square- and hexagonal-shape mushroom structures are used to form the magnetic conductor.

5 - 1 Introduction

A metal sheet is usually used as a reflector or ground plane in antenna designs [121]. The presence of the ground plane redirects one-half of the radiated power into the opposite direction which ideally increases radiation by 3 *dBi* in one side and partially shields objects on the other side of the ground plane [78]. The current on the antenna conductive surface and the image current on the ground plane are out of phase. In other words, the incident and reflected waves are out of phase. However, there are artificial materials known as magnetic conductors where the conductive current and the image current are in-phase rather than being out of phase. Magnetic conductors are very high impedance structures where the tangential magnetic field is small, even for high electric field along the surface [78]. They reflect an incident wave in-phase allowing the radiating element to lie directly adjacent to the surface without any decrease in radiation efficiency [78]. That is to say, the reflection phase from a perfect electric conductor for a normally incident plane wave is equal to 180° , while the reflection phase from a perfect magnetic conductor for such an incident wave is equal to 0° [147], such that, 180° phase difference can be achieved between two waves where one is reflected from

a metal conductor and the other is reflected from a magnetic conductor. One can expand on the idea of wave interaction explained in Chapter 4 by using electric and magnetic conductors to develop a flat ground plane which can increase the antenna gain and directivity. Such a ground plane is called a bi-reflectonal ground plane.

5 - 2 Theoretical Model

When a plane wave is incident upon a bi-reflectonal ground plane, the waves which are reflected from the metal and the magnetic conductor parts are out of phase. Electric and magnetic conductor surface behaviour can be described by one parameter; the surface impedance. This is also true for textured surfaces in practical designs when the effective model condition is satisfied (i.e., the period of the structure is far smaller than the wavelength). The surface impedance is defined as the ratio of the electric field to the magnetic field at the surface. The smooth electric conductor surface has low impedance but in contrast, a magnetic conductor shows very high surface impedance. This is the reason why the surface waves are eliminated over the magnetic conductor surface which will be discussed later.

As illustrated in Fig. 5-1, in the case of an electric conductor with low impedance, the electric field has a node at the surface while the magnetic field has an anti-node. In contrast, in the case of a magnetic conductor, the electric field has an anti-node and the magnetic field has a node [78].

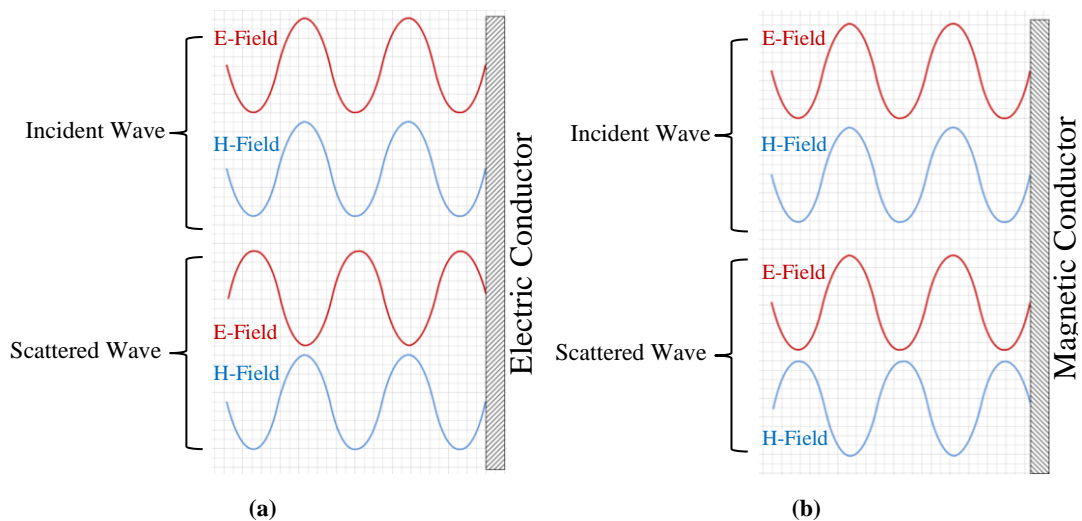


Fig. 5-1. (a) Electric conductor surface; E-field has an anti-node and H-field has a node (b) Magnetic conductor surface; E-field has a node and H-field has an anti-node

Two different scenarios have been considered to model the bi-reflectonal ground plane. In the first model, an electric conductor plane is surrounded by a magnetic conductor plane while, in the second model it is a magnetic conductor which is surrounded by an electric conductor plane.

ANSYS HFSS software was used to model these scenarios. Simply, the Perfect-E boundary condition is used to model the electric conductor. However, to model the magnetic conductor, a planar perfect conductor covered by Perfect-H boundary condition is defined. Here the perfect conductor reflects the incident wave while the Perfect-H boundary condition forces the tangential component of the magnetic field for both the incident and reflected waves to remain the same (i.e., the tangential component of H-field is zero). The model is shown in Fig. 5-2. A Gaussian wave is incident upon both defined bi-reflectonal ground planes and a perfect ground and the reflected power is measured at an evaluation surface, S , for the scattered field using following formula:

$$W = \int_S \text{Re}(\vec{P}) \cdot \hat{n} ds \tag{5-1}$$

Where \vec{P} is the Poynting vector and S is the evaluation surface. Higher energy intensity on top of the ground was observed for the ground in which a magnetic conductor plane was surrounded by an electric conductor plane.

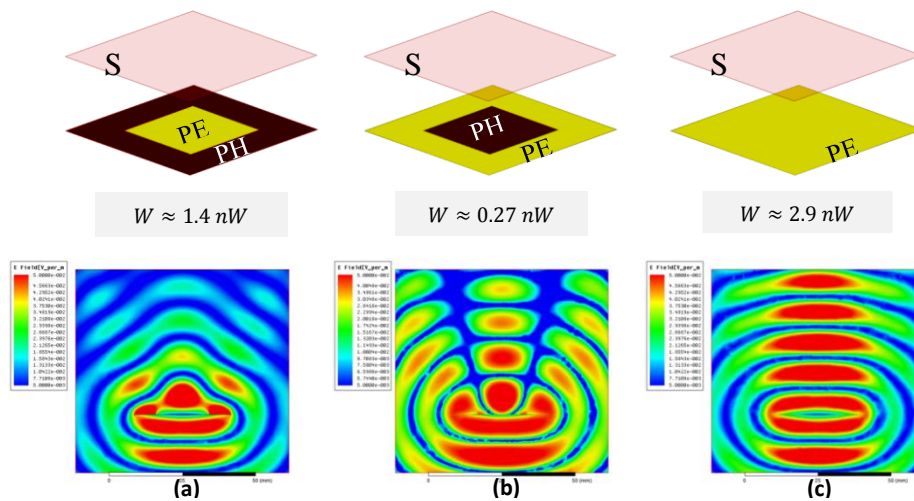


Fig. 5-2. Gaussian wave incident upon different ground plane consisting of (a) PE plane surrounded by PH plane (b) PH Plane surrounded by PE Plane (c) PE plane

Next, a dipole antenna was placed in distance of d above the surface of the bi-reflectional plane. The dipole was designed to work at a frequency of 15 GHz and the total size of the bi-reflectional ground plane was fixed to be $33.6\text{mm} \times 33.6\text{mm}$. The distance d and dimensions of the electric and magnetic conductors were optimised to maximise the concentration of reflected waves above the centre of the bi-reflectional plane using a GA optimisation method. For the sake of simplicity, both the electric and magnetic conductors were defined to be a square in shape. Optimisation parameters and simulation results are shown in Table 5-1 and Fig. 5-3.

Variable		Initial Design (mm)	Final Design (mm)
Bi-reflectional Ground Dimension	a	33.6	33.6
PH Ground Length	b	18	28.8
PH Ground Width	c	10	28.8
Distance from Ground	d	5	8.85

Table 5-1. Bi-reflectional ground optimisation parameters, initial and final values

A maximum gain of 7.84 dBi was obtained by using an ordinary PE ground plane while a peak gain of up to 11.55 dBi was achieved using the bi-reflectional ground plane.

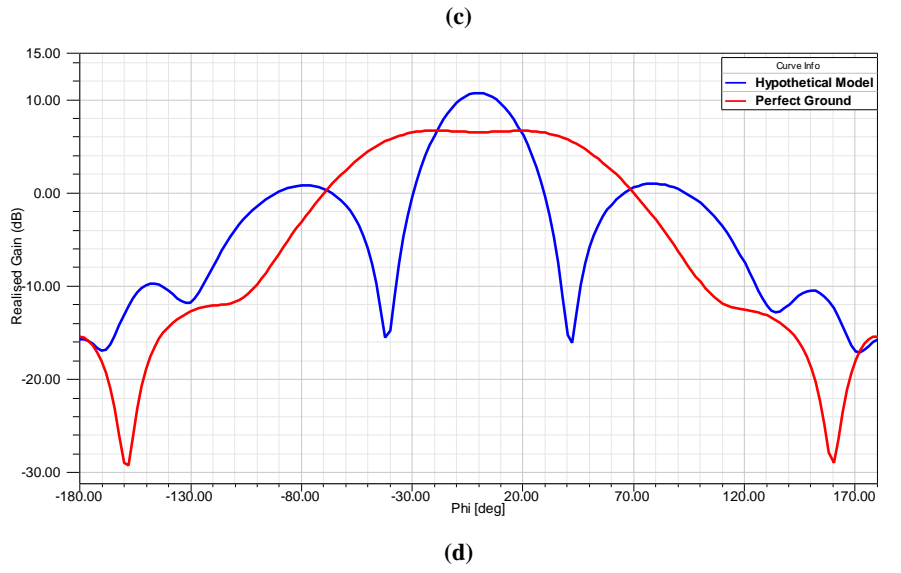
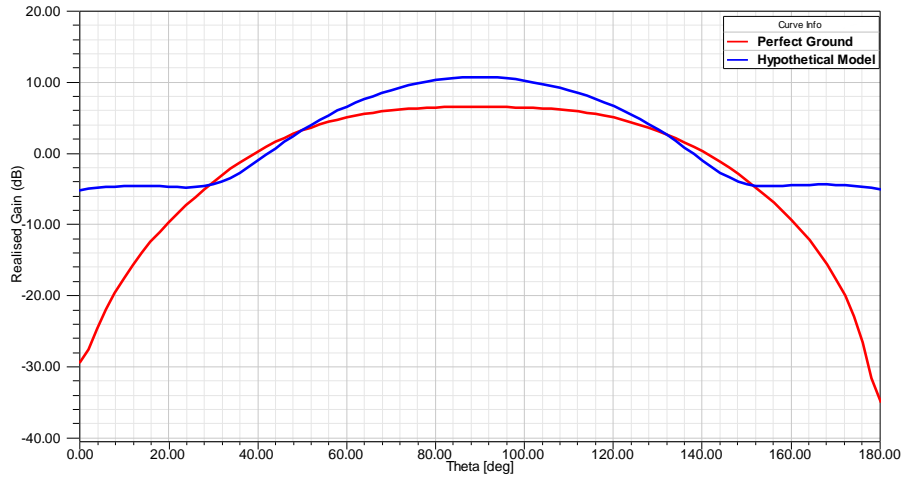
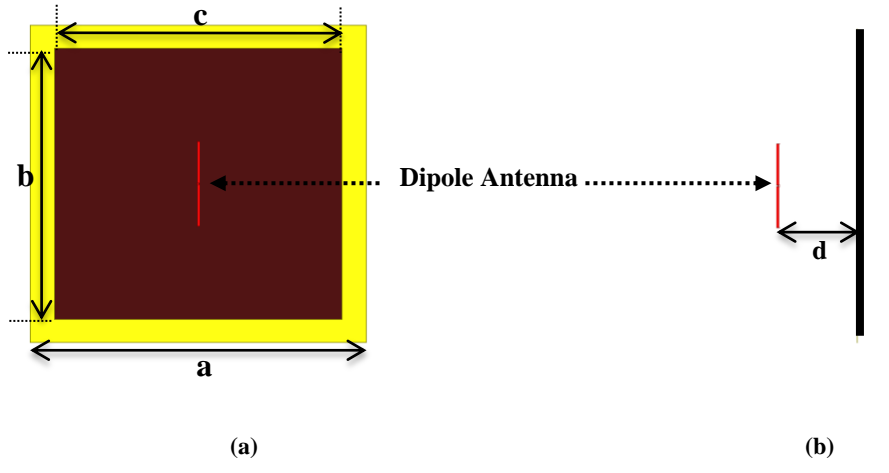


Fig. 5-3. Dipole antenna mounted on top of theoretical bi-reflectonal ground (a) Top view (b) Side view, simulation results for PE and bi-reflectonal ground (c) realised gain at E-Plane (d) realised gain at H-Plane

5 - 3 Practical Design

The theoretical model of a bi-reflectional ground plane confirms promising gain enhancement for a dipole antenna. In practice, fabrication of such a ground plane requires only an electric and a magnetic conductor. Simply, a plane of metal can be used as the electric conductor. However, more design and fabrication effort has to be devoted to the magnetic conductor part as there is no such material in nature.

5 - 3 - 1 Electromagnetic Band Gap (EBG) Structures

Electromagnetic band gap (EBG) structures and their unique electromagnetic properties have been a centre of interest for many years [78, 79, 148]. These are engineered periodic structures with cell size much smaller than the incident wavelength. The unit cell is a resonant structure which exhibits an electromagnetic band gap between two consecutive resonance modes over which surface currents are not able to propagate. The surface wave, reflection phase, surface impedance and effective impedance model concepts are associated with EBG structures which are briefly discussed in the following sections.

5 - 3 - 2 Surface Waves

Surface waves are propagating electromagnetic waves which are bound to the boundary between two dissimilar mediums such as a metal and free space. In the microwave regime, surface waves refer to surface currents which occur on the metal surface since their associated field can extend to thousands of wavelengths into surrounding space [78, 147]. These currents flow over the metal surface and do not couple to external waves if the metal surface is smooth and flat. Like conducting currents, surface currents are scattered and radiate whenever a metal surface has a discontinuity, curve or truncation. Consider Fig. 5-4 where the region $x < 0$ is filled by a dielectric with permittivity ϵ and the region $x > 0$ is filled with vacuum and surface waves propagate on the YZ plane [78].

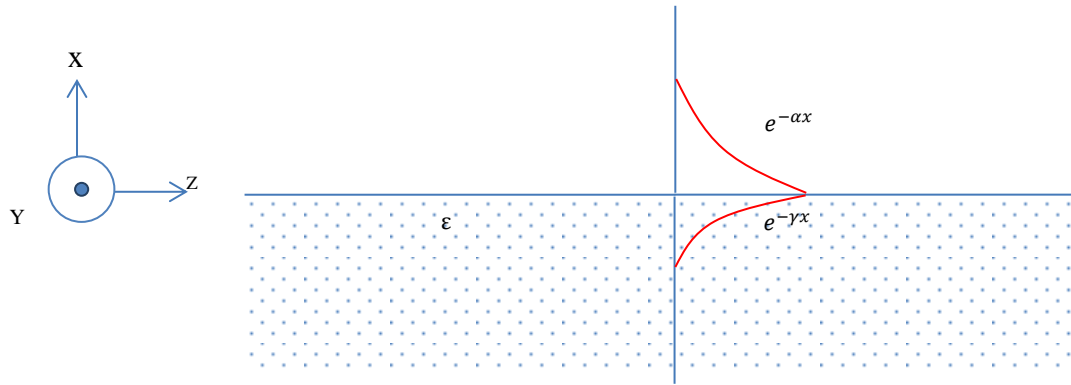


Fig. 5-4. Surface wave on dielectric-vacuum interface

The decay constants for the dielectric and vacuum regions are defined as γ and α , respectively. For a TM polarised surface wave the electric field for the upper medium can be written as:

$$E_1 = (\hat{x}E_{1x} + \hat{z}E_{1z})e^{j(\omega t - kx) - \alpha x} \quad (5-2)$$

For the dielectric region the electric field can be calculated as follows:

$$E_2 = (\hat{x}E_{2x} + \hat{z}E_{2z})e^{j(\omega t - kx) - \gamma x} \quad (5-3)$$

The variables k , α and γ can be derived by solving Maxwell's equations for the above fields [149]:

$$k = \sqrt{\frac{\epsilon}{1 + \epsilon}} \frac{\omega}{c} \quad (5-4)$$

$$\alpha = \sqrt{\frac{-1}{1 + \epsilon}} \frac{\omega}{c} \quad (5-5)$$

$$\gamma = \sqrt{\frac{-\epsilon^2}{1 + \epsilon}} \frac{\omega}{c} \quad (5-6)$$

From (5-4)-(5-6), it can be concluded that if ϵ is positive, then γ and α are imaginary. This means that the waves do not decay as the distance from the dielectric-vacuum interface increases. In other words, TM surface waves do not exist on nonconductive surfaces. Instead, there are plane waves propagating through the interface. However, when ϵ either is less than -1 or imaginary, then (5-4)-(5-6) express surface waves which are bound to the interface. There are TM

surface waves which decay exponentially for metals and other materials with non-positive dielectric constant. In the same way, to calculate TE surface waves, Maxwell's equations can be solved for TE surface waves. According to duality principle, one can use the solutions for a TM surface wave to obtain solutions for a TE surface wave by exchanging the electric fields with the magnetic fields and substituting permeability for permittivity in the TE solutions [78]. The effective dielectric constant of the metal is calculated by [149],

$$\varepsilon = 1 - \frac{j\sigma}{\omega\varepsilon_0} \quad (5-7)$$

Where σ is the metal conductivity and is given by:

$$\sigma = \frac{nq^2\tau/m}{1 + j\omega\tau} \quad (5-8)$$

Where q is the electron charge, τ is the mean electron collision time, n and m are the effective density and mass of conduction electrons, respectively. For microwave frequencies the conductivity is real and greater than unity, such that the dielectric constant is a large imaginary number. The dispersion relationship for radio frequencies, where $f_0 \ll \frac{1}{\tau}$, can be calculated by substituting (5-7) in (5-4):

$$k \approx \frac{\omega}{c} \quad (5-9)$$

Attenuation, α , is calculated by inserting (5-7) into (5-5):

$$\alpha \approx \frac{\omega}{c} \sqrt{\frac{\omega\varepsilon_0}{2\sigma}} (1 - j) \quad (5-10)$$

By inserting (5-7) into (5-6) the surface wave penetration depth also can be calculated:

$$\gamma \approx (1 + j) \sqrt{\frac{\omega\mu_0\sigma}{2}} = \frac{(1 + j)}{\delta} \quad (5-11)$$

The skin depth δ , can be derived from the surface waves penetration. Equations (5-10) and (5-11) describe that for a good conductor at radio frequencies, the

surface waves extend a great distance into the surrounding space. In contrast, they penetrate only a very small distance into metal [78]. Assuming surface waves for a copper surface at a frequency of 10 GHz, the associated electromagnetic waves extend 2300 wavelengths or 70 m, however, the skin depth remains less than 1 μm .

5 - 3 - 3 Impedance of a Flat Metal Sheet

One can calculate the current density on the surface of a flat metal sheet by having the skin depth:

$$J_z(x) = \sigma E_z(x) = \sigma E_0 e^{-x(1+j)/\delta} \quad (5-12)$$

The corresponding magnetic field can be calculated by:

$$H_0 = \int_0^{-\infty} J_z(x) dx = \frac{\sigma\delta}{1+j} E_0 \quad (5-13)$$

Thus, the surface impedance for a flat sheet of metal is obtained by:

$$Z_s = \frac{E_z}{H_y} = \frac{1+j}{\sigma\delta} \quad (5-14)$$

The surface impedance consists of real and imaginary parts where the positive sign of the imaginary part expresses the inductive characteristics of the metal sheet.

5 - 3 - 4 High Impedance Surfaces

Textured surfaces can be engineered to express different surface impedances and thereby alter surface wave propagation properties. Mushroom structures, bumpy surfaces and corrugated metal slabs are some examples of textured surfaces with altered surface wave properties. Such surfaces can be modelled using TL theory where the surface is characterised by an equivalent parallel resonant LC circuit. At low frequencies the circuit exhibits an inductive characteristic and supports TM wave propagation, while at high frequencies it is capacitive. The surface

impedance is very high at resonant frequency which means that the surface wave cannot propagate. Instead, the surface wave radiates to surrounding space [78]. The high impedance surfaces are usually periodic two or three dimensional dielectric and metallic structures which are also known as photonic crystals. Photonic crystal structures exhibit a band gap range over radio frequencies.

5 - 3 - 5 Square-Shape Mushroom Structure

Sievenpiper et al. [78] introduced a new high-impedance structure with an EBG known as the mushroom or thumbtack structure. These structures shown in Fig. 5-5 , consist of a two dimensional array of protrusions on a flat sheet. The protrusions are made as flat patches on top of a substrate which are connected to the ground plane at the bottom side of the substrate by metal vias.

When the structure period is small enough compared to the operating wavelength, TL theory can be applied and the structure can be modelled using lumped elements as a network of parallel resonant LC circuits. The resonant LC circuits act as two dimensional filters which block the flow of current over the conductor sheet. The mushroom structure represents very high impedance over a frequency range where, regardless of the electric field magnitude, the magnetic field amplitude is relatively small. Also, over this frequency range the image currents are in-phase rather than out of phase which provides a reflection phase of zero.

Based on what is discussed here, the high-impedance structures have the desired properties to be used in the design of a practical bi-reflectional ground plane.

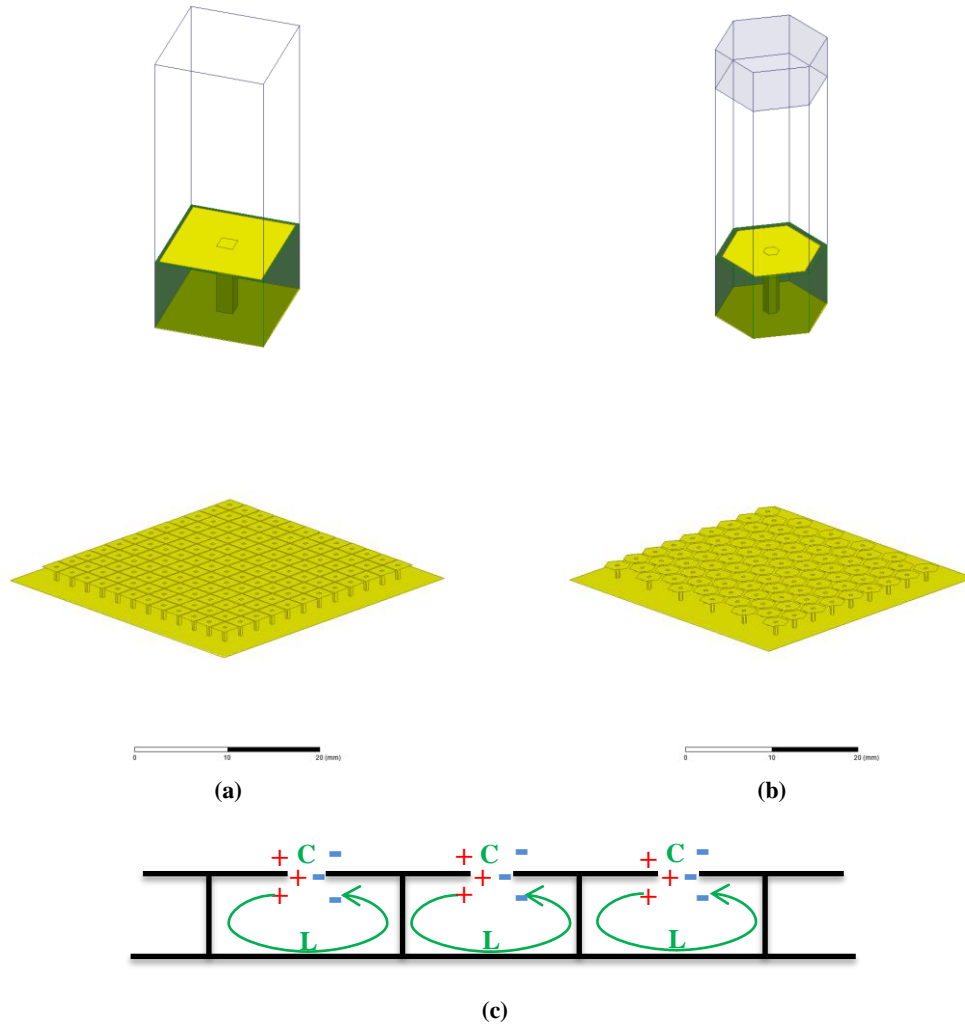


Fig. 5-5. Mushroom structure(a) square geometry unit cell and array (b) hexagonal geometry unit cell and array (c) equivalent circuit of structure for surface currents

The mushroom structure is a CRLH structure with series and shunt resonances which can be modelled using TL theory as shown in Fig. 5-6. As it is illustrated in Fig. 5-5c), incident electromagnetic waves induce currents in the top metal plate. The voltage applied parallel to the top surface causes charge build up at both ends of the top plate which configures the capacitive character of the structure. On the other hand, these charges flow through the via and bottom plate which creates currents and their associated magnetic fields, and thereby the inductive properties. The sheet impedance consists of the sheet capacitance and the sheet inductance that is used to characterise the surface:

$$Z = \frac{i\omega L}{1 - \omega^2 LC} \quad (5-15)$$

Equation (5-15) shows that the surface impedance is inductive at low frequencies and capacitive at high frequencies. It also represents very high impedance around the resonant frequency:

$$\omega_0 = \frac{1}{\sqrt{LC}} \quad (5-16)$$

For the square mushroom structure the series capacitance and shunt inductance can be approximated by [150]:

$$C_R \sim \epsilon_r \times [(L \times L) / h]$$

$$L_L \sim 0.2 \times h \times \ln[4 \times h / r - 1]$$

Where, C_R is the series capacitance, ϵ_r is the dielectric constant, L is the square patch dimension, h is the substrate height, L_L is the shunt inductance and r is the via diameter (see Fig. 5-6). A square mushroom structure supports backward wave propagation below the shunt resonance and forward wave propagation above the series resonance.

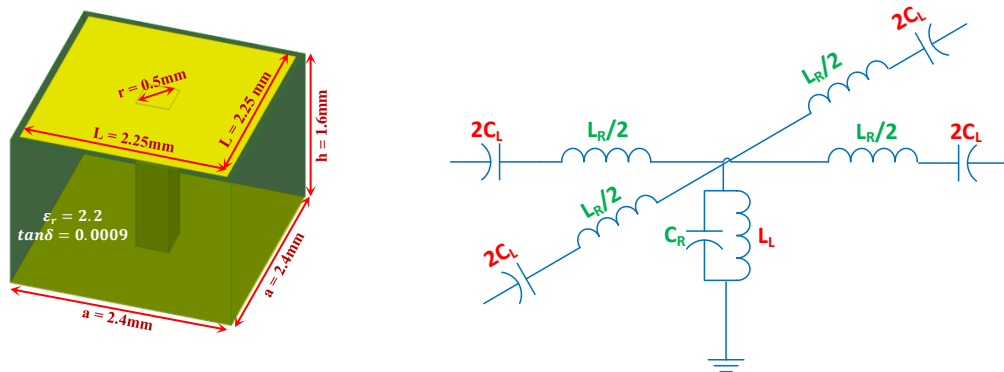


Fig. 5-6. Square mushroom structure transmission line equivalent

For given dimensions of the mushroom structure in Fig. 5-6, the series capacitance and shunt inductance can be approximated as:

$$C_R \approx 2.2 \times 8.85 \times 10^{-12} \times \frac{0.00225^2}{0.0016} = 0.062 \text{ pF} \quad (5-17)$$

$$L_L \approx 0.2 \times 0.0016 \times \ln[2 \times 0.0016 / 0.0005 - 1] = 0.275 \text{ mH} \quad (5-18)$$

Then the shunt resonant frequency is calculated by:

$$f_{sh} = \frac{1}{2\pi\sqrt{C_R L_L}} = \frac{1}{2\pi\sqrt{0.062 \times 10^{-12} \times 0.275 \times 10^{-3}}} \approx 12.2 \text{ GHz} \quad (5-19)$$

For the given dimensions, a resonant frequency of about 12.2 GHz is calculated. The accuracy of this calculation will be investigated by full wave simulation in the following sections of this thesis.

5 - 3 - 5 - 1 Dispersion Diagram

In this section, both one- and two-dimension dispersion diagrams are calculated using the driven and eigenmode approaches. The frequency band gap over which surface waves cannot propagate can be verified from the dispersion diagram.

5 - 3 - 5 - 1 - 1 1-D Dispersion Diagram (Driven Modal)

For the sake of simplicity, first, the one-dimensional dispersion diagram for a unit cell was calculated. To do so, ANSYS HFSS was used to create a model and driven modal solver was used to obtain scattering parameters. Derived S-parameters were then inserted into the dispersion relationship as follows:

$$\beta_{cell} = \cos^{-1} \left[\frac{1 - S_{11}S_{22} + S_{21}S_{12}}{2S_{21}} \right] \quad (5-20)$$

The one-dimensional dispersion diagram provides a quick and accurate result for a wave propagating along one direction. The driven modal solver calculates solutions, x , for the electric field using equation below [151]:

$$Sx + k_0^2 T x = b \quad (5-21)$$

Where S and T are matrices that depend on the boundary conditions, geometry, materials used and mesh of the structure, b is the value of the sources defined in the structure and k_0 is the free space wave number.

Results obtained from this method give an accurate view of the frequency range of the band gap, left-handed and right handed regions, slow wave and fast wave regions and so on. However, it can only show quasi-TEM modes which are excited by the ports. Mode-coupling and the isotropic nature of the unit cell are not considered in this approach. However, one can say these results are valid when other natural resonances of the structure have been taken into account. Later, the eigenmode solver was used to ensure the reliability of the results obtained by this method. In order to use the driven modal solution, the mushroom structure needed to be modified so that ports can be placed on the structure [152]. The modified structure is shown in Fig. 5-7.

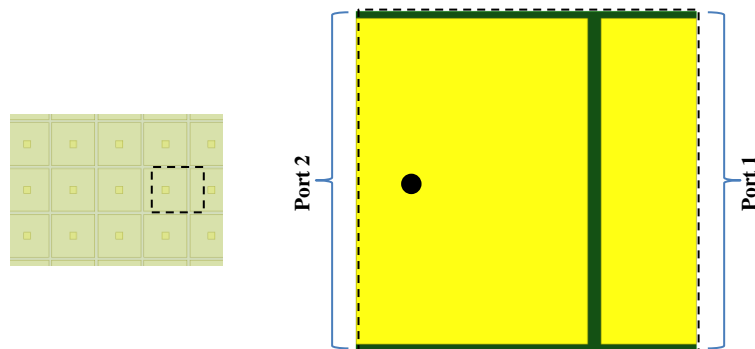


Fig. 5-7. Mushroom structure, modified model to be applicable to driven mode approach

The mesh solution frequency was at 10 GHz and a frequency sweep from 1 GHz to 40 GHz was conducted. The derived S-parameters were used to calculate the dispersion diagram. The dispersion diagram is shown in Fig. 5-8 which shows the existence of EBG characteristics.

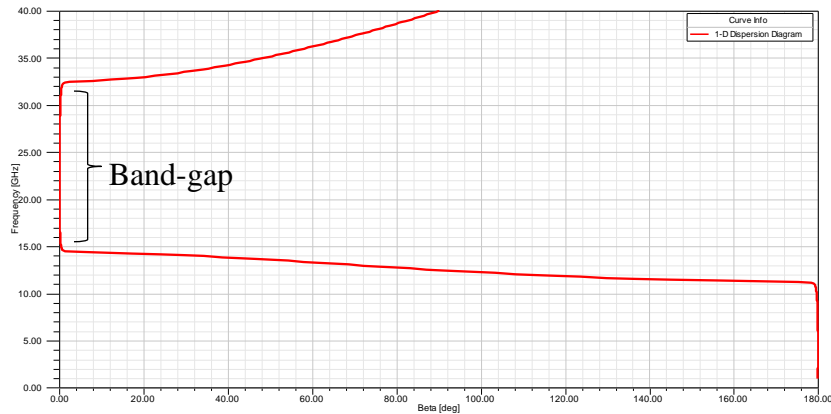


Fig. 5-8. One-dimensional dispersion diagram

5 - 3 - 5 - 1 - 2 2-D Dispersion Diagram (Eigen Mode Solution)

Although, the driven mode approach can be calculated quicker, it can only show quasi-TEM modes which are excited by ports. Mode-coupling and the isotropic nature of a unit cell are not considered in this approach. Full characterisation of the structure can be done by using the eigenmode solver. The 2-D dispersion diagram generation requires an eigenmode solution.

The eigenmode approach solves the problem for natural resonances of the structure and gives information about mode-coupling and structure isotropy. The eigenmode solution needs significantly more resources and time compared to the driven modal method. It calculates the propagation constant for different angles of an incident wave [152]. In order to find the resonances of the structure all input ports are removed from the model i.e., b in (5-21) is set to zero [153]. In this case the eigenmode solver solves the following equation for sets of (k_0, x) , one k_0 for every x :

$$Sx + k_0^2 T x = 0 \quad (5-22)$$

The matrices S and T still depend on the boundary conditions, the geometry, the materials and the mesh of the structure, k_0 is the free space wave number corresponding to that mode [153].

In order to set up the simulation, the linked boundary conditions (LBC) are used. To speed up the adaptive mesh process a mesh operation can be applied to the area of high field concentration to restrict mesh element length to $\lambda/25$. In the

presented design this area is realised as the substrate object and also the top surface of the substrate. The air box height is defined to be 6 – 8 times larger than the substrate thickness. This will guarantee that higher angle of incidence waves are also considered. Fig. 5-9 shows the modal setup and its relative boundary conditions.

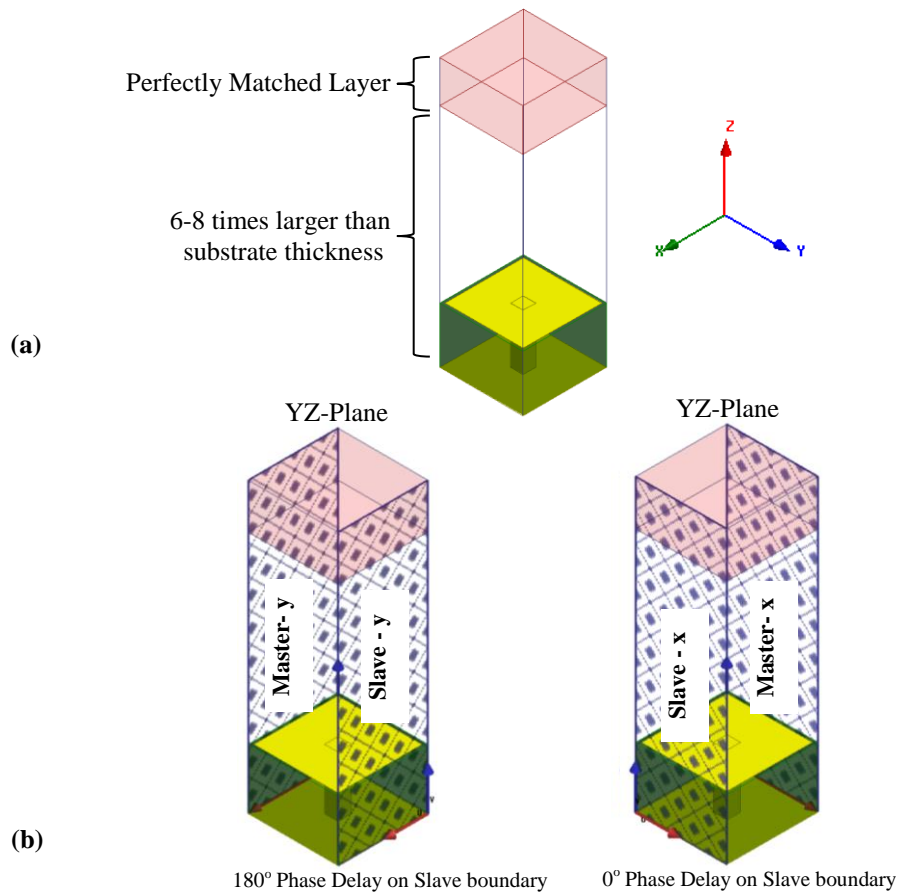


Fig. 5-9. Eigenmode solution (a) Model set up (b) Periodic boundary condition

To generate the 2-D dispersion diagram for the unit cell, shown in Fig. 5-10, a phase sweep with step size of 10° is run along the path Γ to X, X to M and M to Γ of the irreducible Brillouin zone [146].

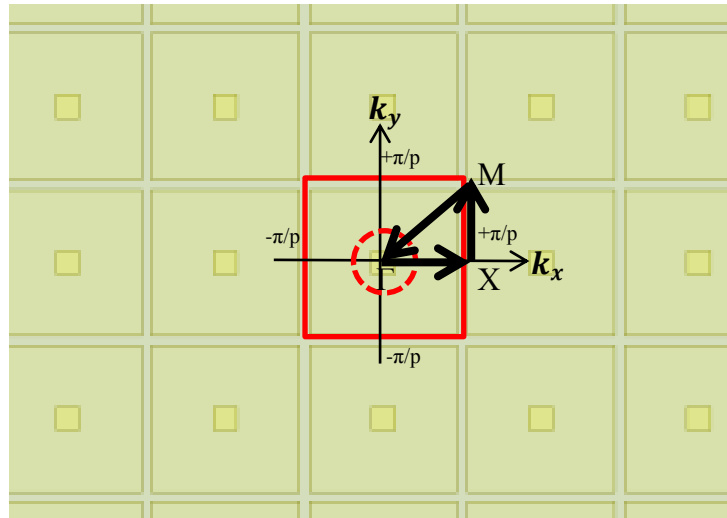
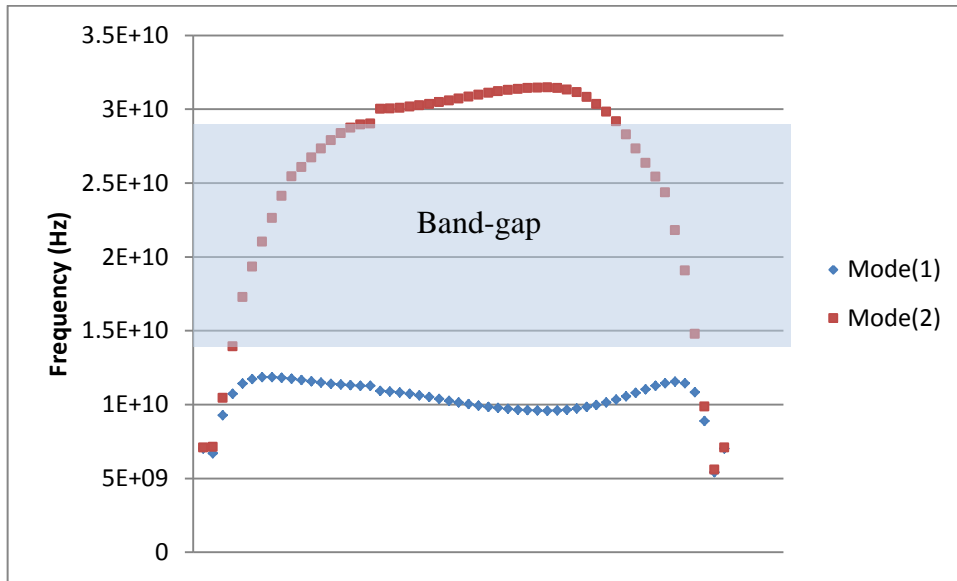


Fig. 5-10. Two-dimensional dispersion diagram for square mushroom structure

The two-dimensional dispersion diagram is generated for the first two resonance modes. It verifies the existence of a band-gap for the mushroom structure where the surface waves cannot propagate on the patch surface. It also shows a good agreement with the one-dimensional dispersion diagram which confirms that the modification that was made to the structure is valid.

5 - 3 - 5 - 2 Phase of Reflected Wave

As it was discussed before, in order to design the bi-reflective ground plane a zero reflection phase is required. The reflection phase is defined as the phase of the reflected electric field at the reflecting surface [154]. At very low frequencies

the mushroom structure acts like an ordinary metal plane where the reflection phase is equal to 180° . However, as frequency increases, the reflection phase slopes downward and finally returns to -180° [78]. There is a frequency range in the vicinity of zero, crossing over which the reflection phase is near zero and image currents are in-phase rather than out of phase. If one considers the TL model of the mushroom structure with lumped capacitors and inductors, then the reflection phase of zero occurs at the resonant frequency [78]. In the next sections, two different approaches that were used to calculate the reflection phase for square mushroom structure are presented.

5 - 3 - 5 - 2 - 1 Wave Guide Simulation

Since the mushroom structure has a simple square shape, to obtain the reflection phase the wave guide simulation can be applied i.e., perfect E/H walls with a wave port excitation. However, this approach cannot be applied to those structures that do not constitute simple planar geometries in a stratified dielectric medium [155]. This method may also introduce some ambiguities in the distribution of fields when a structure's response to the plane wave is asymmetric. Such a drawback may limit polarisation cases for this method [155].

Fig. 5-11 shows the model set up where the Perfect-E and perfect-H boundary conditions were applied to parallel sidewalls. A wave port with only one mode of excitation with polarity shown in Fig. 5-11, is placed reasonably far from the structure to avoid the near field region.

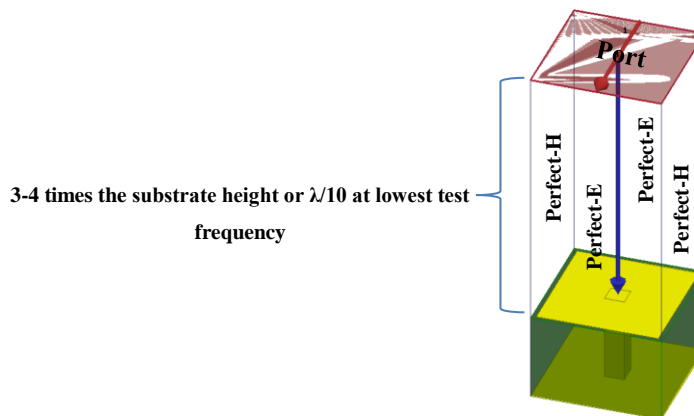


Fig. 5-11. Waveguide simulation for square geometry mushroom structure

This model forces a TEM wave to propagate down through the structure and be incident upon the mushroom. The reflection phase can be obtained simply by measuring the phase of the scattered wave i.e., $\angle S_{11}$. The phase measurement must be made at the top surface of mushroom, such that the port was de-embedded to the top surface of the structure illustrated by the blue arrow in Fig. 5-11.

The reflection phase for the square mushroom structure is shown in Fig. 5-12. It can be seen that as frequency increases the reflection phase slopes downward from π and eventually returns to $-\pi$ crossing zero around 15 GHz. The blue bar in the figure shows the range over which the reflection phase is acceptably small.

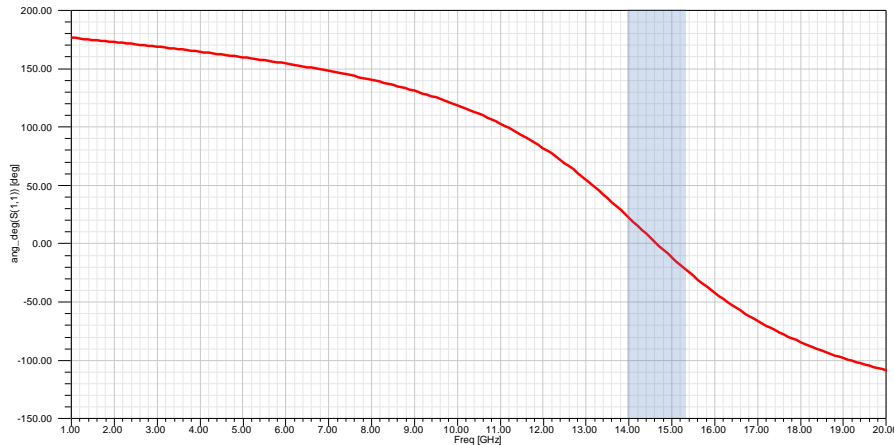


Fig. 5-12. Reflection phase from square mushroom structure

5 - 3 - 5 - 2 - 2 Linked Boundary Condition (LBC) Simulation

In the case of a lattice with non-rectangular unit cell, the wave guide simulation approach cannot be applied. Instead, LBCs are used to obtain the reflection phase. The method introduced in [156] has been used to calculate the reflection phase. In this method, the phase of the electric field is averaged at an evaluation plane, S , calculating following relation:

$$\Phi_{EBG} = \frac{\int_S \text{Phase}(E_{scattered}) \cdot ds}{\int_S S \cdot ds} \quad (5-23)$$

The reflection phase evaluated at a distance d away from a perfect ground plane is given by:

$$\Phi_{PE} = 180^\circ - \frac{d}{\lambda} \times 360^\circ \quad (5-24)$$

The phase difference between two waves reflected from a perfect ground and an EBG surface can be written as:

$$\Delta\Phi = (\Phi_{EBG} - \Phi_{PE}) + 180^\circ \quad (5-25)$$

An adjustment factor of 180° is added to centre the desired results about zero [156]. Model set up is shown in Fig. 5-13. The master-slave boundary conditions are applied to parallel sidewalls. PML boundary condition is applied on the top face. However, for normal and near normal incident waves, PML boundary condition is not necessary and radiation boundary condition works fine. Since LBCs have been used in the model, it was not possible to use the wave port excitation. Alternatively, an incident plane wave was originated at the top surface of the mushroom to excite the structure.

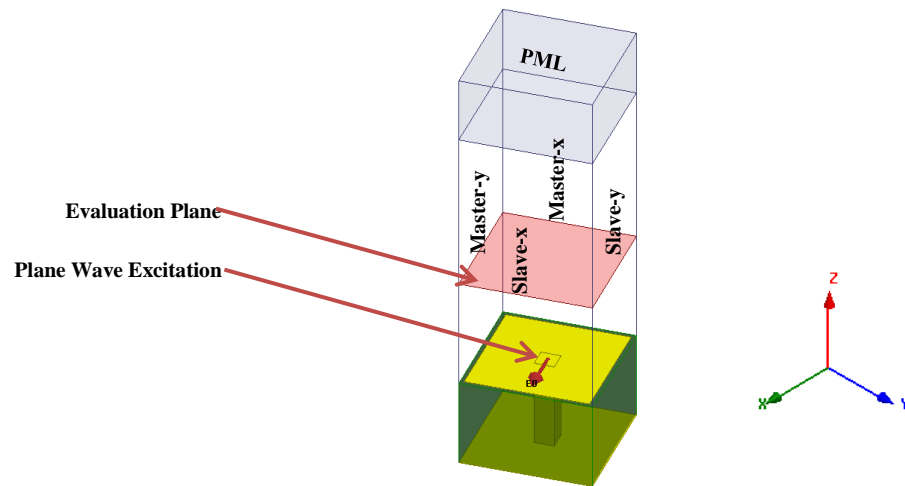


Fig. 5-13. LBC simulation set up for square geometry mushroom structure

The model was simulated for twenty different frequency points as frequency sweep was not available for the incident wave excitation. The simulation results are shown in Fig. 5-14. The reflection phase derived from the LBC simulation

illustrated by blue triangles in the figure shows perfect agreement with those results obtained from the waveguide simulation illustrated by the red dashed line.

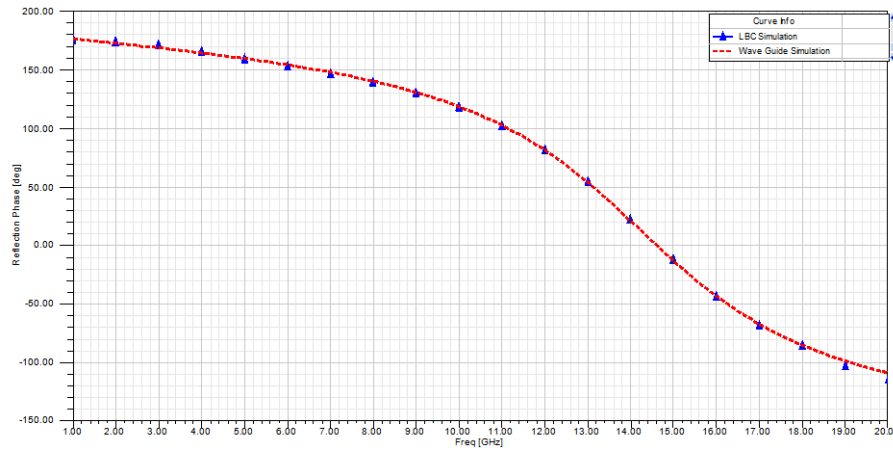


Fig. 5-14. Reflection phase from square mushroom structure

5 - 3 - 6 Dipole Integrated with Proposed Bi-reflectinal Ground Plane

In order to achieve a practical model for the bi-reflectinal ground plane, a lattice of square mushroom structures as the magnetic conductor is surrounded by a layer of copper as the perfect conductor. A dipole antenna is mounted on top of the bi-reflectinal ground at a distance d which is subject to optimisation. Model set up is shown in Fig. 5-15.

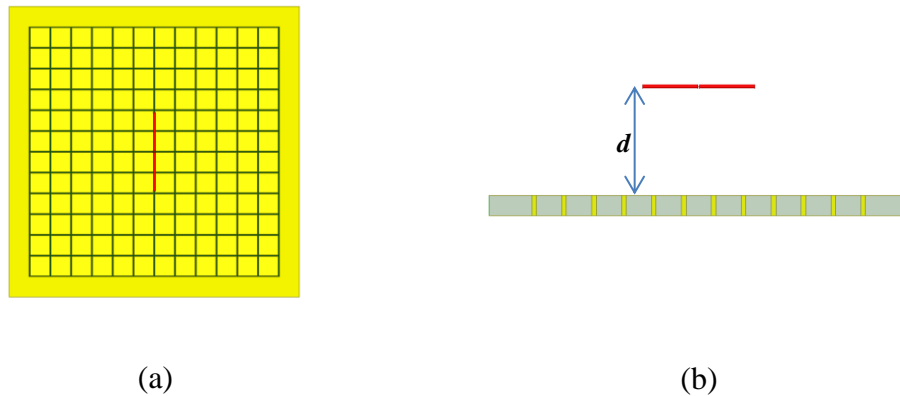


Fig. 5-15. Dipole antenna mounted over a bi-reflectinal ground plane made of square mushroom structure (a) Top view (b) Side view

Further, different lattices consisting of $m \times n$ cells were used to design the bi-reflectional ground plane. The simulation results shown in Fig. 5-16 demonstrate that for a total ground size of $33.6\text{mm} \times 33.6\text{mm}$, the maximum gain enhancement can be obtained for a bi-reflectional ground plane with the lattice dimensions equal to those defined in the optimised hypothetical model in section 5 - 2 (i.e., 28.8 mm).

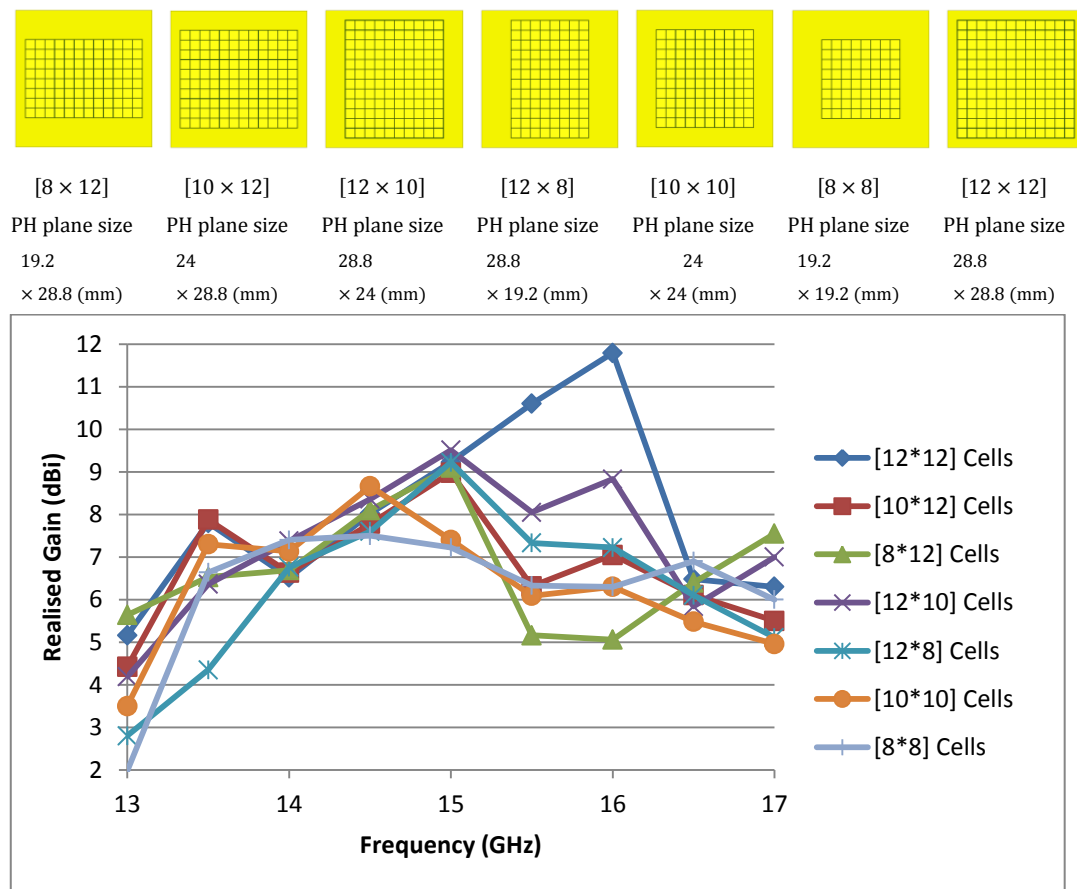


Fig. 5-16. Realised gain (dBi) achieved by bi-reflectional ground plane with different mushroom structure lattice consisting of $m \times n$ cells

Additional ground planes consisting of a $m \times m$ square lattice with a larger total size were also designed. The width of the surrounding conductor was set equal to the one in the optimised hypothetical model (i.e., 2.55 mm). Simulation results, shown in Fig. 5-17, illustrate that for the bi-reflectional ground plane formed by $[12 \times 12]$, $[13 \times 13]$ and $[14 \times 14]$ cells, the realised gain remains within 13 dBi range. However, for larger lattice sizes, the realised gain decreases.

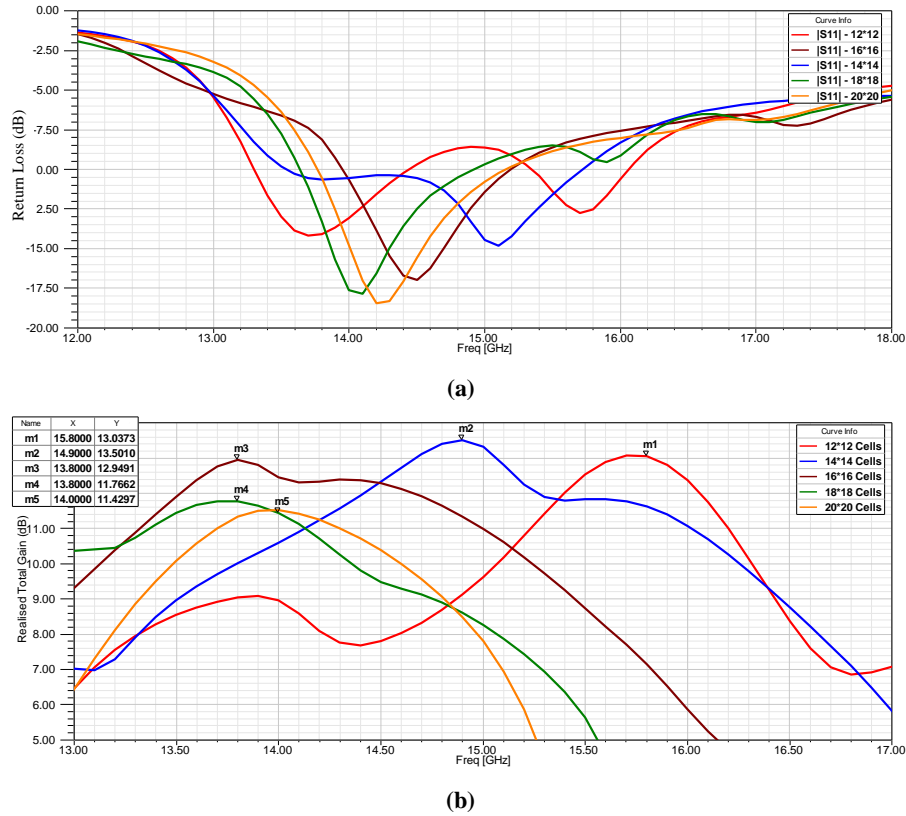


Fig. 5-17. Bi-reflectional ground planes consisting of mushroom lattice of $[m \times m]$ cells (a) return loss (b) realised gain (dBi)

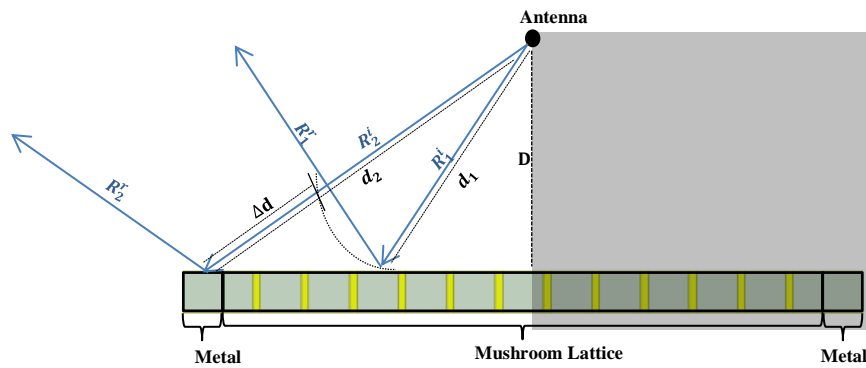
As it can be seen from Fig. 5-17.b), the realised gain peak for a bi-reflectional ground plane with a larger size of mushroom lattice happens at a lower frequency. This can be explained by the geometric optics shown in Fig. 5-18.a. In the left plane of the image, R_1^i and R_2^i are incident rays upon the mushroom lattice and perfect conductor. The difference between the distance travelled by R_1^i and R_2^i , Δd can be calculated by:

$$\Delta d = \sqrt{(\text{Distance from Antenna})^2 + \left(\frac{\text{Lattice Size} + \text{Metal Width}}{2}\right)^2} - \sqrt{(\text{Distance from Antenna})^2 + \left(\frac{\text{Lattice Size}}{4}\right)^2} \quad (5-26)$$

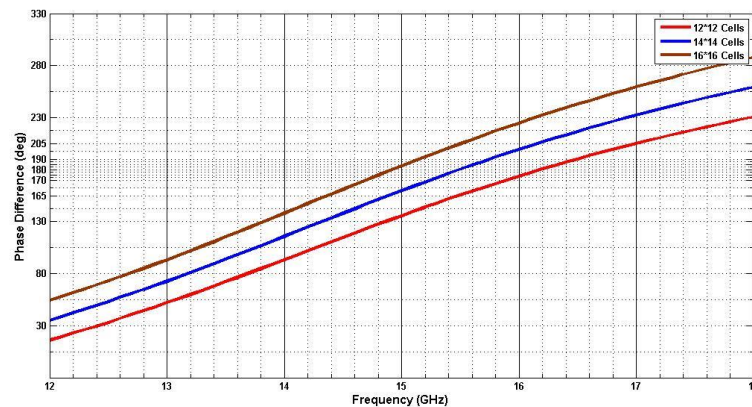
Thus, the phase difference between the reflected phase from the mushroom lattice R_1^r , and the metal R_2^r , can be written as:

$$\Delta\Phi = (\Phi_{Mushroom} - \Phi_{PE}) = \Phi_{Mushroom} - \left(180^\circ + \frac{\Delta d}{\lambda} \times 360^\circ\right) \quad (5-27)$$

Equation (5-27) was implemented in MATLAB where the reflection phase from the mushroom lattice was obtained by full wave simulation conducted by ANSYS HFSS. The phase differences between reflected rays from the bi-reflectonal ground plane made of mushroom lattice of $[12 \times 12]$, $[13 \times 13]$ and $[14 \times 14]$ cells are shown in Fig. 5-18.b). As the mushroom lattice size increases, the 180° phase difference between the reflected ray from the lattice and the perfect conductor occurs at a lower frequency. This explains why for a bi-reflectonal ground plane with a larger mushroom lattice the peak realised gain occurs at a lower frequency (see Fig. 5-17.b).



(a)



(b)

Fig. 5-18. (a) Ray tracing diagram for a bi-reflectonal ground plane (b) phase difference between reflected ray from mushroom lattice and metal

Radiation patterns for a dipole antenna with the perfect electric conventional ground plane, hypothetical bi-reflectonal ground and the bi-reflectonal ground made of a mushroom lattice of 12×12 cells at frequency of 15.7 GHz are compared in Fig. 5-19.

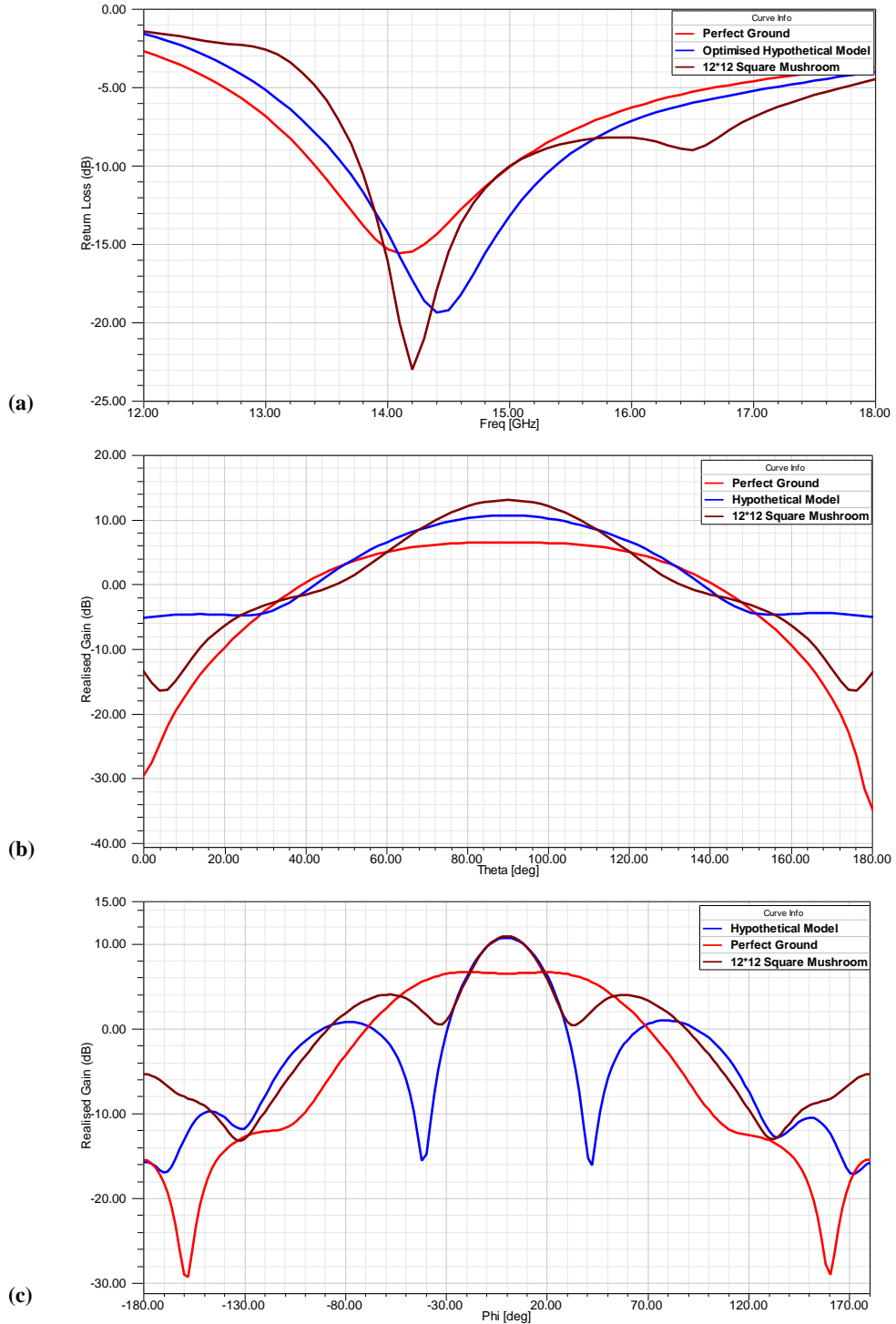


Fig. 5-19. Perfect ground, hypothetical model and ground made of square mushroom (a) Return loss (b) realised gain at E-Plane (c) realised gain at H-Plane

5 - 3 - 7 Hexagonal-Shape Mushroom Structure

A hexagonal mushroom structure is also a high-impedance structure with similar operating principles as the square mushroom structure explained before. The hexagonal mushroom is a CRLH resonant structure which exhibits an EBG property over the frequency band. Since the hexagonal shape has an extra axis of symmetry compared to the square geometry, it can serve more polarisation cases.

5 - 3 - 7 - 1 Phase of Reflected Wave

The wave guide simulation approach can be used to calculate the reflection phase only for square or rectangular structures where the normal E/H walls can be applied. However, for the hexagonal mushroom structure LBC is applied to generate the reflection diagram. It was previously explained that to calculate the reflection phase a plane wave is incident upon the structure while the phase of the electric field of scattered wave is averaged at an evaluation plane. The model set up and simulation results are shown in Fig. 5-20.

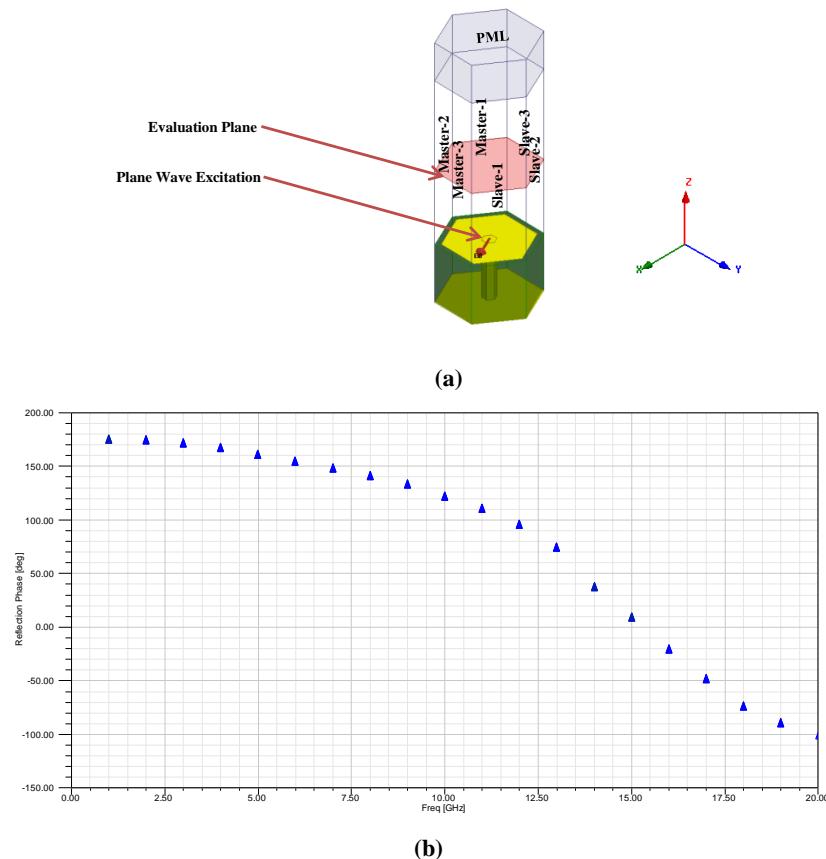


Fig. 5-20. Hexagonal mushroom structure (a) Model set up (b) Reflection phase

5 - 3 - 8 Dipole Integrated with Proposed Bi-reflective Ground Plane

A lattice of the hexagonal mushroom structures can be used to design a bi-reflective ground plane. The dimensions of areas with phase reflection of zero and 180° were kept the same as the theoretical model described in section 5 - 2 . The design is shown in Fig. 5-21. Again here, a dipole antenna was mounted at a distance of d above the surface of the structure. To maximise directivity, a GA was used to optimise the distance d .

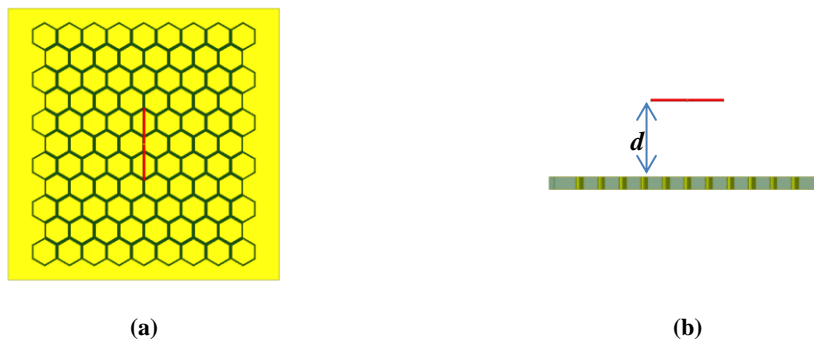


Fig. 5-21. Dipole antenna mounted over a bi-reflective ground plane made of hexagonal mushroom structure (a) Top view (b) Side view

Simulation results for the perfect ground plane, theoretical bi-reflective ground and bi-reflective ground made of the square and hexagonal mushroom structures are shown in Fig. 5-22.

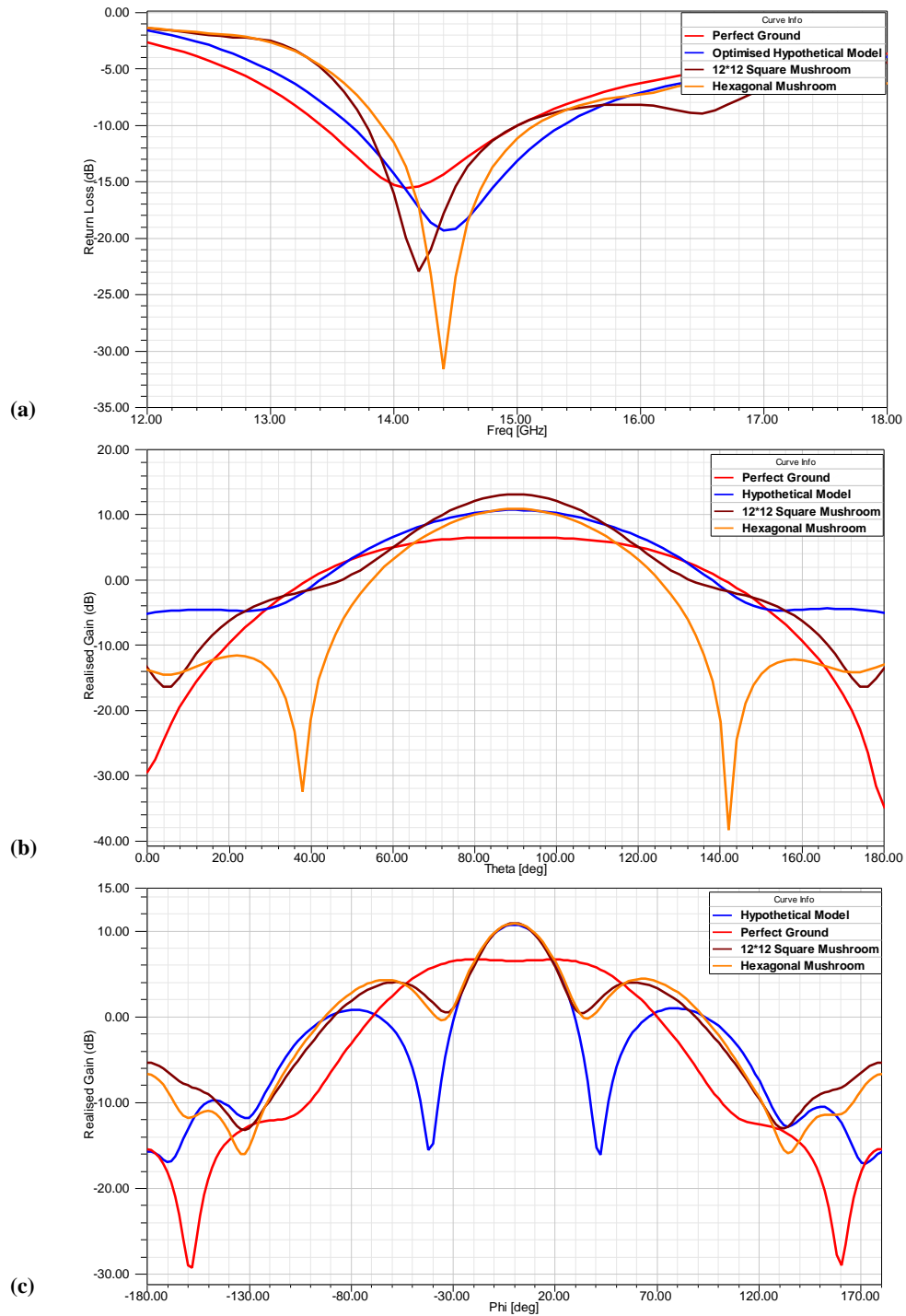


Fig. 5-22. Perfect ground, hypothetical model and ground made of square and hexagonal mushroom results (a) Return loss (b) normalised realised gain at E-Plane (c) Normalised realised gain at H-Plane

A comparison between realised gains for the dipole antenna achieved by different grounds studied is given in Fig. 5-23. The total size of all ground planes is $33.6 \text{ mm} \times 33.6 \text{ mm}$. Simulation results confirm that using a bi-reflectional ground plane can lead to a gain enhancement for frequencies over which the phase

difference between the reflected wave from the magnetic conductor and the electric conductor is closer to 180° . Also, using the square mushroom structure to form the magnetic conductor plane provides a better gain enhancement compared to the hexagonal mushroom structure.

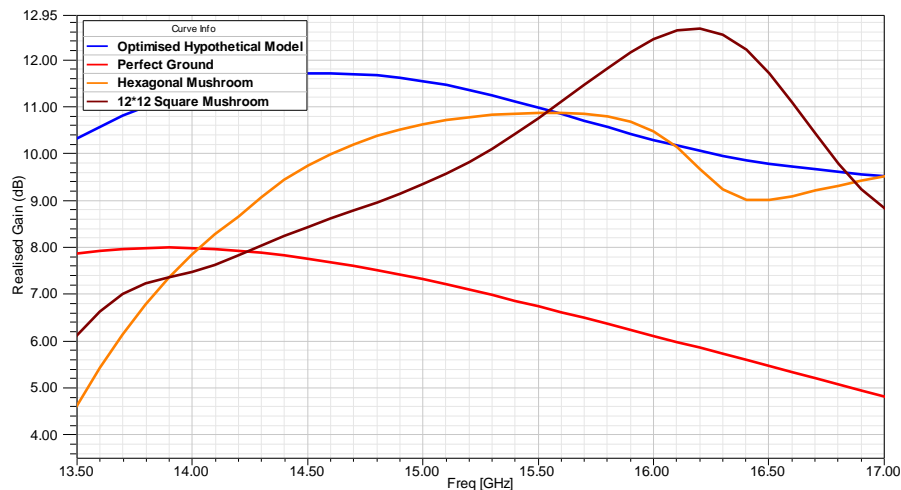


Fig. 5-23. Realised gain achieved for dipole antenna using conventional ground plane, hypothetical bi-reflective ground and bi-reflective ground made of a lattice of square and hexagonal mushroom structure

5 - 4 Summary

In this chapter the phase shift method explained in Chapter 4 was deployed to design a novel directive ground plane which can be used to increase antenna gain. A conventional ground plane, ideally redirects $\frac{1}{2}$ of radiated power to the opposite direction providing up to 3 dBi gain enhancement in one side. The idea pursued here was to design a ground plane which not only redirected the radiated power into the opposite direction but also focuses the redirected power toward the centre of the ground. The proposed ground plane called a “bi-reflective ground plane” was formed by a combination of a conventional ground plane and a perfect-H magnetic conductor plane. The reflection phase from the perfect electric conductor for a normally incident plane wave is equal to 180° . In contrast, the reflection phase from a perfect magnetic conductor for such an incident wave is equal to 0° .

Two different scenarios have been considered to model the bi-reflective ground plane. In the first design, an electric conductor plane was surrounded by a magnetic conductor plane while, in a second design, it was a magnetic conductor

which was surrounded by an electric conductor plane. ANSYS HFSS software was used to model these scenarios. The Perfect-E boundary condition was used to model the electric conductor. However, to model the magnetic conductor, a planar perfect conductor covered by Perfect-H boundary condition was defined. Higher energy intensity was observed above the surface of the ground plane in which a magnetic conductor plane was surrounded by an electric conductor plane. Next, a dipole antenna was designed at a frequency of 15 GHz and mounted on top of the bi-reflectional ground designed in the first scenario. The Perfect-E and perfect-H plane dimensions and the antenna distance from the ground plane were optimised using a genetic algorithm (GA) to maximise the antenna gain. A maximum gain of 11.55 dBi was achieved which showed more than 4.1 dBi gain enhancement compared to the conventional Perfect-E ground plane. Practical realisation of the proposed ground plane was achieved by using a layer of copper as the Perfect-E plane and a textured electromagnetic band gap (EBG) structure as the magnetic conductor.

A square-shape mushroom structure was designed to express the reflection phase of 0° at frequency of 15 GHz. The dipole antenna was mounted on top of the bi-reflectional ground plane formed by the square-shape mushroom structures and the surrounding copper layer.

In a second design, hexagonal-shape mushroom structures were used to form the bi-reflectional ground plane. The dipole antenna distance was optimised to maximise the antenna gain. Simulation results showed a peak realised gain of 12.9 dBi for the bi-reflectional ground plane made of a lattice of square mushroom structures and a peak realised gain of 10.8 dBi for the ground plane formed by the lattice of hexagonal mushroom structures.

Chapter 6

Conclusions

6 - 1 Summary

Utilisation of electromagnetic waves is the basis of many applications such as imaging technologies, wireless, optical communications and aerospace. Some of these applications require electromagnetic properties far beyond the material properties found in nature. However, sub-wavelength structured metamaterials have shown promise to provide engineerable electromagnetic properties which opens new doors to microwave and photonic science and industry.

This thesis studied design and characterisation of metamaterials as well as their application in antenna structures. The aims of the research were mainly to first, increase the operational bandwidth for a specific group of metamaterials known as zero index metamaterials (ZIM); and second, to improve antenna directivity through beam forming conducted by metamaterials.

To begin with, basic concepts and fundamental theories needed in the study of metamaterials were explored. Macro- and micro-scale phenomena that occur within a metamaterial unit cell are investigated, including the study of the electromagnetic field variation over a unit cell. Moreover, two major approaches to characterise a metamaterial structure, known as the resonant approach and the transmission line (TL) approach are explained.

Prior to the work presented here, ZIM structures and their potential application in antenna systems design were known. However, like other metamaterials, ZIM structures suffer from inherently narrow operational bandwidth. To tackle this problem, first, different structures with the electric response have been studied

giving special attention to their operational bandwidth. Metamaterial structures such as rods, C-shape, S-shape, W-shape and meanderline structures have been designed and simulated. Then the standard retrieval technique has been applied to extract the material parameters from the scattering parameters. The results suggest that there is a non-linear relationship between the physical and effective length of the scatterer. It has also been demonstrated that thinner copper trace provides lower resonant frequency and consequently, lower plasma frequency as well as lower losses associated with resonance. It was found that the lowest resonant and plasma frequency can be achieved for a meanderline structure formed by six meanders. The fractional bandwidth (FBW) for different structures was found to be in the range of 8~11%. Two novel broadband ZIM structures have been designed where a maximum FBW of 14% and 33% were achieved. Two types of ZIM embedded antenna structures were developed in this thesis:

- **ZIM shell based antenna** where ZIM cells form a shell around the antenna.
- **ZIM cells integrated on a planar antenna** where ZIM cells are placed on the antenna substrate.

In both cases the ZIM structures act as a lens boosting the antenna directivity. The optical transformation was used to define the required material parameters for the shell to achieve a highly directive emission. Accordingly, epsilon-zero (EZ) cells, mu-zero (MZ) cells and ZIM cells have been used to tailor four different shell designs. In the case of the EZ shell, simulation results confirmed a total gain of 7.84 *dBi* along the direction with epsilon-zero property. This means that the EZ shell provides 5.5 *dBi* gain enhancement compared to gain of the dipole antenna without the shell (i.e., 2.3 *dBi*). In the second case, the dipole antenna was surrounded by the MZ shell where a total gain of 4.9 *dBi* was achieved. This illustrates that the EZ shell is more directive than the MZ shell. However, using more layers to form the MZ shell increases directivity and total gain. The EZ shell and MZ shell were then combined to form a ZIM shell with simultaneously zero permittivity and permeability. However, designing the ZIM shell using the EZ and MZ structures proposed earlier is not geometrically possible due to the EZ and MZ cells intersection. Two structures have been suggested as the ZIM shell; in the first ZIM shell design, the EZ cells were placed within the layers of the MZ shell

where a total gain of 7 *dBi* was achieved. In contrast, the second ZIM shell was designed by placing the MZ cells between the EZ shell layers where a total gain of up to 9.15 *dBi* was obtained.

The proposed ZIM structure was then integrated into the quasi-Yagi antenna. Simulation results showed that the antenna gain increases more than 2 *dBi* for a frequency range over which the proposed metamaterial structure exhibits ZIM properties (10.4 – 11.8 *GHz*). The design is very simple and easy to fabricate. It has been demonstrated that the antenna gain can be improved even further by using two rows of the ZIM structure while the antenna operational bandwidth remains almost the same. Additional gain enhancement could be achieved by using multiple layers of the ZIM structure. However, it will increase the overall antenna profile.

Pursuing the aim of antenna gain enhancement, a new technique has been developed based on wave interference phenomena to define required spatial properties for highly directive emission. It has been theoretically demonstrated that waves with different phases can be interfered coherently with the intension of having a focused emission. Since this method does not need extraction of material parameters (i.e., permittivity and permeability), the extraction validation concerns such as homogenisation and reciprocity conditions are no longer required. Instead, the focus is on phase advance over a unit cell and the total metamaterial structure. It has been illustrated that highly directive emission can be obtained when two propagating waves with the same frequency, intensity and polarisation axis, but 180° phase difference, are interfering. A hypothetical lens slab was defined to provide 180° phase shift (i.e., $\epsilon_r = \mu_r = 3$) between waves propagating through the slab and waves propagating through the surrounding air. Then, the lens slab was placed on top of a patch antenna to increase the antenna gain. A total gain of 15 *dBi* was achieved which shows more than 8 *dBi* gain enhancement. Further, metamaterial realisation of the hypothetical lens slab has been designed using the capacitively loaded ring resonator (CLRR) unit cell. Each unit cell was designed to shift the phase by 30° by which cascading six unit cells provides 180° phase shift. The metamaterial lens slab was placed on top of the patch antenna to increase its directivity. The simulation results demonstrated a gain of up to

13.56 *dBi* for the proposed antenna structure which shows almost 6.6 *dBi* gain enhancement.

The coherent wave interference was deployed to design a novel directive ground plane which can be used to increase the antenna gain. A conventional ground plane, ideally redirects $\frac{1}{2}$ of radiated power to the opposite direction providing up to 3 *dBi* gain enhancement in one side. However, a novel ground plane was proposed which not only redirects the radiated power into the opposite direction but also focuses the redirected power toward the centre of the ground plane. The proposed ground plane called a “bi-reflectional ground plane” was formed by a perfect magnetic conductor plane surrounded by a perfect electric conductor. The reflection phase from the perfect electric conductor for a normally incident plane wave is equal to 180° . In contrast, the reflection phase from a perfect magnetic conductor for such an incident wave is equal to 0° .

Next, a dipole antenna was designed at frequency of 15 *GHz* and mounted on the top of the bi-reflectional ground. A maximum gain of 11.55 *dBi* was achieved which shows more than 4.1 *dBi* gain enhancement compared to the dipole antenna mounted at $\lambda/4$ distance from of the conventional Perfect-E ground plane. Practical realisation of the proposed ground plane has been designed by using a layer of copper as the Perfect-E plane and a textured electromagnetic band gap (EBG) structure as the magnetic conductor. The square-shape mushroom structure was designed to express the reflection phase of 0° at frequency of 15 *GHz*. The dipole antenna was mounted on the top of the bi-reflectional ground plane formed by the square-shape mushroom structures and the surrounding copper layer.

In a second design, the hexagonal-shape mushroom structures were used to form the bi-reflectional ground plane. The dipole antenna distance was optimised to maximise the antenna gain. Simulation results showed a peak realised gain of 12.9 *dBi* for the bi-reflectional ground plane made of a lattice of square mushroom structures and a peak realised gain of 10.8 *dBi* for the ground plane formed by the lattice of hexagonal mushroom structures.

6 - 2 Future Research

In the first part of this thesis, ZIM structure characteristics and their electromagnetic properties were studied with special attention given to their operational bandwidth improvement. A similar investigation could be conducted looking at other types of metamaterials such as negative refractive index metamaterials, metamaterial absorbers and so on.

The work presented here was limited to distributed element metamaterials which usually operate in the GHz range. Since many widely-used wireless devices such as mobile phones, TV broadcasting antennae and radar systems work in lower frequencies than the operational frequencies of presented designs in this thesis; it would be interesting to extend this work to the lump element metamaterials which could bring the operational bandwidth down to the MHz range. This would provide numerous applications for metamaterial lenses and specially, for the bi-reflectional ground plane.

It has been theoretically demonstrated that waves with different phases can be interfered coherently with the intension of having a focused emission. Instead of passive metamaterial structures used to form the 180° metamaterial phase shifter in this work, active metamaterial structures could be used to control the phase shift provided by the metamaterial slab. This could be deployed to achieve tuneable steering of an antenna radiation beam.

Appendix MATLAB Codes

{ These codes were used to build an interface between ANSYS HFSS and MATLAB. Using MATLAB environment, different ZIM structures were coded into the Visual Basic Scripting Edition (VBScript) format which is executable by ANSYS HFSS. Each ZIM structure was coded and stored in a file and then, was imported into ANSYS HFSS to create the geometry and to conduct the full wave simulation. The obtained S-parameters by ANSYS HFSS were then exported back into MATLAB for further analysis. }

```
clear all;
close all;
% add paths to the required m-files.
addpath('D:/Matlab_HFSS_CODE/MeanderLine/3dmodeler');
addpath('D:/Matlab_HFSS_CODE/MeanderLine/general');
addpath('D:/Matlab_HFSS_CODE/MeanderLine/analysis');
addpath('D:/Matlab_HFSS_CODE/MeanderLine/boundary');

% constants
rad=pi/180;
eps0=8.85e-12;           %Permittivity of Free Space
mu0=4*pi*1e-7;         %Permeability of Free Space
eta0=sqrt(mu0/eps0);   % Impedance of Free
c=1/sqrt(eps0*mu0);    %Speed Of Light in Free Space

% Antenna Parameters.
fs = 10e9;              % Solution Frequency.
fr=9.5e9;              %Frequency of Interest
fActual=5e9;           % Initializing resonant Frequency

% HFSS Simulation Parameters.
fLow = 1e9;
fHigh = 25e9;
nPoints = 401;

% Temporary Files. These files can be deleted after the
optimization
% is complete. We have to specify the complete path for all of
them.
tmpPrjFile = 'D:\Matlab_HFSS_CODE\MeanderLine\tmpML.hfss';
tmpDataFile = 'D:\Matlab_HFSS_CODE\MeanderLine\tmpData.m';
tmpScriptFile = 'D:\Matlab_HFSS_CODE\MeanderLine\MeanderLine.vbs';

% HFSS Executable Path.
hfssExePath = 'C:\Program
Files\ANSYSEM\HFSS15.0\Win64\hfss.exe';

% Plot Colors.
pltCols1 = {'b-', 'r-', 'k-', 'g-', 'm-', 'c-', 'y-'};
pltCols2 = {'b--', 'r--', 'k--', 'g--', 'm--', 'c--', 'y--'};
nCols = length(pltCols1);

disp('Creating the Script File for meanderline...');
```

```

%Project Parameters

ax=4;      %Substrate width
ay=4;      %Substrate Length
w=0.2;     %copper width
mx=3.77;  %meanderline width
my=2.7;   %meanderline length
h=0.5;    %Substrate thickness
H=0.017;  %Copper thickness
delta_L=0.5; %step size
nCell=2;   %number of meandering

ax=floor(ax*100)/100;
ay=floor(ay*100)/100;
w=floor(w*100)/100;
mx=floor(mx*100)/100;
my=floor(my*100)/100;
H=floor(H*100)/100;
h=floor(h*100)/100;
delta_L=floor(delta_L*10000)/10000;
A=1;
for nCell=8:10
    B=1;
    for h=0.4:0.1:0.6
        C=1;
        for w=0.05:0.05:0.3
            D=1;
            nCell=10
            w=0.3
            h=0.653

            d=(mx-(nCell+1)*w)/nCell;
            d=floor(d*100)/100;

            for my=0.3:delta_L:ax
                my=3.3;
                % Create a new temporary HFSS script file.
                fid = fopen(tmpScriptFile, 'wt');
                dim(A,B,C,D,:)=[ax ay h mx my w H];
                avrg_lngth(A,B,C,D)=(nCell+1)*(my-w/2)+nCell*(d+w);

                % Create a new HFSS Project and insert a new design.
                hfssNewProject(fid);
                hfssInsertDesign(fid,
                sprintf('Ncell=%d_h=%0.2f_w=%0.2f_My=%0.2f_',nCell,h,w,my));

                %Create Geometry of Design In HFSS

                hfssBox(fid, 'Substrate', [-ax, -ay, 0]/2, [ax, ay, h], 'mm');
                hfssAssignMaterial(fid, 'Substrate', 'FR4_epoxy');

                hfssBox(fid, 'part1', [floor((-ax/2+(ax-mx)/2)*100)/100, -
                my/2, h], [w ,my, H], 'mm');
                p=2;
                for i=1:nCell
                    hfssBox(fid, sprintf('part%i',p), [floor((-ax/2+(ax-
                    mx)/2+i*w+(i-1)*d)*100)/100, mod(i,2)*my-my/2, h], [d ,
                    mod(i,2)*2*w+w, H], 'mm');
                    p=p+1;

```

```

        hfssBox(fid, sprintf('part%i',p), [floor((-ax/2+(ax-
mx)/2+i*(w+d))*100)/100, mod(i,2)*my-my/2, h], [w ,-
mod(i,2)*2*my+my, H], 'mm');
        p=p+1;
    end

    for i=1:2*nCell+1
        Objects{i}=sprintf('part%i',i);
    end
    nObjects=numel(Objects);
    fprintf(fid, '\n');
    fprintf(fid, 'oEditor.Unite _\n');
    fprintf(fid, 'Array("NAME:Selections", _\n');
    fprintf(fid, '"Selections:=", ');
    fprintf(fid, '');
    for iP = 1:nObjects-1,
        fprintf(fid, '%s,', Objects{iP});
    end
    fprintf(fid, '%s", _\n', Objects{nObjects});
    fprintf(fid, 'Array("NAME:UniteParameters", "KeepOriginals:=",
false)\n');

    hfssAssignMaterial(fid, 'part1', 'copper');

    % Add an Airbox.

    hfssBox(fid, 'AirBox', [-ax, -ay, -ax]/2, [ax, ay, ax], 'mm');

    fprintf(fid, 'Dim faceid1 \n');
    fprintf(fid, 'faceid1 =
oEditor.GetFaceByPosition(Array("NAME:Parameters", _\n');
    fprintf(fid, '"BodyName:=", "AirBox", "XPosition:=", "0mm",
"YPosition:=", _\n');
    fprintf(fid, '"0mm", "ZPosition:=", "%fmm") \n', ax/2);

    fprintf(fid, 'Dim faceid2 \n');
    fprintf(fid, 'faceid2 =
oEditor.GetFaceByPosition(Array("NAME:Parameters", _\n');
    fprintf(fid, '"BodyName:=", "AirBox", "XPosition:=", "0mm",
"YPosition:=", _\n');
    fprintf(fid, '"0mm", "ZPosition:=", "%fmm") \n', -ax/2);

    %Assign PE & PH boundary Conditions to the design simulate TEM
mode (Plane Wave)
    fprintf(fid, 'Set oModule =
oDesign.GetModule("BoundarySetup")\n');
    fprintf(fid, 'oModule.AssignPerfectH Array("NAME:%s", _
\n', 'PerH');
    fprintf(fid, '"objects:=", "Airbox", _ \n');
    fprintf(fid, '"Faces:=", Array(faceid1, faceid2)) \n');
    %fprintf(fid, '"Faces:=", Array(456, 457)) \n');

    fprintf(fid, 'Dim faceid3 \n');

```



```

    fprintf(fid, 'faceid3 =
oEditor.GetFaceByPosition(Array("NAME:Parameters", _\n');
    fprintf(fid, "BodyName:=", "AirBox", "XPosition:=", "%fmm",
"YPosition:=", _\n', ax/2);
    fprintf(fid, "0mm", "ZPosition:=", "0mm")) \n');

    fprintf(fid, 'Dim faceid4 \n');
    fprintf(fid, 'faceid4 =
oEditor.GetFaceByPosition(Array("NAME:Parameters", _\n');
    fprintf(fid, "BodyName:=", "AirBox", "XPosition:=", "%fmm",
"YPosition:=", _\n', -ax/2);
    fprintf(fid, "0mm", "ZPosition:=", "0mm")) \n');

    fprintf(fid, 'Set oModule = oDesign.GetModule("BoundarySetup")
\n');
    fprintf(fid, 'oModule.AssignPerfectE Array("NAME:%s", _
\n', 'PerE');
    fprintf(fid, "InfGroundPlane:=", false, _\n');
    fprintf(fid, "objects:=", "Airbox", _\n');
    fprintf(fid, "Faces:=", Array(faceid3, faceid4)) \n');
    fprintf(fid, '\n');

    %Assign Wave Ports
    fprintf(fid, 'Dim faceid5 \n');
    fprintf(fid, 'faceid5 =
oEditor.GetFaceByPosition(Array("NAME:Parameters", _\n');
    fprintf(fid, "BodyName:=", "AirBox", "XPosition:=", "0mm",
"YPosition:=", _\n');
    fprintf(fid, "%fmm", "ZPosition:=", "0mm")) \n', ay/2);

    fprintf(fid, 'Dim faceid6 \n');
    fprintf(fid, 'faceid6 =
oEditor.GetFaceByPosition(Array("NAME:Parameters", _\n');
    fprintf(fid, "BodyName:=", "AirBox", "XPosition:=", "0mm",
"YPosition:=", _\n');
    fprintf(fid, "%fmm", "ZPosition:=", "0mm")) \n', -ay/2);

    hfssAssignWavePort(fid, 'WavePort2', 'faceid5', 1, true, [-
ax, ay, 0]/2, [ax, ay, 0]/2, 'mm');
    fprintf(fid, '\n');
    hfssAssignWavePort(fid, 'WavePort1', 'faceid6', 1, true, [-ax, -
ay, 0]/2, [ax, -ay, 0]/2, 'mm');

    % Add a Solution Setup.
    hfssInsertSolution(fid, sprintf('Setup%dGhz', fs/1e9), fs/1e9);
    hfssInterpolatingSweep(fid,
sprintf('sweep%dto%d', fLow/1e9, fHigh/1e9),
sprintf('Setup%dGhz', fs/1e9), ...
    fLow/1e9, fHigh/1e9, nPoints);

    % Save the project to a temporary file and solve it.
    hfssSaveProject(fid, tmpPrjFile, true);
    hfssSolveSetup(fid, sprintf('Setup%dGhz', fs/1e9));

```

```

    % Export the Network data as an m-file.
    hfssExportNetworkData(fid, tmpDataFile,
    sprintf('Setup%dGhz', fs/1e9),
    sprintf('sweep%dto%d', fLow/1e9, fHigh/1e9));

    % Close the HFSS Script File.
    fclose(fid);

    % Execute the Script by starting HFSS.
    disp('Solving using HFSS ..');
    hfssExecuteScript(hfssExePath, tmpScriptFile, false, false);

    tmpData;
    %*****
    % constants
    rad=pi/180;
    eps0=8.85e-12;
    mu0=4*pi*1e-7;
    eta0=sqrt(mu0/eps0); % free space
    c=1/sqrt(eps0*mu0);
    %*****
    % variables
    % thickness of the sample
    f1=f(1,1); df=f(1,2)-f(1,1); f2=f(1,end); Nf=floor((f2-
f1)/df)+1; % frequency range and spacing
    if Nf~=size(f)
        Nf=Nf+1;
    end
    %*****

    S11=S(:,1,1);
    S21=S(:,2,1);
    S22=S(:,2,2);
    P11=angle(S(:,1,1))/rad;
    P21=angle(S(:,2,1))/rad;
    P22=angle(S(:,2,2))/rad;

    p11=-unwrap(P11,180);
    p21=-unwrap(P21,180);
    p22=-unwrap(P22,180);
    %*****
    % frequency loop begin
    for it=1:Nf
        f=f1+(it-1)*df;
        Fr(it)=f;
        Fghz(it)=f/1e9;
        fghz=f/1e9;
        Z0=eta0; W=2*pi*Fr(it); k0=W/c;
        % combine magnitude and phase of the S11 and S21
        S11(it)=abs(S11(it))*exp(j*p11(it)*rad);
        S21(it)=abs(S21(it))*exp(j*p21(it)*rad);
        dd=ax*1e-3; % slab thickness
        %*****56
        %compute refractive index & wave impedance

        z(A,B,C,D,it)=sqrt(((1+S11(it))^2-S21(it)^2)/((1-
S11(it))^2-S21(it)^2));
    end
end

```

```

n(A,B,C,D,it)=acos((1-
S11(it)^2+S21(it)^2)/(2*S21(it)))/(k0*dd);

%casualty Condition
if imag(n(A,B,C,D,it))<0
    n(A,B,C,D,it)=-n(A,B,C,D,it);
end

if real(z(A,B,C,D,it))<0
    z(A,B,C,D,it)=-z(A,B,C,D,it);
end

er(A,B,C,D,it)=n(A,B,C,D,it)/z(A,B,C,D,it);% effective
permittivity
mu(A,B,C,D,it)=n(A,B,C,D,it)*z(A,B,C,D,it);% effective
permeability
end

[max_img_er(A,B,C,D), Nf0e(A,B,C,D)]=max(imag(er(A,B,C,D,:)));
[min_real_er(A,B,C,D),
NRe_er_min(A,B,C,D)]=min(real(er(A,B,C,D,:)));
f0e(A,B,C,D)=Fr(Nf0e(A,B,C,D));

for N=NRe_er_min(A,B,C,D):numel(er(A,B,C,D,:))
    if real(er(A,B,C,D,N-1))*real(er(A,B,C,D,N))<=0
        N_ZIM(A,B,C,D)=round((2*N-1)/2);
        break
    else N_ZIM(A,B,C,D)=nPoints
    end
end

N1=find(real(er(A,B,C,D,N_ZIM(A,B,C,D):numel(er(A,B,C,D,:)))>=0.2)
,1,'first');
if isempty(N1)
    N11=nPoints;
else
    N11(A,B,C,D)=N_ZIM(A,B,C,D)+N1;
end
N2=find(real(er(A,B,C,D,NRe_er_min(A,B,C,D):N_ZIM(A,B,C,D)))>=-
0.2),1,'first');
if isempty(N2)
    N22(A,B,C,D)=nPoints;
else
    N22(A,B,C,D)=NRe_er_min(A,B,C,D)+N2;
end
BW(A,B,C,D)=abs(N22(A,B,C,D)-N11(A,B,C,D))*df;

D=D+1;
end
C=C+1;
end
B=B+1
end
A=A+1
end

```

```
figure(1)
subplot(231)
plot(Fghz,abs(S11),'b');
xlabel('Frequency in GHz');
ylabel('Magnitude of S');
grid on
xbounds = xlim;
set(gca,'XTick',xbounds(1):xbounds(2));
hold on
plot(Fghz,abs(S21),'r');
subplot(232);
plot(Fghz,P11,'b');
xlabel('Frequency in GHz');
ylabel('Phase of S');
grid on
xbounds = xlim;
set(gca,'XTick',xbounds(1):xbounds(2));
hold on
plot(Fghz,P21,'r');
subplot(233)
plot(Fghz,real(n),'b');
xlabel('Frequency in GHz');
ylabel('Refractive Index');
grid on
xbounds = xlim;
set(gca,'XTick',xbounds(1):xbounds(2));
hold on
plot(Fghz,imag(n),'r');
subplot(234);
plot(Fghz,real(z),'b');
xlabel('Frequency in GHz');
ylabel('Impedance');
grid on
xbounds = xlim;
set(gca,'XTick',xbounds(1):xbounds(2));
hold on
subplot(235)
plot(Fghz,real(er),'b');
xlabel('Frequency in GHz');
ylabel('Permittivity');
grid on
xbounds = xlim;
set(gca,'XTick',xbounds(1):xbounds(2));
hold on
plot(Fghz,imag(er),'r');
subplot(236);
plot(Fghz,real(mu),'b');
xlabel('Frequency in GHz');
ylabel('Permeability');
grid on
xbounds = xlim;
set(gca,'XTick',xbounds(1):xbounds(2));
hold on
plot(Fghz,imag(mu),'r');
```

References

- [1] A. Sihvola, "Metamaterials in electromagnetics," *Metamaterials*, vol. 1, pp. 2-11, 2007.
- [2] E. Plum, *Chirality and Metamaterials*, 2010.
- [3] T. J. Cui, D. Smith and R. Liu, *Metamaterials: Theory, Design, and Applications*. Springer, 2009.
- [4] V. G. Veselago, "The Electrodynamics Of Substances With Simultaneously Negative Values Of ϵ And μ ," *Physics-Uspekhi*, vol. 10, pp. 509-514, 1968.
- [5] D. R. Smith, W. J. Padilla, D. Vier, S. C. Nemat-Nasser and S. Schultz, "Composite medium with simultaneously negative permeability and permittivity," *Phys. Rev. Lett.*, vol. 84, pp. 4184, 2000.
- [6] R. W. Ziolkowski, "Design, fabrication, and testing of double negative metamaterials," *Antennae and Propagation, IEEE Transactions On*, vol. 51, pp. 1516-1529, 2003.
- [7] N. Engheta and R. W. Ziolkowski, "A positive future for double-negative metamaterials," *Microwave Theory and Techniques, IEEE Transactions On*, vol. 53, pp. 1535-1556, 2005.
- [8] A. Erentok, D. C. Vier, S. Schultz, R. W. Ziolkowski, J. A. Nielsen, R. B. Gregor, C. G. Parazzoli, M. H. Tanielian, Steven A. Cummer, Bogdan-Ioan Popa and Thomas Hand, "Low frequency lumped element-based negative index metamaterial," *Applied Physics Letters*, vol. 75, pp. 184104-184104-3, 2007.
- [9] G. V. Eleftheriades and K. G. Balmain, *Negative-Refraction Metamaterials: Fundamental Principles and Applications*. John Wiley & Sons, 2005.
- [10] Anonymous "Transformation optics and metamaterials," *Nature Materials*, vol. 9, pp. 387-396, 2010.
- [11] B. Choudhury and R. Jha, "A Review of Metamaterial Invisibility Cloaks," *CMC-Computers Materials & Continua*, vol. 33, pp. 275-308, 2013.
- [12] B. Wood, "Metamaterials and invisibility," *Comptes Rendus - Physique*, vol. 10, pp. 379-390, 2009.
- [13] C. Sabah and S. Uckun, "Multilayer system of Lorentz/Drude type metamaterials with dielectric slabs and its application to electromagnetic filters," *Progress in Electromagnetics Research*, vol. 91, pp. 349-364, 2009.

- [14] K. Aydin, I. Bulu and E. Ozbay, "Subwavelength resolution with a negative-index metamaterial superlens," *Applied Physics Letters*, vol. 75, pp. 254102-254102-3, 2007.
- [15] N. Fang and X. Zhang, "Imaging properties of a metamaterial superlens," *Appl. Phys. Lett.*, vol. 75, pp. 161-163, 2003.
- [16] A. K. Iyer and G. V. Eleftheriades, "Free-Space Imaging Beyond the Diffraction Limit Using a Veselago-Pendry Transmission-Line Metamaterial Superlens," *IEEE Transactions on Antennae and Propagation*, vol. 57, pp. 1720-1727, 2009.
- [17] G. X. Li, H. L. Tam, F. Y. Wang and K. W. Cheah, "Superlens from complementary anisotropic metamaterials," *J. Appl. Phys.*, vol. 104, pp. 116101-116101-3, 2007.
- [18] J. B. Pendry and D. R. Smith, "The Quest for the Superlens," *Scientific American [H.W. Wilson - GS]*, vol. 295, pp. 60, 2006.
- [19] R. W. Ziolkowski, P. Jin and C. Lin, "Metamaterial-inspired engineering of antennae," *Proc IEEE*, vol. 99, pp. 1720-1731, 2011.
- [20] F. Bilotti, A. Alu and L. Vegni, "Design of miniaturized metamaterial patch antennae with-negative loading," *Antennae and Propagation, IEEE Transactions On*, vol. 56, pp. 1640-1647, 2008.
- [21] P. M. Ikonen, P. Alitalo and S. A. Tretyakov, "On impedance bandwidth of resonant patch antennae implemented using structures with engineered dispersion," *Antennae and Wireless Propagation Letters, IEEE*, vol. 6, pp. 186-190, 2007.
- [22] K. Buell, H. Mosallaei and K. Sarabandi, "A substrate for small patch antennae providing tunable miniaturization factors," *Microwave Theory and Techniques, IEEE Transactions On*, vol. 54, pp. 135-146, 2006.
- [23] A. Alù, F. Bilotti, N. Engheta and L. Vegni, "Subwavelength, compact, resonant patch antennae loaded with metamaterials," *Antennae and Propagation, IEEE Transactions On*, vol. 55, pp. 13-25, 2007.
- [24] A. Sanada, M. Kimura, I. Awai, C. Caloz and T. Itoh, "A planar zeroth-order resonator antenna using a left-handed transmission line," in *Microwave Conference, 2004. 34th European*, 2004, pp. 1341-1344.
- [25] J. Park, Y. Ryu, J. Lee and J. Lee, "Epsilon negative zeroth-order resonator antenna," *Antennae and Propagation, IEEE Transactions On*, vol. 55, pp. 3710-3712, 2007.

- [26] A. Lai, K. M. Leong and T. Itoh, "Infinite wavelength resonant antennae with monopolar radiation pattern based on periodic structures," *Antennae and Propagation, IEEE Transactions On*, vol. 55, pp. 868-876, 2007.
- [27] G. Eleftheriades, M. Antoniades and F. Qureshi, "Antenna applications of negative-refractive-index transmission-line structures," *IET Microwaves, Antennae & Propagation*, vol. 1, pp. 12-22, 2007.
- [28] C. Caloz, T. Itoh and A. Rennings, "CRLH metamaterial leaky-wave and resonant antennae," *IEEE Antennae Propagation Magazine*, vol. 50, pp. 25-39, 2008.
- [29] P. Jin and R. W. Ziolkowski, "Broadband, efficient, electrically small metamaterial-inspired antennae facilitated by active near-field resonant parasitic elements," *Antennae and Propagation, IEEE Transactions On*, vol. 58, pp. 318-327, 2010.
- [30] R. W. Ziolkowski and A. D. Kipple, "Application of double negative materials to increase the power radiated by electrically small antennae," *Antennae and Propagation, IEEE Transactions On*, vol. 51, pp. 2626-2640, 2003.
- [31] H. R. Stuart and A. Pidwerbetsky, "Electrically small antenna elements using negative permittivity resonators," *Antennae and Propagation, IEEE Transactions On*, vol. 54, pp. 1644-1653, 2006.
- [32] F. Qureshi, M. A. Antoniades and G. V. Eleftheriades, "A compact and low-profile metamaterial ring antenna with vertical polarisation," *Antennae and Wireless Propagation Letters, IEEE*, vol. 4, pp. 333-336, 2005.
- [33] R. W. Ziolkowski and A. Erentok, "Metamaterial-based efficient electrically small antennae," *Antennae and Propagation, IEEE Transactions On*, vol. 54, pp. 2113-2130, 2006.
- [34] A. Erentok and R. W. Ziolkowski, "A hybrid optimization method to analyze metamaterial-based electrically small antennae," *Antennae and Propagation, IEEE Transactions On*, vol. 55, pp. 731-741, 2007.
- [35] R. Ziolkowski and A. Erentok, "At and below the Chu limit: passive and active broad bandwidth metamaterial-based electrically small antennae," *IET Microwaves, Antennae & Propagation*, vol. 1, pp. 116-128, 2007.
- [36] M. A. Antoniades and G. V. Eleftheriades, "A folded-monopole model for electrically small NRI-TL metamaterial antennae," *Antennae and Wireless Propagation Letters, IEEE*, vol. 7, pp. 425-428, 2008.
- [37] H. R. Stuart and C. Tran, "Subwavelength microwave resonators exhibiting strong coupling to radiation modes," *Appl. Phys. Lett.*, vol. 87, pp. 151108-151108-3, 2005.

- [38] R. W. Ziolkowski, "An efficient, electrically small antenna designed for VHF and UHF applications," *IEEE Antennae Wireless Propag. Lett.*, vol. 7, pp. 217-220, 2008.
- [39] D. H. Lee, A. Chauraya, Y. Vardaxoglou and W. S. Park, "A compact and low-profile tunable loop antenna integrated with inductors," *Antennae and Wireless Propagation Letters, IEEE*, vol. 7, pp. 621-624, 2008.
- [40] O. S. Kim and O. Breinbjerg, "Miniaturised self-resonant split-ring resonator antenna," *Electron. Lett.*, vol. 45, pp. 196-197, 2009.
- [41] R. W. Ziolkowski, "Efficient electrically small antenna facilitated by a near-field resonant parasitic," *Antennae and Wireless Propagation Letters, IEEE*, vol. 7, pp. 581-584, 2008.
- [42] R. Greigor, C. Parazzoli, J. A. Nielsen, M. H. Tanielian, D. Vier, S. Schultz, C. L. Holloway and R. W. Ziolkowski, "Demonstration of impedance matching using a mu-negative (MNG) metamaterial," *Antennae and Wireless Propagation Letters, IEEE*, vol. 8, pp. 92-95, 2009.
- [43] R. W. Ziolkowski, P. Jin, J. Nielsen, M. Tanielian and C. L. Holloway, "Experimental verification of Z antennae at UHF frequencies," *Antennae and Wireless Propagation Letters*, vol. 8, pp. 1329-1333, 2009.
- [44] G. Mumcu, K. Sertel and J. L. Volakis, "Miniature antenna using printed coupled lines emulating degenerate band edge crystals," *Antennae and Propagation, IEEE Transactions On*, vol. 57, pp. 1618-1624, 2009.
- [45] R. W. Ziolkowski, C. Lin, J. A. Nielsen, M. H. Tanielian and C. L. Holloway, "Design and experimental verification of a 3D magnetic EZ antenna at 300 MHz," *Antennae and Wireless Propagation Letters, IEEE*, vol. 8, pp. 989-993, 2009.
- [46] R. Remski, "Analysis of photonic bandgap surfaces using Ansoft HFSS," *MICROWAVE JOURNAL-EUROGLOBAL EDITION*-, vol. 43, pp. 190-199, 2000.
- [47] A. Erentok, P. L. Luljak and R. W. Ziolkowski, "Characterization of a volumetric metamaterial realization of an artificial magnetic conductor for antenna applications," *IEEE Transactions on Antennae and Propagation*, vol. 53, pp. 160-172, 2005.
- [48] A. Erentok, D. Lee and R. W. Ziolkowski, "Numerical analysis of a printed dipole antenna integrated with a 3D AMC block," *IEEE Antennae Wireless Propag. Lett.*, vol. 6, pp. 134-136, 2007.
- [49] S. Enoch, G. Tayeb, P. Sabouroux, N. Guérin and P. Vincent, "A metamaterial for directive emission," *Phys. Rev. Lett.*, vol. 89, pp. 213902, 2002.

- [50] S. J. Franson and R. W. Ziolkowski, "Confirmation of zero-N behavior in a high gain grid structure at millimeter-wave frequencies," *Antennae and Wireless Propagation Letters*, vol. 8, pp. 387-390, 2009.
- [51] M. A. Antoniades and G. V. Eleftheriades, "A broadband dual-mode monopole antenna using NRI-TL metamaterial loading," *Antennae and Wireless Propagation Letters, IEEE*, vol. 8, pp. 258-261, 2009.
- [52] E. Sáenz, R. Gonzalo, I. Ederra, J. C. Vardaxoglou and P. de Maagt, "Resonant meta-surface superstrate for single and multifrequency dipole antenna arrays," *Antennae and Propagation, IEEE Transactions On*, vol. 56, pp. 951-960, 2008.
- [53] F. J. Herraiz-Martínez, L. E. García-Muñoz, D. Gonzalez-Ovejero, V. Gonzalez-Posadas and D. Segovia-Vargas, "Dual-frequency printed dipole loaded with split ring resonators," *Antennae and Wireless Propagation Letters, IEEE*, vol. 8, pp. 137-140, 2009.
- [54] P. Jin and R. W. Ziolkowski, "Multi-frequency, linear and circular polarized, metamaterial-inspired, near-field resonant parasitic antennae," *Antennae and Propagation, IEEE Transactions On*, vol. 59, pp. 1446-1459, 2011.
- [55] P. Jin and R. Ziolkowski, "Multiband extensions of the electrically small, near-field resonant parasitic Z antenna," *IET Microwaves, Antennae & Propagation*, vol. 4, pp. 1016-1025, 2010.
- [56] J. Zhu, M. A. Antoniades and G. V. Eleftheriades, "A compact tri-band monopole antenna with single-cell metamaterial loading," *Antennae and Propagation, IEEE Transactions On*, vol. 58, pp. 1031-1038, 2010.
- [57] P. Jin and R. W. Ziolkowski, "Metamaterial-inspired, electrically small Huygens sources," *Antennae and Wireless Propagation Letters, IEEE*, vol. 9, pp. 501-505, 2010.
- [58] Y. Dong and T. Itoh, "Metamaterial-based antennae," *Proc IEEE*, vol. 100, pp. 2271-2285, 2012.
- [59] Y. Dong and T. Itoh, "Miniaturized substrate integrated waveguide slot antennae based on negative order resonance," *Antennae and Propagation, IEEE Transactions On*, vol. 58, pp. 3856-3864, 2010.
- [60] T. Jang, J. Choi and S. Lim, "Compact coplanar waveguide (CPW)-fed zeroth-order resonant antennae with extended bandwidth and high efficiency on vialess single layer," *Antennae and Propagation, IEEE Transactions On*, vol. 59, pp. 363-372, 2011.
- [61] Y. Dong, H. Toyao and T. Itoh, "Compact circularly-polarized patch antenna loaded with metamaterial structures," *Antennae and Propagation, IEEE Transactions On*, vol. 59, pp. 4329-4333, 2011.

- [62] A. Erentok and R. W. Ziolkowski, "Metamaterial-inspired efficient electrically small antennae," *Antennae and Propagation, IEEE Transactions On*, vol. 56, pp. 691-707, 2008.
- [63] S. R. Best, "Low Q electrically small linear and elliptical polarized spherical dipole antennae," *Antennae and Propagation, IEEE Transactions On*, vol. 53, pp. 1047-1053, 2005.
- [64] H. A. Wheeler, "The spherical coil as an inductor, shield, or antenna," *Proceedings of the IRE*, vol. 46, pp. 1595-1602, 1958.
- [65] H. R. Stuart and A. D. Yaghjian, "Approaching the lower bounds on Q for electrically small electric-dipole antennae using high permeability shells," *Antennae and Propagation, IEEE Transactions On*, vol. 58, pp. 3865-3872, 2010.
- [66] P. Jin, "Linearly and circularly polarized, planar, electrically small, metamaterial-engineered dipole antennae," in *2010 IEEE Antennae and Propagation Society International Symposium*, 2010, pp. 1-4.
- [67] P. Jin and R. W. Ziolkowski, "Low-Q, electrically small, efficient near-field resonant parasitic antennae," *Antennae and Propagation, IEEE Transactions On*, vol. 57, pp. 2548-2563, 2009.
- [68] K. B. Alici and E. Özbay, "Radiation properties of a split ring resonator and monopole composite," *Physica Status Solidi (B)*, vol. 244, pp. 1192-1196, 2007.
- [69] J. L. Volakis and K. Sertel, "Narrowband and Wideband Metamaterial Antennae Based on Degenerate Band Edge and Magnetic Photonic Crystals," *Proceedings of the IEEE*, vol. 94, pp. 1732-1745, 2011.
- [70] J. Park, Y. Ryu and J. Lee, "Mu-Zero Resonance Antenna," *IEEE Transactions on Antennae and Propagation*, vol. 54, pp. 1865-1875, 2010.
- [71] I. K. Kim and V. V. Varadan, "Electrically small, millimeter wave dual band meta-resonator antennae," *Antennae and Propagation, IEEE Transactions On*, vol. 58, pp. 3458-3463, 2010.
- [72] Y. D. Dong, T. Yang and T. Itoh, "Substrate integrated waveguide loaded by complementary split-ring resonators and its applications to miniaturized waveguide filters," *Microwave Theory and Techniques, IEEE Transactions On*, vol. 57, pp. 2211-2223, 2009.
- [73] H. Zhang, Y. Li, X. Chen, Y. Fu and N. Yuan, "Design of circular/dual-frequency linear polarisation antennae based on the anisotropic complementary split ring resonator," *Antennae and Propagation, IEEE Transactions On*, vol. 57, pp. 3352-3355, 2009.

- [74] O. S. Kim, "Low-Q electrically small spherical magnetic dipole antennae," *Antennae and Propagation, IEEE Transactions On*, vol. 58, pp. 2210-2217, 2010.
- [75] K. B. Alici and E. Ozbay, "Electrically small split ring resonator antennae," *J. Appl. Phys.*, vol. 101, pp. 083104, 2007.
- [76] Y. Dong, H. Toyao and T. Itoh, "Design and characterization of miniaturized patch antennae loaded with complementary split-ring resonators," *Antennae and Propagation, IEEE Transactions On*, vol. 60, pp. 772-785, 2012.
- [77] Fan Yang and Y. Rahmat-Samii, "Reflection phase characterizations of the EBG ground plane for low profile wire antenna applications," *IEEE Transactions on Antennae and Propagation*, vol. 51, pp. 2691-2703, 2003.
- [78] D. Sievenpiper, D. Sievenpiper, Lijun Zhang, R. F. J. Broas, N. G. Alexopolous and E. Yablonovitch, "High-impedance electromagnetic surfaces with a forbidden frequency band," *IEEE Trans. Microwave Theory Tech.*, vol. 47, pp. 2059-2074, 1999.
- [79] F. Yang, K. Ma, Y. Qian and T. Itoh, "A uniplanar compact photonic-bandgap (UC-PBG) structure and its applications for microwave circuit," *Microwave Theory and Techniques, IEEE Transactions On*, vol. 47, pp. 1509-1514, 1999.
- [80] A. E. Lamminen, A. R. Vimpri and J. Saily, "UC-EBG on LTCC for 60-GHz frequency band antenna applications," *Antennae and Propagation, IEEE Transactions On*, vol. 57, pp. 2904-2912, 2009.
- [81] A. P. Feresidis, G. Goussetis, S. Wang and J. C. Vardaxoglou, "Artificial magnetic conductor surfaces and their application to low-profile high-gain planar antennae," *Antennae and Propagation, IEEE Transactions On*, vol. 53, pp. 209-215, 2005.
- [82] G. Goussetis, A. P. Feresidis and J. C. Vardaxoglou, "Tailoring the AMC and EBG characteristics of periodic metallic arrays printed on grounded dielectric substrate," *Antennae and Propagation, IEEE Transactions On*, vol. 54, pp. 82-89, 2006.
- [83] H. Mosallaei and K. Sarabandi, "Antenna miniaturization and bandwidth enhancement using a reactive impedance substrate," *Antennae and Propagation, IEEE Transactions On*, vol. 52, pp. 2403-2414, 2004.
- [84] Y. Zhang, J. von Hagen, M. Younis, C. Fischer and W. Wiesbeck, "Planar artificial magnetic conductors and patch antennae," *Antennae and Propagation, IEEE Transactions On*, vol. 51, pp. 2704-2712, 2003.

- [85] S. Zhu and R. Langley, "Dual-band wearable textile antenna on an EBG substrate," *Antennae and Propagation, IEEE Transactions On*, vol. 57, pp. 926-935, 2009.
- [86] Y. Dong, H. Toyao and T. Itoh, "Miniaturized zeroth order resonance antenna over a reactive impedance surface," in *Antenna Technology (iWAT), 2011 International Workshop On*, 2011, pp. 58-61.
- [87] R. Haghpanahan and R. Nilavalan, "Planar quasi-yagi antenna gain enhancement using zero-index metamaterials," in *Antennae and Propagation Conference (LAPC), 2014 Loughborough*, 2014, pp. 736-739.
- [88] R. A. Shelby, D. R. Smith and S. Schultz, "Experimental Verification of a Negative Index of Refraction," *Science*, vol. 292, pp. 77-79, 2001.
- [89] C. Caloz, T. Itoh and I. Books24x7, *Electromagnetic Metamaterials: Transmission Line Theory and Microwave Applications : The Engineering Approach*. Hoboken, N.J: John Wiley & Sons, 2006.
- [90] D. R. Smith and J. B. Pendry, "Homogenization of metamaterials by field averaging," *JOSA B*, vol. 23, pp. 391-403, 2006.
- [91] R. Liu, T. J. Cui, D. Huang, B. Zhao and D. R. Smith, "Description and explanation of electromagnetic behaviors in artificial metamaterials based on effective medium theory," *Physical Review E*, vol. 76, pp. 026606, 2007.
- [92] D. R. Smith, D. C. Vier, T. Koschny and C. M. Soukoulis, "Electromagnetic parameter retrieval from inhomogeneous metamaterials," *Physical Review E, Statistical, Nonlinear, and Soft Matter Physics*, vol. 71, pp. 036617, 2005.
- [93] J. Pendry, A. Holden, D. Robbins and W. Stewart, "Magnetism from conductors and enhanced nonlinear phenomena," *IEEE Trans. Microwave Theory Tech.*, vol. 47, pp. 2075-2084, 1999.
- [94] F. Capolino, *Theory and Phenomena of Metamaterials*. CRC Press, 2009.
- [95] J. D. Jackson, *Classical Electrodynamics*. London (etc.): Wiley, 1975.
- [96] L. D. Landau, E. M. Lifšic, J. B. Sykes, J. S. Bell, M. Kearsley and L. P. Pitaevskii, *Electrodynamics of Continuous Media*. Pergamon press Oxford, 1960.
- [97] T. Koschny, P. Markoš, D. Smith and C. Soukoulis, "Resonant and antiresonant frequency dependence of the effective parameters of metamaterials," *Physical Review E*, vol. 68, pp. 065602, 2003.
- [98] K. Aydin, I. Bulu, K. Guven, M. Kafesaki, C. M. Soukoulis and E. Ozbay, "Investigation of magnetic resonances for different split-ring resonator parameters and designs," *New Journal of Physics*, vol. 7, pp. 168-168, 2005.

- [99] C. R. Simovski, "Bloch material parameters of magneto-dielectric metamaterials and the concept of Bloch lattices," *Metamaterials*, vol. 1, pp. 62-80, 2007.
- [100] C. R. Simovski and S. A. Tretyakov, "Local constitutive parameters of metamaterials from an effective-medium perspective," *Physical Review B*, vol. 75, pp. 195111, 2007.
- [101] R. Liu, T. J. Cui, D. Huang, B. Zhao and D. R. Smith, "Description and explanation of electromagnetic behaviors in artificial metamaterials based on effective medium theory," *Physical Review E*, vol. 76, pp. 026606, 2007.
- [102] A. M. Nicolson and G. F. Ross, "Measurement of the Intrinsic Properties of Materials by Time-Domain Techniques," *IEEE Transactions on Instrumentation and Measurement*, vol. 19, pp. 377-382, 1970.
- [103] N. Patel. Theory, Simulation, Fabrication and Testing of Double Negative and Epsilon Near Zero Metamaterials for Microwave Applications. 2008.
- [104] R. W. Ziolkowski, "Design, fabrication, and testing of double negative metamaterials," *IEEE Transactions on Antennae and Propagation*, vol. 51, pp. 1516-1529, 2003.
- [105] D. M. Pozar, "Microwave engineering, 3rd," *Danvers, MA: Wiley*, 2005.
- [106] X. Wu, *Experimental and Theoretical Study of Microwave Heating of Thermal Runaway Materials*, 2002.
- [107] A. Lai, T. Itoh and C. Caloz, "Composite right/left-handed transmission line metamaterials," *Microwave Magazine, IEEE*, vol. 5, pp. 34-50, 2004.
- [108] C. Caloz and T. Itoh, *Electromagnetic Metamaterials: Transmission Line Theory and Microwave Applications*. John Wiley & Sons, 2005.
- [109] J. Hao, W. Yan and M. Qiu, "Super-reflection and cloaking based on zero index metamaterial," *Appl. Phys. Lett.*, vol. 96, pp. 101109, 2010.
- [110] H. Zhou, Z. Pei, S. Qu, S. Zhang, J. Wang, Q. Li and Z. Xu, "A planar zero-index metamaterial for directive emission," *Journal of Electromagnetic Waves and Applications*, vol. 23, pp. 953-962, 2009.
- [111] B. Wu, W. Wang, J. Pacheco, X. Chen, T. M. Grzegorzczuk and J. A. Kong, "A study of using metamaterials as antenna substrate to enhance gain," *Progress in Electromagnetics Research*, vol. 51, pp. 295-328, 2005.
- [112] Q. Wu, P. Pan, F. Meng, L. Li and J. Wu, "A novel flat lens horn antenna designed based on zero refraction principle of metamaterials," *Applied Physics A*, vol. 87, pp. 151-156, 2007.

- [113] G. Lovat, P. Burghignoli, F. Capolino, D. R. Jackson and D. R. Wilton, "Analysis of directive radiation from a line source in a metamaterial slab with low permittivity," *Antennae and Propagation, IEEE Transactions On*, vol. 54, pp. 1017-1030, 2006.
- [114] C. Tsao and J. Chern, "Field propagation of a metallic grid slab that acts as a metamaterial," *Physics Letters A*, vol. 353, pp. 171-178, 2006.
- [115] Y. Yuan, L. Shen, L. Ran, T. Jiang, J. Huangfu and J. A. Kong, "Directive emission based on anisotropic metamaterials," *Physical Review A*, vol. 77, pp. 053821, 2008.
- [116] Y. Ma, P. Wang, X. Chen and C. Ong, "Near-field plane-wave-like beam emitting antenna fabricated by anisotropic metamaterial," *Appl. Phys. Lett.*, vol. 94, pp. 044107, 2009.
- [117] J. Pendry, A. Holden, D. Robbins and W. Stewart, "Low frequency plasmons in thin-wire structures," *Journal of Physics: Condensed Matter*, vol. 10, pp. 4785, 1998.
- [118] Y. Itin, "Dispersion relation for electromagnetic waves in anisotropic media," *Physics Letters A*, vol. 374, pp. 1113-1116, 2010.
- [119] Z. H. Jiang, M. D. Gregory and D. H. Werner, "Broadband high directivity multibeam emission through transformation optics-enabled metamaterial lenses," *Antennae and Propagation, IEEE Transactions On*, vol. 60, pp. 5063-5074, 2012.
- [120] B. Zhou and T. Cui, "Directivity Enhancement to Vivaldi Antennae Using Compactly Anisotropic Zero-Index Metamaterials," *IEEE Antennae and Wireless Propagation Letters*, vol. 10, pp. 326-329, 2011.
- [121] C. A. Balanis, *Antenna Theory: Analysis and Design*. Hoboken, NJ: John Wiley, 2005.
- [122] C. A. Balanis, *Advanced Engineering Electromagnetics*. Hoboken, NJ: John Wiley & Sons, 1989.
- [123] L. G. Maloratsky, "Using Modified Microstrip Lines to Improve Circuit Performance," 2011.
- [124] J. B. Pendry, D. Schurig and D. R. Smith, "Controlling electromagnetic fields," *Science*, vol. 312, pp. 1780-1782, Jun 23, 2006.
- [125] D. Smith, S. Schultz, P. Markoš and C. Soukoulis, "Determination of effective permittivity and permeability of metamaterials from reflection and transmission coefficients," *Physical Review B*, vol. 65, pp. 195104, 2002.

- [126] M. Rahm, S. A. Cummer, D. Schurig, J. B. Pendry and D. R. Smith, "Optical design of reflectionless complex media by finite embedded coordinate transformations," *Phys. Rev. Lett.*, vol. 100, pp. 063903, 2008.
- [127] U. Leonhardt and T. G. Philbin, "General relativity in electrical engineering," *New Journal of Physics*, vol. 8, pp. 247, 2006.
- [128] U. Leonhardt and T. G. Philbin, "Transformation optics and the geometry of light," *Progress in Optics*, vol. 53, pp. 69-152, 2009.
- [129] D. Schurig, J. Pendry and D. R. Smith, "Calculation of material properties and ray tracing in transformation media," *Optics Express*, vol. 14, pp. 9794-9804, 2006.
- [130] G. W. Milton, M. Briane and J. R. Willis, "On cloaking for elasticity and physical equations with a transformation invariant form," *New Journal of Physics*, vol. 8, pp. 248, 2006.
- [131] N. Kaneda, W. Deal, Y. Qian, R. Waterhouse and T. Itoh, "A broadband planar quasi-Yagi antenna," *Antennae and Propagation, IEEE Transactions On*, vol. 50, pp. 1158-1160, 2002.
- [132] H. Song, M. Bialkowski and P. Kabacik, "Parameter study of a broadband uniplanar quasi-yagi antenna," in *Microwaves, Radar and Wireless Communications. 2000. MIKON-2000. 13th International Conference On*, 2000, pp. 166-169.
- [133] J. Sor, *Analysis of the Quasi-Yagi Antenna for Phased-Array Applications*, 2000.
- [134] Anonymous "The physics classroom," .
- [135] F. J. Dyson, "The S Matrix in Quantum Electrodynamics," *Physical Review*, vol. 75, pp. 1736-1755, 1949.
- [136] J. Dowling and J. Geabanacloche, "The Specular Reflection of Light off Light," *American Journal of Physics*, vol. 60, pp. 28-34, 1992.
- [137] U. Leonhardt, "Notes on waves with negative phase velocity," *IEEE Journal of Selected Topics in Quantum Electronics*, vol. 9, pp. 102-105, 2003.
- [138] D. R. Smith, D. C. Vier, T. Koschny and C. M. Soukoulis, "Electromagnetic parameter retrieval from inhomogeneous metamaterials," *Physical Review.E, Statistical, Nonlinear, and Soft Matter Physics*, vol. 71, pp. 036617, 2005.
- [139] K. W. Eccleston and K. W. Eccleston, "Beam forming using a zero-phase-shift metamaterial," in 2008, pp. 1-4.

- [140] A. Lai, K. M. K. H. Leong and T. Itoh, "A novel N-port series divider using infinite wavelength phenomena," in 2005, pp. 4 pp.
- [141] D. Seetharamdoo, R. Sauleau, K. Mahdjoubi and A. Tarot, "Effective parameters of resonant negative refractive index metamaterials: Interpretation and validity," *J. Appl. Phys.*, vol. 104, pp. 063505-063505-4, 2005.
- [142] S. Arslanagic, T. V. Hansen, N. A. Mortensen, A. H. Gregersen, O. Sigmund, R. Ziolkowski and O. Breinbjerg, "A review of the scattering-parameter extraction method with clarification of ambiguity issues in relation to metamaterial homogenization," *Antennae and Propagation Magazine, IEEE*, vol. 55, pp. 91-106, 2013.
- [143] G. L. Matthaei, L. Young and E. M. Jones, *Design of Microwave Filters, Impedance-matching Networks, and Coupling Structures. Volume 2*, 1963.
- [144] Anonymous "Practical genetic algorithms, 2d ed. (CD-ROM included)," *Scitech Book News*, vol. 28, 2004.
- [145] R. L. Haupt and D. H. Werner, *Genetic Algorithms in Electromagnetics*. US: Wiley-IEEE Press, 2007.
- [146] C. Kittel, *Introduction to Solid State Physics*. New Jersey: John Wiley & Sons, 2005.
- [147] F. Yang and Y. Rahmat-Samii, "Reflection phase characterizations of the EBG ground plane for low profile wire antenna applications," *IEEE Transactions on Antennae and Propagation*, vol. 51, pp. 2691-2703, 2003.
- [148] J. Broeng, D. Mogilevstev, S. E. Barkou and A. Bjarklev, "Photonic crystal fibers: A new class of optical waveguides," *Optical Fiber Technology*, vol. 5, pp. 305-330, 1999.
- [149] N. M. N. Ashcroft, Ed., *Solid State Physics*. Orlando: Saunders College, 1976.
- [150] A. Lai, *Left-Handed Metamaterials for Microwave Engineering Applications*, 2009.
- [151] Ansoft Corporation, *An Introduction to HFSS, Fundamental Principles, Concepts, and Use*. Pittsburgh, PA 15219: Ansoft, LLC., 2009.
- [152] Ansoft Corporation, Ed., *Left-Handed Metamaterial Design Guide*. Pittsburgh, PA 15219, USA: Ansoft LLC, 2007.
- [153] Ansoft Corporation, *user's Guide – High Frequency Structure Simulator* Pittsburgh, PA 15219, USA: Ansoft, LLC, June, 2005.

[154] F. Yang and Y. Rahmat-Samii, "Reflection phase characterizations of the EBG ground plane for low profile wire antenna applications," *IEEE Transactions on Antennae and Propagation*, vol. 51, pp. 2691-2703, 2003.

[155] R. Remski, M. Commens and J. Silvestro, "Techniques for Analyzing Antenna Lattice Structures," .

[156] R. Remski, "Analysis of photonic bandgap surfaces using Ansoft HFSS," *Microwave Journal-Euroglobal Edition*, vol. 43, pp. 190-199, 2000.